Life Together: Modeling the Collective Behavior of Cellular Communities

Katherine Owens

A dissertation
submitted in partial fulfillment of the
requirements for the degree of

Doctor of Philosophy

University of Washington

2022

Reading Committee:

J. Nathan Kutz, Chair

Ivana Bozic, Chair

Prof. Aimée Dudley

Program Authorized to Offer Degree:
UW Applied Mathematics

University of Washington

Abstract

Life Together: Modeling the Collective Behavior of Cellular Communities

Katherine Owens

Co-Chairs of the Supervisory Committee:
Robert Bolles and Yasuko Endo Professor J. Nathan Kutz
Applied Mathematics

Assistant Professor Ivana Bozic
Applied Mathematics

Our lives as eukaryotic organisms are defined by the collective behaviors of cellular systems. Together groups of cells form intricate structures and accomplish complex tasks. Where an individual cell cycles through growth, reproduction, and death, a group of cells can live more richly. Among other functions, multicellular communities form patterns, share resources, colonize new environments, and even communicate. In this work, I deploy data-driven and classical modeling techniques to understand these collective behaviors in three contexts. First, I consider synchronization in networks of coupled oscillators. Can we learn the rules governing patterns of group behavior exclusively from measurements of the state of the individuals? Towards this goal, I develop a data-driven method for coarse-graining system dynamics even under conditions of spatio-temporal heterogeneity. Next I model tumor growth and it's mitigation via CAR T-cell therapy, a novel cellular based immunotherapy. I develop an ordinary differential equation model for testing combinations of chemotherapeutic preconditioning and CAR T-cell infusion for treating blood cancers. Simulation results and sensitivity analysis support several potential refinements to current clinical protocols. I then extend this ODE model into a reaction-diffusion model, which I use to test local administration of CAR T-cells for the treatment of solid tumors. These simulations suggest that the optimal mode of local administration depends on tumor growth characteristics. In the final chapter, I present a pipeline for high-throughput phenotype

quantification from images of yeast patches, including the complexity of pattern formation. I implemented this algorithm in an open source python package, PyPl8, which has enabled novel genetic analysis.

TABLE OF CONTENTS

Page

LIST OF FIGURES

ACKNOWLEDGMENTS

I am deeply grateful for my friends, colleagues, teachers, and mentors from the University of Washington department of Applied Mathematics. Thank you for helping me grow as a mathematician, scientist, and human. This body of work would not exist without the guidance, encouragement, and support of many.

In my year in the masters program at UW, I felt welcomed and valued enough to continue in the field. Every insightful office hour, collaborative homework session, late-night Lewis chat, and soccer game with the first-year cohort helped me feel like I belonged. I appreciate the students ahead of me in the program, who gave me personal and professional advice, shared many mugs of tea, and helped me envision what the next steps would look like. To my PhD cohort, thank you. You got me through the season of homework and qualifying exams and generally figuring out what research was all about. Your questions and enthusiasm inspired me, especially in moments of doubt. Through happy hours, office chats, and lunch dates I am happy to have become not just math friends, but life-long friends who also like to talk about math. Particular thanks to Nora, Diya, and Micah. I am lucky to have entered this program alongside you and benefited from your intelligence, humor, kindness, and baking prowess.

I would like to thank Aimée and all the members of the Dudley Lab: Russell, Gareth, Michelle, Lauren, Marty, Julee, Michael, and Kevin. You have welcomed me into your team, taught me a lot of cool genetics, and given me space to learn the skills I needed to contribute. Your trust and patience was a gift. It is an honor to collaborate with you all. I would also like to thank Andrew for his help getting PyPl8 up and running!

A huge thank you goes to my co-advisor Ivana for guiding me in my CAR T-cell modeling efforts. Your insightful questions pushed these projects to be more interesting and relevant, and your patient leadership as I stumbled through the publication process for the first

time taught me many valuable lessons. I would also like to thank Amin for being a great collaborator in developing our PDE model, and for being a great friend.

I cannot express enough gratitude to my co-advisor Nathan for his support and guidance through the years. From before I even arrived at UW to the last months preparing for my defense, you have always been there with optimism, good advice, and, of course, good coffee. Thank you for helping me build confidence as a researcher and grow professionally, while also meeting me where I was at as a person each week.

Thank you also to my friends outside of the applied math department, especially those who have stuck with me during the early homework years of grad school and these last few thesis months. Whether on a walk, over a picnic, or on a zoom call, so many people have kept me grounded and balanced.

Thank you to my extended family, the Schulz and Lacy clans. You have always believed in me and showed me that it's cool to be nerdy.

Thank you to my second family, David, Tina, Devan and Sam. I continually marvel at the luck I have in joining you.

Thank you to my parents. Mom and Dad, you taught me the value of hard work and modeled approaching the world with curiosity, gentleness, and grace. I am blessed to be your daughter.

Thank you to my sisters. Megan, you have always blazed the trail in life with confidence and care. I am lucky to follow in your foot steps. Brianna, you have been by my side since before day one. You inspire me to grow towards the best version of myself–more accepting, more thoughtful, more diligent and sillier in a good way.

Finally, thank you to Colin. Luckily for me, my five years in a PhD program have coincided with five years of marriage to a patient, steady, and wise man. Your love anchors me. Your humor delights me. I am excited for the next five years and beyond.

DEDICATION

to my community,

and in particular to my husband Colin.

It is a gift to share a life together with you.

Chapter 1

INTRODUCTION

1.1 Multi-scale biology

When studying a biological system, whether you are considering the fundamental unit of life, an individual cell, or a large population in ecology, you are bound to observe the motif of simple individual behaviors on one scale leading to interesting group behaviors at a larger scale. A multi-scale perspective postulates that behavior at a larger scale emerges naturally from collective action at smaller scales. This outlook has led to great progress advancing physics by studying atoms, chemistry by studying molecules, and biology by studying genes. However, in biology when we build models from the bottom up, ascending time and spatial scales, we consistently encounter the clichéd reality that the whole is greater than the sum of its parts. We refer to this phenomenon as emergent behavior or emergence. Philosophically, "emergence occurs when an entity is observed to have properties its parts do not have on their own [67]." We may try to study the building blocks of biology in isolation, but observations we make are not guaranteed to hold true in a real cell or in a real organism. This makes it challenging to lift strategies from physics and chemistry and apply them directly to problems in biology. However, by working closely with biologists, remaining rooted in high quality data, and customizing mathematical tools to the system in question, we can still build insightful models.

In this thesis, I specifically focus on biological scenarios that span the level between individual cells and populations of interacting cells. I use mathematical tools to predict and provide insight into the macroscale behaviors of cellular communities. In particular, I consider three potential collective behaviors: synchronization in networks of coupled oscillators, tumor growth or eradication in immunotherapy for cancer treatment, and pattern-formation in yeast colonies.

1.1.1 Synchronization

Dynamical systems on networks provide a rich theoretical playground for the study of emergent behavior. In this context, a network is a collection of entities, or nodes, which are connected to each other via edges in a meaningful way. The state of each node obeys its own internal ordinary differential equation, so studying the dynamics of the whole network entails studying a large system of coupled ODEs. The structure of the network encodes which nodes interact with each other, and the governing ODEs define the nature of the interactions. Over time, in systems with sufficient coupling between neighbors, collective behavior patterns such as mode-locking lasers [63], swarming birds [33], or a pandemic [12], may appear in the population. In Chapter 2, I will consider networks of oscillators. This class of dynamical system has been widely studied in varied forms [99, 167, 150, 142].

Networked oscillators model multiscale networks of interacting periodic processes. Many systems in biology including cellular and metabolic networks, neuronal networks, and myocardial muscle cell contractions are governed by such processes. The function–or dysfunction–of these networks depends on the collective dynamics of the interacting oscillatory individuals. One of the most prominent collective behaviors of an oscillator network occurs when nodes synchronize and oscillate in unison. Synchrony could mean phase synchrony where the states align exactly, or frequency synchrony where the oscillators' frequencies coincide, and it may be global or localized.

In many biological applications, we don't necessarily understand how synchrony leads to function, but it appears to be important. For example, some level of synchrony is observed in the brain across multiple scales [178]. At the same time, abnormal synchrony patterns are associated with malfunction in disorders such as epilepsy and Parkinson's disease [61].

1.1.2 Growth

Growth models are among the earliest applications of mathematical biology, arguably starting with Fibonacci's counting of rabbit reproduction in 1202. Simple exponential models of bacterial replication or tumor growth have been widely used in industrial and medical settings. In particular in Chapter 3, I will build models that involve cancerous tumor

growth.

Cancer results from a number of changes (mutations) in the genes in our body that control cell growth or regulate the detection and repair of DNA damage. Normal organ function depends on successful regulation of cell death and division. Unlike healthy cells, cancer cells ignore signals to stop dividing, to specialize, or to die and be shed. Instead cancer cells grow in an uncontrollable manner and, unable to recognize their own natural boundary, can spread to areas of the body where they do not belong. As a tumor grows and becomes established, it shapes the normal cells, molecules, and blood vessels that surround and feed it. The dynamic interactions of cancer cells with their microenvironment stimulate the heterogeneity of cancer cells, driving clonal evolution which can increase multidrug resistance ending in cancer cell progression and metastasis.

Cancer treatments aim to interfere with these processes, eliminating malignant cells and restoring the body to health. Adoptive cellular therapies like CAR T-cell therapy, which we will consider in Chapter 3, introduce engineered immune cells that have an improved ability to recognize and destroy tumor cells into the patient's body. I will consider cellular therapies through the lens of a predator-prey system in which immune cells are the predators and tumor cells are the prey. In practice, clinicians have control over how and when the immune cells are introduced. Formulating a dynamic model allows us to study potential treatment plans with tools from nonlinear dynamical systems. Models can inform the creation of treatment plans by predicting how the two cell populations will co-evolve depending on the tumor state and the drug dosage.

1.1.3 Pattern formation

Pattern formation, or the development of visibly ordered outcomes through self-organization in a system, has fascinated mathematicians from the outset of mathematical biology. In his landmark 1952 paper, "The Chemical Basis of Morphogenesis," Turing proposed a model wherein two homogeneously distributed substances interact to produce stable patterns during morphogenesis (the creation of diverse anatomies from similar genes) [176]. Turing was interested in learning how patterns in nature, such as stripes and spots, can arise naturally

and autonomously from a homogeneous, uniform state. Subsequent generations of mathematical biologists continued to use reaction-diffusion models to try to elucidate the role of chemical processes in development [124, 115]. Subsequently, Jim Murray and contemporaries pioneered alternative mechanical models of pattern formation. They showed that the coordinated movement of cell populations governed by chemotaxis, haptotaxis, contact guidance, contact inhibition, etc. were sufficient to produce regular patterned aggregates of cells [123]. Numerical simulation of mechanochemical PDEs remain a leading method for studying pattern formation across temporal and spatial scales, from animal coat patterning to the structure of slime molds.

In Chapter 4 of this work, I present a method for quantifying the complexity of pattern formation in yeast colonies. The macroscopic behaviors of microbial communities present fascinating examples of emergent pattern formation. One such behavior is the formation of biofilms, organized groups of microbial cells adhering to a surface. These communities are ubiquitous–humans and all other higher organisms are colonized by microorganisms which form biofilms. Better understanding of their structure and function is of great interest to healthcare and other industries. Bacterial biofilms have been studied in detail and are known to facilitate sophisticated social behaviors. In contrast, the formation of fungal biofilms, like wrinkled textures on yeast colonies, is less well studied. In either case, the complex structures formed by microbial communities make an excellent case study for a multi-cellular, cooperative developmental process.

1.2 Mathematical modeling in biology

The application of mathematical models in biology and medicine has a long and storied history. A sparse number of papers in the first half of the twentieth century established theoretical roots for the field, with many crediting the origins to D'Arcy Thompson's 1917 book "On Form and Function" [173]. Decades of struggle in the cultural divide between the mathematical and the biological sciences followed, though particular inroads were made in ecology where Lotka and Volterra modeled fluctuating animal populations [106, 182], in epidemiology with Kermack and McKendrick's epidemic modeling [87], physiology with models of morphogenesis from Turing [176], enzyme kinetics from Michaelis and Menten

[116] and firing neurons from Hodgkin and Huxley [66], and population genetics with Fisher and Haldane's work towards quantifying natural selection [50, 60]. The first professional society in the field, *The Society for Mathematical Biology*, was founded in 1973 by Nicholas Rashevsky and students. Not coincidentally, the rise of the nascent field coincided with the maturation of nonlinear dynamics and chaos theory–necessary tools for modeling many of the complex phenomena displayed by living systems. The ongoing growth of computational power has also broadened the field, allowing for the productive study of complicated models through numerical simulation. Today, mathematical biology is a vast discipline with thousands of active researchers. Within the scientific community, there is an increasing interest in *in silico* experimentation due to ethical considerations, risk, unreliability and other complications involved in human and animal research. We are also at an exciting frontier in biological data. Increasingly, experimentalists are collecting the highly resolved spatiotemporal data that will unlock new modeling possibilities.

Mathematical biology seeks to understand and predict a diverse set of phenomena, that (as of yet) are not derived from a few simple principles. Translating biological questions into mathematical equations requires numerous context-specific assumptions. Evolution develops complex, nuanced ways to accomplish the same task different ways in different species and strains. This makes it difficult to discover fundamental, universal structural relationships. However, it also opens opportunities for the use of diverse mathematical methods. The complexity of living systems has pushed the field of mathematical biology to expand to incorporate tools from many branches of mathematics, and has contributed to the development of new mathematical techniques. I will briefly introduce the concept of dynamic models and survey some of the most common continuous time modeling paradigms.

Dynamic models are simplified representations of some real-world entity formulated as equations or logical rules that describe how system properties change over time. Mathematics, computation, and computer simulations can all be used to analyze models, producing results that shed light on the study system. Such models are valuable because they allow us to examine relationships that could not be disambiguated by purely experimental approaches, and to forecast future system behavior in situations beyond interpolating existing data points. Dynamic models consist of two components: **state variables** that summarize

the properties of interest in the study system, and **dynamic equations** that specify how the state variables change over time as a function of the current and past values of the state variables. Because a dynamic model is built to reflect the processes driving system behavior, it can be used to make predictions in circumstances where the same causal processes are presumed to operate. This provides a basis for predicting long-term trends in a system.

Generally, dynamic models in biology can be classified depending on the form of the dynamic equations. Models may operate in continuous or discrete time, and potential outcomes may be deterministic or stochastic. From a design standpoint, we can also classify models as practical vs. theoretical. A practical model is built to inform a concrete goal such as resource management, design, and prediction. In this context, quantitative numerical accuracy is likely essential. At the other end of the spectrum, a purely theoretical model serves the goal of deepening theoretical understanding and developing theories about how a system operates or behaves. In this context, many irrelevant details can be ignored and we are likely most interested in qualitative or relative outcomes. Here, we review some modeling paradigms commonly used in mathematical biology.

To model systems with continuous time and spatially homogeneous dynamics in a deterministic manner, we use Ordinary Differential Equations (ODEs). Generically, these systems take the form

$$\frac{\mathrm{d}\mathbf{x}}{\mathrm{d}t} = f(\mathbf{x}) \tag{1.1}$$

where $\mathbf{x} \in \mathbb{R}^n$ contains the state variables and the governing dynamics, f, can be a linear or nonlinear function of the state variables. For nonlinear functions f, these models often cannot be solved analytically. However, we can determine qualitative behaviors of solutions by finding fixed points of the system (x^* such that $f(\mathbf{x}^*) = 0$) and analyzing their stability by locally linearizing the dynamics. Bifurcation theory and center manifold reductions provide tools for characterizing model dependence on parameters and can capture key regime changes that occur in natural systems. The maturation of nonlinear dynamics and chaos theory was pivotal for the expansion of mathematical biology as a field because of the nonlinear nature of many biological processes. Some examples of well-known ODE models include the Lotka-Volterra predator-prey model put forward for fitting fluctuations in species

populations, the Susceptible-Infected-Recovered models for epidemics based on Kermack and McKendrick's seminal paper, and the logistic function for density-dependent growth proposed by Verhulst. Each of these classical examples are highly simplified, but influential and informative models. At the other end of the spectrum, ODE models can also be intricate and high dimensional, including tens or even hundreds of state variables to represent all of the elements in a system of interest. Often termed compartmental models, these are of notable use in the drug industry for the study of pharmacokinetics. That is the study of the absorption, redistribution, and transformation of drugs or other ingested systems within the body. Modeling these processes in a quantitatively accurate manner is essential in clinical trial design because it allows researchers to extrapolate experimental data from one species (rats) to another (humans), as well as to extrapolate effects and from low drug doses to high doses. Though ODEs provide a flexible and easily implemented tool, they do rest on a key assumption: well mixed state variables. This assumption of spatial homogeneity simply does not hold for many systems in biology.

In order to allow for spatial heterogeneity in a system, but still work with continuous time and deterministic dynamics, a modeler can turn to the tools of Partial Differential Equations. PDE models consider the time evolution of the state variables to be a function not just of the state, but also of spatial derivatives. Generically

$$\frac{\partial u}{\partial t} = N[u] \tag{1.2}$$

where now the state of the system is a continuous function $u(x,t)$, and the dynamics are given by N, a, possibly nonlinear, differential operator. As with ODE models, we use tools like linear stability analysis and bifurcation theory to characterize system behavior. In this case instead of looking for stationary *states* we are interested in the stability of stationary *solutions*, $u(x,t) = u^*(x)$, or we may be looking for structures like travelling wave solutions. For example, Fisher described the spread of an advantageous gene through a population by pairing diffusion with logistic growth

$$\frac{\partial u}{\partial t} = D\frac{\partial^2 u}{\partial x^2} + au(1-u). \tag{1.3}$$

For every wave speed $c \geq 2\sqrt{aD}$, Fisher's equation admits travelling wave solutions of the form $u(x,t) = v(x \pm ct)$ as the solution switches from the equilibrium state $u = 0$ (gene

is absent) to the equilibrium state $u = 1$ (gene is universal) across the spatial domain. Other notable uses of PDEs in mathematical biology include the reaction diffusion models of Turing patterns, models for pattern formation in ecology, and models of aspects of tumor development like angiogenesis or diffusive growth. The numerical lift necessary to simulate PDEs of interest on asymmetrical, biologically relevent domains is heavier than for ODEs, but certainly possible with finite element methods. For example, Swanson et al. successfully fit models of glioma growth to brain scans from real patients, using the outline of the brain as their computational domain [168]. For many systems of biological interest, deterministic dynamics are based on simplifications. In particular, they neglect noise, which is inherent to biological processes. Often these simplifications still yield informative results. However, where the copy numbers of involved components are small and random fluctuations are thus significant, we may require different tools.

For some systems in biology it is desirable to introduce a stochastic element to the dynamic equations. This might be the case if we truly believe the underlying causal processes are random. For example, experiments at the cellular level show that individual cell dynamics are intrinsically noisy. Or it could be that there are factors influencing our system that we do not understand or cannot measure accurately which we want to represent with some degree of noise. Incorporating stochasticity into a model may enhance, diminish, or even completely change the system behavior. A common stochastic version of an ordinary differential equation is to perturb the right hand side with a term dependent on a white noise variable. This class of stochastic differential equations has the general form

$$dX_t = \mu(X_t, t)dt + \sigma(X_t, t)dW_t. \tag{1.4}$$

where dW_t denotes the differential form of Brownian motion. Now the current state of the system at time t is a random variable, X_t, which depends on a deterministic component of the dynamics, μ, often called the drift and a non-deterministic component, σ, often called the diffusion term. Working with the differential form of Brownian motion requires the development of stochastic calculus. However, intuitively, the form of writing the system dynamics shown in Eq. 1.4 suggests a scheme for simulation: given the current state X_t, calculate the deterministic update as you would with an ODE, draw a random variable to

determine the direction of the Brownian motion, and update the stochastic component of the dynamics accordingly. One could then use this scheme to simulate many possible state trajectories in time and compute features of the resulting distribution. A modeler could be interested in expected solution paths and features like expected stopping or crossing times. When the population consists of a small number of individuals, say in studying a population of endangered species, the stochastic components of dynamics may strongly influence important quantities like extinction probability. So far we have considered systems with state variables that change continuously in time. However, if we are considering finite population sizes and accounting for individuals within a biological system, then the populations may be best described by discrete states.

For stochastic systems that occupy discrete states, we can model dynamics using Markov chains. For example, we might be counting the individual number of cells in a petri dish, tracking population dynamics in a wild orca community, or monitoring whether a receptor is bound or unbound (as Michaelis and Menten measured to derive their model of enzyme kinetics). A Markov chain is a mathematical system that experiences transitions from one state to another according to certain probabilistic rules. The defining characteristic of a Markov chain is that the probability of each future event depends only on the present state. Because of this "memorylessness", the transition probabilities from one moment in time to the next can be encoded in a transition matrix for discrete time systems or in a transition rate matrix for continuous time systems. For simplicity, let's think about a discrete-time system with state X_n at time n. In this case, the dynamic rules are encoded in the transition matrix, P, where entry $p_{ji} = Prob\{X_{n+1} = j | X_n = i\}$. The transition matrix P has dimension equal to the number of possible states, which may be finite or countably infinite. One common example of a Markov chain in biology is a birth-death process. In this case think of X_n as the number of individuals in the population at time n. Suppose that over a given time step, the population can increase by one if a birth event occurs, say with probability p_i, decrease by one if a death event occurs, say with probability

d_i, or stay the same if neither event occurs. So, for this system

$$p_{ji} = \begin{cases} b_i & j = i+1 \\ d_i & j = i-1 \\ 1-(b_i+d_i) & j = i \\ 0 & \text{otherwise.} \end{cases}$$

To translate this concept to continuous time, we introduce an exponential random variable to track the waiting time between events, then determine the event according to a discrete time markov chain. Continuous time birth-death processes have been used to model viral phylogenies, with births representing the initiation of new strains of the virus [108]. Along with closely related branching process models, they have been used to model finite populations of tumor cells, or other populations of interest [9, 133]. To characterize the behavior of these models, we can calculate stationary distributions or other properties like hitting times. As in the case of Michaelis-Menten enzyme kinetics, we can write down probabalistic rules for the behavior of a system with a finite number of individuals, N, and in the limit of large N, the dynamics look more and more deterministic, often recovering familiar ODEs from population level models.

Another intuitive approach to take when thinking about emergent behavior based on rules set at an individual level leads to the formulation of agent-based models. The idea of this paradigm is to assign individuals in a system their own intrinsic dynamics and local update rules, and then track the state of all of these individuals or agents over time. The local update rules may be deterministic, stochastic, or a combination of both. In any case, we can program the desired logic into our agents, watch the system evolve in time, and study the macroscale patterns that emerge at the population level. Notably, agent based simulations have been used to model starling murmurations and other swarming behaviors. Modelers showed that based solely on local update rules, the population can exhibit complex swirling patterns [31]. There is no need for a universal leader or conductor. Agent based models have been applied widely in the fields of ecology and epidemiology [78, 72]. These types of models can be computationally intensive, but yield interesting and powerful results.

Choosing any of the above modeling formats guides the types of questions that we can

pose and answer about a system of interest. A model codifies a hypothesis about the study system and lets you compare that hypothesis with data. Can given processes account for an observed pattern? Which of several contested assumptions is best able to account for the data? If we know that certain processes occur, what patterns do we expect to see? Knowing what to look for may help guide experiments. Although mathematics can never provide a complete solution to a biological problem on it's own, models can be useful in so far as they allow us to test hypotheses and make predictions. The most successful modeling efforts have been interdisciplinary partnerships where experiment and theory inform each other. At it's best, mathematical biology has the potential to inform medical practice, shape conservation efforts, and deepen basic biological understanding.

1.2.1 Data-driven modeling

With all these mathematical methods available to us, what makes something mathematical *biology* specifically? How do we decide whether a set of equations are biologically relevant? In data-driven modeling, data serves as our guide to answering these questions. Selecting a model in a data-driven manner involves testing multiple potential models (often formed from different hypotheses about underlying mechanisms) and selecting one based on the best fit to the available data. A natural follow-up question is what criteria make a model the "best"? The unsatisfactory answer is of course, it depends. Given a chosen form of a model and sufficient data, we can use statistical methods like curve fitting, maximum likelihood estimates, or Bayesian model fitting, to determine the specific model parameters that yield the best quantitative agreement between that model and data. The latter two methods involve making some assumptions about the noise in the measurements against which we are comparing model behavior. An additional challenge for data-driven multi-scale model selection is whether to treat each scale separately, and how to match dynamics at the interface between scales. Prioritizing the agreement between the model predictions and data is one option. However, when we are choosing the underlying form of the model, there is usually a trade-off between model complexity and agreement with data. The more parameters that we introduce, the more precisely we may be able to fit our available data. In

some applications this is desirable (as long as there is sufficient data). However, seeking too strong of agreement with the data can often limit the scope of the model, because it will no longer generalize to other contexts. And if your purpose in building the model is theoretical understanding, then you may be obscuring the key components of the dynamics with the additional complexity. There are some approaches to trying to strike this balance between accuracy and generalization/simplicity. From information theory and the quantitative social sciences, we can borrow two quantities that try to balance simplicity and accuracy: Akaike's Information Criteria (AIC) and Bayesian Information Criteria (BIC) [2, 19]. In machine learning, it is more common to evaluate model performance using a resampling technique, such as k-fold cross-validation. Developing such criteria is still an ongoing area of research within the data-driven modeling community.

The classical supervised dynamic modeling approach entails starting with a conceptual model about how system works, diagraming expected interactions between species, introducing equations for the rates of each process in the diagram, and then fitting the model parameters to data. This requires some level of intuition, luck, and skill on the modelers part to choose a good set of equations for the right-hand side of our dynamic rules. In biology in particular, it has been hard to make headway in some study systems because the lack of unifying theory leaves us without sufficient intuition to design these equations. However, there has been growing interest in model discovery and methods for taking a more fully data-driven approach to model selection. One example is the Sparse Identification of Nonlinear Dynamics (SINDy) framework proposed by Brunton et al. [16]. Instead of fitting just one model, or maybe testing a handful of models, a library of potential terms in the governing equations is built and fit to the derivative of the system. By promoting sparsity during this fit, SINDy produces parsimonious models for the system dynamics. Genetic algorithms take another approach. Inspired by the idea of natural selection, at each generation the most successful candidate models are allowed to replicate with some level of mutation. Over many generations this process can yield effective models [8].

With the rise of big data, there has been a simultaneous rise in "data science" across scientific disciplines, including in the field of biology. Early breakthroughs in biological data tended to be static, like the sequencing of the human genome. Hence the huge success

of bioinformatics and structural models. These methods elucidate static features or steady behavior of living organisms. However, much of life happens far from equilibrium and understanding the causative influences in a system requires a dynamic model. The construction of successful dynamic models in biology is constrained by what we can measure. Data is necessary both to estimate parameters and to validate model predictions. For validation, models in mathematical biology typically rely on spatio-temporally resolved data. Advances in technology (particularly imaging, and time-series -omics data) are generating the appropriate data for dynamic models. With increasingly accumulated time-series data, we have the opportunity to develop dynamics-based approaches based on physical and biological laws to reveal dynamic features and complex behavior of biological systems

1.3 Organization of thesis

I have organized the remainder of this thesis into three main chapters, each focused on a particular cellular community of interest. Within each context, I will develop and implement a mathematical method to predict or characterize the collective behavior of that community. I start with a theoretical example in Chapter 2: synchronization in networks of coupled oscillators. For these systems, I develop a data-driven method for coarse-graining heterogenous spatio-temporal dynamics. In Chapter 3, I pivot to thinking about CAR T-cell therapy for treating cancer. To study this novel therapy with limited available data, I take a classical modeling approach. I model T-cells and tumor cells as a predator-prey type system first with an ordinary differential equations model in section 3.2 and then with a reaction-diffusion model in section 3.3. In Chapter 4 I focus on characterizing patterns formed by yeast patches. Working with rich data generated from this simple, but powerful model organism I utilize tools from machine learning and classical image analysis to facilitate highly-powered genetic analysis.

Chapter 2

SYNCHRONIZATION

In this chapter we leverage data-driven model discovery methods to determine the governing equations for the emergent behavior of heterogeneous networked dynamical systems. Specifically, we consider networks of coupled nonlinear oscillators whose collective behaviour approaches a limit cycle. Stable limit-cycles are of interest in many biological applications as they model self-sustained oscillations (e.g. heart beats, chemical oscillations, neurons firing, circadian rhythm). For systems that display relaxation oscillations, our method automatically detects boundary (time) layer structures in the dynamics, fitting inner and outer solutions and matching them in a data-driven manner. We demonstrate the method on well-studied systems: the Rayleigh Oscillator and the Van der Pol Oscillator. We then apply the mathematical framework to discovering low-dimensional dynamics in networks of semi-synchronized Kuramoto, Rayleigh, Rossler, and Fitzhugh-Nagumo oscillators, as well as heterogeneous combinations thereof. We also provide a numerical exploration of the dimension of collective network dynamics as a function of several network parameters, showing that the discovery of coarse-grained variables and dynamics can be accomplished with the proposed architecture.

2.1 Introduction

Data-driven modeling paradigms are an increasingly important tool for the characterization of behavior in complex, high-dimensional systems. For instance, *Reduced order models* (ROMs) [6] aim to exploit the ubiquitous observation from experiment and/or computation that meaningful input/output signals in high-dimensional systems are encoded in low-dimensional patterns of dynamic activity. However, many complex systems of interest exhibit behavior across multiple temporal or spatial scales, which poses unique challenges for modeling and predicting their behavior. It is often the case that while we are primar-

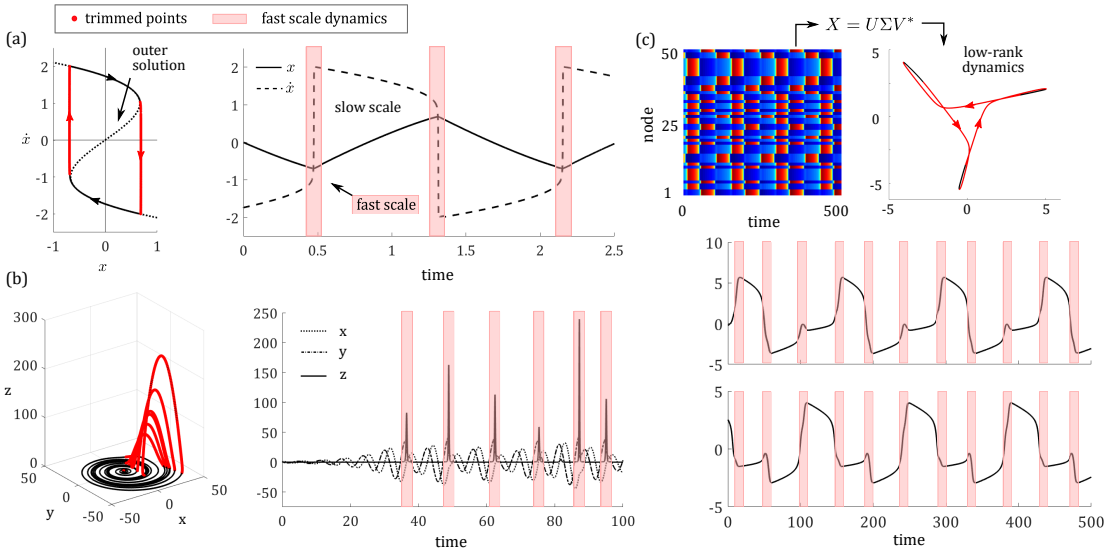

Figure 2.1: Sparse Identification of Nonlinear Dynamics (SINDy) with data-trimming disambiguates fast-scale versus slow-scale dynamics. (a) For a sample trajectory on the limit cycle of a Rayleigh oscillator, the trimmed points are those that deviate from the asymptotic outer solution. (b) For a sample trajectory on the Rossler attractor, trimming isolates rapid excursions in the z plane. (c) The dynamics of a network of coupled Fitzhugh-Nagumo oscillators can be projected onto the first 2 principal components. In this low dimensional representation, SINDy with trimming isolates intervals of spiking and rapid relaxation.

ily interested in macroscale phenomena, the microscale dynamics must also be modeled and understood, as they play a central role in driving the macroscale behavior. This can make dealing with multiscale systems particularly difficult unless the time scales are disambiguated in a principled way. There is a significant body of research focused on modeling multiscale systems to produce coarse-grained descriptions: notably the *equation-free* (EF) method[90] for linking scales and the *heterogeneous multiscale modeling* (HMM) framework [186]. Additional work has focused on testing for the presence of multiscale dynamics so that analyzing and simulating multiscale systems is more computationally efficient [52, 53]. Many of the same issues that make modeling multiscale systems difficult can also present challenges for model discovery and system identification. These challenges motivate the de-

velopment of specialized methods for performing model discovery on problems with multiple time scales, taking into account the unique properties of multiscale systems. Specifically, we integrate dimensionality-reduction, sparse regression, and robust statistics to discover governing evolution equations for coarse-grained heterogeneous network dynamics as well as to explicitly disambiguate and model multiscale temporal phenomena (See Fig. 2.3).

The discovery and pairing of coordinates and dynamics is the hallmark feature of scientific modeling. For instance, the second century Ptolemaic description of celestial mechanics featured an earth-centric coordinate systems with the retrograde planetary dynamics expressed as linear superposition of circular motion of different frequencies, i.e. the doctrine of the perfect circle. By Newton's time in the seventeenth century, the heliocentric coordinate system was established allowing for an $\mathbf{F} = m\mathbf{a}$ description of planetary motion with the inverse square law of gravitation. Thus it is not surprising that methods for jointly finding coordinates and dynamics have emerged as a central theme in modern data-driven science. Indeed, there is significant diversity in mathematical approaches for pairing a coordinate representation with an accompanying dynamical model that characterizes the evolution. *Reduced order models* (ROMs) accomplish this pairing by constructing coordinates from the most dominant correlated activity, or *proper orthogonal decomposition* (POD) [68, 6], and then Galerkin projecting on the governing equations [6]. More broadly, modal decomposition techniques, such as POD and *dynamic mode decomposition* (DMD) [102], approximate *linear* subspaces using dominant correlations in spatio-temporal data [170]. Linear subspaces, however, are highly restrictive and ill-suited to handle parametric dependencies. Attempts to circumvent these shortcomings include using multiple linear subspaces covering different temporal or spatial domains [40, 11, 169, 145], multi-resolution DMD [103], diffusion map embeddings [29, 28, 27, 125], or more recently, using deep learning to compute underlying nonlinear subspaces which are advantageous for dynamics, both linear and nonlinear [16, 107, 22, 24, 141]. These techniques represent data-driven architectures for extracting order-parameter descriptions of the underlying spatio-temporal dynamics observed [32].

Such flexibility and diversity in algorithms for the joint discovery of coordinates and dynamics has allowed for many new representations of physical systems, including in the

networked dynamical systems of interest here. Specifically, we are interested in modeling the emergent coarse-grained heterogenous behavior that arises in high-dimensional, networked dynamical systems whose underlying dynamics are strongly nonlinear. In particular, we consider networks of coupled nonlinear oscillators whose collective behavior approaches relaxation-oscillation limit cycle dynamics. Recently, oscillatory phenomena have been coarse-grained into learned and/or collective coordinates (intrinsic coordinates) for modeling their evolution [86, 58, 21, 164, 119, 131]. Gottwald originally introduced collective coordinates to describe coupled phase oscillators of the Kuramoto model [58], and then extended the mathematical framework to reduce infinite-dimensional stochastic partial differential equations (SPDEs) with symmetry to a set of finite-dimensional stochastic differential equations which describe the shape of the solution and the dynamics along the symmetry group [21]. Shlizerman et al [164] coarse-grained using coordinates associated with the dominant correlated activity, or singular value decomposition, and projected into a framework of neural activity measures. Kemeth et al [86] instead learn collective dynamics on a slow manifold, after initial transients have died out, which can be approximated through a learned model based on local *spatial* partial derivatives in the emergent coordinates. These works are closely related to the present work, as their aims are well-aligned with the goals of our method. However, there are key differences. Specifically, we consider coarse-graining on a system for which regions of fast activity are critical for characterizing the dynamics, i.e. the dynamics produce temporal boundary layers. In particular, we wish to learn the dominant balance dynamics that occur in both fast and slow temporal regimes on network level dynamics.

In this work, we leverage dimensionality-reduction, sparse regression, and robust statistics to discover coarse-grained models of heterogeneous networked dynamical systems. We consider networks consisting of several types of oscillators and explore how changing the network structure influences the collective dynamics. Nishikawa et al [131] and Motter et al [120] consider synchronization of networks, including scale free and small world, as a function of the homogeneous or heterogeneous distribution of connectivity, showing that homogeneous networks are more easily synchronized. Here, we focus on aspects of the emergent dynamics that arise from the heterogeneity of the oscillators themselves. Specifically,

in many regimes, the emergent dynamics exhibit two key features we aim to model: (i) non-trivial coarse-grained dynamics (relaxation-oscillations), and (ii) temporal boundary layers (rapid transient dynamics). Specifically, the proposed mathematical architecture discovers parsimonious governing evolution equations for coarse-grained network dynamics and, if desired, explicitly disambiguates emergent temporal boundary layer phenomena. The developed algorithm starts simply by projecting onto coordinates associated with the dominant correlated activity, i.e. by taking the singular value decomposition. We then identify rapid transition regions associated with transients in the time dynamics of the dominant modes by applying the *sparse identification of nonlinear dynamics* (SINDy)) [16] algorithm with data-trimming [23], which is a standard analysis tool from robust statistics. The governing equations produced by this stage of the method can be used to describe the full limit cycle. However, if a more detailed model is desired, the results of trimming are used to segment the coarse-grained trajectory, separating regions of rapid transition from the slow-temporal field, which is equivalent to the slow center-manifold considered previously [86, 58]. We then utilize the SINDy framework again to discover parsimonious governing equations for each region of the coarse-grained trajectory, constructing a hybrid model for the overall dynamics. Here we apply the full method to a network of coupled Fitzhugh-Nagumo oscillators, which produce rapid (spiking) behavior. The strongly nonlinear nature of the underlying agents leads to the existence of temporal boundary layers in the collective dynamics. The overall architecture allows for a data-driven approach to characterizing dominant-balance physics [32, 20] and singularly perturbed problems [5, 89, 101], which is a classic technique for understanding, for instance, boundary layer formation in fluid dynamics.

2.2 Coarse-graining and SINDy for multi-scale systems

Coarse-graining is of broad scientific interest across a diversity of disciplines. Coarse-graining seeks to determine a set of variables that successfully summarize the detailed state of a network of interacting agents. Analytical and computational approaches have long been sought for achieving this end, with the former leveraging the dynamical systems theory of center manifold reductions, normal forms, bifurcation theory and perturbation analysis. Indeed, the seminal review of Cross and Hohenberg [32] detail the many mathe-

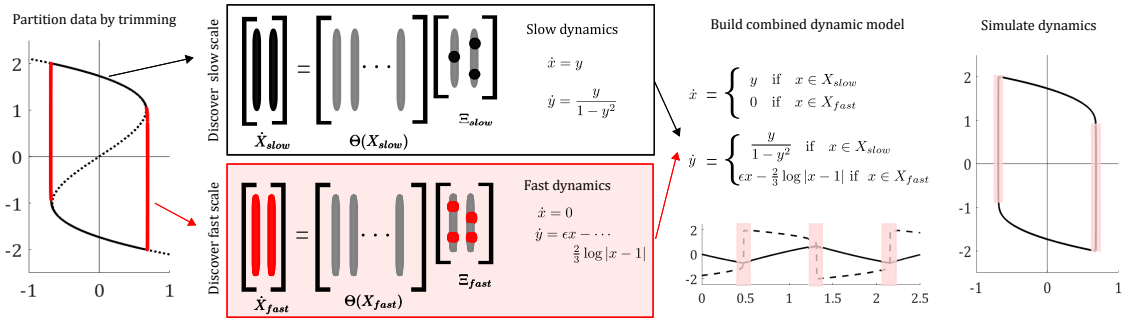

Figure 2.2: Overview of SINDy with trimming for discovering fast and slow dynamics illustrated on the Rayleigh Oscillator. First, data is partitioned by performing SINDy with trimming. Next, SINDy is applied to the points from each time scale separately. Subsequently, a combined dynamic model is built which applies the fast or slow model appropriately at each step depending on the state of the system. Simulated dynamics closely match the input trajectory.

matical architectures available for deriving order-parameter descriptions, or coarse-grained models, that characterize the dynamics. More recent computational approaches include statistical and machine learning algorithms [7, 122] for network clustering, principal component analysis, and, for instance, algorithms for detecting density (k-core decomposition). The diversity of methods developed allow for a new coordinate representation for the collective dynamics. This representation can then be leveraged by model discovery methods such as SINDy to determine the dynamics on the coarse-grained coordinates.

SINDy recovers parsimonious representations of the dynamics from measurement data by sparse regression to a library of candidate models [16]. Thus the goal of SINDy is to promote a parsimonious representation of the complex system by traditional and interpretable governing equations. Consider the nonlinear dynamical system, which will ultimately be our coarse-grained representation,

$$\frac{d\mathbf{x}}{dt} = f(\mathbf{x}, t) \tag{2.1}$$

which is measured at time points $\mathbf{t} = [t_1, t_2, \cdots, t_m]$. From measurements, we construct the matrix $\mathbf{X}(\mathbf{t}) = [\mathbf{x}_1(\mathbf{t})\ \mathbf{x}_2(\mathbf{t})\ \ldots\ \mathbf{x}_n(\mathbf{t})] \in \mathbb{R}^{m\times n}$. The method introduced in [16] seeks to

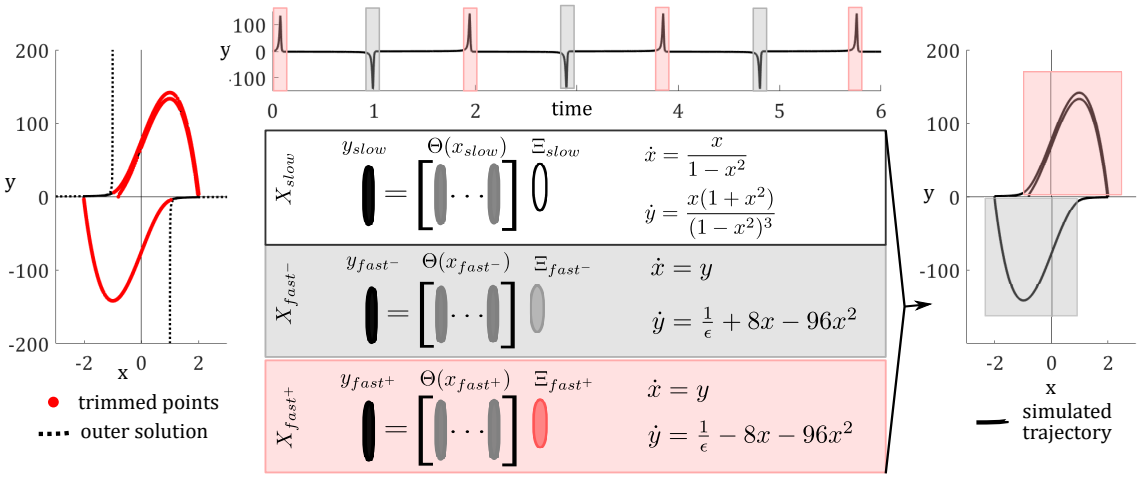

Figure 2.3: SINDy with trimming for the Van der Pol Oscillator. As with the Rayleigh example, data is partitioned by performing SINDy with trimming. The trimmed points (red) are those that deviate from the outer solution (dotted line). Then, SINDy is applied to the points from each time scale successively. Models are fit to the fast scale dynamics in the lower half-plane and the upper half-plane separately, but we can see that under the change of variable $\hat{x} = -x$, the resulting equations for $\dot{y}$ in the gray and red boxes are the same. Combining these equations in the appropriate regions, the hybrid model can then be used to simulate the Van der Pol system.

identify $\mathbf{f}$ via sequential threshold least-squares, which is a proxy for the sparsifying zero-norm. The set of n state measurements are used to populate a library of candidate nonlinear terms $\boldsymbol{\Theta}(\mathbf{X}) = [\mathbf{1}^\top \ \mathbf{X}^\top \ (\mathbf{X} \otimes \mathbf{X})^\top \ \cdots \ \sin(\mathbf{X})^\top]$, where $\mathbf{x} \otimes \mathbf{y}$ defines the vector of all product combinations of the state components. Each candidate term should be unique, as a suitable library is crucial in the SINDy algorithm. A common strategy is start with polynomials and increase the complexity of the library with other terms, such as trigonometric functions. Thus, the system in (2.1) is approximated by:

$$\dot{\mathbf{X}} = \boldsymbol{\Theta}(\mathbf{X})\boldsymbol{\Xi}. \tag{2.2}$$

The time derivatives $\dot{\mathbf{X}}(\mathbf{t}) = [\dot{\mathbf{x}}_1(\mathbf{t}) \ \dot{\mathbf{x}}_2(\mathbf{t}) \ \ldots \ \dot{\mathbf{x}}_n(\mathbf{t})]$, if not measured directly, can be found

via numerical differentiation and should be appropriately de-noised, if necessary (low pass Butterworth, total variation regularization, etc.) [179]. The coefficients $\boldsymbol{\Xi}$ are the *sparse* weightings of the corresponding candidate library terms. Therefore, our regression relies on sparse regularization to enforce a parsimonious $\boldsymbol{\Xi}$ corresponding to the fewest nonlinear terms in our library that describe our dynamics well:

$$\boldsymbol{\Xi} = \arg\min_{\hat{\boldsymbol{\Xi}}} \|\boldsymbol{\Theta}(\mathbf{X})\hat{\boldsymbol{\Xi}} - \dot{\mathbf{X}}\|_2 + \lambda\|\hat{\boldsymbol{\Xi}}\|_0 \tag{2.3}$$

Regressing to the zero-norm is often achieved by relaxing the the one-norm. However, modern optimization frameworks are allowing for computationally tractable proxies for the zero-norm that are superior to the one-norm relaxation [23, 195]. SINDy is modular and adaptible, allowing for modifications which include the discovery of spatio-temporal systems [160, 163], multiscale dynamics [22], parametric dependencies [158], hybrid dynamical systems [112], systems subject to control [82, 17], and implicit dynamics [113, 114, 81]. Further, it can be used in the low-data limit [152, 65, 49] and with denoising architectures [159, 80]. The SINDy algorithm, which has an accompanying python package [84], is the workhorse algorithm for our coarse-graining method.

To disambiguate fast scale dynamics, our coarse-graining method exploits a key extension of SINDy: data trimming. Modifying Eq. (2.3) to include trimming yields:

$$\begin{aligned} \boldsymbol{\Xi}, \mathbf{v} \;=\; & \arg\min_{\hat{\boldsymbol{\Xi}}, \mathbf{v}} \sum_{i=1}^{m} \frac{1}{2} v_i \|(\boldsymbol{\Theta}(\mathbf{X})\hat{\boldsymbol{\Xi}} - \dot{\mathbf{X}})_{\mathbf{i}}\|_2 + \lambda\|\hat{\boldsymbol{\Xi}}\|_0 \\ & \text{s.t.} \quad 0 \le v_i \le 1, \qquad \mathbf{1}^T\mathbf{v} = \mathbf{h}, \end{aligned} \tag{2.4}$$

where $h < m$ is an estimate of the number of the m input data points that are considered "inliers." See the work of Champion et al. for a thorough explanation [23]. After the SINDy with trimming algorithm is applied, the vector $\mathbf{v}$ has lower entries where data points are harder to fit to a parsimonious model of system dynamics. In systems that exhibit multi-scale temporal dynamics, these troublesome points often correspond to spikes in the derivative. Thus, trimming effectively identifies regions of rapid change.

As an example, in Fig. 2.1a we illustrate how data-trimming partitions the limit cycle of a Rayleigh oscillator: the points which deviate from the slow-scale outer solution are trimmed, coinciding with the two boundary layers in the limit cycle. Trimming applied

to Rossler dynamics on a strange attractor identifies rapid excursions in the z-component of the system (Fig. 2.1b). When applied to a low-rank representation of a network of spiking Fitzhugh-Nagumo (FHN) oscillators, trimming identifies regions of rapid spiking and relaxation (Fig. 2.1c). In each of these examples, the trimmed fraction, or $1-h/m$, is a hyperparameter of the method that must be tuned according to the proportion of the input measurements that appear to belong to regions of fast-scale dynamics. If the fraction is set too high, then points adjacent to the fast scale dynamics will also be trimmed. Conversely, if the trimmed fraction is set too low then only a subset of the fast-scale dynamics will be identified. Another factor to consider in applying this method is that in order to effectively repurpose an outlier-detection technique from robust statistics to partition our data, the data must be clean. If the input trajectory is noisy, then data trimming will pull out the noisy data points and their neighbors, whose derivative estimates are corrupted, and, possibly, also the desired regions of rapid scale dynamics.

2.3 Hybrid models for relaxation oscillators

The steps of our method for data-driven identification of temporal boundary layer phenomena in relaxation oscillations are outlined on the canonical Rayleigh oscillator in Fig. 2.2. First, SINDy with trimming is applied to the input trajectory to partition the data. Any reasonable library can be used at this point, as we only need the output from trimming, i.e. the vector $\mathbf{v}$ from (2.4), not the model coefficients. The entries of $\mathbf{v}$ are compared to a threshold value, and points with entries below the threshold are assigned to the fast-scale group, X_{fast}, while points with an entry above the threshold are assigned to the slow-scale group, X_{slow}. Next, the locations of the points belonging to X_{fast} within the phase space are used to bound the region in which the fast scale dynamics will apply. The bounding box is formed around each stretch of consecutive trimmed points, and then overlapping boxes are joined resulting in one region for each segment of the limit cycle displaying fast-scale dynamics. Points outside of these bounding boxes are assigned to X_{slow} during simulation. Then, SINDy is applied separately to data in X_{fast} and X_{slow}. For the slow-scale group, the candidate library of functions is built using $x \in X_{slow}$. For the fast scale group, the candidate library of functions is built using $x \in X_{fast}$. With these two dynamic models in

hand, and a partition on the phase space determining when each model applies, we can simulate the system dynamics. At each time step, before calculating an update to the system position, we check whether the point belongs to X_{fast} or X_{slow}. If $x \in X_{fast}$, then the fast scale dynamics are used to calculate an update. If $x \in X_{slow}$, then the slow scale dynamics are used to calculate an update. Note that the hybrid model is only valid for points on the limit cycle of the system. In this example, trajectories initiated elsewhere in the phase space either remain on the line $y = 0$, approach the line $y = 1$ in the upper half plane, or approach the line $y = -1$ in the negative half plane.

We also demonstrate this hybrid model approach on the limit cycle of a Van der Pol oscillator exhibiting relaxation-oscillations, as shown in Fig. 2.3. Like the Rayleigh Oscillator example, we first partition the input trajectory using trimming. Note that the trimmed points, shown in red, are those points that deviate from the outer solution predicted by asymptotic approximation theory, shown by a dashed line. We then use the set of trimmed points to bound the regions of phase space governed by fast scale dynamics, and the remaining phase space is considered to be governed by slow scale dynamics. Next we apply SINDy to data points from the slow scale scale region, fitting the dynamics to a library that depends on x and includes rational functions. In this case, we fit the dynamics of the two regions of fast scale dynamics separately, calling those in the lower half plane X_{fast^-} and those in the upper half plane X_{fast^+}. For both subsets of data, we fit the dynamics to a library of cubic polynomials in x and y. We treat the two segments of fast dynamics separately because fitting both regions at once results in an average between the two desired models that does not approximate either branch fully. We note, however, that the resulting models for X_{fast^-} and X_{fast^+} reported in Fig. 2.3, can easily be transformed to match each other by applying an absolute value sign to x. If such symmetries are clear from viewing the limit cycle of a system, then the library of candidate functions used in SINDy could be built using polynomials of $|x|$, and both regions of fast scale dynamics could be fit together. Again simulation of the system is accomplished by checking whether the current state belongs to X_{slow}, X_{fast^+}, or X_{fast^-}, making an update with the appropriate dynamic rules, and then iterating these two steps until the desired time span is covered.

2.4 Coarse-graining heterogeneous spatio-temporal dynamics

For our coarse-graining method, a reduced-order basis is first derived through the singular value decomposition [100, 15] (Fig. 2.4) and second, SINDy is deployed to discover the dynamics in this reduced order basis (Fig. 2.4). If the low-rank dynamics exhibit multiscale temporal behavior, then SINDy with trimming can be used instead to identify regions of fast-scale dynamics and fit a hybrid model to the data, facilitating analysis of the dominant balance physics in distinct dynamic intervals of the collective limit cycle. This method allows us to tackle coarse-graining for networks displaying heterogenous spatio-temporal dynamics that are not tractable with analytical approaches. For very high-dimensional problems, randomized algorithms [48] and compressed decompositions [47] can be exploited in order to compute the low-rank subspaces more efficiently.

The systems that we consider here are networks of coupled oscillators of the form

$$\frac{d\mathbf{x}}{dt} = f(\mathbf{x}, t), \tag{2.5}$$

where $\mathbf{x}(t) = (x_1, x_2, .., x_n)$ is a vector of state variables, or nodes, and $f(\mathbf{x}) = (f_1(\mathbf{x}), f_2(\mathbf{x}), ..., f_n(\mathbf{x}))$ is a vector of functions encoding the dynamics on each node. The dynamics depend on intrinsic properties of each node as well as coupling to neighboring nodes. Neighbors are defined by a symmetric, unweighted adjacency matrix, $A \in \mathbb{R}^{n\times n}$, where the entries $A_{ij} = A_{ji} = 1$ if node i and node j are connected and $A_{ij} = A_{ji} = 0$ otherwise. Here we consider Erdos-Renyi adjacency matrices, so A may be sparse or highly connected as we tune the edge probability, p. The functions $f_i(\mathbf{x})$ could take on any arbitrary form, but we limit our attention to a selection of well-known oscillators.

Before applying our method to heterogeneous systems, we establish that it is producing reasonable results by considering a network consisting of Kuramoto oscillators with sinusoidal coupling. For the ubiquitous Kuramoto oscillator, the phase of node j, denoted θ_j, is governed by

$$\dot{\theta}_j = \omega_j + \frac{K}{n}\sum_{i=1}^{n} A_{ij}\sin(\theta_i - \theta_j). \tag{2.6}$$

The key parameters besides the aforementioned adjacency matrix, are the connectivity strength $K > 0$, and the intrinsic frequency ω_j. For each node in the system, ω_j is drawn

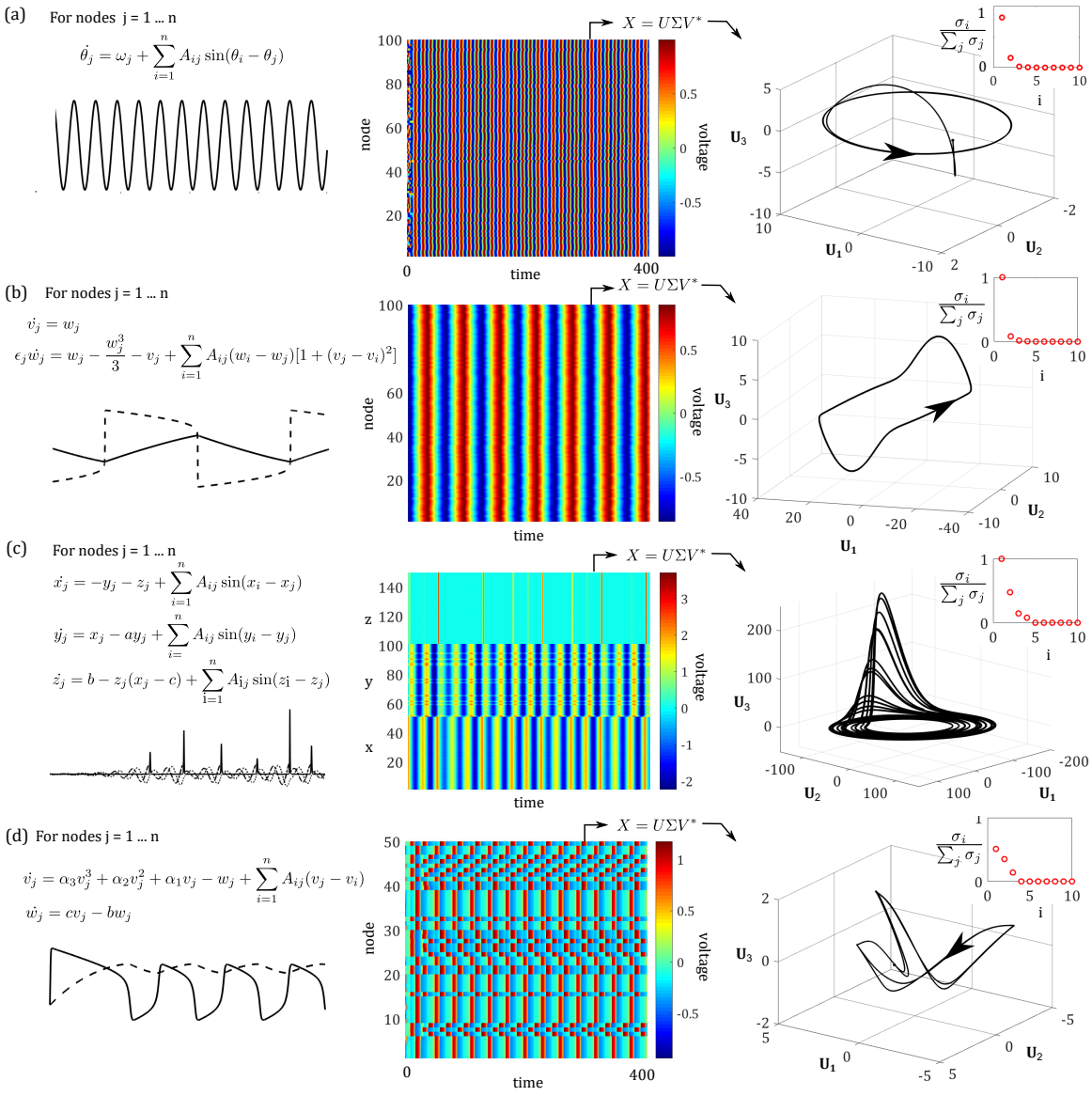

Figure 2.4: In appropriate parameter regimes, the dynamics of networked oscillators can be reduced to a low dimensional representation by taking the singular value decomposition and projecting the state of the system at each time point onto the first few singular vectors. Here we illustrate the low-dimensional limit cycle that results for (a) coupled Kuramoto oscillators with different intrinsic frequencies, (b) coupled Rayleigh oscillators with different damping parameters, (c) linearly coupled Rossler oscillators, and (d) linearly coupled Fitzhugh-Nagumo (FHN) oscillators.

Figure 2.5: SINDy applied to the low-dimensional representations of network dynamics produces governing equations which can be used to accurately simulate the low-rank dynamics over an appropriate time horizon. (a) For a network of Kuramoto oscillators, SINDy produces a very simple model that remains accurate for long time. (b) For a network of Rayleigh oscillators, SINDy produces a 3rd order model that comes out of phase after around one lap of the limit cycle. The discovered dynamics are attracted to a slightly smaller stable limit cycle than the actual system. (c) For a network of Rossler oscillators, SINDy produces a model that is linear in two dimensions and second order in the third. The predicted dyanamics sync up well for a while, but the prediction of spikes in U_3 starts to degrade, impacting the predictions of all three components over time. (d) For a network of FHN oscillators, trimming identifies regions of the limit cycle that correspond with semi-synchronized spiking. The resulting model is linear in the recovery-variable modes and 3rd order in the voltage variable modes. Although it is not sparse, the model predicts system dynamics accurately over a long time horizon.

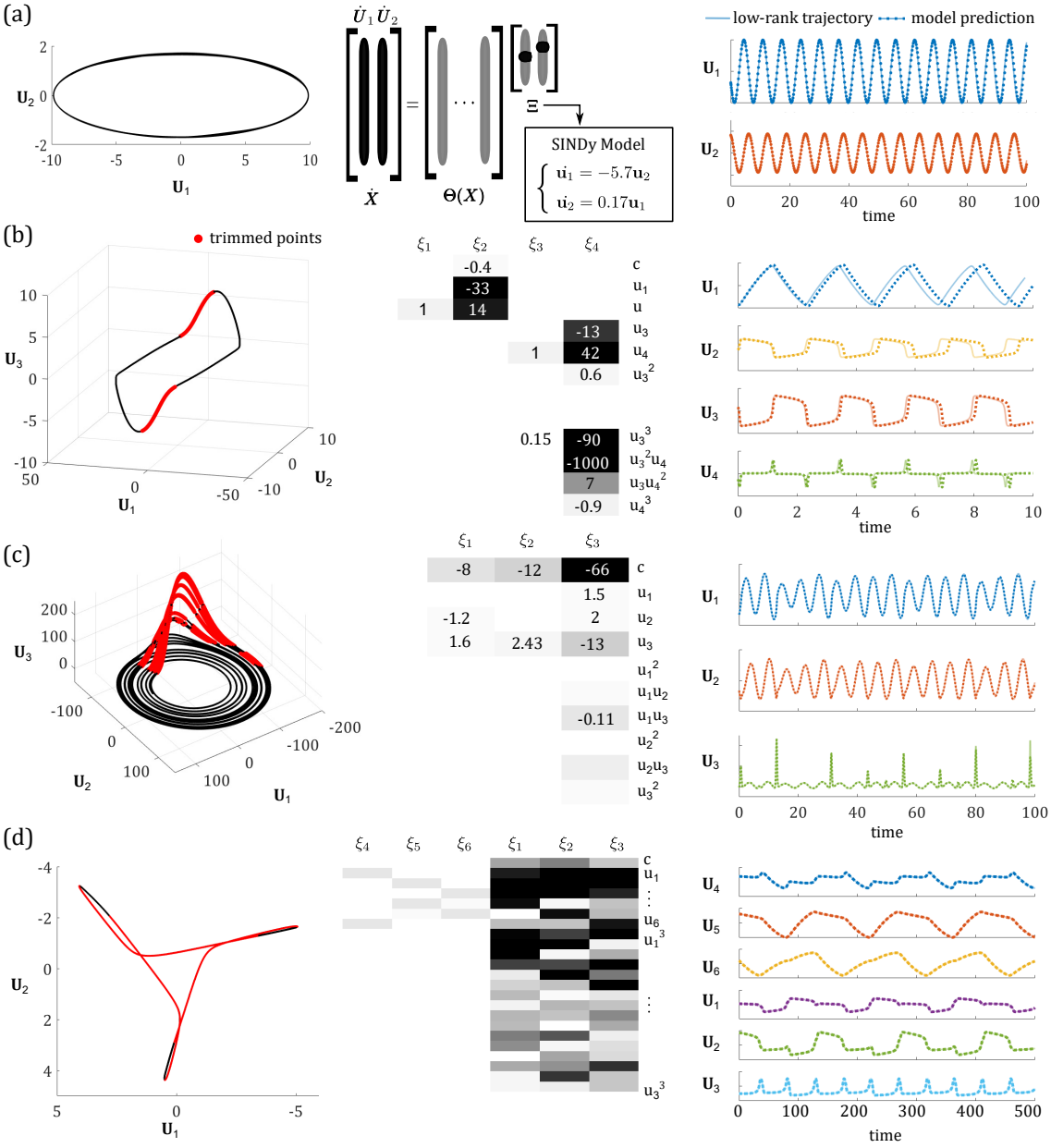
(a)
$\dot{U}_1\dot{U}_2$
$\dot{X}$
$\Theta(X)$
Ξ
SINDy Model
$\dot{u}_1 = -5.7u_2$
$\dot{u}_2 = 0.17u_1$
low-rank trajectory
model prediction
time
(b)
trimmed points
(c)
(d)

from a uniform distribution. Kuramoto oscillators have been widely studied and exhibit a well-known phase transition from asynchrony below a critical coupling threshold to partial synchrony above this threshold. The system continues to synchronize more fully as the coupling parameter is further increased. Panel (a) of Figure 2.4 illustrates the behavior of a single Kuramoto oscillator as well as the full system dynamics for a network of Kuramoto oscillators. Note that we are visualising the cosine of the phase. Taking the singular value decomposition and projecting onto the first few modes reduces the system dynamics to a stable elliptical limit cycle. Retaining two of these modes and applying the SINDy method to the 2D limit cycle produces a simple and accurate set of governing equations which can be used to simulate the system dynamics (Fig. 2.4a, final column). With this friendly, linear collective behavior no trimming is required to recover useful model equations.

Next, we consider a slightly more complicated system: Rayleigh oscillators with nonlinear coupling. In this case each node follows the second order governing equation

$$\epsilon_j \ddot{x}_j = \dot{x}_j - \frac{\dot{x}^3}{3} - x + \frac{K}{n} \sum_{i=1}^{n} A_{ij}(1 + (x_j - x_i)^2)(\dot{x}_i - \dot{x}_j) \tag{2.7}$$

where $\epsilon_j << 1$ is drawn from a uniform distribution and again $K > 0$ is the connectivity parameter. The nonlinear coupling strategy, termed Haken-Kelso-Bunz (HKB) coupling, was introduced to study human bimanual experiments and applied to data capturing the synchronization of people rocking chairs by Alderisio et al. [3]. In numerical simulations, we observe partial synchrony in these systems when there is sufficient coupling (Fig. 2.4b). This collective behavior is captured by a nonlinear limit cycle in the low-dimensional representation. Applying SINDy to the 4D projection with trimming pulls out regions of rapid relaxation along the direction of U_4 and produces a model that is linear in U_1 and U_2 and cubic in U_3 and U_4. Here each oscillator has an intrinsic ϵ_j on the order of 10^{-3}. The multi-scale nature of the collective system dynamics is evident in the fact that the coefficients learned for modes U_2 and U_4 are much higher than those learned for U_1 and U_3. With a distribution of ϵ values centered closer to 1, we would see a smaller gap between scales as $1/\epsilon \to 1$. Comparing the trajectory predicted by the model against the true low-rank trajectory of the system (final column of Fig. 2.4), we see that after one lap of the limit cycle, the prediction gets out of phase with the true trajectory. The SINDy model is attracted to

a smaller stable limit cycle parallel to the true dynamics. Applying this method to systems with larger values of ϵ, i.e. systems for which the boundary layers are less sharp, results in model dynamics that stay on track for longer time.

We also demonstrate our method on a network of Rossler oscillators with sinusoidal coupling. In this case each node has 3 state variables governed by

$$\begin{aligned}
\dot{x}_j &= -y_j - z_j + \frac{K}{n}\sum_{i=1}^{n} A_{ij}\sin(x_j - x_i) \\
\dot{y}_j &= x_j + a y_j + \frac{K}{n}\sum_{i=1}^{n} A_{ij}\sin(y_j - y_i) \\
\dot{z}_j &= b + z_j(x_j - c) + \frac{K}{n}\sum_{i=1}^{n} A_{ij}\sin(z_j - z_i)
\end{aligned} \tag{2.8}$$

The parameters (a, b, c) are uniform across all nodes in the network for a given run. In the example shown in Fig. 2.4c, $(a = 0.2, b = 0.2, c = 5.7)$. The trajectory of each node is drawn to a similarly shaped strange attractor, however the attractors may be translated in phase space depending on the initial condition of the node. The nodes of the network largely synchronize phases and frequencies in their x component, synchronize frequencies of their y component, and partially synchronize the timing of excursions in the z component. Projecting onto the first three singular vectors, the system lands on an attractor that resembles a Rossler attractor with a few differences. Specifically, the attractor is tilted slightly with respect to the axes, so there is a background oscillation rate in U_3. Due to this tilt, the U_3 "excursions" also disrupt the background activity along U_1 and U_2 slightly. Applying SINDy with trimming to this low-dimensional trajectory results in a linear model for U_1 and U_2 and a dense cubic equation for the dynamics of U_3. Because the attractor for the collective dynamics is tilted in the SVD-space compared to an attractor for a single Rossler oscillator, these cross terms are necessary to capture the background frequency and the excursions. Observe that trimmed points are mostly spikes along the U_3 direction. In this case, the model predictions and the true trajectory match up very well for time steps that were used in the SVD projection initially. However, about time 80 in Fig. 2.4c you can start to see that the model prediction is deviating from the true trajectory–capturing less of the U_3 excursions. Continuing to predict beyond the training data, the model still

produces dynamics that resemble a collective Rossler oscillator but they lose fidelity to the true system dynamics.

The last type of oscillator that we considered were linearly coupled Fitzhugh-Nagumo oscillators. This simplified model of a neuron has two state variables: a voltage variable which displays rapid spiking and relaxation under an external stimulus and a slower recovery variable. Each FHN node is governed by the pair of equations

$$\begin{aligned} \dot{v}_j &= \alpha_3 v_j^3 + \alpha_2 v_j^2 + \alpha_1 v_j - w_j + \frac{K}{n}\sum_{i=1}^{n} A_{ij}(v_j - v_i) \\ \dot{w}_j &= c v_j - b w_j + \frac{K}{n}\sum_{i=1}^{n} A_{ij}(w_j - w_i). \end{aligned} \tag{2.9}$$

For these simulations we use parameters $\alpha = (-0.1, 1.1, -1)$, $c = 0.1$, and $b = 0.1$ as studied in [164]. This combination yields semicoherent spiking behavior across the network (Fig. 2.4d). In the raster plot of the network, we see that subsets of the nodes are firing together. The limit-cycle that emerges from projecting this onto 3 SVD modes has a distinctive triangular shape. Each edge appears to result from the spiking of a different subset of nodes. Note that for different parameter values, the system may cease spiking and settle to a steady state or spiking may be more chaotic. For this system we projected to low dimensions by taking the SVD of the voltage and the recovery variables within the nodes separately. U_1, U_2 and U_3 are the first three modes in the voltage variable. U_4, U_5, and U_6 are the first three modes in the recovery variable. Applying SINDy with trimming to this highly nonlinear, 6-dimensional limit cycle yields a model that is linear in the recovery variables and cubic in the voltage variables. The model predictions and the true dynamics of the system match up very well even over long time horizons (Fig. 2.4d).

The multiscale nature of the limit-cycle in the low-rank representation of our FHN network makes it a prime candidate for building a hybrid model. After the network dynamics are reduced to 6 dimensions, we can apply the same steps as outlined for the Rayleigh and Van der Pol oscillators. First, we apply SINDy with trimming. Trimming identifies regions of fast-scale dynamics along directions U_1 through U_4, which correspond to the three subsets of partially synchronized oscillators firing. In the low-rank dynamics these are the three corners of the triangular limit-cycle on the recovery modes and the three edges of the limit-

cycle on the voltage modes (Fig. 2.6a). Along the limit cycle, alternating segments of fast and slow scale dynamics are used to partition phase-space into 6 regions, each of which has unique dominant-balance dynamics. So rather than just X_{fast} and X_{slow}, we have X^1_{fast}, X^2_{fast}, X^3_{fast}, X^1_{slow}, X^2_{slow}, and X^3_{slow}. These six intervals are color coded in Fig. (2.6b). The derivatives of the low-rank state variables in each of the six regions are fit using a linear library. We can see that the slow dynamic regions (blue, orange and yellow) show great agreement in all variables. The fast dynamic regions are also well matched in the recovery modes, 4,5 and 6. The fit is not as clean at the ends of each fast region in the voltage modes, 1, 2 and 3. The coefficients for the 6 dynamic models can be used to assess the system behavior within each region (2.6c).

2.4.1 Heterogenous oscillator networks

By considering networks of nodes displaying relaxation-oscillations and chaotic dynamics, we demonstrated the power of this method to disambiguate and capture spatio-temporal heterogeneity. However, we are not limited to networks consisting of a single type of oscillator. We can enhance the heterogeneity of the system by mixing two or three types of oscillators together in one network and apply the same coarse-graining method (Fig. 2.7 and 2.10).

As a case study on networks of two types of oscillators, we coupled together n_K nodes governed by Kuramoto dynamics and n_F nodes governed by FHN dynamics where $n_K+n_F = 100$. When coupling FHN nodes to Kuramoto nodes equations (2.6) and (2.9) apply to the appropriate subset of nodes in the system, except that FHN nodes are coupled to the sine of the Kuramoto node to maintain a consistent scale. For visualization purposes we ordered the system such that the first $1, .., n_k$ nodes are Kuramoto and the next $n_k + 1, ..., 100$ are FHN. The adjacency matrices for these simulations are Erdos-Renyi graphs with connection probability $p = 0.2$. The FHN parameters are $\alpha = (-0.1, 1.1, -1)$, $c = 0.1$, and $b = 0.1$ with connectivity strength $K_F = 0.2$. The intrinsic frequencies for Kuramoto oscillators are drawn from a uniform distribution centered at 0.6, so the population would naturally oscillate much more quickly than the FHN firing rate. The connectivity strength

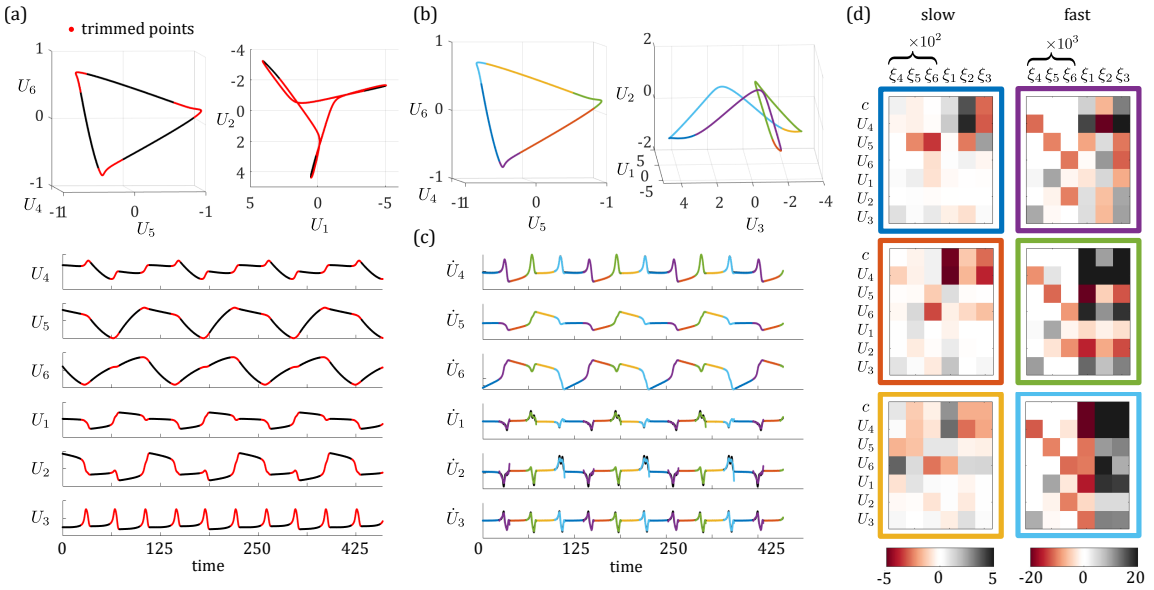

Figure 2.6: SINDy with trimming can be used to build a linear hybrid model for the low-rank dynamics of an FHN network. (a) Trimming identifies regions of rapid change along directions U_1 through U_4, which corresponds to the corners of the triangular limit-cycle in the recovery modes U_6 and U_5. (b) The alternating segments of fast and slow scale dynamics along the limit cycle are used to partition phase-space into 6 regions with unique dominant-balance dynamics. (c) The derivative of each low-rank state variable in each of the six regions are fit using a linear library. The slow dynamic regions (blue, orange and yellow) show great agreement in all variables. The fast dynamic regions are also well matched in modes the recovery modes, 4,5 and 6. The fit is not as clean in the voltage modes, 1, 2 and 3. (d) The coefficients for the 6 dynamic models can be used to assess the system behavior within each region.

for Kuramoto oscillators is $K_K = 10$, so this bloc also synchronizes more quickly than the FHN bloc.

With this set of parameters, we can simulate many different network instances at all possible ratios of Kuramoto to FHN oscillators. When $n_K = 0$, the system matches the all FHN network discussed previously with collective dynamics landing on a triangular limit cycle. When $n_K = 100$, the system matches the all Kuramoto network, with low rank dynamics attracted to a stable, elliptical limit cycle. For ratios in between the low-rank dynamics evolve from the triangular FHN cycle to the elliptical Kuramoto cycle (Fig. 2.7). When $n_K \in [1, 40]$, the FHN bloc dominates the collective dynamics and the Kuramoto oscillators synchronize to what is typically the third mode of the FHN network. As the number of Kuramoto oscillators increases, this strengthens the influence of the third mode, widening the variation in this direction and rounding out the sharp corners of the triangular cycle. When the numbers of Kuramoto and FHN nodes are more equal, around $n_K \in [40, 60]$, the system dynamics often collapse to a stationary state over time. Then continuing to increase n_K into the range $[60, 70]$, there is a window of interesting mixed dynamics. In this range, the Kuramoto bloc sets the pace for a background pulse that is shared across all nodes, including the FHN nodes. However, the FHN nodes still fire periodically. The corresponding low rank dynamics always have a dominant oscillatory first mode. For some networks, the FHN recovery periods stretch the period of the Kuramoto oscillators, and so an echo of the FHN triangle is captured in modes 2 and 3 as shown in Fig. 2.7c. In other cases, the Kuramoto oscillators are not strongly entrained to the FHN firing, so the second mode is also oscillatory and mode 3 captures chaotic oscillations. These collective dynamics land on a figure-8 shaped attractor. Finally, increasing n_K still further into the range $[70, 90]$ causes the Kuramoto bloc to dominates as it entrains the FHN nodes to pulse at the mean Kuramoto frequency. These synchronized oscillations are well captured by a curved ellipse in the SVD projection. The collective low-rank dynamics appear almost entirely Kuramoto-like, ie. follow an elliptical limit cycle, beyond $n_k = 90$. In this example, we thoroughly explored the dynamics observed for one set of parameters on a mixed Kuramoto-FHN network. However, many other potential parameter sets could be considered and would lead to different collective dynamics.

For each ratio of n_K to n_F and this fixed set of parameters, we estimated the dimensions of the collective dynamics by calculating the number of SVD modes required to reconstruct the network dynamics to 90, 95, and 99% accuracy with respect to the Frobenius norm. This estimate was repeated for 1000 network iterations at each ratio, and the mean and standard deviation were calculated (Fig. 2.7). The expected dynamic dimension of the network is the highest when the FHN bloc is dominant. It is low around a 50:50 ratio when the system often goes to a steady state and again above $n_K = 90$ when the Kuramoto bloc fully dominates. There is a jump in dimension for the window around $n_K = 60$ to 70 where we see the system exhibiting collective dynamics that are a fairly even balance between the two styles of oscillator. These estimates of the dynamic dimension give a hint as to how many modes need to be used when fitting a SINDy model to the collective limit cycle. In Fig. 2.8, we apply our coarse graining method to produce models for the example in panels (a) and (d) of Fig. 2.7. For the network in panel Fig. 2.8a, which is mostly dominated by Kuramoto oscillators, though the FHN influence makes the limit cycle non-linear, our method produces a stable model that can be used to predict network dynamics over a long time period. The first mode is quite dominant, we see much larger coefficients on these dynamics compared to the other two modes. In contrast, to accurately fit the derivative for the network that is FHN dominated, we need 9 modes and a cubic library. In this case the SVD was applied to the Kuramoto and the FHN blocs separately, akin to learning coarse grained variables for subsets of the nodes in a network as in the method of Antonsen and Ott [136]. The voltage variables of the FHN nodes and the Kuramoto operate on a fast scale, whereas the recovery variables of the FHN nodes operate on a slow scale. The recovered model fits the derivative well, however it is unstable. This is an inherent challenge in the standard SINDy implementation, which can be addressed through further modifications that ensure model stability. There are several stabilization approaches introduced in [39, 65]. In addition to varying the ratio of Kuramoto to FHN oscillators, we also estimated the dimension of collective network dynamics as a function of other network parameters. We tested a wide range of network connectivities and differed the scale between the FHN and Kuramoto oscillations. These explorations are mapped out in Figure 2.4.1. Note that the white dotted line indicates the parameter set that was illustrated in Fig. 2.7:

the mean Kuramoto frequency is 0.6, the connectivity threshold (1 minus the connectivity probability) on the adjacency matrix is 0.8, and the Kuramoto connectivity strength is 10, while $n_K \in [0, 100]$. When constructing these figures, the dimension of a given instance of a network was estimated by simulating the network until time $t = 2000$, taking the SVD of the system dynamics from time $t = 1000$ onwards, and then calculating the number of singular values required to retain $90, 95$ and 99% accuracy in reconstruction. Imposing a time delay before computing the SVD allows the system to settle onto the long-term limit cycle, so our estimate of the dimension discounts the early transient behavior of the system. For a given parameter set, 1000 instances of independent networks were simulated and the average dimension for each accuracy threshold was calculated. As we change two parameters defining the network structure and two parameters defining the Kuramoto nodes' internal dynamics, we observe wide variation in the typical dimension of the collective dynamics.

Starting in the top row of Figure 2.4.1, we see that the dimension of the collective dynamics increases sharply with the mean Kuramoto frequency when the ratio $n_K : n_F$ is around 1. At higher frequencies, the intrinsic Kuramoto dynamics are on a very different time scale than the instrinsic FHN dynamics so we no longer achieve entrainment of one group by the other for equal size blocs. There is a narrow region of low dimension that persists for oscillator ratios above 50 up to a mean frequency of about 1. This is the region in which many system instances go to a steady stationary state. When the Kuramoto bloc is dominant, the dimension does not vary significantly as the mean frequency changes because the oscillators synchronize to one speed; no matter how fast or slow that speed is, the dynamics will be low-dimensional. When the FHN bloc is fully dominant, the dimension does not vary significantly with the kuramoto oscillator frequency because the dynamics of all nodes are driven almost exclusively by coupling to the FHN nodes.

In the second row of Figure 2.4.1, we vary the connection probability, p, when constructing the adjacency matrix for the network. As the connectivity threshold, $1 - p$, increases, the coupling across all nodes is weakened until the network becomes disconnected. In the upper half of these maps, when the collective dynamics are dominated by Kuramoto oscillators, we observe the phase transition from a synchronized or semi-sychronized state with dimension less than 3 to an asynchronous state with dimensions well above 10. This transi-

Figure 2.7: Systems of coupled heterogenous oscillators also display low-rank dynamics which can be coarse-grained via the SVD. Here we illustrate dynamics of networks mixing Kuramoto and FHN oscillators in different ratios. Networks without Kuramoto oscillators resemble the FHN behavior shown in Fig. 2.4, whereas networks with 100% Kuramoto oscillators have the same exact behavior as the Kuramoto system shown in Fig. 2.4. When the number of Kuramoto oscillators increases above zero, the Kuramoto oscillators synchronize to what is typically the 3rd FHN mode. This causes the system behavior to develop a progressively stronger pulse along one dimension compared to the purely FHN-like cycle. Eventually, around a 50-50 Kuramoto-FHN split, the majority of simulations progress towards a stable steady state rather than sustaining oscillations. Then as the number of Kuramoto oscillators increases again, there is an interesting region where sometimes the system dynamics resemble those shown in (c) with a dominant oscillatory first mode and the echo of the FHN triangular cycle in modes 2 and 3. Other times the behavior lands on a figure-8 like attractor. As the number of Kuramoto oscillators continues to increase past 70, their combined signal dominates, inducing synchronous low amplitude oscillations in the FHN nodes. One thousand simulations were run for each ratio of Kuramoto to FHN oscillators and the dimension of the resulting dynamics was estimated by tracking the number of modes needed to capture 90, 95, and 99% of the Frobenius norm. The mean "dimensions" as defined by each threshold are shown by solid lines and the corresponding standard deviations are shaded.

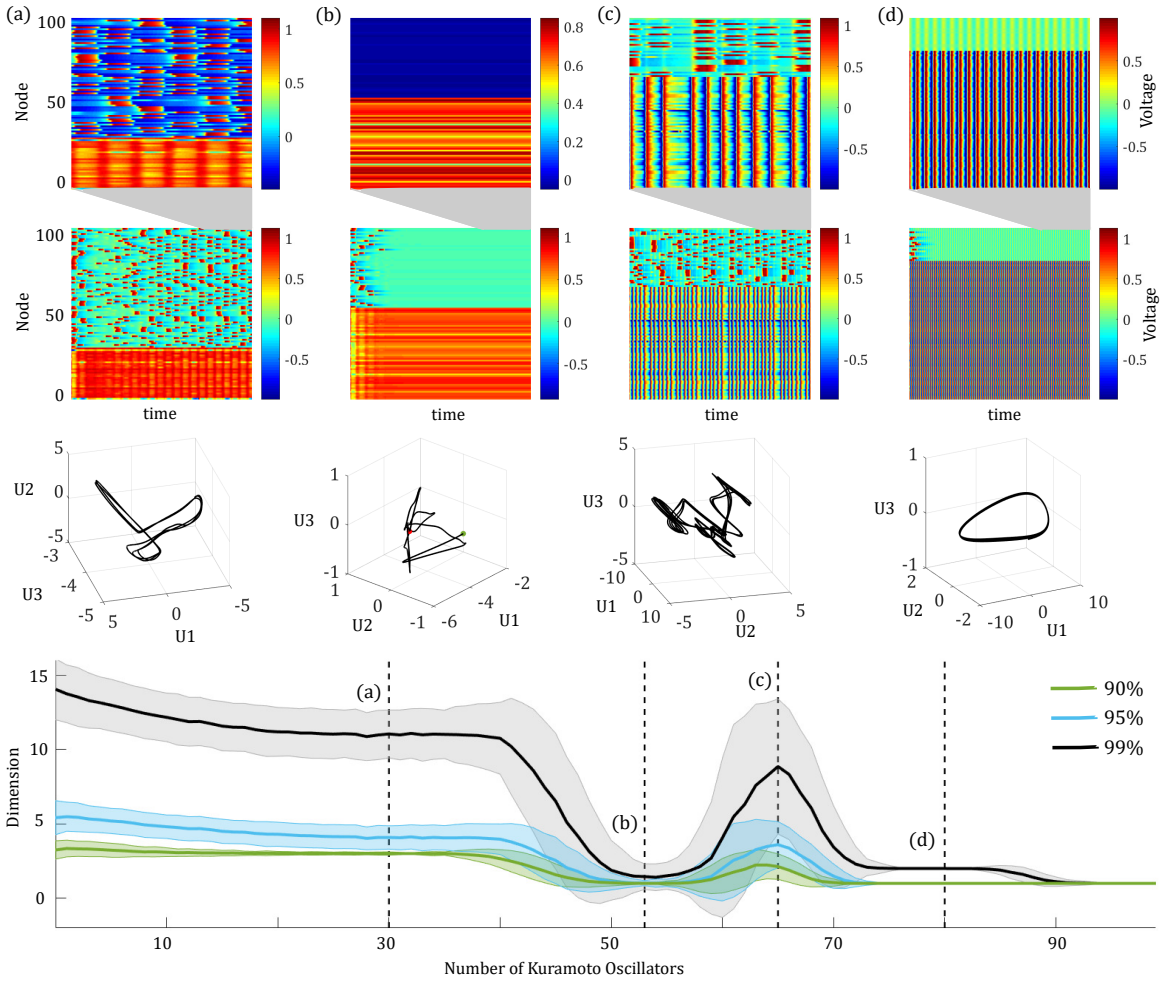
(a)
(b)
(c)
(d)
Node
time
Voltage
U1
U2
U3
(a)
(b)
(c)
(d)
90%
95%
99%
Dimension
Number of Kuramoto Oscillators

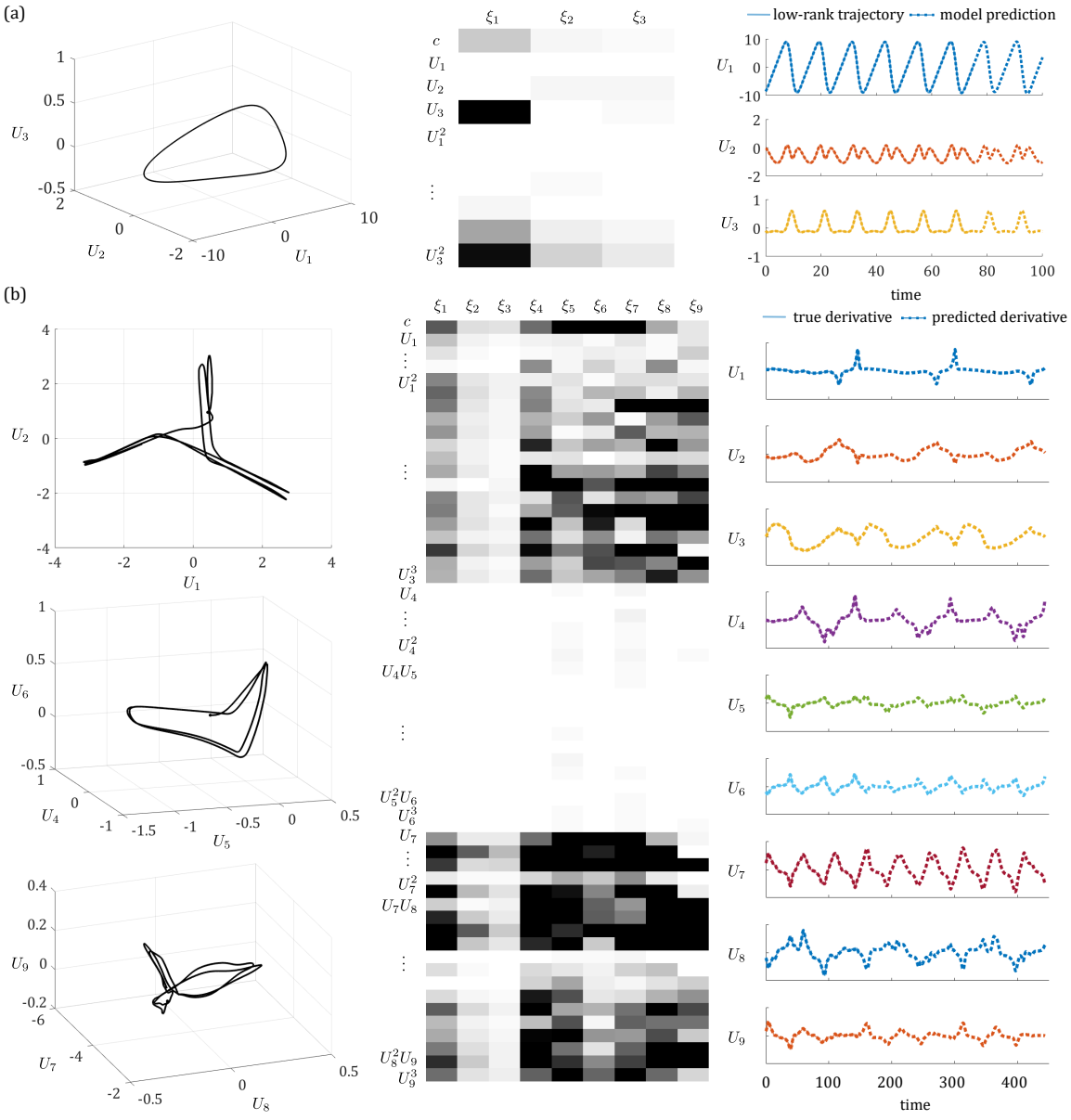

Figure 2.8: SINDy can be applied to the low-rank representation of collective dynamics of mixed FHN-Kuramoto networks. (a) In cases where the collective dynamics are quite low-dimensional and relatively simple, a stable model is recovered. (b) However, for a network with higher intrinsic dimension to its dynamics that is navigating a highly non-linear limit cycle, we may need to use many modes to accurately match the derivative and the resulting models may be quite dense.

tion is apparent as a black region for high n_K and high connectivity thresholds because the dimension is increasing so rapidly that the contour lines are on top of each other. When FHN nodes make up a significant amount of the population, this rapid jump in dimension is ameliorated because as FHN nodes become disconnected, they lose the driving force needed to maintain tonic spiking instead relaxing to a stable steady state. The constant signal from the FHN nodes reduces the overall dimension of the system. When FHN nodes dominate the system ($n_K < 20$), there is a phase transition from tonic spiking behavior for connectivity thresholds in the range $[0.7, 0.9)$ to a constant steady state above 0.9, again visible as a black region where contour lines are on top of each other in the 99% plot.

Finally, we examined the dimension of network dynamics as we varied the connectivity strength amongst the bloc of Kuramoto oscillators (Fig. 2.4.1, row 3). In this case higher values of K_K indicate stronger coupling and higher synchronization within the Kuramoto bloc. Lower connectivity leads to higher dimension collective dynamics and higher connectivity leads to lower dimension collective dynamics if the number of Kuramoto oscillators is above 1. As with the connectivity threshold, we observe a sharp phase transition between partial synchronicity and asynchronicity as a black region on the maps when $n_K > 50$. For smaller values of n_K the transition is more gradual because the FHN modes are well-connected and offset the chaotic firing of the Kuramoto bloc. When n_K is very small, the dynamic dimension is independent of K_K because the FHN dynamics are fully dominant.

We also applied our coarse-graining method to networks consisting of three different types of oscillators: Kuramoto, FHN, and Rossler. With this level of heterogeneity, the possible sets of network parameters to consider quickly grows, making a thorough exploration intractable. However, for some parameter regimes and initial conditions we demonstrate that the collective dynamics are low-dimensional and can be captured by a small number of SVD modes. Possible behaviors include high frequency, low amplitude background oscillations with periodic high amplitude spikes across the full system (Fig. 2.10a), FHN-like semi-synchronized spiking with Rossler oscillators adding higher-frequency oscillations during the relaxation period (Fig. 2.10b), or a repeated high-frequency, nonlinear oscillation at a low amplitude across the Kuramoto bloc (Fig. 2.10c). In each of these examples, we can apply SINDy with trimming to isolate regions of differing dynamics. In panel (a) from

Figure 2.9: The typical dimension of dynamics for systems of coupled Kuramoto and FHN oscillators is a function of several system parameters: the ratio of Kuramoto to FHN oscillators in the network, the mean intrinsic frequency of Kuramoto oscillators, the Erdos-Renyi connectivity threshold used to construct the adjacency graph, and the connectivity strength among the Kuramoto oscillators. For each parameter combination, one thousand independent systems were simulated and the mean number of modes needed to capture 90%, 95%, and 99% of the Frobenius norm was calculated. In row 1, observe that as the mean frequency of the Kuramoto oscillators increases, the dimension of systems with substantial numbers of both Kuramoto and FHN nodes increases. However, systems that are dominated by Kuramoto-type behavior remain low dimensional across all frequencies. In row 2, note that as the connectivity threshold increases (coupling is universally weaker) the Kuramoto dominant networks rapidly jump in dimension reflecting the bifurcation between synchronicity and asynchronicity in the system. On the other hand, the FHN-dominant networks actually decrease in dimension as coupling weakens because without sufficient input from neighbors, these nodes will cease spiking. The third row shows variation in the connectivity specifically within the Kuramoto population. In this case higher connectivity strength means a more connected Kuramoto bloc. Again, as connectivity weakens the dimension of Kuramoto-dominant systems increases sharply below a threshold around 2.5. For networks with small numbers of Kuramoto oscillators, the system dimension stays fairly constant as the connectivity strength changes because the FHN bloc is dominant and remains unaffected. The white dotted line indicates the parameter regime explored in Fig. 2.7.

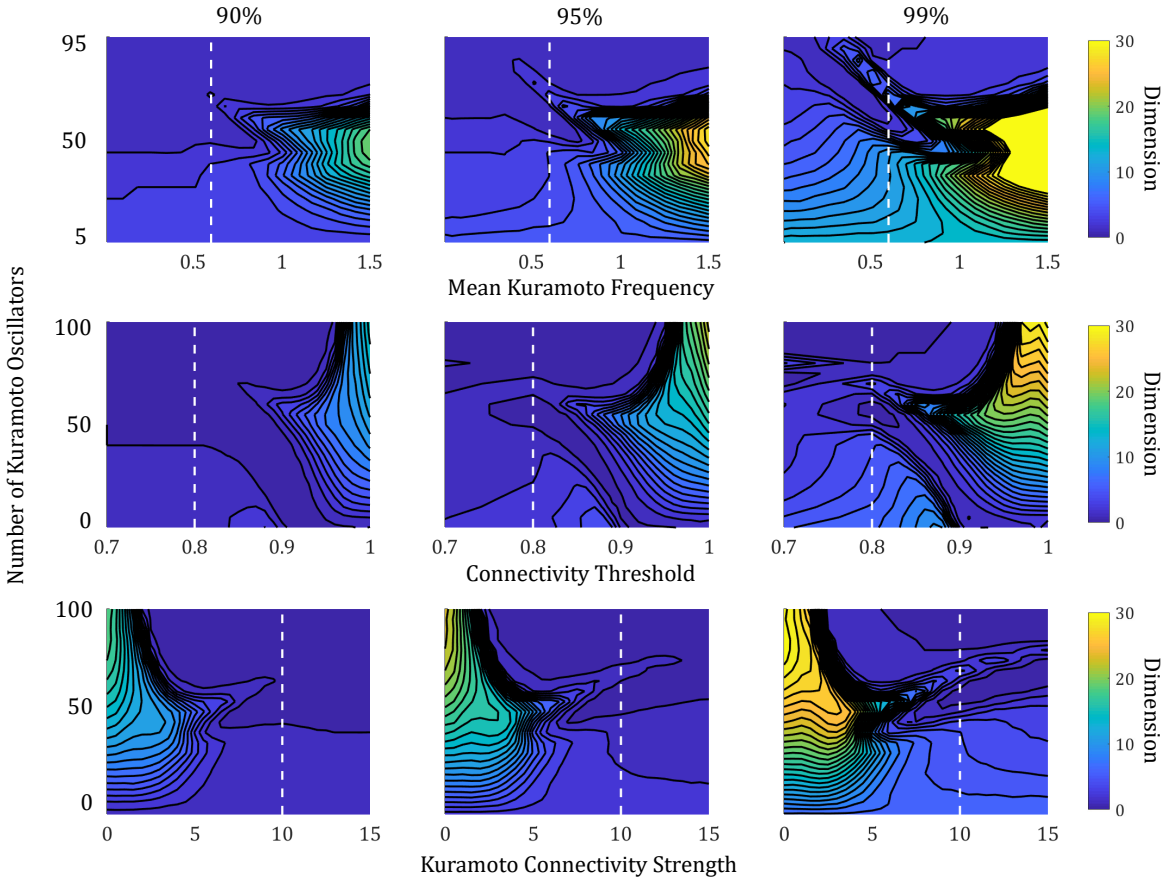
90%
95%
99%
Number of Kuramoto Oscillators
Mean Kuramoto Frequency
Connectivity Threshold
Kuramoto Connectivity Strength
Dimension
Dimension
Dimension

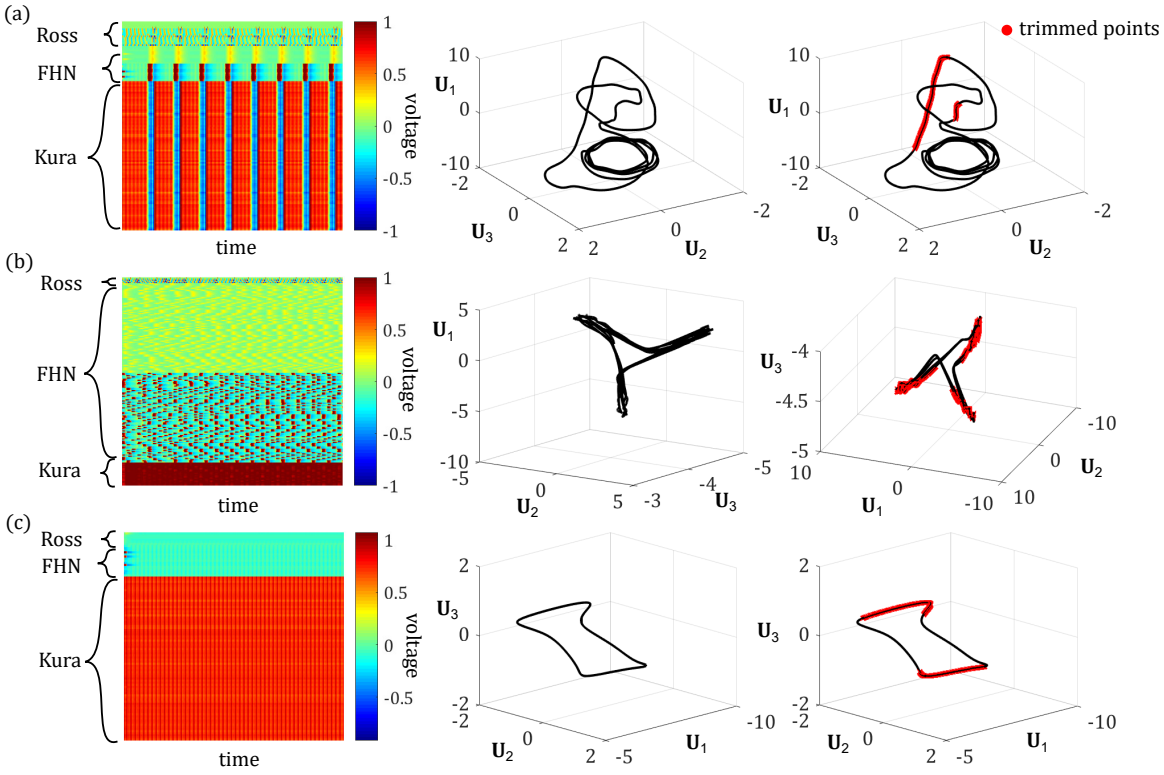

Figure 2.10: Heterogenous oscillator networks mixing Kuramoto, FHN, and Rossler nodes can also display low rank dynamics in certain regimes. Here we show several examples and the corresponding limit cycle resulting from projecting the system onto its first 3 singular vectors. SINDy with trimming again partitions the trajectory into fast vs. slow-scale dynamics. (a) All nodes across the system synchronize to a background frequency with low amplitude, on top of which there are periodic large spikes. Trimming pulls out the rapid relaxation following these large spikes and the steepest portion of the spike. (b) When the majority of the nodes are FHN, the system is dominated by FHN-like behavior. However, for this system there are small spikes along the three corners of the FHN-cycle resulting from the Rossler nodes. Trimming identifies the contribution of the Rossler nodes to the overall limit cycle. (c) Here Kuramoto oscillators dominate system behavior, but oscillations are damped because the FHN nodes have settled to a steady state. This produces an elegant non-linear limit cycle. Trimming pulls out regions of rapid change along U_1.

Fig. 2.10, the points corresponding to the universal rapid relaxation across the system are trimmed along with the steepest portion of the collective spike. In panel (b) from Fig. 2.10, the low dimensional dynamics look like the now familiar triangular FHN limit cycle, but there are irregular oscillations allow the corner wings of the triangle. There portions seem to be contributed by the small bloc of Rossler oscillators in the system and are precisely the points picked out by trimming. In panel (c) from Fig. 2.10, trimming identifies regions of rapid change along the U_1 dimension, while U_3 is constant and U_2 is nearly constant.

2.5 Discussion

Modeling heterogeneous, multiscale physics remains a mathematically challenging proposition. Indeed, traditional computational techniques quickly become intractable when attempting to resolve such systems in both space and time. Emerging data-driven methods are enabling new mathematical architectures that can automate the discovery of coarse-grained coordinates and dynamics that are low-dimensional and parsimonious. This renders approximate models that allow for rapid evaluation of the heterogeneous, multiscale physics. More than that, these techniques can also be constructed to produce interpretable physics models.

We have proposed a set of algorithms for modeling heterogeneous, high-dimensional networked dynamical systems. Specifically, we have leveraged dimensionality-reduction, sparse regression, and robust statistics to discover interpretable, coarse-grained models of the underlying physics. The method further allows us to disambiguate between the resulting fast and slow scale dynamics of the system. Used in combination, these methods are able to: (i) identify low-dimensional embeddings (coordinates) on which to construct models, (ii) identify different time scales using the statistical robustification technique of data trimming, and (iii) identify interpretable parsimonious models of the coarse-grained dynamics at different timescales.

The mathematical architecture has been demonstrated with a series of numerical experiments on networked nonlinear oscillators. The oscillators, whether a single type of oscillator or a heterogeneous set of oscillators, evolve and interact to produce low-rank dynamics that often include relaxation oscillations. The literature is largely devoid of the consideration of

such systems due to their complexity. However, the mathematical architecture developed here is able to extract meaningful models even with such high-dimensional heterogeneous interactions.

Acknowledgements

The authors acknowledge funding support from the Air Force Office of Scientific Research (AFOSR FA9550-19-1-0386) and from the National Science Foundation AI Institute in Dynamic Systems grant number 2112085 for the work discussed in this chapter.

Chapter 3

UNCONTROLLED GROWTH

3.1 CAR T-cell therapy

Cancer arises from the mutation of one or more cells leading to uncontrolled, malignant growth. There are many forms of cancer depending on the tissue in which said mutation occurs and the nature of that mutation, each constituting it's own disease and requiring a particular treatment. Cancer treatment plans often draw upon multiple treatment modalities, including surgery, radiation, chemotherapy, and immunotherapy, in order to combat disease [117, 118, 140, 91, 190]. Immunotherapies aim to enhance the body's natural defense mechanisms against tumor cells. Immunotherapy approaches include injections of molecules that promote immune activity like interleukins, antibodies, checkpoint inhibitors, and vaccines, as well as adoptive cellular therapies (ACT) in which T-cells are isolated from the patient, expanded ex vivo, and then reintroduced into the patient [98].

Advances in gene-editing during the 1990s enabled a new type of ACT in which a patient's T-cells are genetically engineered to recognize markers displayed on the surface of tumor cells [4]. These genetically engineered T-cells, called CAR T-cells, were first reported to effectively eradicate lymphoma cells in a murine model in 2010 [96]. Following this breakthrough, CAR T-cell therapy showed dramatic success against lymphomas and leukemias in a series of clinical trials with complete remission rates in the range of 65-90% [4]. In late 2017 the FDA approved two CAR T-cell therapies for treatment of relapsed and refractory Acute Lymphoblastic Leukemia and for diffuse large B-cell lymphoma [79]. Continued advances in T-cell engineering, genetic editing, selection of targets, and cell manufacturing have the potential to broaden applications of CAR T-cell therapy to treat diseases beyond leukemia and lymphoma [4, 14, 146].

Although CAR T-cell therapies show great promise in the fight against cancer, there are multiple challenges hindering their universal adoption, including potentially fatal in-

flammatory side effects that occur in up to 10% of patients who have positive responses to the infusion [146]. The toxic side effects of CAR T-cell therapy include neurologic effects, B-cell aplasia, and Cytokine Release Syndrome (CRS), ranging in severity from mild flu-like symptoms to death. Studies associate higher levels of tumor burden at the time of treatment with more serious side effects [14].

Under current medical practice, care providers administer a lymphodepleting round of chemotherapy prior to CAR T-cell injections in order to increase efficacy and reduce side effects of treatment [111]. It has been hypothesized that by reducing tumor burden and the number of normal immune cells, chemotherapy allows CAR T-cells to proliferate and overcome the cancer cells more easily. Though the use of such preconditioning regimen is common, the optimal combination of chemotherapy and CAR T-cells has not yet been determined. A mathematical model illustrating how these two forms of treatment interact for any given patient could help address this question. This motivated the development of an ODE model for CAR T-cell therapy accounting for patient preconditioning presented in section 3.2.

The success of CAR T-cell therapies in combating previously untreatable hematologic malignancies has generated significant interest in adapting CAR T-cell technology to treat solid tumors [54]. Advances in CAR T-cell specificity [25], endurance [185], and trafficking [70, 55] are being pursued in order to overcome the challenges presented by the complex biology of solid tumors. Clinical trials are underway testing the safety and efficacy of CAR T-cell treatment for glioma (NCT03423992), breast cancer (NCT02792114), liver cancer (NCT02932956), and non-small cell lung cancer (NCT04025216) among others. As the reach of CAR T-cell therapy expands to solid tumors, questions arise that the ODE model developed in section 3.2 is not suited to address.

When considering the treatment of solid tumors, we cannot assume that cell populations are well-mixed throughout the course of treatment. It has been observed through *in vivo* experiments and early stage clinical trials that the failure of systemically administered CAR T-cells to penetrate into the center of the tumor can be a mode of tumor escape [70]. A model which accounts for spatial variation in cell concentration is necessary in order to gain insight into how the geometry of the delivery of CAR T-cells impacts their effect on a

solid tumor. This motivated the development of the reaction-diffusion model of CAR T-cell therapy for solid tumors presented in section 3.3.

3.2 ODE Model for CAR T-cell Therapy with Patient Preconditioning

The Federal Drug Administration (FDA) approved the first Chimeric Antigen Receptor T-cell (CAR T-cell) therapies for the treatment of several blood cancers in 2017, and efforts are underway to broaden CAR T technology to address other cancer types. Standard treatment protocols incorporate a preconditioning regimen of lymphodepleting chemotherapy prior to CAR T-cell infusion. However, the connection between preconditioning regimens and patient outcomes is still not fully understood. Optimizing patient preconditioning plans and reducing the CAR T-cell dose necessary for achieving remission could make therapy safer. In this section, we test treatment regimens consisting of sequential administration of chemotherapy and CAR T-cell therapy on a system of differential equations that models the tumor-immune interaction. We use numerical simulations of treatment plans from within the scope of current medical practice to assess the effect of preconditioning plans on the success of CAR T-cell therapy. Model results affirm clinical observations that preconditioning can be crucial for most patients, not just to reduce side effects, but to even achieve remission at all. We demonstrate that preconditioning plans using the same CAR T-cell dose and the same total concentration of chemotherapy can lead to different patient outcomes due to different delivery schedules. Results from sensitivity analysis of the model parameters suggest that making small improvements in the effectiveness of CAR T-cells in attacking cancer cells will significantly reduce the minimum dose required for successful treatment. Our modeling framework represents a starting point for evaluating the efficacy of patient preconditioning in the context of CAR T-cell therapy.

3.2.1 Model Formulation

Here we formulate a model of the tumor-immune interaction by updating Kuznetsov's influential 1994 model [104]. Our goal is to incorporate CAR T-cell treatment, chemotherapy, and experimentally validated interaction terms while maintaining the simplicity of low-dimensional models of tumor-immune interaction. In order to make useful suggestions about

potential treatment plans, we require our model to meet reasonable biological assumptions. With appropriate parameter values, we expect to observe

- Uncontrolled growth of tumor cells in the absence of immune response,
- Immune cells reduce the number of tumor cells,
- Both immune cells and tumor cells decrease under chemotherapy.

In addition, we want the model to reflect that additional immune cells are activated and recruited by interactions between cancer cells and immune cells. The activation of tumor-killing cytotoxic T-cells is dependent on interactions between surface molecules on the T-cell and a tumor cell. Once activated, a T-cell undergoes clonal expansion, increasing the number of cells specific for the target antigen that can then travel throughout the body in search of antigen-positive tumor cells [62, 166]. Additional T-cells may also be activated by fragments of tumor cells that have been lysed by other cells [71].

The model should also reflect the results of CAR T-cell therapy studies, which have observed that sufficient lymphodepletion is an important factor in determining a durable response to treatment [95]. We expect there to be some level of competition between endogenous effector cells and CAR T-cells, because both rely on cytokines such as interleukin 7 (IL7) and IL15, to proliferate [156].

Finally, we want our model to reflect that immune cells can become inactivated through repeated interaction with tumor cells. Upon repeated exposure to tumor cells some T-cells experience exhaustion, an altered functional state in which they cannot effectively attack foreign cells [172].

We started from Kuznetsov's model, which includes only one group of activated immune cells or "effector" cells rather than multiple subpopulations of endogenous immune cells [104]. Kuznetsov's model is

$$\frac{\mathrm{d}T}{\mathrm{d}t} = aT(1-bT) - dET, \tag{3.1a}$$

$$\frac{\mathrm{d}E}{\mathrm{d}t} = g - mE + jE\frac{T}{k+T} - qET, \tag{3.1b}$$

where $T(t)$ is the population of tumor cells at time t and $E(t)$ is the population of effector cells at time t. For our model, we introduce a third equation to model the population of CAR T-cells and a fourth equation to model the concentration of chemotherapy. By including time-dependent source terms in these equations, we will be able to test treatment plans combining different CAR T-cell doses and lymphodepleting chemotherapy regimens. We also replace the second term in Eq. (3.1a) and the third term in Eq. (3.1b) with experimentally-validated, ratio-dependent interaction terms which [37] demonstrated achieve a better fit to experimental data from cytotoxicity assays compared to simpler, classical choices such as mass action or Michaelis-Menten (which are used in the Kusnetsov model). We chose to adopt their novel interaction terms into the Kuznetsov model, rather than working with de Pillis et al.'s 5-equation model system, in order to focus on the minimal set of equations that would produce desired biological behaviors.

At time t, let $T(t)$ be the number of tumor cells, $E(t)$ be the number of endogenous effector cells, $C(t)$ be the number of CAR T-cells, and $M(t)$ be the concentration of a chemotherapy drug. The model system with treatment is

$$\frac{\mathrm{d}T}{\mathrm{d}t} = aT(1-bT) - D_E - D_C - K_T(1-e^{-M})T \tag{3.2a}$$

$$\frac{\mathrm{d}E}{\mathrm{d}t} = g - m_E E - j_E \ln\left(\frac{E+C}{K}\right)\frac{D_E^2}{k+D_E^2}E - q_E ET - K_E(1-e^{-M})E \tag{3.2b}$$

$$\frac{\mathrm{d}C}{\mathrm{d}t} = v_C(t) - m_C C - j_C \ln\left(\frac{E+C}{K}\right)\frac{D_C^2}{k+D_C^2}C - q_C CT - K_C(1-e^{-M})C \tag{3.2c}$$

$$\frac{\mathrm{d}M}{\mathrm{d}t} = v_M(t) - \gamma\ M \tag{3.2d}$$

where

$$D_E = d_E\frac{(E/T)^l}{s+(E/T)^l}T \quad \text{and} \quad D_C = d_C\frac{(C/T)^l}{s+(C/T)^l}T. \tag{3.3}$$

In the absence of treatment and effector cells, tumor cells grow logistically towards a carrying capacity of b^{-1}. In the absence of tumor cells, effector cells are produced at a fixed rate, g, and decay at a rate proportional to the population, $m_E E$.

Endogenous effector cells and CAR T-cells kill tumor cells according to a ratio-dependent tumor cell death term, D_E and D_C respectively, proposed by de Pillis et al. (2005). Nu-

merous studies indicate that percent cell lysis is a function of the ratio of effector immune cells to tumor cells [184, 192]. In modeling the anti-tumor activity of $CD8^+$T-cells, de Pillis et al. (2005) considered the behavior of cells with a range of antitumor activity, from non-transduced cells, which have not been exposed to a target antigen and thus only mount a non-specific immune response, to primed $CD8^+$T-cells which have previously been exposed to the target antigen and mount a highly effective immune response. The authors found that the more effective the immune cells are at lysing their target cells, the more they follow a rational law dynamic. They speculated that this is because the highly effective cells operate closer to the saturation regime than other types of immune cells. Because we are modelling adoptive cellular therapies, which have shown very high anti-tumor activity [83, 184], this is an important model feature. For further exploration of the tumor cell lysis rate and how associated model parameters impact trajectories please see Appendix C: Numerical Simulations and Sensitivity Analysis.

Effector cells and CAR T-cells are both recruited at a rate dependent on tumor cell lysis through a modified Michaelis-Menten term, $j_E D_E^2 E/(k+D_E^2)$ and $j_C D_C^2 C/(k+D_C^2)$ respectively. This recruitment term is then scaled by a competition factor $-\ln((E+C)/K)$, which limits the proliferation of immune cells when the size of the combined immune population approaches the carrying capacity, K. This competition factor, adopted from a CAR T-cell therapy model proposed by Kimmel et al. (2019), reflects the fact that there is a limited amount of immunological "space" which effector cells can occupy. The inactivation of immune cells upon exposure to tumor cells is incorporated through mass-action terms, $q_E ET$ and $q_C CT$, capturing the phenomenon of immune-cell exhaustion [172]. Model parameters are defined in Table 1, and for details of parameter selection, please refer to Appendix B.

We have incorporated CAR T-cell therapy into the model by including a governing equation for the engineered cell population [92, 162]. The dynamics for the CAR T-cell population consist of the same functional forms as the endogenous effector cells except that instead of a constant source term, CAR T-cell injections of dose level P are modeled as a

one-time increase in the number of engineered effector cells, $v_C(t)$, where

$$v_C(t) = \begin{cases} 0 & \text{if } t \neq \text{injection time} \\ \mathrm{P} & \text{if } t = \text{injection time.} \end{cases} \tag{3.4}$$

By separating the dynamics of the endogenous effector cells from the engineered CAR T-cells, we are able to use different parameter values to define each population and incorporate competition between the two types of cells, creating a flexible framework to consider different adoptive cellular therapies.

Following the method of [36], we also introduced a governing equation for the chemotherapy drug concentration. Here γ is the decay rate of chemotherapy and $v_M(t)$ is a time-dependent forcing term encoding the dose strength, S (μM/day). The dosing schedule is

$$v_M(t) = \begin{cases} 0 & \text{if } t \notin \text{injection times} \\ \mathrm{S} & \text{if } t \in \text{injection times} \end{cases} \tag{3.5}$$

where the injection times are the times during which a patient is receiving an infusion of chemotherapy. In the case of lymphodepleting chemotherapy, we are modeling regimens in which patients receive a uniform dose of chemotherapy over the course of one half hour each day for several days in a row. Consequently $v_M(t)$ takes on the form of a collection of hat functions located at the start of each infusion period with height equal to the dose strength and width equal to one half hour. Elsewhere $v_M(t)$ is uniformly zero.

We model the impact of chemotherapy by introducing saturating fractional cell-kill terms, $K_T(1 - e^{-M})T$, $K_E(1 - e^{-M})E$, and $K_C(1 - e^{-M})C$, to the equations for each cell population in Sys. (3.2a)-c, again following the method of de Pillis et al. (2006). These expressions are nearly linear for low concentrations of chemotherapy drug, $M(t)$, but the kill rate rapidly plateaus to the parameters K_T, K_E and K_C respectively as the concentration increases. This functional form has been shown to match dose-response curves from the literature [56]. Note that different types of chemotherapy can be considered by varying the associated parameters: γ, K_T, K_E, and K_C.

3.2.2 Results

Model Behavior

In clinical practice, preconditioning chemotherapy is administered over a short time period, typically 3-5 days, followed by 2-14 days of rest, after which a single CAR T-cell injection is administered. Thus, in clinically relevant scenarios, the chemotherapy concentration $M(t)$ will decay fairly rapidly to zero, which is the only chemotherapy concentration steady-state relevant to our setting. Thus when discussing the stability of the model given by Sys. (3.2), we assume that $M(t) = 0$ and focus our analysis on the the first three equations, which govern the dynamics of the tumor, effector, and CAR T-cell populations. The details of analyzing this 3-dimensional system (A.1) are given in Appendix A. In particular, we scale the tumor cell count by the tumor carrying capacity, yielding $x = bT$, and we scale the immune cell populations by the ratio between the intrinsic effector cell growth rate and the tumor cell growth rate, yielding $y = aE/g$ and $z = aC/g$, to non-dimensionalize Sys. (A.1) before proceeding with linear stability analysis.

We show analytically that for a wide range of biologically relevant parameters, Sys. (A.1) has at least two stable equilibria, both of which reside in the $C = 0$ plane, a zero-tumor (or tumor-free) equilibrium occurs at the point and a high-tumor equilibrium occurs where the tumor cell population is near the carrying capacity. Nullsurfaces and equilibria of the nondimensionalized system (Sys. (A.3)) in the plane $z = 0$ are plotted in Fig.3.1a for the Patient 3 parameter set (column 5 of Table 1). The tumor-free equilibrium is at the point $(x = 0, y = 1/m_y, z = 0)$ and the high-tumor equilibrium is at the point $(x \approx 1, y \approx 1/(q_y + m_y), z = 0)$. We also determined numerically that, as indicated in Fig.3.1a, there is a saddle point for a relatively small number of tumor and effector cells. Note that in Fig. 3.1a-b we are only plotting the positive quadrant because it is an invariant set for this system. Thus, if we start with a non-negative initial condition, the model will never predict a negative population of cells, a desired property for biological interpretability.

We numerically located and assessed the stability of interior equilibria of the nondimensionalized system (A.3) as well (Fig.3.1b). For the parameter sets considered here (listed in Table 1 and described in Section 3.2.2, with further details in Appendix B), there is a

saddle point located at a moderate tumor cell population, low effector cell population, and high CAR T-cell population. This saddle point significantly shapes trajectories, causing non-monotonic behavior, notably pseudo-progression of the tumor whereby the tumor initially increases after CAR T-cell treatment before ultimately being eradicated. The stable manifold of this saddle point separates the basin of attraction for healthy outcomes from the basin of attraction for unhealthy outcomes. There is an additional unstable interior equilibrium at a low population level for all three cell types which contributes to the spike in CAR T-cell populations seen in healthy trajectories before the CAR T-cell population starts declining.

For the Patient 1 and 2 parameters sets given in Table 1, only the two interior equilibria mentioned above exist. However, for some parameter values, including Patients 3 and 4 from Table 1, two additional equilibria appear near the high-tumor equilibrium. One is a stable node, which we refer to as the coexistence equilibrium because all 3 cell populations persist at non-zero levels. Due to the fact that the tumor burden remains at around 95% of the high-tumor value, trajectories that approach this steady-state are also considered an unhealthy outcome. The other equilibrium that appears is a third saddle point, with the stable manifold now separating trajectories that approach the high-tumor equilibrium from those that approach the coexistence equilibrium.

Changing the parameter values characterizing CAR T-cells causes interior equilibria to appear and disappear. The maximum CAR T-cell recruitment rate, j_C, can be tuned to observe the sequence of saddle node bifurcations creating and destroying the interior equilibria (Fig.3.1c). When $j_C = 0$, the only CAR T-cell nullsurface is the plane $C = 0$ and there are no interior equilibria. For small values of j_C, an unstable node and saddle point appear near the origin. As j_C increases, the saddle point moves higher (in an x-axis and z-axis sense) along the tumor-cell null surface, allowing larger spikes in CAR T-cells to occur for trajectories that ultimately reach the high-tumor outcome. Patient parameter sets 1 and 2 lie in this regime. Increasing j_C still further pushes the system past a critical threshold in which the recruitment of CAR T-cells in response to the high tumor burden balances the natural death and deactivation rate of CAR T-cells, so the CAR T-cell population is able to persist for some initial conditions. Patient parameter sets 3 and 4 lie in this regime, in

Figure 3.1: Nullsurfaces and equilibria for the non-dimensionalized system (A.3) are shown for the Patient 3 parameters (column 5 of Table 1). The nondimensional state variables are $x = bT$, $y = aE/g$, and $z = aC/g$. (a) Boundary equilibria lie at the intersections of the effector and tumor cell nullsurfaces on the CAR T-cell nullsurface $z = 0$, plotted here. For a wide range of parameters, there are two stable equilibria (solid circles) and a saddle point (open circle). (b) Interior steady states lie at the intersections of the non-zero nullsurfaces for the tumor, effector, and CAR T-cell populations. Intersections between the the effector cell nullsurface and the nullsurfaces for the other two cell populations are emphasized with black lines. For this set of parameters, there is one stable interior equilibrium (solid circle). There are three unstable interior steady states indicated by open circles: an unstable node near the origin, a saddle point at a high number of CAR T-cells and moderate tumor cell count, and another saddle point at x just less than 1 and a very small number of CAR T-cells. (c) Bifurcation diagram created by varying the maximum CAR T-cell recruitment rate, j_C, while fixing all other parameters at their Patient 3 value. For each value of j_C, the tumor cell counts, x^*, of all existing equilibria were computed numerically. The three boundary equilibria that lie in the $z = 0$ plane (shown in a) remain constant for all values of j_C, and are denoted by solid lines (stable) and a dashed line (unstable) in panel (c). As j_C changes, interior equilibria appear and disappear in a sequence of 3 saddle node bifurcations. Unstable interior equilibria are marked by open gray circles and the stable interior equilibrium, referred to as the coexistence state, is marked by black circles

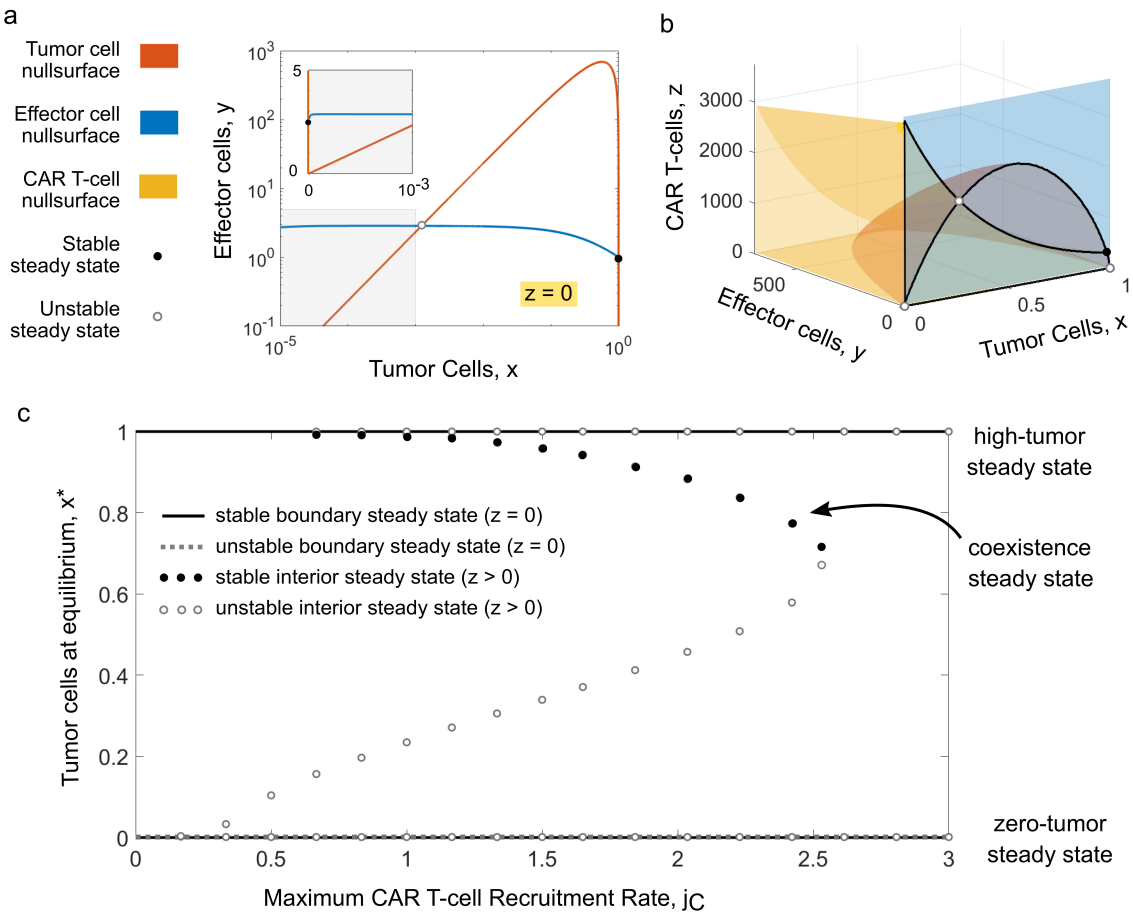
a
Tumor cell nullsurface
Effector cell nullsurface
CAR T-cell nullsurface
Stable steady state
Unstable steady state
Effector cells, y
Tumor Cells, x
z = 0
b
CAR T-cells, z
Effector cells, y
Tumor Cells, x
c
Tumor cells at equilibrium, x*
Maximum CAR T-cell Recruitment Rate, jC
stable boundary steady state (z = 0)
unstable boundary steady state (z = 0)
stable interior steady state (z > 0)
unstable interior steady state (z > 0)
high-tumor steady state
coexistence steady state
zero-tumor steady state

which the stable coexistence equilibrium has appeared simultaneously with a saddle point near the high tumor equilibrium. As j_C continues to increase, the co-existence equilibrium shifts to lower and lower tumor values, and the saddle point causing spikes in the CAR T-cell population shifts to higher tumor values. Eventually, the two collide and disappear, leaving three unstable interior equilibria. The equilibria in the $C = 0$ plane remain unchanged throughout because they are independent of j_C.

Evaluation of Treatment plans

Standard treatment protocols incorporate a lymphodepleting preconditioning regimen which consists of a round of chemotherapy prior to CAR T-cell infusion. We tested realistic combinations of chemotherapy preconditioning and CAR T-cell doses by simulating treatment plans with parameter sets from several different cancer types using Sys. (3.2) and evaluating the outcomes. Here we discuss the scenarios considered and simulation results.

Treatment plans considered

We explored combinations of chemotherapy preconditioning and CAR T-cell doses from a range that encompasses the standard procedures for the two FDA approved CAR T-cell treatments, Yescarta [93] and Kymriah [132]. The guidelines for dosing CAR T-cells prescribe $0.2 - 5.0 \times 10^6$ cells per kilogram of body weight up to a maximum of 2.5×10^8 cells [93] or 6×10^8 cells [132]. We consider injections of $P = 1 \times 10^7$ cells, $P = 1 \times 10^8$ cells, and $P = 2.5 \times 10^8$ cells referred to as dose level 1 (DL1), dose level 2 (DL2), and dose level 3 (DL3) respectively. However, studies have shown that only a small fraction of injected CAR T-cells remain in circulation in the blood [177]. To reflect this in our numerical simulations, we scaled down the effective dose, P, to be 1% of the injected dose level [177].

The standard chemotherapeutic preconditioning regimen for both drugs is a combination of fludarabine and cyclophosphamide administered over three to five days. We considered two chemotherapy regimens, either medium strength for one half hour each day for 5 days (C5), or high strength for one half hour each day for 3 days (C3). The strengths were chosen so that the peak concentration of chemotherapy during the five day regimen matched the

value reported in a pharmacokinetic study of fludarabine [77], and the overall exposure in the two plans was equal (measured by the area under the chemotherapy concentration curve). In practice, lymphodepletion is followed by either a 3-day rest period for Yescarta [93] or 2-14 days rest for Kymriah [132] before T-cell injection. For all combinations, we started by enforcing the minimum rest period of 2 days between the end of chemotherapy and the T-cell injection. The initial conditions tested for each patient cover a range of tumor magnitudes. For Patient 3 and 4 the minimum value is close to the smallest detectable tumor size and the maximum is the carrying capacity for tumor cells in the absence of effector cells. The values considered were a low tumor burden (low TB) at 1×10^8 tumor cells, medium tumor burden (medium TB) at 5×10^8 tumor cells, and high tumor burden (high TB) at 9.8×10^8 tumor cells [36]. For Patient 1 and 2, we tested initial conditions an order of magnitude higher to reflect the higher tumor cell carrying capacity. The values considered for Patients 1-2 were a low tumor burden (low TB) at 1×10^9 tumor cells, medium tumor burden (medium TB) at 5×10^9 tumor cells, and high tumor burden (high TB) at 1×10^{10} tumor cells. The initial number of effector cells was set to 4×10^5 cells, which is the average of the zero-tumor equilibrium values for all four patient parameter sets [155]. The estimated average number of T-cells activated against a given antigen is higher; however, cancer cells are notoriously hard for the immune system to recognize, so it is reasonable to consider a smaller initial immune response [143].

Patients

We considered four parameter sets in our evaluation, each representing a different theoretical "patient". The first patient constitutes typical parameter values for diffuse large B-cell lymphoma [155]. Rösch et al. estimated a range of model parameters using data from randomized clinical trials in elderly patients. Our second patient parameter set is drawn from typical parameter values for B-cell chronic lymphocytic leukemia [127]. Nanda et al. analyzed existing data in the medical literature to determine ranges of values for model parameters and calibrated their model to clinical patient data. Currently CAR T-cell therapy has been approved for use with several blood cancers; however, numerous clinical trials are

Figure 3.2: Combination treatment trajectories in a 3-dimensional view of phase space showing the tumor, effector, and CAR T-cells. The surface separating the basin of attraction for the healthy zero-tumor steady state from the basin of attraction for unhealthy outcomes is shown in gray (computed numerically for Sys. (A.1)). Example trajectories in which the initial condition was treated with chemotherapy at strength $S = 125$ for one half-hour each day for 3 days, followed by 4 days of rest before a CAR T-cell dose of 10^7 cells were simulated for (a) Patient 1 (column 3 of Table 1) and (b) Patient 3 (column 5 of Table 1) using Sys. (3.2). The dotted portion of each trajectory precedes CAR T-cell injection and thus is confined to the plane $C = 0$. The dashed vertical line shows the CAR T-cell dose administered. After this injection, if the patient condition lies above the surface it will ultimately approach the healthy zero-tumor outcome (blue trajectories), but if the patient condition is still below the surface it will approach an unhealthy patient outcome. The magenta trajectories in panel (a) approach the high-tumor equilibrium beyond the edge of the plot at the point $(T^* = 2 \times 10^{12}, E^* = 2.05 \times 10, C^* = 0)$, and the red trajectories in panel (b) approach the coexistence equilibrium. In both patients, successful CAR T-cell treatments result in higher, more prominent CAR T-cell peaks compared to unsuccessful treatments. In the patient scenarios shown in (c) (Patient 1) and (d) (Patient 3), when a dose of 10^7 CAR T-cells is administered at the patient initial condition (blue dot), CAR T-cells expand post injection, but the tumor progresses monotonically towards an unhealthy equilibrium—the high-tumor steady state beyond the edge of the plot in the case of Patient 1 and the coexistence equilibrium in the case of Patient 3. However, under the chemotherapeutic preconditioning described above, the patient condition is shifted to a lower tumor and effector cell burden prior to CAR T-cell injection. From this preconditioned state, the same CAR T-cell dose of 10^7 cells now succeeds at shifting both patients to the healthy basin of attraction

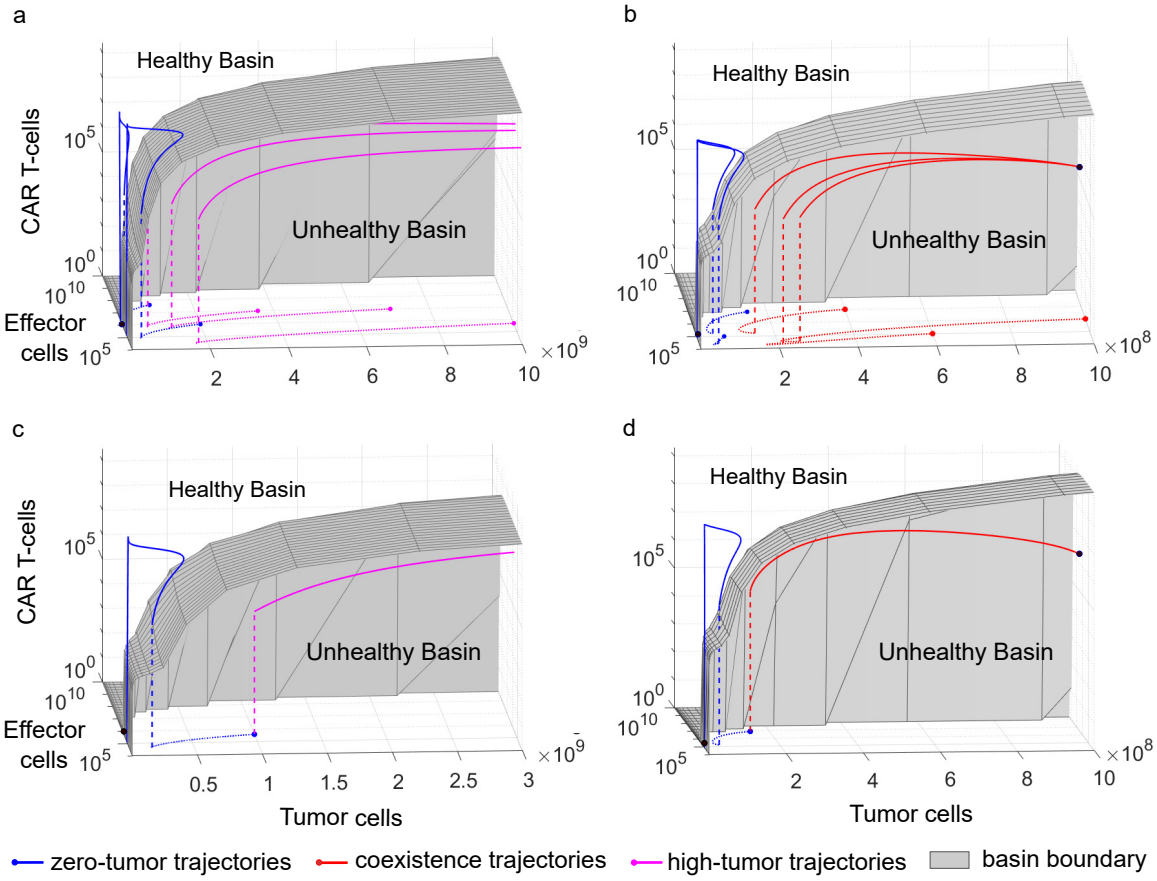

testing its potential for treatment of solid cancers as well, including melanoma [14, 193]. De Pillis et al. ([37]) used data from two metastatic melanoma patients reported in a clinical trial to fit their model for mixed chemotherapy and immunotherapy treatment. We use their resulting parameter values for our last two patient parameter sets. The model assumptions are predicated on CAR T-cells effectively targeting tumor cells. Hence simulation results suggest possible outcomes once good target antigens have been identified for metastatic melanoma. Parameters characterizing the CAR T-cell population were adapted from a model put forward by Kimmel et al. (2019). Their model parameters were fit to data from the ZUMA-1 clinical trial of CAR T-cell therapy for adults with refractory aggressive Non-Hodgkin Lymphoma. The parameters we used for Patient 1-4 are listed in Table 1, and the details of parameter selection are discussed in Appendix B.

Given a set of patient parameters, partitioning the phase space into basins of attraction for the healthy versus unhealthy outcomes provides intuition into how that patient will respond to treatment. Basins of attraction computed using the 3-equation model (Sys. (A.3)), which governs the dynamics of the tumor, effector, and CAR T-cell populations, are illustrated for Patients 1 and 3 in Fig.3.2.2. Panels a-b show an ensemble of initial conditions which have been treated with 3 days of high strength chemotherapy and 10^7 CAR T-cells, with 4 days of rest in between. The trajectories illustrated in Fig. 2a-b would all approach an unhealthy outcome in the absence of treatment, illustrated by the fact that the initial conditions lie within the unhealthy basin (region below gray surface). For moderate to large tumors, the CAR T-cell dose necessary to move the patient condition to the healthy basin of attraction (region above gray surface) scales with the tumor burden, rapidly climbing to medically infeasible levels. However, as illustrated by the dashed portion of trajectories, chemotherapeutic preconditioning shifts initial conditions towards the origin, reducing tumor burden and lowering the number of effector cells potentially competing with injected CAR T-cells. For some conditions, this shift is sufficient to allow medically feasible injections of CAR T-cells to proliferate and eradicate the tumor, but if a trajectory is still in the unhealthy basin of attraction for a given patient after both chemotherapy and CAR T-cell injection, that treatment plan will not be effective. In these cases, after tumor regression under chemotherapy, the tumor progresses again. Panels c and d of Fig. 3.2.2 highlight outcomes from a single initial condition for each patient. Without preconditioning, the CAR T-cell dose does not lift the condition out of the unhealthy basin of attraction, and the tumor burden grows towards either the high-tumor steady state (Patient 1 in Fig. 2c) or the coexistence state (Patient 3 in Fig 2d). However, with preconditioning, the CAR T-cell dose succeeds for both patients, and the trajectory approaches the healthy zero-tumor steady state. We observe that the successful CAR T-cell trajectories reach a higher, sharper CAR T-cell peak than the unsuccessful trajectories Fig. 3.2.2.

Single treatment plan outcomes

First, we tested the CAR T-cell doses and lymphodepleting regimens one at a time to verify the impact on each tumor burden. In all scenarios, lymphodepleting chemotherapy alone initially reduced the tumor burden and endogenous immune cells, but ultimately resulted in tumor progression. CAR T-cell injection without prior lymphodepletion also failed in all scenarios. When the endogenous effector cell population is high, even at a moderate tumor burden, the CAR T-cell population is unable to mount an effective response due to competition from the endogenous cells. Generally, the dosage of CAR T-cells necessary to treat a patient initial condition without preconditioning lies well beyond the maximum dosage deemed safe, unless the initial tumor burden is very small. This limitation drives the need to combine these two treatment modalities in order to effectively combat cancer.

Combination treatment plan outcomes

After testing single-modality treatments, we considered combination treatments. In Fig. 3.3 we illustrate a range of possible patient trajectories from numerical simulations of combination treatment for Patients 1-4 at medium tumor burden. The effect of the 3-day high strength chemotherapy plan, followed by 4 days of rest before a CAR T-cell injection at DL3 is shown for Patients 1 and 2 (Fig. 3a-c). In both cases, the system would have monotonically progressed to the high-tumor steady state without intervention. Under this combined treatment plan, tumor cells initially decrease during chemotherapy for both patients, but then progress again when chemotherapy stops. After CAR T-cell injection, the CAR T-cell population increases. For Patient 1, the CAR T-cell expansion is not sufficient to reverse tumor progression and, as the tumor continues to grow, eventually the immune cells become exhausted and the CAR T-cell population is driven down to zero. However, for Patient 2, though the tumor initially progresses after CAR T-cell injection, the engineered cells expand enough to reverse tumor growth and eliminate the tumor around 30 days post-injection. Once the tumor is eliminated, the CAR T-cell population gradually declines and the endogenous effector cell population continues to recover from a post-chemotherapy low. The effect of the 5-day medium strength chemotherapy plan, followed by 2 days of rest

before a CAR T-cell injection at DL2 is shown for Patients 3 and 4 (Fig. 3d-f). Again, for both patients the system would have rapidly progressed to the high-tumor steady state without intervention. Similarly to Patients 1 and 2, during preconditioning the tumor initially decreases, but then progresses once chemotherapy stops, and the CAR T-cell population increases immediately following injection. In the case of Patient 3, CAR T-cells peak at 12 days, but after this point the cell populations converge to their coexistence values, which involves an unsustainable tumor burden and is thus an unsuccessful patient outcome. In Patient 4, however, CAR T-cells expand sufficiently well to reverse initial pseudo-progression of the tumor and eliminate tumor cells around 18 days after CAR T-cell injection. Again, when the tumor is eliminated, the CAR T-cell population gradually declines and the endogenous effector cell population recovers.

Fig. 3.4 summarizes the outcomes of combination treatments for all theoretical patient scenarios. Notably, for all patients, we observe conditions that cannot be treated by medically feasible CAR T-cell injection alone, but are treatable with chemotherapy and CAR T-cell injection in combination. For the dose levels considered here, CAR T-cell injection and lymphodepleting chemotherapy were never effective for Patient 1 with high TB.

Between the fixed preconditioning regimens considered, the 3-day high-strength and the 5-day medium-strength chemotherapy dosing schedules often had similar outcomes. However, there are several cases in which preconditioning with the 5-day plan results in successful treatment where the 3-day plan fails. For example, in Patient 1 medium TB, combining 5-day chemotherapy with DL1 was effective in eliminating the tumor, but combining 3-day chemotherapy with the same dose of CAR T-cells was not.The same result occurs for Patient 2 medium TB and DL1, Patient 2 high TB and DL3, Patient 3 high TB and DL3, Patient 4 medium TB DL1, and Patient 4 high TB DL2. Plots of the time course of the trajectories under these two treatment plans for Patient 1 medium TB are shown in Fig. 3.5. Without treatment the tumor-cell count climbs towards the carrying capacity and the effector-cell count drops, approaching the high-tumor equilibrium. Introducing 3 days of high strength chemotherapy reduces the tumor burden, but when chemotherapy ends and the CAR T-cell injection is administered on day 5, the tumor progresses towards its carrying capacity despite an initial increase in the CAR T-cell population, which ultimately

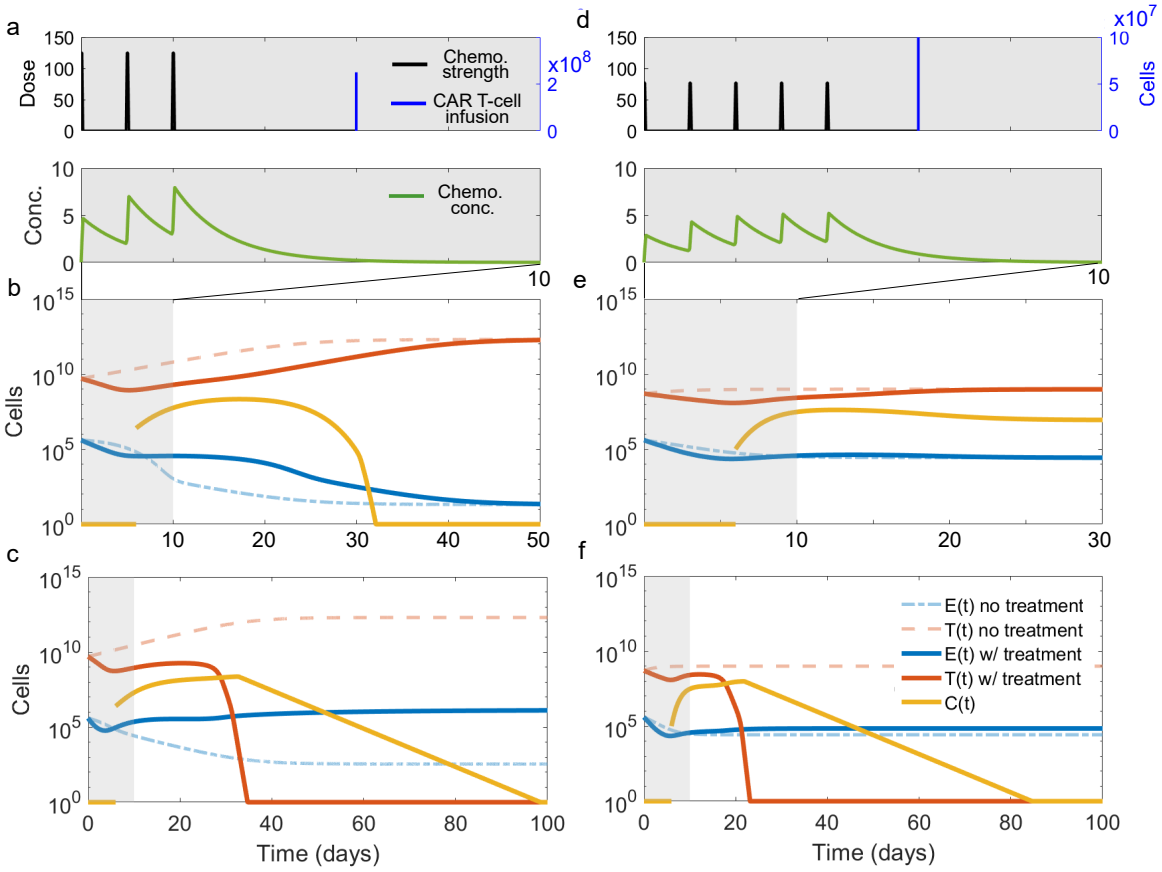

Figure 3.3: Example combination treatments in four patients simulated using Sys. (3.2). In all cases, the system without treatment (no chemotherapy or CAR T-cell dose) would approach the high-tumor steady state. Combining the 3-day high strength chemotherapy plan with a 4-day rest period and an injection of DL3 $= 2.5 \times 10^8$ CAR T-cells illustrated in (a) produces an unsuccessful outcome for (b) Patient 1, but succeeds for (c) Patient 2. Combining the 5-day medium strength chemotherapy plan with a 2-day rest period and an injection of DL1 $= 10^7$ CAR T-cells illustrated in (d) produces a successful outcome for (e) Patient 3, but an unsuccessful outcome for (f) Patient 4. The first 10 days are shaded gray in each plot to show when treatment is being applied

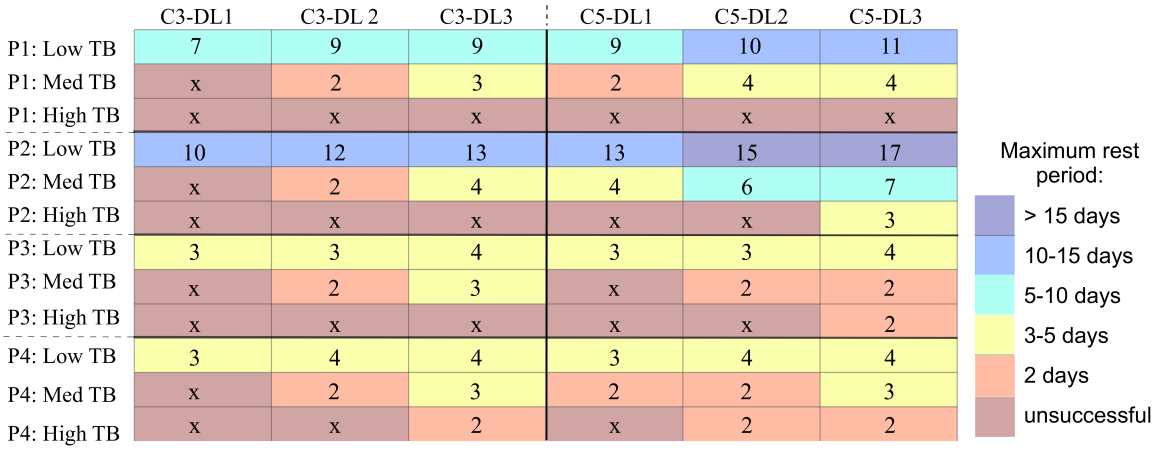

Figure 3.4: The maximum number of rest days between indicated chemotherapy plan and CAR T-cell dose resulting in a successful treatment outcome for three initial conditions based on numerical simulations using the parameter sets for Patients 1-4 recorded according to the following key: DL1 $= 1 \times 10^7$ cells, DL2 $= 1 \times 10^8$ cells, DL3 $= 2.5 \times 10^8$ cells, C3 is 3 days of chemotherapy at high strength, C5 is 5 days of chemotherapy at medium strength. Treatment combinations that failed even with the minimum rest period of 2 days are shaded red and indicated by an x

drops to zero (Fig. 3.5a). In contrast, 5 days of medium strength chemotherapy reduces the tumor burden and endogenous effector cell population enough so that after CAR T-cell injection on day 7, the engineered cells climb to a higher and later peak. Initially, the tumor progresses, but around day 20 the tumor-cell count begins to steadily decline to zero. Once the tumor burden is reduced, the CAR T-cell population begins to decline while the endogenous effector cells slowly recover (Fig. 3.5b). Although the area under the chemotherapy concentration curve is the same in these two scenarios, spreading the concentration over 5 days instead of 3 dramatically changes the patient's outcome. The tumor and effector cell counts on day 3 of the high strength plan are lower than the cell counts on day 3 of the medium strength plan. However, the doses are high enough that the advantage of the higher dose in the 3-day high strength plan is only slight and does not compensate for the longer exposure of the 5-day medium strength plan. The advantage of the 5-day plan then holds throughout the subsequent rest period and causes the difference in post CAR T-cell injection outcomes. The difference between the kill rates for the two plans is small due to the saturating nature of the chemotherapy cell kill term, a property which has been widely supported in the literature [36, 56, 147, 153].

Finally, our simulations showed that the rest period between the end of preconditioning and T-cell injection impacts patient outcome. For example, administering 5 days of high-strength chemotherapy, allowing 4 days of rest, and then administering an injection of CAR T-cells at DL3 is not an effective intervention for Patient 2 high TB (Fig. 3.6a). However, if the rest period is limited to 3 days instead of 4, the combination is successful (Fig. 3.6b). During the extended rest period, the tumor-cell count climbs high enough that a CAR T-cell injection that would be effective with a shorter rest period fails. For each combination of chemotherapy and CAR T-cell therapy that succeeded with a 2-day rest period where the CAR T-cell dose alone failed, we determined the maximum possible rest period with which the combination was still effective (Fig. 3.4). Over 70% of these scenarios failed if the rest period was 5 days or greater. Nearly 90% of the scenarios failed if the rest period was longer than 12 days. All of the scenarios failed if the rest period was longer than 17 days. This suggests that the length of the rest period between chemotherapeutic lymphodepletion and CAR T-cell injection can have important implications for patient outcome. As rest periods

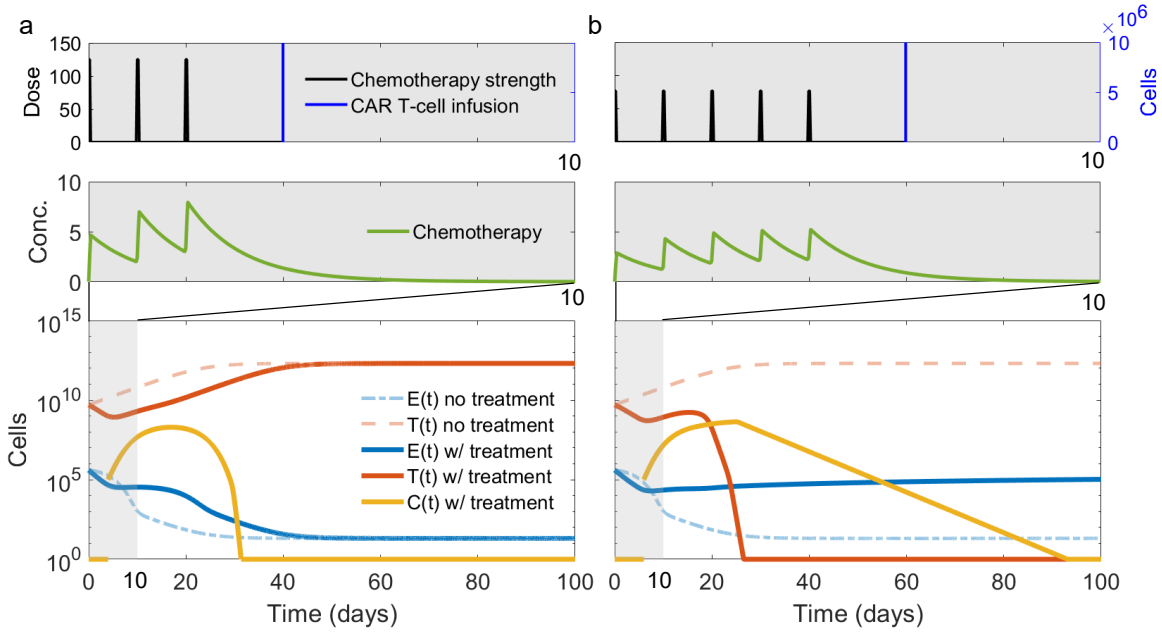

Figure 3.5: Numerical simulations of treatment of medium TB for Patient 1. (a) Three days of high-strength chemotherapy are combined with a CAR T-cell injection of 1×10^7 cells, producing an unhealthy outcome. (b) The 5-day medium strength chemotherapy plan is combined with the same CAR T- cell injection resulting in a successful patient outcome. The relevant treatment plan is illustrated in the panels above the cell population trajectories, and the first 10 days are shaded gray in all panels, emphasizing when treatment is occurring

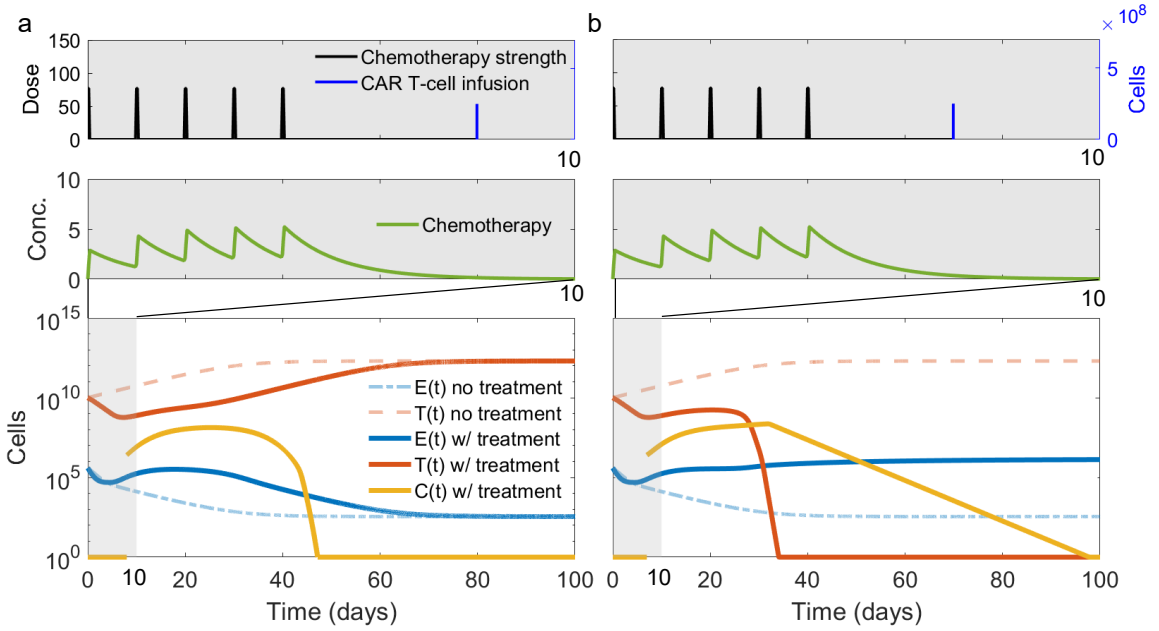

Figure 3.6: (a) Combining 5 days of high-strength chemotherapy and 2×10^8 CAR T-cells sequentially with a 4-day rest period in between allows the tumor to escape. (b) However, combining the two treatments with a 3-day rest period results in tumor elimination and a healthy outcome. Both simulations were run using parameters from Patient 2 and assuming high TB. The relevant treatment plan is illustrated in the panels above the cell population trajectories, and the first 10 days are shaded gray in all panels to emphasize when treatment is occurring

can range widely under current guidelines, from 2-14 days, this is an important aspect of treatment to investigate more thoroughly.

Sensitivity Analysis

We performed a sensitivity analysis on the model proposed in Sys. (A.1) to identify which parameters have the largest impact on the effectiveness of CAR T-cell injections. For each patient, we calculated the precise dose of CAR T-cells necessary to shift the low-TB initial condition to a healthy patient outcome. We call this number of CAR T-cells the CAR T-cell success threshold, because any treatment plan which injects a dose of CAR T-cells exceeding this quantity will be successful (in theory) against tumor burdens up to and including the low TB (Fig. 3.2.2a).

For the sensitivity analysis we varied each parameter up and down by 1% while holding the other parameters constant and calculated the resulting change in the CAR T-cell success threshold. (See Appendix C for details of sensitivity analysis.) Across all patients, the exponent in the tumor-cell lysis rate, l, had the largest impact on the high-tumor threshold (Fig. 3.2.2b). A 1% change in l results in a $5-7\%$ shift in the threshold, which indicates that small changes in the effectiveness of CAR T-cell against tumor cells will affect clinical outcomes. The tumor growth rate, a had a significant impact on the threshold for all parameter sets, indicating that cancers characterized by a higher growth rate will require higher CAR T-cell doses for a given initial condition. Across the four patients, a 1% change in the maximum CAR T-cell recruitment rate, j_C, resulted in a $3-5\%$ change in the CAR T-cell success threshold, supporting the notion that improving the ability of CAR T-cells to expand can significantly lower the necessary number of injected cells.

Of the remaining parameters, those characterizing CAR T-cells had the largest impact on the CAR T-cell success threshold. The maximum tumor cell lysis rate by CAR T-cells, d_C, the death rate m_C, the deactivation rate by tumor cells q_C, the half-saturation value of tumor cell lysis, s, and the joint carrying capacity K all had a smaller, but non-negligible impact on the high-tumor threshold. Targeting these aspects of CAR T-cell function could be helpful. In contrast, changes in the parameters defining the steepness of the immune cell

recruitment curves, k, and the remaining parameters defining effector cell dynamics, g, d_E, j_E, k_E, m_E and q_E, had little effect on the CAR T-cell success threshold.

De Pillis et al. performed a sensitivity analysis on their 2005 model, from which we adapted several interaction terms. They found that the tumor size at $t = 25$ days was most sensitive to the tumor growth rate a and the exponent in the tumor lysis rate, l. Our results confirm the importance of these two parameters even when measuring a different model feature.

3.2.3 Discussion and conclusion

We have developed and analyzed a mathematical model consisting of a system of ordinary differential equations that can be used to test combinations of preconditioning chemotherapy regimens and CAR T-cell doses. We also found that under biologically relevant parameter values the system has at least two stable equilibrium points, one "healthy," tumor-free equilibrium and one "unhealthy," high-tumor equilibrium. Adjusting the parameters characterizing CAR T-cell interactions with tumor cells can also cause an "unhealthy," stable coexistence equilibrium to emerge. The basins of attraction for these equilibria were determined numerically. The variation between the shapes of the basins of attraction for different parameter sets reflect the fact that responses to treatment will not be uniform across patients.

We tested treatment plans that adhere to standard CAR T-cell therapy protocols on patient parameter sets from several cancer types. Our goal was not to propose any novel therapy plans or unrealistic dosing schedules, but rather to uncover refinements that are attainable within current practice and that merit additional attention. We observed a variety of outcomes supporting three main conclusions:

First, our model predicts that, without preconditioning, medically infeasible CAR T-cell injections would be required to successfully treat moderate to large tumor burdens. The necessary CAR T-cell dose can be quantified by characterizing the boundary between the basin of attraction for the healthy versus unhealthy equilibria for a patient parameter set. Successful preconditioning shifts a patient initial condition to lower tumor and endogenous

Figure 3.7: (a) We define the CAR T-cell success threshold as the minimum number of CAR T-cells needed to contain the low-tumor burden without chemotherapy. (b) Here sensitivity analysis shows that the CAR T success threshold is most sensitive to the tumor-cell lysis rate exponent (l) for Patient 1. The other model parameters tested are the tumor growth rate (a), the inverse of the tumor cell carrying capacity (b), the maximum tumor cell kill rate by endogenous effector cells (E cells) (d_E), the maximum tumor cell kill rate by CAR T-cells (d_C), the E cell growth rate (g), the maximum recruitment rate of E cells (j_E), the maximum recruitment rate of CAR T-cells, the half-saturation value of E cell proliferation, (k_E), the half-saturation of CAR T-cell proliferation (k_C), the E cell death rate (m_E), the CAR T-cell death rate (m_C), the E cell inactivation rate by tumor cells (q_E), the CAR T-cell inactivation rate by tumor cells (q_C), the half-saturation value of the tumor cell lysis rate (s), and the joint carrying capacity of E and CAR T-cells (K). Similar figures for the other patient parameter sets are included in Appendix C

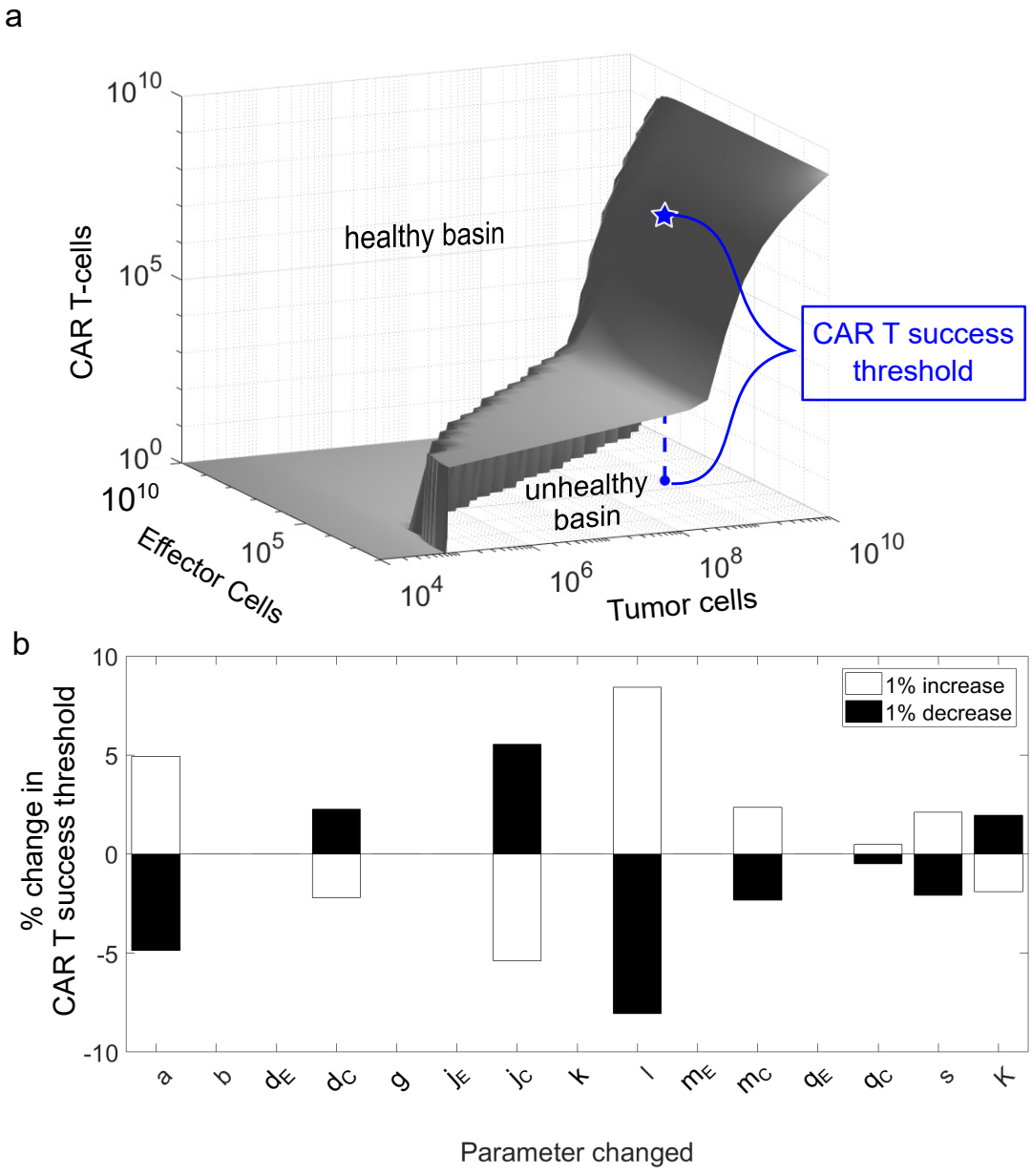
a
CAR T-cells
10^{10}
10^{5}
10^{0}
healthy basin
unhealthy basin
CAR T success threshold
10^{10}
10^{5}
Effector Cells
10^{4}
10^{6}
10^{8}
10^{10}
Tumor cells
b
% change in CAR T success threshold
10
5
0
-5
-10
1% increase
1% decrease
a
b
d_E
d_C
g
j_E
j_C
k
l
m_E
m_C
q_E
q_C
s
K
Parameter changed

effector cell counts where the boundary to reach the healthy basin of attraction is lower, and so safe levels of CAR T-cell therapy are effective (Fig. 7a). We have shown that CAR T-cell doses currently used in clinical practice are sufficient to move patient conditions to the healthy basin of attraction after preconditioning chemotherapy, resulting in a successful treatment outcome, in a significant proportion of patient scenarios. One model parameter closely associated with the height of the boundary between healthy and unhealthy patient outcomes is the exponent of the tumor-cell lysis rate, l, which relates to how effectively CAR T-cells kill tumor cells. This observation suggests that small changes in the effectiveness of CAR T-cells can have a large impact on the dosage required for successful adoptive cellular therapy.

Second, appropriate chemotherapeutic lymphodepletion can reduce the CAR T-cell dosage necessary for successful treatment. Lymphodepletion lowers the necessary dose of CAR T-cells through two modes: reducing the tumor burden, and reducing the endogenous effector cell population, thereby allowing the injected cells to expand. This was observed in treatment scenarios for all four patients considered. Lower tumor burden at the time of injection and lower CAR T-cell doses are associated with milder side effects, which implies that selecting the appropriate lymphodepletion plan can make CAR T-cell therapy safer.

Finally, the recovery period between the end of preconditioning chemotherapy and the administration of a CAR T-cell injection matters. If the recovery period is too long, the benefits of lymphodepletion may be lost. This finding in particular warrants further investigation as under current practice the rest period can vary from as low as 2 up to as high as 14 days. Notably, for the two patient parameter sets with large tumor growth rates, Patients 3 and 4, the maximum successful rest window was less than 5 days. According to our sensitivity analysis, the tumor growth rate, a, was also an influential factor determining the minimum CAR T-cell dose necessary for successful treatment. Ideally, model parameters could be tuned to match a patient's tumor growth rate in order to suggest how strictly the rest period should be limited.

The model proposed and explored here has several limitations. First, the choice of an ODE model assumes that tumor and immune cell populations are well mixed. This does not hold for CAR T-cell treatment of solid tumors. However, starting with a non-spatial

model allows us to mine relevant parameters from the literature, is simple enough to allow analysis, and can still provide useful insight.

Additionally, there are elements of cancer biology that are excluded from the model. Studies of CAR T-cell treatment have shown that a patient's homeostatic cytokine profile is a key determinant of successful chemotherapeutic preconditioning for CAR T-cell therapy [64, 129, 156]. Our model does not explicitly account for cytokines and other supporting immune molecules, but their influence shows up indirectly through competition between endogenous effector cells and CAR T-cells. A more detailed treatment of supporting immune molecules would be interesting, but for the sake of simplicity we exclude them here.

For our model, we also assume that all tumor cells are vulnerable to attack by the injected CAR T-cells. This may not necessarily be the case, for example, in the presence resistance to CAR T-cell therapy. The model could be extended to include a subpopulation of cancer cells that are not recognized by the CAR T-cells, perhaps because they do not display the target ligand. This would be an interesting and relevant problem to address. Different types of CAR T-cells could also be compared by modifying the parameters describing CAR T-cell activity if there is appropriate data from cytotoxicity assays available.

CAR T-cells have transformed treatment of hematological cancers and show enormous potential for further innovation and application. One challenge facing this technology is the ubiquity of severe side-effects. Standard treatment protocol includes a chemotherapeutic preconditioning regimen, yet the optimal combination of chemotherapy and CAR T-cells to minimize side-effects while maintaining efficacy has not been determined. Addressing the question of how these two forms of treatment interact for any given patient with a simple mathematical model takes an inexpensive first step towards informing further investigations.

3.2.4 Appendix A: Model Analysis

Here we present a linear stability analysis for our model post-treatment. Because the treatment plans we consider are generally confined to within 5-20 days total for both chemotherapy and CAR T-cell injection, the dose schedules, $\nu_M(t)$ and $\nu_C(t)$, are zero for t greater than 5-20 days. Furthermore, the chemotherapy plans used for lymphodepletion are on

Table 3.1: Parameter values from ranges for large B-cell lymphoma reported by [155] were selected for Patient 1. Parameter values from ranges for B cell Chronic Lymphocytic Leukemia reported by [127] were selected for Patient 2. The Patient 3 and 4 parameter values come from two metastatic melanoma patients, reported by [37]. CAR T-cell related parameters are adapted from [92]

Parameter	Description	Patient 1	Patient 2	Patient 3	Patient 4
a	tumor growth rate (day^{-1})	2.55e−1	1.76e−1	5.14e−1	5.14e−1
$1/b$	tumor carrying capacity (cells)	2e12	2e12	9.804e8	9.804e8
d_E	saturation level of tumor kill by effector cells (day^{-1})	2.03	2.03	5.8	4.23
d_C	saturation level of tumor kill by CAR T-cells (day^{-1})	2.25	2.25	2.25	2.25
g	base recruitment rate of effector cells (cells/day)	1.4e3	4.7e4	1.3e4	1.3e4
j_E	max recruitment rate of effector cells by tumor lysis (day^{-1})	1.1e−2	7.46e−3	2.7e−2	2.7e−2
j_C	max recruitment rate of CAR T-cells by tumor lysis (day^{-1})	2.42e−1	1.65e−1	6.0e−1	6.0e−1
K	effector cell carrying capacity (cells)	1.65e9	1.65e9	1.65e8	1.65e8
k	steepness of effector cell recruitment curve ($\text{cells}^2\text{day}^{-2}$)	2.019e5	7.0e7	2.0e7	2.0e7
l	exponent of tumor lysis by effector cells (unit-less)	1.395	1.419	1.36	1.43
m_E	effector cell death rate (day^{-1})	7e−3	3.4e−2	2e−2	2e−2
m_C	CAR T-cell death rate (day^{-1})	2.93e−2	2.93e−2	2.93e−2	2.93e−2
q_E	effector cell inactivation by tumor ($\text{cells}^{-1}\text{day}^{-1}$)	3.42e−11	6.716e−13	3.42e−10	3.42e−10
q_C	CAR T-cell inactivation by tumor ($\text{cells}^{-1}\text{day}^{-1}$)	3.0e−11	3.0e−11	1.53e−9	1.53e−9
s	steepness of fractional tumor cell kill by effector cells (unit-less)	3.05e−1	3.05e−1	2.5e−1	3.6e−1
K_T	fractional tumor cell kill by chemotherapy (day^{-1})				7.00e−1
K_E, K_C	fractional healthy cell kill by chemotherapy (day^{-1})				6.00e−1
γ	chemotherapy decay rate (day^{-1})				9.00e−1

the shorter end of this, spanning only 3-5 days. When $\nu_M(t) = 0$, the concentration of chemotherapy rapidly declines to zero and the only possible chemotherapy concentration at equilibrium is $M(t) = 0$. Thus, we can characterize the relevant equilibria for our model scenarios by analyzing Sys. (3.2a-c) with $\nu_M(t) = 0$ and $\nu_C(t) = 0$,

$$\frac{dT}{dt} = aT(1 - bT) - D_E - D_C, \tag{A.1a}$$

$$\frac{dE}{dt} = g - j_E \frac{D_E^2}{k + D_E^2} \ln\left(\frac{E + C}{K}\right) E - q_E ET - m_E E, \tag{A.1b}$$

$$\frac{dC}{dt} = -j_C \frac{D_C^2}{k + D_C^2} \ln\left(\frac{E + C}{K}\right) C - q_C CT - m_C C, \tag{A.1c}$$

where D_E and D_C are still the tumor cell lysis terms,

$$D_E = d_E \frac{(E/T)^l}{s + (E/T)^l} T \qquad \text{and} \qquad D_C = d_C \frac{(C/T)^l}{s + (C/T)^l} T. \tag{A.2}$$

To begin our analysis, we first non-dimensionalize Sys. (A.1) as follows. Let $x = bT$, $y = aE/g$, $z = aC/g$, $D_y = D_E/a$, $D_z = D_C/a$ and $t^* = at$. This results in twelve non-dimensional parameters,

$$d_y = d_E/a, \quad d_z = d_C/a, \quad j_y = j_E/a, \quad j_z = j_C/a, \quad k^* = b^2 k/a^2,$$

$$K^* = aK/g, \quad m_y = m_E/a, \quad m_z = m_C/a, \quad q_y = q_E/(ab), \quad q_z = q_C/(ab),$$

and $s^* = s(a/(gb))^l$. The parameter l is nondimensional in the original system, and so remains unchanged. Dropping stars for notational simplicity, the non-dimensionalized system without chemotherapy or additional CAR T-cell doses is given by

$$\frac{dx}{dt} = x(1 - x) - D_y - D_z, \tag{A.3a}$$

$$\frac{dy}{dt} = 1 - y\left(j_y \frac{D_y^2}{k + D_y^2} \ln\left(\frac{y + z}{K}\right) + q_y x + m_y\right), \tag{A.3b}$$

$$\frac{dz}{dt} = -z\left(j_z \frac{D_z^2}{k + D_z^2} \ln\left(\frac{y + z}{K}\right) + q_z x + m_z\right), \tag{A.3c}$$

where D_x and D_y are now dimensionless ratio terms,

$$D_y = d_y \frac{(y/x)^l}{s + (y/x)^l} x \qquad \text{and} \qquad D_z = d_z \frac{(z/x)^l}{s + (z/x)^l} x. \tag{A.4}$$

Next, we find the equilibria of the system, which occur at the intersections of the tumor, effector, and CAR T-cell nullclines, where $\dot{x} = 0$, $\dot{y} = 0$, and $\dot{z} = 0$ respectively. From Eq. (A.3a) we see that the tumor cell nullclines are $x = 0$ and

$$x = 1 - d_y \frac{(y/x)^l}{s + (y/x)^l} - d_z \frac{(z/x)^l}{s + (z/x)^l}. \tag{A.5}$$

For the effector cell nullcline, we set the right hand side of Eq. (A.1b) equal to zero and find that $\dot{y} = 0$ when

$$y = \left(m_y + q_y x + j_y \frac{D_y^2}{k + D_y^2} \ln\left(\frac{y+z}{K}\right) \right)^{-1}. \tag{A.6}$$

From Eq. (A.3c), we can see that CAR T-cell population change will be zero when $z = 0$, or when the following implicit equation is satisfied

$$0 = m_z + q_z x + j_z \frac{D_z^2}{k + D_z^2} \ln\left(\frac{y+z}{K}\right). \tag{A.7}$$

We will refer to the intersection between the tumor nullcline $x = 0$, the effector cell nullcline, Eq. (A.6), and the CAR T-cell nullcline $z = 0$ as the zero-tumor or tumor-free equilibrium. We refer to equilibria that occur at the intersection between the tumor nullcline Eq. (A.5), the effector cell nullcline, Eq. (A.6), and the CAR T-cell nullcline $z = 0$ as nonzero-tumor boundary equilibria. Equilibria that occur at the intersection between the tumor nullcline Eq. (A.5), the effector cell nullcline, Eq. (A.6), and CAR T-cell nullcline Eq. (A.7) will be referred to as interior equilibria.

In order to determine the stability of the steady states, we apply linear stability analysis. The linearized system at point (x, y, z) is summarized by the Jacobian, H, of Sys. (A.3) evaluated at (x, y, z). Let

$$J_y = -j_y \frac{D_y^2}{k + D_y^2} \ln\left(\frac{y+z}{K}\right) y \quad \text{and} \quad J_z = -j_z \frac{D_z^2}{k + D_z^2} \ln\left(\frac{y+z}{K}\right) z \tag{A.8}$$

Then the Jacobian of Eq. (A.3) evaluated at that point (x, y, z) is,

$$H|_{(x,y,z)} = \begin{pmatrix} 1 - \left(2x + \frac{\partial D_y}{\partial x} + \frac{\partial D_z}{\partial x}\right) & -\frac{\partial D_y}{\partial y} & -\frac{\partial D_z}{\partial z} \\ \\ \frac{\partial J_y}{\partial x} - q_y y & \frac{\partial J_y}{\partial y} - q_y x - m_y & \frac{\partial J_y}{\partial z} \\ \\ \frac{\partial J_z}{\partial x} - q_z z & \frac{\partial J_z}{\partial y} & \frac{\partial J_z}{\partial z} - q_z x - m_z \end{pmatrix}. \tag{A.9}$$

Let

$$H|_{(x,y,z)} = \begin{pmatrix} h_{11} & h_{12} & h_{13} \\ h_{21} & h_{22} & h_{23} \\ h_{31} & h_{32} & h_{33} \end{pmatrix},$$

so that substituting the partial derivatives into Eq. (A.9) gives

$$h_{11} = 1 - \left(2x + \frac{D_y}{x}\left(1 - \frac{ls}{s + (y/x)^l}\right) + \frac{D_z}{x}\left(1 - \frac{ls}{s + (z/x)^l}\right)\right), \tag{A.10a}$$

$$h_{12} = -D_y\left(\frac{ls}{s + (y/x)^l}\right), \tag{A.10b}$$

$$h_{13} = -D_z\left(\frac{ls}{s + (z/x)^l}\right) \tag{A.10c}$$

$$h_{21} = \frac{1}{x}\left(\frac{2kJ_y}{k + D_y^2}\left(\frac{ls}{s + (y/x)^l} - 1\right) - q_y xy\right), \tag{A.10d}$$

$$h_{22} = \frac{J_y}{y}\left(1 + \frac{2k}{k + D_y^2}\frac{ls}{s + (y/x)^l}\right) - m_y - q_y x - \frac{y}{K(y+z)}\frac{j_y D_y^2}{k + D_y^2} \tag{A.10e}$$

$$h_{23} = \frac{-j_y y}{y + z}\frac{D_y^2}{k + D_y^2} \tag{A.10f}$$

$$h_{31} = \frac{1}{x}\left(\frac{2kJ_z}{k + D_z^2}\left(\frac{ls}{s + (z/x)^l} - 1\right) - q_z xz\right) \tag{A.10g}$$

$$h_{32} = \frac{-j_z z}{y + z}\frac{D_z^2}{k + D_z^2} \tag{A.10h}$$

$$h_{33} = \frac{J_z}{z}\left(1 + \frac{2k}{k + D_z^2}\frac{ls}{s + (z/x)^l}\right) - m_z - q_z x - \frac{z}{K(y+z)}\frac{j_z D_z^2}{k + D_z^2} \tag{A.10i}$$

The simplest steady-state to characterize is the tumor-free equilibrium. Evaluating the effector cell nullcline at $x = 0$ and $z = 0$ yields $y = 1/m$. Hence, the tumor-free equilibrium occurs at $(x_0^*, y_0^*, z_0^*) = (0, 1/m, 0)$. Linearizing about this point, the Jacobian is

$$H|_{\left(0,\frac{1}{m},0\right)} = \begin{pmatrix} 1 - d_y - d_z & 0 & 0 \\ \frac{-q}{m_y} & -m_y & 0 \\ 0 & 0 & -m_z \end{pmatrix}, \tag{A.11}$$

which has eigenvalues $\lambda_1 = 1 - d_z - d_y$, $\lambda_2 = -m_y$, and $\lambda_3 = -m_z$. The parameter values d_y, d_z, m_y, and m_z will always be positive real numbers. It follows that λ_1, λ_2 and λ_3 are always real and negative when $d_y + d_z > 1$. For the biologically relevant cases we considered, the parameters $d_y > 1$ and $d_z > 1$, so this condition is satisfied. Hence the equilibrium point will be a stable node, which aligns with the results reported by de Pillis et al. for their 2006 model. The stability of the tumor-free equilibrium reflects the idea that, once activated, the immune system can contain a tumor if it is small enough.

Now we turn our attention to the nonzero-tumor boundary equilibria. For these equilibria, $z = 0$ still, but now

$$x = 1 - D_y - D_z = 1 - d_y \frac{(y/x)^l}{s + (y/x)^l}. \tag{A.12}$$

In this case we can solve Eq. A.12 for y as a function of x along the tumor nullcline,

$$L_1(x) = \left(\frac{s(1-x)x^l}{d_y - (1-x)} \right)^{1/l}. \tag{A.13}$$

Substituting Eq.(A.12) and $z = 0$ into the effector cell nullcline yields an implicit curve in the plane $z = 0$,

$$L_2(x, y): \quad y = \left(m_y + q_y x + j_y \frac{(1-x)^2 x^2}{k + (1-x)^2 x^2} \ln\left(\frac{y}{K}\right) \right)^{-1}. \tag{A.14}$$

The nonzero-tumor boundary equilibrium points are the intersections of Eq. (A.13) and Eq. (A.14) for each set of parameters. See Fig. 3.1a for a plot of $L_1(x)$ (tumor cell nullcline) and $L_2(x, y)$ (effector cell nullcline) for the Patient 3 parameters with equilibria marked. For reasonable parameter ranges, reported in Table 1, we observed that the model has two positive nonzero-tumor equilibrium points in the plane $z = 0$ because the parameter s is large enough that $L_1(x)$ exceeds $L_2(x, y)$ for most of the interval $x \in (0, 1)$, but $L_1(0) = 0 < L_2(0, 1/m)$ and $L_1(1) = 0 < L_2(1, y^*)$.

The first nonzero-tumor boundary equilibrium occurs at a large number of tumor cells, $x_1^* \approx 1$, a small number of effector cells, $y_1^* \approx L_1(1) = 1/(q + m)$, and $z_1^* = 0$. Due to the location near the tumor cell carrying capacity, we call this the high-tumor equilibrium. The second non-zero tumor boundary equilibrium occurs at a small number of tumor cells, a

moderate number of effector cells and $z = 0$. Although it is not possible to find exact, closed-form expressions for the nonzero-tumor boundary equilibria because it requires finding the roots of a quintic polynomial, we can use the Routh-Hurwitz criterion to find conditions under which the high-tumor equilibrium is stable [187, p. 14]. Let $\tau(M)$ denote the trace of a matrix M and $\Delta(M)$ denote the determinant of a matrix M. For a 3 dimensional system, the Routh Hurwitz criterion says that all eigenvalues of matrix H will have negative real part if the following criteria are satisfied,

1. $\tau(H) < 0$,

2. $\Delta(H) < 0$,

3. $\tau(H^2) - \tau(H)^2 < 2\Delta(H)/\tau(H)$.

First, we use the nullclines to simplify the Jacobian. Substituting $z = 0$ and $D_y = (1 - x)x$ from Eq. (A.12) into Sys. (A.11), the Jacobian has entries

$$h_{11} = -x + \frac{ls(1-x)}{s + (y/x)^l}, \tag{A.15a}$$

$$h_{12} = -x\left(\frac{ls(1-x)}{s + (y/x)^l}\right), \tag{A.15b}$$

$$h_{13} = 0 \tag{A.15c}$$

$$h_{21} = \frac{1}{x}\left(\frac{2kJ_y}{k + (1-x)^2x^2}\left(\frac{ls}{s + (y/x)^l} - 1\right) - q_y xy\right), \tag{A.15d}$$

$$\begin{aligned} h_{22} = {} & \frac{J_y}{y}\left[\left(\frac{2k}{k + (1-x)^2x^2}\right)\left(\frac{ls}{s + (y/x)^l}\right) + 1\right] \\ & - q_y x - m_y - \frac{j_y}{K}\left(\frac{(1-x)^2x^2}{k + (1-x)^2x^2}\right) \end{aligned} \tag{A.15e}$$

$$h_{23} = -j_y\frac{(1-x)^2x^2}{k + (1-x)^2x^2} \tag{A.15f}$$

$$h_{31} = 0 \tag{A.15g}$$

$$h_{32} = 0 \tag{A.15h}$$

$$h_{33} = -m_z - q_z x \tag{A.15i}$$

Before applying the Routh Hurwitz Criterion, we will need to compute $\tau(H)$, $\Delta(H)$, and $\tau(H^2)$. The trace of the Jacobian is

$$\tau(H) = h_{11} + h_{22} + h_{33}. \tag{A.16}$$

This will be negative, satisfying criterion 1, when the three diagonal entries are negative. Next consider the determinant of the Jacobian

$$\Delta(H) = h_{11}h_{22}h_{33} - h_{12}h_{21}h_{33}, \tag{A.17}$$

due to zero entries in the Jacobian. Furthermore, with $x \approx 1$, h_{12} will be very nearly 0 and so we can consider

$$\Delta(H) = h_{11}h_{22}h_{33}. \tag{A.18}$$

Hence the determinant will also be negative, satisfying criterion 2, when the three diagonal entries share the same sign. Squaring H and summing the diagonal entries yields

$$\tau(H^2) = h_{11}^2 + h_{22}^2 + h_{33}^2 + 2h_{12}h_{21} \tag{A.19}$$

$$= h_{11}^2 + h_{22}^2 + h_{33}^2, \tag{A.20}$$

again because h_{12} goes to zero for $x \approx 1$. We know that $\Delta(H)/\tau(H) > 0$ when both are negative, so showing $\tau(H^2) < \tau(H)^2$ will be sufficient to satisfy the 3rd criterion if the first two are met. Squaring $\tau(H)$ yields

$$\tau(H)^2 = h_{11}^2 + h_{22}^2 + h_{33}^2 + 2h_{11}h_{22} + 2h_{22}h_{33} + 2h_{11}h_{33}. \tag{A.21}$$

All the terms in the sum will be positive when $h_{11} < 0$, $h_{22} < 0$, and $h_{33} < 0$ in which case it is clear that $\tau(H^2) < \tau(H)^2$. Thus, all three of the Routh-Hurwitz criterion will hold when the three diagonal entries of H are negative.

We start with the first diagonal entry. From Eq. (A.15a), we can see that when $x \approx 1$ it follows that that $h_{11} \approx -1$.

Next we consider the second diagonal entry, h_{22}, defined in Eq. (A.15e). Substituting in $J_y/y = 1/y - m_y - q_y x$ yields,

$$\begin{aligned} h_{22} = \frac{1}{y}&\left[\left(\frac{2k}{k+(1-x)^2x^2}\right)\left(\frac{ls}{s+(y/x)^l}\right)+1\right] \\ &- (q_y x + m_y)\left[\left(\frac{2k}{k+(1-x)^2x^2}\right)\left(\frac{ls}{s+(y/x)^l}\right)+2\right] \\ &- \frac{j_y}{K}\left(\frac{(1-x)^2x^2}{k+(1-x)^2x^2}\right) \end{aligned} \tag{A.22}$$

Then noting that the final term will be negative, but close to zero and he first fractional term will approach 2 when $x \approx 1$, h_{22} will be less than 0 when

$$\frac{1}{y} < (q_y + m_y)\frac{2\left(\frac{ls}{s+(y/x)^l}\right)+2}{2\left(\frac{ls}{s+(y/x)^l}\right)+1}. \tag{A.23}$$

Hence when $x \approx 1$, the entry h_{22} will be negative when

$$y > \frac{1}{q_y + m_y}. \tag{A.24}$$

Finally, from Eq. (A.15i), we can see that for any positive value of x, including $x \approx 1$, $h_{33} < 0$ because both parameter values, m_z and q_z, are real and positive.

Thus when $z = 0$, $x \approx 1$, and $y > 1/(q_y + m_y)$, the diagonal entries of H, h_{11}, h_{22} and h_{33}, will all be negative. Hence the Routh-Hurwitz Criterion will be satisfied and all eigenvalues of the system will have negative real parts. These conditions are satisfied by the high-tumor equilibrium for the patient parameters considered here, so it follows by the Routh-Hurwitz criterion that the high-tumor steady state is stable.

Characterizing the interior equilibria analytically is intractable. However, we located equilibria at the intersection of nullsurfaces, and characterized their stability numerically. For the parameter sets considered here, there are up to four interior equilibria with $x \geq 0$, $y \geq 0$, and $z \geq 0$. To explore these equilibria, we constructed a bifurcation diagram by varying the maximum CAR T-cell recruitment rate, j_C, from 0 to 3 while holding all other parameters at their Patient 3 value (Fig. 1c). With strictly positive parameter values, an unstable node and a saddle point are present at a low (but non-zero) population level for all three cell types. The stable manifold of this saddle point separates the basin of attraction for healthy outcomes from the basin of attraction for unhealthy outcomes. Increasing j_C causes this saddle point to move towards larger tumor and CAR T-cell values as the non-zero CAR T-cell nullcline shifts upwards with respect to tumor and CAR T-cells. For the patient 3 values, a saddle node bifurcation occurs when $j_C = 0.5105$ and a stable node appears simultaneously with another saddle point near the tumor cell carrying capacity. The stable manifold of this saddle point separates the basins of attraction for the high-tumor equilibrium from the basin of attraction for this new, stable coexistence equilibrium. Fig. 1b shows the null surfaces with the unperturbed patient 3 parameter set, i.e. with $j_C = 0.6$, so all four interior equilibria are visible. Continuing to increase j_C past the point $j_C = 2.56$, the non-zero CAR T-cell nullcline shifts far enough upwards with respect to tumor and CAR T-cells that the stable coexistence equilibrium and the saddle node at high CAR T-cell values collide and disappear in another saddle-node bifurcation. This leaves two remaining unstable interior equilibria, and the stable manifold of the remaining saddle node now separates the basins of attraction for the low tumor and high-tumor equilibria. Varying other parameters associated with CAR T-cells can also shift the non-zero CAR

T-cell nullsurface through this sequence of bifurcations.

The positive quadrant is an invariant set of system A.1. In order for a trajectory to leave the first quadrant, it would have to cross an axis, which requires $\dot{x} < 0$ somewhere along the $x = 0$ axis, $\dot{y} < 0$ somewhere along the $y = 0$ axis or $\dot{z} < 0$ somewhere along the $z = 0$ axis. However, when $x = 0$ it is clear from Eq. (A.1a) that $\dot{x} = 0$. From Eq. (A.1b), we can also see that when $y = 0$, it follows that $\dot{y} = 1$, which is positive. And when $z = 0$, $\dot{z} = 0$ also.

3.2.5 Appendix B: Parameter Selection

We selected parameters based on previous models in the literature. The metastatic melanoma parameter sets came directly from the parameter values for Patients 9 and 10 in the governing equations for tumor cells and $CD8^+$ T-cells reported by [37]. However to counteract the effect of eliminating the other immune cell types (NK cells and circulating lymphocytes) that stimulate $CD8^+$T cells, the base recruitment rate of effector cells from [104] was taken to be the base recruitment rate of effector cells for Patients 3 and 4.

We set the parameter values for our diffuse large B-cell lymphoma patient, Patient 1, to the midpoint of the ranges reported by [155] when there was an analogous term. We could use most parameters directly from [155]. However, the parameters involved in the novel tumor-cell lysis term introduced by de Pillis et al. did not correspond directly to parameters in Rösch's model. We expect endogenous T-cells in lymphoma patients to be less effective at killing tumor cells than CAR T-cells, so we set $d_E = 2.02$, or roughly 90% as effective as CAR T-cells. We set the remaining two parameters, l and s, to the average of the two patients considered in the model from [37]. The Rosch et al. model assumed exponential tumor growth, rather than logistic so we set $b = 5 \times 10^{-13}$ because this choice allows tumor cells to exhibit essentially exponential growth towards the number of lymphocytes in the body in the absence of an immune response.

The chronic lymphocytic leukemia patient parameter values were set to the midpoint of the ranges reported by [127] when there was an analogous term, adjusting for differences in units. The Nanda et al. model also assumed exponential tumor growth, rather than logistic

so we set $b = 5 \times 10^{-13}$. Under the same reasoning as the lymphoma parameters, we set $d_E = 2.02$, and set the final parameters involved in the novel interaction term (l and s) to the average of the two patients considered in the model from [37].

CAR T-cell parameters that differ from corresponding parameter in the endogenous effector cells (d_C, m_C, j_C, and q_C) were determined from the values reported by Kimmel et al. (2019). For all patients, the CAR T-cell death rate and the maximum CAR T-cell kill rate were set to the median value for their deterministic model, converting units if necessary. Note that the maximum tumor kill rate is lower for CAR T-cells than for endogenous effector cells in the metastatic melanoma patients. This may seem counter-intuitive; however, the parameter values from de Pillis et al. (2005) were fit to clinical trials of successful Tumor Infiltrating Lymphocyte (TIL) treatment. TILs are currently more effective than CAR T-cells against metastatic melanoma [73]. The CAR T-cell exhaustion rate and the effector cell carrying capacity for blood cancers (Patients 1 and 2), came from converting the corresponding values in the model from Kimmel et. al (2019) to the our units. For the metastatic melanoma parameter sets (Patient 3 and 4), we use a higher inactivation rate so that the order of magnitude of the ratio of the tumor carrying capacity to deactivation is preserved. Numerous studies have shown the microenvironment around solid tumors to be more hostile to immune cells than in the case of hematologic cancers [181]. For metastatic melanoma patients we also was scaled down the carrying capacity of effector cells by 10% to account for the lower access of T-cells to solid tumor cells [181, 76]. In their model, Kimmel et al. (2019) use a functional form which places our maximum CAR T-cell recruitment rate, j_C, in the interval $[0.11, 1.31]$. We chose to set the CAR T-cell recruitment rate to be a factor larger than the endogenous cell recruitment rate: $j_C = 22 j_E$. The choice of 22 as a scale factor places the resulting values within the range reported by Kimmel et al. and produces simulation results spanning an interesting range of biological outcomes.

The kill parameters relating to chemotherapy were taken from [36], since the patients in the metastatic melanoma study were also treated with fludarabine. The fractional cell kills used by de Pillis et al. were $K_T = 0.9$ and $K_E = 0.6$ which assumes that chemotherapy is one log-kill and that it kills a larger fraction of tumor cells than host cells. However, to reflect the fact that CAR T-cell treatment is commonly used for patients whose disease

is less responsive to chemotherapy, we reduced K_T to 0.7. We set $K_C = K_E = 0.6$, therein assuming that CAR T-cells will be impacted by chemotherapy at the same rate as endogenous T-cells. The decay rate γ can be calculated from the half-life of a substance, τ, by $\gamma = \ln(2)/\tau$. The choice of strength for chemotherapy regimens was chosen by working backwards to see what values resulted in reasonable concentrations of fludarabine building up in the system, where "reasonable" concentrations matched those reported by Ju et al. [77] in a pharmacokinetic study of the drug (2014). For 25 mg of fludarabine administered over one half hour each day for 5 days, Ju et al. reported a peak concentration of $C_{max} = 1,222(668 - 1,732)\text{ng/mL} = 3.34\ \mu\text{M}$. We found that a dose strength of $S = 77\ \mu\text{Mday}^{-1}$ achieved this C_{max} in our simulations, so this was used as medium strength. The high strength was set to be $S = 125\ \mu\text{Mday}^{-1}$ in order to achieve the same area under the concentration curve with only 3 days of injections. If we chose to instead match the dose administered (area under $\nu_M(t)$) between the two plans, the patient outcomes were qualitatively similar.

Note that while the treatment parameters are well-founded in pharmacokinetic data, the patient parameters have been drawn from previous theoretical studies for different cancer types. Some have been fit to patient data, but not all. In order to strengthen the impact of any suggestions made by this model it remains to calibrate parameters model to data from previous CAR T cell therapy patients and validate the model by evaluating its predictive performance on untrained data.

3.2.6 Appendix C: Numerical Simulations and Sensitivity Analysis

We implemented numerical simulations with parameters for Patient 1-4 listed in Table 3.2.3 using a combination of 4th order Runge-Kutta integration schemes in MATLAB. During chemotherapy, we enforced a fixed step size of $\mathrm{d}t = 0.0208$ corresponding to approximately one half hour or 1/48 of a day using ode4(). The remainder of each simulation was completed with ode45(), which dynamically chooses the time-step.

To discover which components of the model contribute most significantly to the effectiveness of CAR T-cell injections, we performed a numerical sensitivity analysis assessing how

the model parameters impact the shape of the separatrix between the basin of attraction for the high-tumor equilibrium and the basin of attraction for the tumor-free equilibrium.

As a baseline for Patients 1-4, we calculated the precise threshold of CAR T-cells above which a patient initial condition will move towards the healthy, tumor-free equilibrium when the system starts at the low-TB initial condition. We call this number of effector cells the CAR T-cell success threshold, because any treatment plan which injects a dose of CAR T-cells exceeding this quantity will be successful (in theory) against tumor burdens up to and including the low TB, (Fig. (3.2.2a)). For the reasonable patient initial conditions considered in our simulations, post-chemotherapy tumor burdens generally fell below the low TB value at the time of CAR T-cell injection. After calculating the threshold with unperturbed parameters, each parameter was increased by 1% while holding all other parameter values constant. The relative change in the CAR T-cell success threshold was computed by subtracting the unperturbed CAR T-cell success threshold from the perturbed CAR T-cell success threshold and dividing the difference by the unperturbed threshold. The same procedure was followed for a 1% decrease in each parameter. The results of sensitivity analysis for Patient 1 are shown in Fig. (3.2.2b) and the results for Patients 2-4 are shown in Fig. (3.2.6).

For all patients, varying the tumor growth rate, a, had a significant impact on the CAR T-cell success threshold, indicating that cancers characterized by a higher growth rate will require higher CAR T-cell doses if administered at the same patient initial condition. In contrast with Patients 1-2, the tumor carrying capacity, $1/b$, also had a non-negligible effect on the success threshold for Patients 3-4. This seems to be a consequence of the fact that the low TB condition is only one order of magnitude below the tumor carrying capacity for Patient's 3 and 4, so the behavior of the tumor population can enter the saturating regime of logistic growth, shaped by the carrying capacity.

The parameters characterizing the activity of CAR T-cells also have a nonnegligible impact on the success threshold. For all patients, changing the exponent in the tumor-cell lysis rate, l, has the largest impact on the CAR T success threshold, with a 1% change in l leading to a $5-7\%$ change in the threshold. The parameter l encodes how the lysis rate depends on the ratio of CAR T-cells/tumor cells. Thinking of this ratio as a chemical

Figure 3.8: Results of sensitivity analysis for (a) Patient 2, (b) Patient 3, and (c) Patient 4. The dose of CAR T-cells required to achieve a healthy patient outcome from the low tumor initial condition is most sensitive to the tumor growth rate, a, and the exponent of the tumor cell lysis rate, l (a parameter associated with the cooperativity of CAR T-cells). Other parameters dictating the behavior of CAR T-cells also have a non-negligible impact on the CAR T-cell success threshold. The inverse of the tumor cell carrying capacity, b, has little effect on the threshold for Patients 1-2, but a noticeable effect for Patients 3-4. It is worth noting that the low tumor initial condition is relatively close to the tumor carrying capacity for Patients 3-4 compared to Patients 1-2

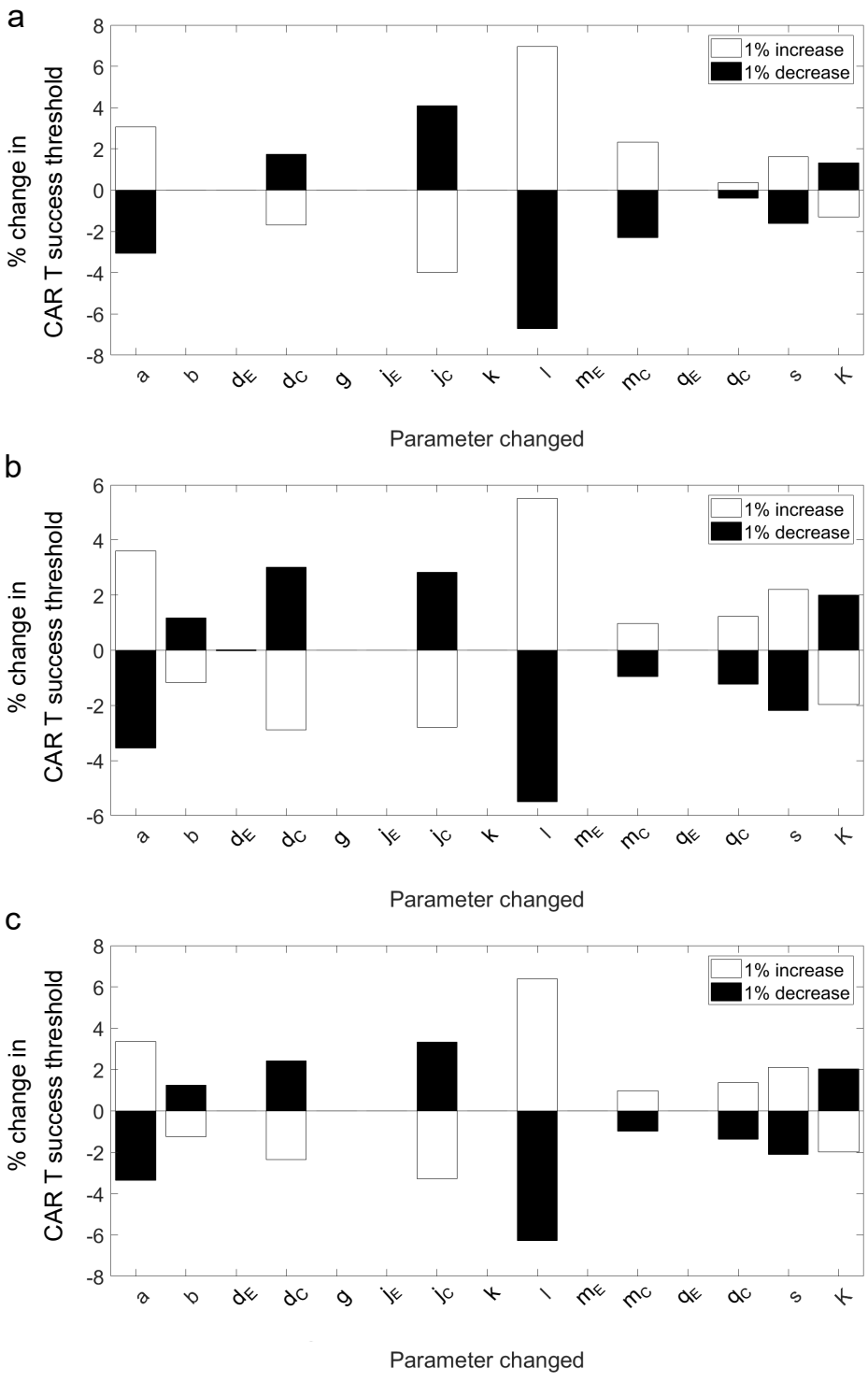
a
b
c
% change in CAR T success threshold
1% increase
1% decrease
Parameter changed
a
b
dE
dC
g
jE
jC
k
l
mE
mC
qE
qC
s
K

Figure 3.9: Impact of varying parameters characterizing the lysis of tumor cells by CAR T-cells on patient trajectories initiated at $(T_0 = 5 \times 10^8, E_0 = 3 \times 10^4, C_0 = 10^6)$ for Patient 1 and $(T_0 = 10^8, E_0 = 3 \times 10^4, C_0 = 10^6)$ for Patient 3. The maximum tumor cell lysis rate, d_C, was varied between 0 and 10 for (a) Patient 1 and (b) Patient 3. At low values of d_C, trajectories approach an unhealthy patient outcome. As d_C increases, CAR T-cells are able to mount a larger response against the tumor, and eventually trajectories transition to approaching the healthy outcome. Continuing to increase d_C, CAR T-cells eradicate the tumor more quickly and with a smaller peak. The exponent in the tumor cell lysis rate, l, was varied from 0 to 3 for (c) Patient 1 and (d) Patient 3. For low values of l, CAR T-cells effectively kill tumor cells independently so trajectories rapidly reach the zero-tumor burden with low spikes in CAR T-cells. As l increases, higher cooperation between CAR T-cells is required and so larger peaks in CAR T-cells are seen. Eventually, the level of cooperation required is too high, and trajectories now approach an unhealthy outcome, though CAR T-cells still increase initially. Once $l > 2$, the CAR T-cells no longer spike after injection, as trajectories quickly approach the high-tumor state. The half-saturation value in the tumor cell lysis rate, s, was varied from 0 to 1 for (e) Patient 1 and (f) Patient 3. Increasing s increases the effector-target ratio required to reach the saturation regime of tumor cell lysis. For low values of s the tumor is eradicated quickly with few CAR T-cells. As s increases, more CAR T-cells are required to eliminate the tumor observed in larger CAR T-cell peaks, until eventually this dose of CAR T-cells can no longer mount an effective response to this tumor burden. Further increasing s decreases the peak of the failed response

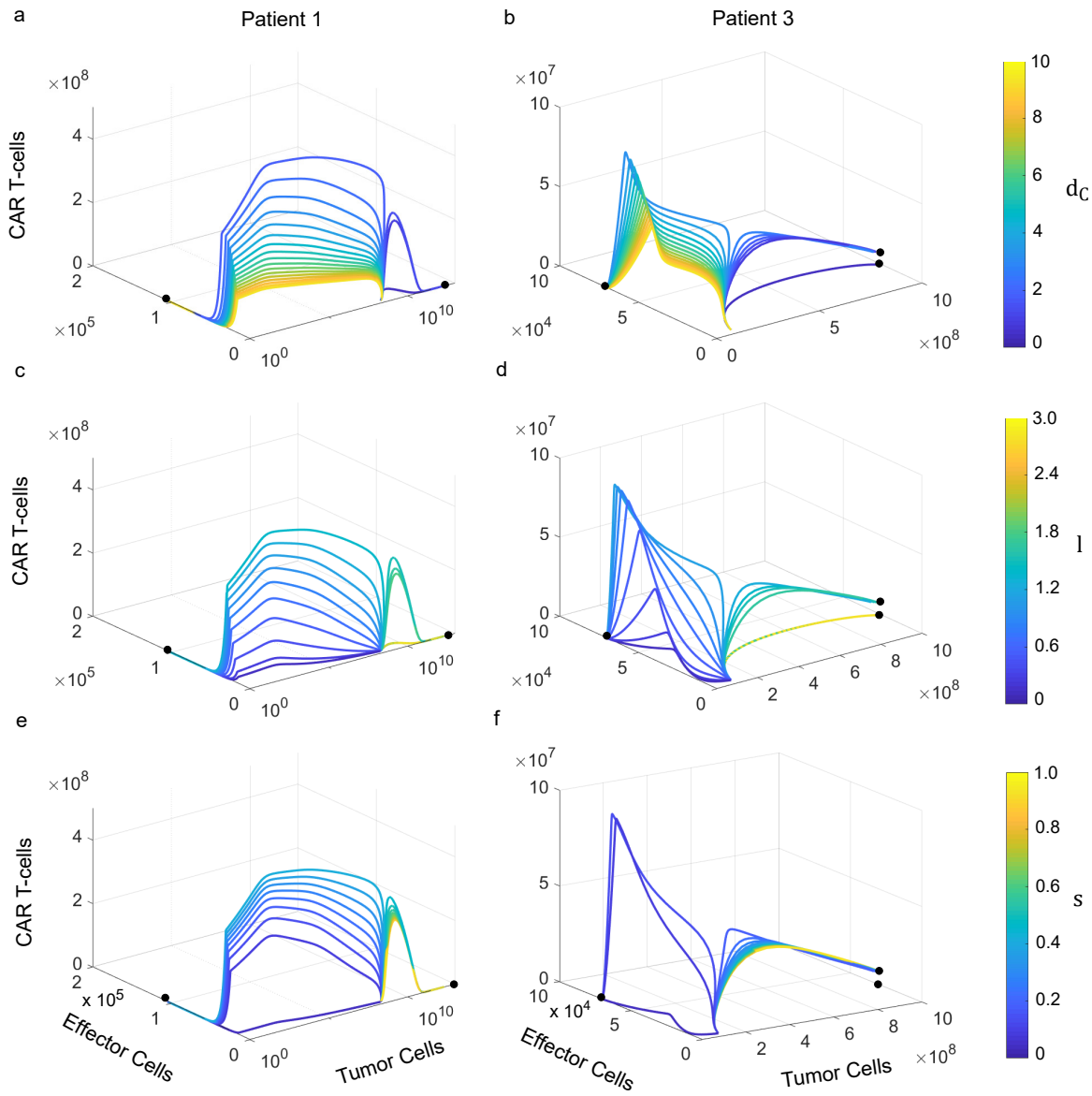
a
Patient 1
b
Patient 3
c
d
e
f
CAR T-cells
Effector Cells
Tumor Cells
x 10^5
x 10^4
d_C
l
s

concentration we can think of varying l as allowing the expression D to range between non-cooperative (completely independent) binding between CAR T-cells and surface antigens on the tumor cells when $l = 1$, and cooperative binding when $l > 1$. The fact that a 1% change in l can result in a 7% shift in the threshold indicates that small changes in CAR T-cell cooperativity will affect clinical outcomes. For Patients 1-2, and 4, the next most inlfuential parameter is the maximum recruitment rate of CAR T-cells, j_C. Larger values of j_C decrease the necessary injected dose of CAR T-cells because those cells that are injected are able to expand further. For Patient 3, perturbations to the maximum tumor kill rate by CAR T-cells, d_C, have the most outsized impact after l. This parameter defines the upper limit of the ratio-dependent cell-lysis term, suggesting that small improvements to the effectiveness of CAR T-cell activity could significantly reduce the dose required by patients.

Sensitivity analysis based on the the high tumor burden indicated that the parameters associated with tumor cell lysis by CAR T-cells, d_C, l, and s, play an important role in the success of CAR T-cell treatment so we performed further numerical investigations to show how varying these parameters impacts patient trajectories. Figure 9 shows patient trajectories resulting from running simulations with the Patient 1 and Patient 3 parameter sets from an initial condition near the separatrix between the basins of attraction for the different equilibria. Either d_C, l, or s was varied through a relevant range while holding all other parameter values constant at the value listed in Table 1 and the trajectories were color coded according to the value of the parameter in question.

First the maximum tumor cell lysis rate, d_C, was varied between 0 and 10. When tumor cell lysis is zero, the CAR T-cell recruitment is also affected, and CAR T-cells cannot proliferate so the trajectory proceeds in the $C = 0$ plane to the high-tumor equilibrium. As d_C increases a larger spike in CAR T-cells is seen. Though trajectories still reach the high-tumor equilibrium for Patient 1, they now approach the unhealthy coexistence equilibrium for Patient 3. Eventually the maximum kill rate is high enough that a large spike in CAR T-cells is sufficient to move the patient to the healthy zero-tumor outcome. Continuing to increase d_C the system approaches the healthy zero-tumor equilibrium faster and with a shorter and shorter spike in CAR T-cells.

Next, the exponent in the tumor cell lysis rate,l, was varied from 0 to 3. When $l = 0$, with even one CAR T-cell present tumor cells are killed at a rate independent of further increases in CAR T-cells. Consequently the tumor is eradicated very quickly with very little expansion of CAR T-cells beyond the initial dose. As l increases more cooperation is required between CAR T-cells to attack tumor cells, so we see larger and larger spikes in CAR T-cells needed to contain the tumor and reach a healthy outcome. Eventually the level of cooperativity required is too great for this CAR T-cell dose to handle this tumor burden. At this point, even though CAR T-cells expand post injection, trajectories approach an unhealthy outcome. Once l is greater than 2, the injection of CAR T-cells has virtually no effect on the disease, and CAR T-cells and tumor cells monotonically approach the high-tumor equilibrium.

The half-saturation value in the tumor cell lysis rate, s, was varied from 0 to 1. Increasing s increases the effector-target ratio required to reach the saturation regime of tumor cell lysis. When $s = 0$, the lysis of tumor cells by CAR T-cells transitions to the saturation regime immediately and so the tumor is eradicated rapidly by a small number of CAR T-cells. As s increases the CAR T-cell to tumor cell ratio needed to reach the saturation kill rate increases, and the eradication time and fold-increase in CAR T-cells increases along with it. At a critical value around $s = 0.5$ for Patient 1 and $s = 0.25$ for Patient 3, trajectories now approach an unhealthy outcome and the peak CAR T-cell population decreases as s increases. The effector to target ratio required to reach the saturation regime is now too high for this dose to handle this initial condition.

3.3 A Reaction-Diffusion Model for CAR T-cell Treatment of solid tumors

Due to the widespread success of CAR T-cell treatment combating blood cancers, interest has grown in expanding this technology to address other types of cancer. Current attempts at adapting CAR T-cells to address solid tumors must overcome several challenges including the inherent heterogeneity of solid tumors, their hostile tumor micro-environment, and the problem of CAR T-cell localization to the tumor site. One method currently being explored to address this last challenge is administering CAR T-cells locally instead of systemically.

Several methods of administering CAR T-cells for treatment of solid tumors are being

tested in clinical trials. In many cases, CAR T-cells are administered systemically, following the same method as the approved treatments for hematological malignancies. However, local delivery of CAR T-cells can allow the engineered cells to bypass physical barriers and reduce on-target/off-tumor effects. These methods of administration are especially applicable in order to bypass the blood-brain barrier when using CAR T-cell therapy to treat glioblastoma, as summarized by Maggs et al. in a 2021 review of the clinical trial landscape [110]. Notably, in one anecdote of successful treatment, a patient with highly aggressive recurrent glioblastoma went into complete tumor regression following infusion of CAR T cells into the resected tumor cavity and into the ventricular system [13]. Intracranial delivery of CAR T cells was also effective in a mouse model of HER2+ breast cancer with brain metastasis [151] and in a mouse model of glioblastoma [34]. Nellan et al., working with another mouse model of medulloblastoma, found that intratumoral injections required a lower dose of cells than systemic administration [130]. In addition to brain tumors, regional delivery of CAR T-cells is also being tested for the treatment of breast cancer, liver cancer, and human pleural malignancy ([171, 1], NCT04951141).

Comparing the effectiveness of possible modes of local injection of CAR T-cell therapy requires a model that accounts for spatial heterogeneity in the intial distribution of CAR T-cells. Towards this goal, we derive a spatio-temporal dynamical model for the proliferation, spread, and interaction of tumor cells and CAR T-cells. Specifically we use a pair of partial differential equations to describe the density of CAR T-cells and tumor cells over time, incorporating cell movement through diffusion and cell proliferation and death through forcing terms. These forcing terms are adapted from the ODE model presented in section 3.1 by dropping the equation for endogenous effector cells and modifying the recruitment rate of CAR T-cells upon interaction with tumor cells. This reaction-diffusion model allows us to study CAR T-cell treatment of solid and diffusive tumors.

3.3.1 Mathematical Model

Let the density of tumor cells and CAR T-cells at location x and time t be given by $u(x,t)$ and $v(x,t)$ respectively. According to conservation of mass, the rate of change in the density

of the tumor at a given point in space is the sum of diffusion and net cell proliferation, so we write the evolution equation for the tumor concentration as

$$\frac{\partial u}{\partial t} = \nabla \cdot (D_T(u)\nabla u) + F_1(\mathbf{x}, t), \tag{1}$$

where $F_1(\mathbf{x}, t)$ is a biologically motivated forcing function and $D_T(u)$ encodes thresholded-diffusion for tumor cell spread

$$D_T(u) = \begin{cases} 0 & u(\mathbf{x}, t) \leq u^*, \\ D_T^* & u(\mathbf{x}, t) > u^*. \end{cases} \tag{2}$$

We enforce an essentially free boundary as r increases, and a consistency condition at $r = 0$,

$$u(r = \infty) = 0, \quad |u(r = 0)| < \infty.$$

The evolution of the CAR T-cells is described by a purely diffusive process combined with an appropriate net cell proliferation term, yielding

$$\frac{\partial v}{\partial t} = \nabla \cdot (D_C \nabla u) + F_2(\mathbf{x}, t). \tag{3}$$

For the CAR T-cells, the boundary conditions are formulated in order to allow for a reasonably sized spatial domain in numerical simulation without impacting the biological interpretation of the model. Because we are most interested in the behavior of CAR T-cells near the tumor, we enforce

$$\left.\frac{\partial v}{\partial r}\right|_{r=3\max(\Omega)} = 0$$

where Ω consists of the radial values such that $u > 0$, i.e. the region of the spatial domain occupied by the tumor. This Neumann boundary condition at a moderate distance from the tumor is used to allow for proliferation at the edge of the tumor region without precipitous leakage. With local injection, most CAR T-cells remain near the tumor and for the parameter regimes considered here CAR T-cells reach the boundary $r = 3\max(\Omega)$ only in negligible concentrations, so using a Neumann boundary condition at this finite r rather than a boundary condition at infinity remains biologically reasonable. For model consistency, we again enforce that the cell concentration is finite at the origin, i.e.,

$$|v(r = 0)| < \infty.$$

For the forcing functions, F_1 and F_2, we use terms for the cell proliferation and interaction rates adapted from the ODE model studied by Owens and Bozic [139]. Let

$$F_1(\mathbf{x},t) = au(\mathbf{x},t)(1-bu(\mathbf{x},t)) - D(\mathbf{x},t) \tag{4a}$$

and

$$F_2(\mathbf{x},t) = j\ln\left(\frac{K}{v(\mathbf{x},t)}\right)\frac{D(\mathbf{x},t)}{k+D(\mathbf{x},t)}v(\mathbf{x},t) - mv(\mathbf{x},t) - qv(\mathbf{x},t)u(\mathbf{x},t), \tag{4b}$$

where

$$D(\mathbf{x},t) = d\frac{(u(\mathbf{x},t)/v(\mathbf{x},t))^l}{s+(u(\mathbf{x},t)/v(\mathbf{x},t))^l}u(\mathbf{x},t).$$

Note that the recruitment rate of CAR T-cells has been simplified slightly to depend on cell lysis directly rather than the square of cell lysis.

In this model, tumor cells diffuse in a density-dependent manner. Diffusion does not occur below a given critical tumor concentration, u^*, but above the critical concentration cells diffuse at a constant rate, D_T^*. This tacitly incorporates two stages of tumor growth at each spatial point: an initial phase in which the tumor grows non-diffusively, followed by a diffusive growth phase [168]. Models in the mathematical biology literature that assume Fickian diffusion for the density of tumor cells, notably the work of Swanson et al. [168] and Greenspan et al. [59] initiate simulations at the onset of the diffusive growth phase, bypassing the need for density dependent-diffusion. However, there are diverse cancer invasion routes and programs [51], so not all cancer progression is well-described by simple Fickian diffusion. With this model, we can compare high-grade, aggressively invasive tumors vs. low-grade, minimally invasive tumors by varying the growth rate of the tumor density, a, the diffusion coefficient of the tumor, D_T^*, and the diffusion threshold, u^*, making this a reasonable place to start.

Understanding the motility of CAR T-cells within a patient is still an area of active study [43]. Because we are assuming local delivery of the T-cells, they do not need to migrate to the tumor site. This allows us to reduce the complexity of our model by ignoring chemotaxis and haptotaxis. In a comprehensive imaging study of local injection of CAR T-cells, Mulazzani et al. found that CAR T-cells disperse evenly throughout the tumor over

the coarse of tumor eradication [121]. This supports the use of diffusion to describe CAR T-cell movement.

The forcing function for tumor tumor density in our model was drawn directly from the ODE model for CAR T-cell therapy from Owens and Bozic [139]. In the absence of CAR T-cells, the proliferation of tumor cells is driven by logistic growth. Previous reaction-diffusion models of tumor growth have considered exponential, gompertzian, and logistic growth [174]. For more details on the justification behind this nonlinear interaction term, see the modeling work of de Pillis et al. [37]. The proliferation terms governing CAR T-cells are adapted slightly from the Owens and Bozic model [139]. Modifications to the recruitment term were required because we do not include endogenous effector cells in this model, and we further simplified the relationship between CAR T-cell recruitment and tumor cell lysis. Removing the squared term results in a more binary local CAR T-cell response: either CAR T-cells expand in a given location, out-competing the tumor cells, or they are reduced to zero. We do not see long-term coexistence as was possible with the ODE model in the previous chapter. The dynamics of CAR T-cells within a patient are still not well characterized, but as more information emerges, this model can easily be adapted by changing the form of F_2 to accommodate different functional forms of CAR T proliferation and death.

In this work, we consider the evolution of a radially symmetric, spherical tumor growing on an infinite domain. This approach was also taken by Burgess et al. in their 3 dimensional extension of the work of Swanson et al. modelling glioma [18]. With the assumption of spherical symmetry, we can test two medically relevant methods of local CAR T-cell administration. First, we consider intratumoral injection of CAR T-cells by initiating treatment with a high concentration in the center of the tumor. Next, we consider intracavitary injection of CAR T-cells by initiating treatment with a uniform concentration of CAR T-cells along the boundary of the tumor. This simple geometry could also be used to consider treatment plans involving multiple doses, combinations of the above approaches, or the use of CAR T-cell therapy after tumor resection.

Applying the preceding geometric considerations to equations (1) and (3) while keeping

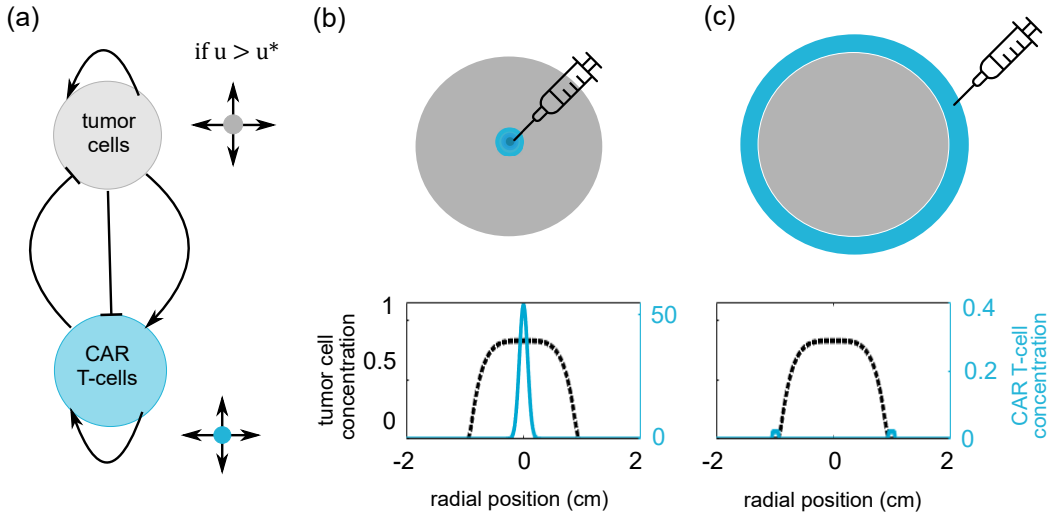

Figure 3.10: Overview of reaction-diffusion model for studying local administration of CAR T-cell therapy (a) Schematic of PDE model. Tumor density grows logistically and can be decreased by interaction with CAR T-cells. The tumor mass diffuses after surpassing a critical threshold, u^*. CAR T-cell proliferation is stimulated by the presence of tumor cells, but cells can also be deactivated through repeated interaction with the tumor. CAR T-cell density spreads through constant diffusion. (b-c) We consider two possible methods of CAR T-cell administration: intratumoral injection and intracavitary injection. Intratumoral injection is modeled with an initial high concentration of CAR T-cells in the center of the tumor. Intracavitary administration is modeled as a thin layer of CAR T-cells along the surface of the tumor.

the boundary conditions consistent, yields

$$\frac{\partial u}{\partial t} = \frac{1}{r^2}\frac{\partial}{\partial r}\left(D_T(u) r^2 \frac{\partial u}{\partial r}\right) + F_1(r,t); \qquad D_T = \begin{cases} 0 & u(r,t) \le u^*, \\ D_T^* & u(r,t) > u^*; \end{cases} \tag{5a}$$

and

$$\frac{\partial v}{\partial t} = \frac{1}{r^2}\frac{\partial}{\partial r}\left(D_C r^2 \frac{\partial v}{\partial r}\right) + F_2(r,t); \tag{5b}$$

A schematic of the model and illustrations of the initial CAR T-cell profile for the two

administration methods that we will compare is given in Fig. 3.10. Further, the nondimensional version of the model is derived in Appendix 3.3.5.

3.3.2 Parameter Estimation

In order to carry out informative numerical analysis and simulations of the model, we estimated some parameter values from experimental data and identified others from previous modeling work.

We first introduce the parameters that determine tumor growth in the absence of treatment. There are numerous reaction-diffusion models for tumor growth and estimates of the diffusion coefficient for tumor cells vary widely in the literature, reflecting the heterogeneous behavior of the different types of cancer being modeled. Swanson et al. [168] used diffusion coefficients on the order of $D_{T^*} = 10^{-4} - 10^{-3}\text{cm}^2/\text{day}$ to model glioma, a highly aggressive form of cancer. However they also noted that, *in vitro* and *in vivo* studies by Silbergeld and Chicoine reported velocities of $4.8 - 12.5\mu\text{m/hr}$ for rat glioma cells [18, 165]. Using the expected root-mean-square distance from the origin, one can relate this linear velocity to the diffusion coefficient via $\langle r^2 \rangle = 6D_{T^*}t$, where t is time. This yields diffusion coefficients an order of magnitude smaller, $D_{T^*} = 2.2 \times 10^{-5} - 1.5 \times 10^{-4}\text{cm}^2/\text{day}$. Other reaction-diffusion models of solid tumors have used even smaller diffusion coefficients, generally on the order of $D_{T^*} = 10^{-6}\text{cm}^2/\text{day}$ as in [104]. Here we consider diffusion coefficients in the range of 1×10^{-5} to 1×10^{-4} cm^2/day. Specifically, for tumors with low diffusivity, we let $D_{T^*} = 3 \times 10^{-5}$, whereas for high diffusivity, we let $D_{T^*} = 9 \times 10^{-5}$.

We set the tumor density carrying capacity to $1/b = 2.34 \times 10^8$. This reflects the physical constraints of how tightly cells can be packed together [38]. To consider solid, compact tumors we set the critical density for diffusion, u^*, to be half of this local density carrying capacity such that tumor cells will start to diffuse as their environment becomes crowded and slows the local rate of growth. Lower values of u^* decrease the tumor volume doubling time and cause the leading edge of the tumor to have a lower slope, i.e. the tumor is less compact at the boundary as it advances. Higher values of u^* have the opposite effect, and can result in staltatory growth patterns in which the tumor advances and then fills in

the new territory before advancing again. With this in mind, to model diffusive tumors, we set u^* to be 1% of the local density carrying capacity.

For a fixed diffusion coefficient and density carrying capacity, we can fit the growth rate of tumor density, a, to tumor volume doubling times for the cancer types of interest reported in table 3.2. The growth rates are on the order of 10^{-2} to 10^{-1}. Here we consider a high proliferation rate of $a = 0.25$ day^{-1} and a low proliferation rate of $a = 0.018$ day^{-1}. A thorough exploration of the model behavior in the absence of treatment is mapped out as a function of the tumor growth parameters in Fig. 3.17.

We now turn our attention to the parameters governing CAR T-cell dynamics. To determine the motility of CAR T-cells, we note that Mullazzani et al. reported CAR T-cell intratumoral velocities on the order of $2 - 20\mu$m/min. As with tumor cell diffusivity, we can use the expected root-mean-sqaure distance from the origin of a diffusing particle, $\langle r^2 \rangle = 6D_C t$, to compute the diffusion coefficient from these linear velocities. Taking the low end of the range reported in [121] yields a value of $D_C = 0.0138\text{cm}^2/\text{day}$. Finally, for the parameters determining CAR T-cell proliferation and interaction with tumor cells we use values from the range explored in the ODE model studied by Bozic et al. [139]:

$$
\begin{aligned}
&a = 0.018 \text{ or } 0.25\ day^{-1}, && b = \text{1.02e-9}\ cells^{-1},\\
&d = 2.25\ day^{-1}, && j = 0.6\ day^{-1},\\
&s = 0.25, && l = 1.36,\\
&k = \text{2.019e7}\ cells/day, && K = \text{1.65e8}\ cells,\\
&m = 0.293\ day^{-1}, && q = \text{5e-10}\ cells^{-1}day^{-1}.
\end{aligned}
$$

Before continuing with model simulations and numerical analysis, we nondimensionalized the system as outlined in section 3.3.5.

3.3.3 Results

We solved the non-dimensionalized model using a Crank-Nicolson scheme with a moving boundary as outlined in section 3.3.6. Simulations were run for a range of initial conditions with the parameter values identified in section 3.3.2. We first established the behavior

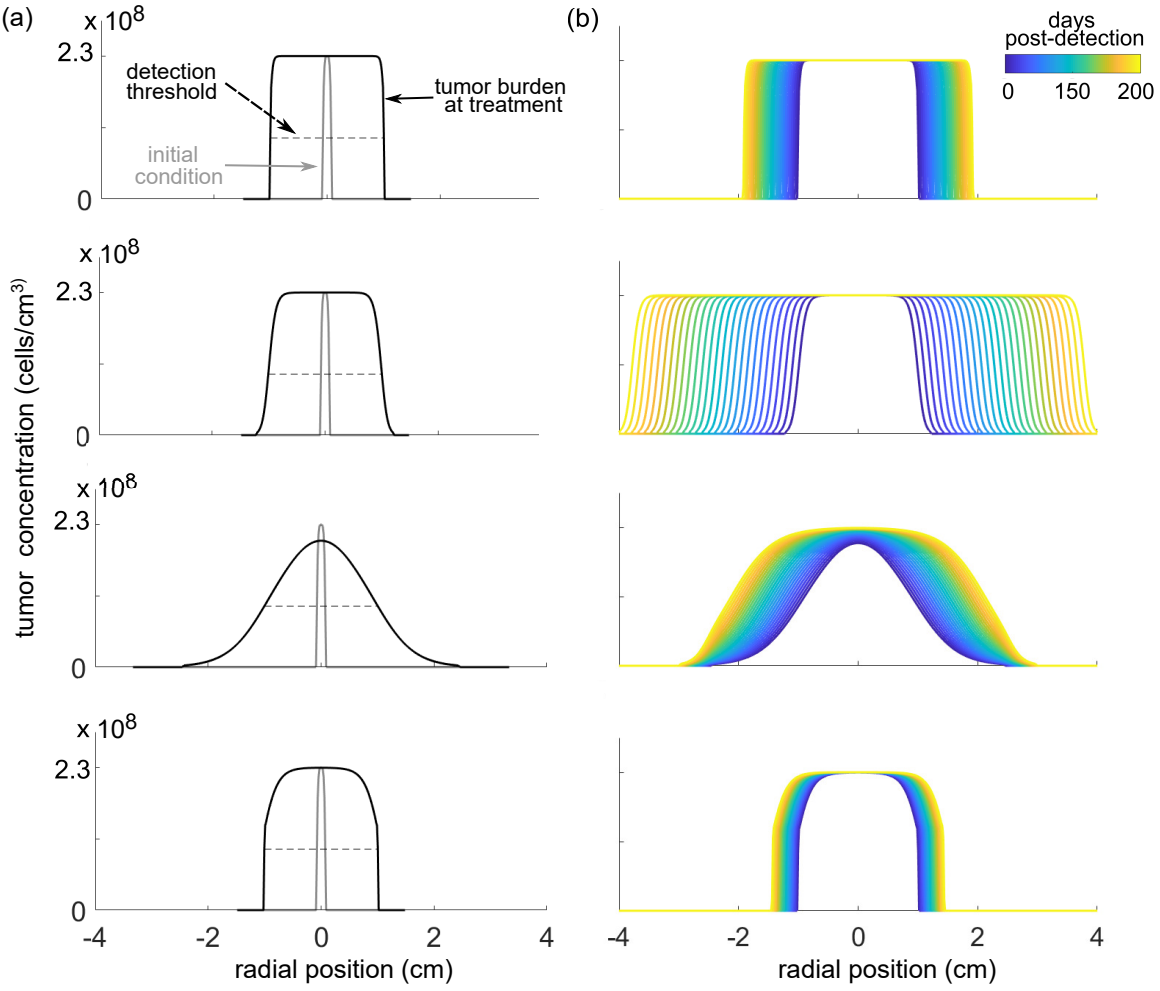

Figure 3.11: We model CAR T-cell treatment for 4 types of tumors: Type I has high proliferation and low diffusion, Type II has high proliferation and high diffusion, Type III has low proliferation and high diffusion, and Type IV both low proliferation and low diffusion. Panel (a) shows the density profile for each of these types of tumors when initiated from a 1 mm tumor and allowed to grow until the detectable radius reaches 1 cm. The black line shows the tumor burden at the time of CAR T-cell injection. If these four tumor types remain untreated, their expansion would continue. In panel (b) we illustrate the growth of the untreated tumors over 200 days.

Cancer type	Tumor Volume Doubling Time	Source
Malignant Glioma	15-21 days	Yamashita et al., 1983 [191]
Breast Cancer	46-825 days	Ryu et al., 2014 [161]
Liver Cancer	85-150 days	Nathani et al., 2021 [128]
NSCLC	100 - 191 days	Nakamura et al., 2014 [126]
Mesothelioma	153-241 days	[46, 85]

Table 3.2: Tumor volume doubling times for cancer types with ongoing clinical trials testing CAR T-cell therapy.

of the model for tumor growth alone, defining four tumor types on which to test locally administered CAR T-cell therapy. Each of these tumor types develops a signature density profile which constitutes the tumor burden at the time of CAR T-cell injection. The initial CAR T-cell distribution was either concentrated at the center of the tumor in a narrow compact gaussian, representing intratumoral injection, or concentrated along the boundary of the tumor in a narrow layer, representing intracavitary injection. We can visualize density profiles of the tumor and CAR T-cell populations along the radial dimension to get a sense of the spatial distribution of the two types of cells at different time points. We also integrate the cell densities over the spatial domain to construct a time series of the total cell populations. Examining these results for both modes of CAR T-cell administration, we can categorize the model behavior into one of 4 possible dynamic outcomes: rapid tumor eradication, tumor expansion followed by tumor eradication, initial tumor remission followed by relapse, or rapid tumor escape.

Tumor Growth

Our model provides a flexible framework to simulate a wide range of solid tumor behaviors. Tumor expansion varies along two main axes: the proliferation rate of cells controlled via the proliferation rate, a, and the diffusivity controlled via both the diffusion coefficient, D_T^*, and the diffusion threshold, u^*. A compact and aggressive solid tumor will maintain a

consistently high tumor density as it expands rapidly across the domain, where as a compact but slow-growing solid tumor will create a similar density profile expanding slowly across the domain. Diffusive tumors such as gliomas will have a high density core but extend outwards at low density near their periphery. Here we consider four types of tumors characterized by either high proliferation or low proliferation and either high diffusivity or low diffusivity. These serve as representatives models for different types of real tumors. Beyond these four examples, I explore the sensitivity of tumor growth to changes tumor parameters more thoroughly in section 3.3.7.

The four tumor types we consider are distinguished by their proliferation rate, a, tumor diffusion coefficient, D_{T^*}, and density threshold above which proliferating tumor cells will spread, u^*. We use a value of $a = 0.25\text{day}^{-1}$ for high proliferation compared with $a = 0.018\text{day}^{-1}$ for low proliferation. For high diffusivity, $u^* = 0.01b$ cells/cm^3, and $D_{T^*} = 9 \times 10^{-5}$ cm^2/day whereas for low diffusivity $u^* = 0.5b$ cells/cm^3, and $D_{T^*} = 3 \times 10^{-5}$ cm^2/day. Tumor type I has a high proliferation rate and lower diffusivity resulting in a tumor with a volume doubling time (VDT) of 76 days and an almost uniform, highly dense profile. This type of growth pattern represents aggressive but compact solid tumors, which could describe some liver or breast cancers. Tumor type II has a high proliferation rate and high diffusivity, which results in a tumor with a VDT of 33 days and a moderately compact cell density profile. This class is the most aggressive and could represent high-grade diffusive tumors such as some gliomas. Tumor type III has a low proliferation rate but a high diffusivity, resulting in the longest VDT, 228 days. This tumor type has a longer VDT even though the tumor grows substantially because the balance between diffusion and proliferation produces an invasive but low density growth front that is able to advance undetected. This type of diffuse growth is characteristic of a subset of gliomas. Finally, tumor type IV is the least aggressive with both low proliferation and a low diffusivity. More slowly growing compact tumors like mesothelioma or some breast cancers could fall into this category, which has a VDT of 196 days.

For each tumor type, we generated a tumor density profile to represent the tumor burden at the time of CAR T-cell treatment. We generated these tumor burden profiles by initiating a simulation with a spherical tumor of radius of 1 mm and uniform density at the carrying

capacity $1/b$ and then running it forward in time with the appropriate parameter set until the detectable tumor radius (density greater than 10^8 cells/cm^3) reached 1 cm. Note that modern diagnostic technologies are more sensitive than our chosen threshold. However, CAR T-cell preparation can take several weeks so using an artificially high detection threshold serves as a proxy for disease progression that would occur during treatment delay. The density profiles for the four tumor types are illustrated in Fig. 3.3.2a. For tumor types I-IV, the TBs at detection are 1.02×10^9, 1.01×10^9, 1.32×10^9, and 8.96×10^8 cells respectively.

From this "detectable" condition, we simulated progression of the tumor over the course of 200 days in the absence of treatment, highlighting the similarities and differences across the four tumor types Fig. 3.3.2b. Tumor type I expands from 1 cm in radius to nearly 2 cm in radius and remains uniformly dense across the full domain. Tumor type II expands much further, from radius 1 cm to nearly 4 cm. Like type I, the detectable radius of tumor type III also expands from about 1 cm to around 2 cm. However, the extend of non-zero tumor density is nearly 3 cm as a large portion of the tumor extends below the detection threshold. Finally, tumor type IV expands only from 1 cm to about 1.4 cm over the 200 days and has a noticeably lower density at the proliferation front that in the center. This is the least aggressive tumor in terms of radial expansion.

Intratumoral Injection

We simulate intratumoral CAR T-cell injection by starting with one of the four tumor burdens defined in the previous section and a high concentration of CAR T-cells in the center of the tumor. Specifically, we use a compact gaussian with a width of 1 mm and height determined by the dose level. The system then evolves according to the dynamics of equations (5a) and (5b), using the appropriate tumor growth parameters for the current tumor type. In all scenarios, the CAR T-cell population initially starts to migrate from the center of the tumor outwards, making some dent in the tumor density as it proceeds.

There are two possible paths to eradication. In the most robust CAR T-cell response, the tumor is eradicated quickly before expanding in volume. This behavior is observed

when the CAR T-cells reach the leading edge of the tumor and accumulate in high enough concentration to prevent the onset of diffusion (Fig. 3.3.3a). If the tumor has slightly more aggressive qualities (lower diffusion threshold, higher diffusivity, higher growth rate), a lower CAR T-cell dose allows the tumor to expand in radius before CAR T-cells eventually amass a high enough concentration at the edge of the tumor to prevent further diffusion (Fig. 3.3.3b). Once tumor advancement has been contained, the CAR T-cells eliminate the remaining tumor cells. In both of these scenarios the peak density of CAR T-cells moves from the center of the tumor radially outward towards the edge, maintaining a peak density at the front of interaction with the remaining tumor cells. Interestingly, in scenarios where the tumor is able to expand prior to eradication higher initial doses of CAR T-cells actually lead to earlier but lower peak numbers of CAR T-cells. Because the tumor is eradicated earlier, a lower total number of tumor cells must be eliminated, requiring a lower expansion of CAR T-cells in the process.

There are also several paths to treatment failure. With lower doses, CAR T-cells may proliferate transiently but the tumor escapes. CAR T-cells make a dent in the tumor density at the center of the domain, but are not able to fully distribute across the tumor before becoming exhausted and so the tumor persists and recovers. In the most extreme cases, observed with tumor type I, the tumor is reduced to as low as 1/10th of it's size at treatment before re-growing (Fig. 3.3.3c). The TB drops below what we have defined as the detectable threshold, hence, this may appear clinically like tumor remission followed by a fairly rapid relapse, a phenomenon which has been observed following CAR T-cell therapy. For example, 49% percent of relapses after CAR T-cell treatment in relapsed/refractory DLBCL occur within the first month [180]. With even lower doses, the injected CAR T-cells never proliferate, though they may persist and slow tumor advancement transiently (Fig. 3.3.3d). Failure of CAR T-cells to successfully engraft and proliferate is also a documented failure mode, particularly in the hostile solid tumor micro-environment [44].

Figure 3.12: Across the four tumor types, intratumoral injection of CAR T-cells can result in (a) tumor eradication, (b) tumor expansion followed by eradication, (c) initial tumor regression followed by relapse, or (d) transient CAR T-cell persistence despite tumor escape. In these four cases, the initial CAR T-cell dose diffuses outwards from the center of the tumor, killing tumor cells at the core first. In the more promising scenarios, the CAR T-cell population increases in density as it moves outwards towards the surface of the tumor. In the two successful scenarios, CAR T-cells reach the surface with high enough numbers to overcome the tumor cells and eliminate the disease.

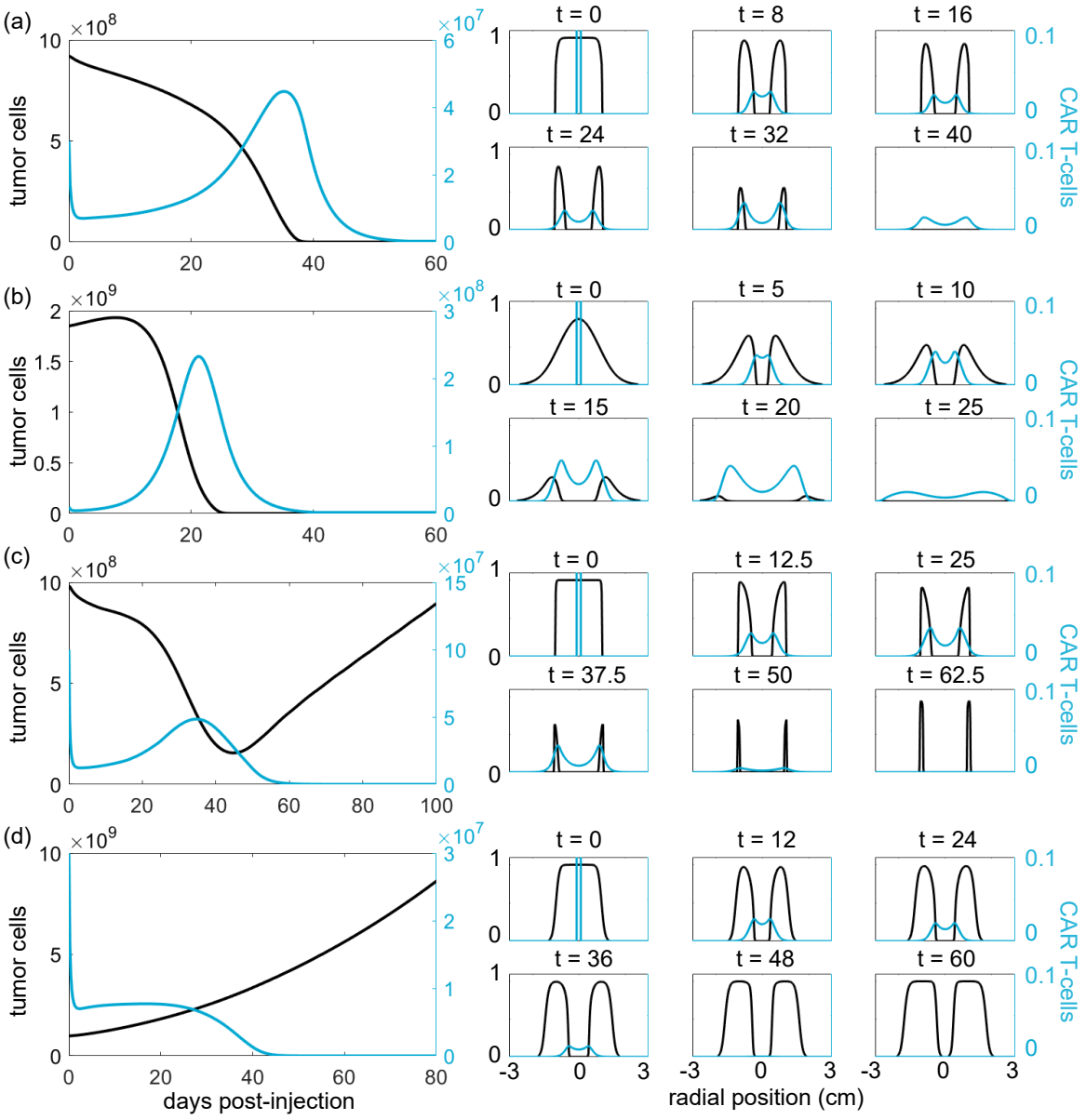
(a)
(b)
(c)
(d)
tumor cells
CAR T-cells
days post-injection
radial position (cm)
t = 0
t = 8
t = 16
t = 24
t = 32
t = 40
t = 5
t = 10
t = 15
t = 20
t = 25
t = 12.5
t = 37.5
t = 50
t = 62.5
t = 12
t = 36
t = 48
t = 60

Figure 3.13: Intracavitary injection of CAR T-cells can result in (a) tumor eradication, (b) tumor expansion followed by eradication, (c) tumor regression followed by relapse, or (d) transient CAR persistence and tumor escape. Upon intracavitary injection, the initial dose of CAR T-cells diffuses across the surface of the tumor. Then CAR T-cells start to proliferate as the wave continues inwards, preventing or hindering tumor expansion at the surface. In the three more effective scenarios, the advancing CAR T-cells coalesce in the center of the tumor, peaking in density while the tumor burden is greatly reduced. On the other hand, in many unsuccessful scenarios, CAR T-cells grow exhausted and inactivated, failing to penetrate the core of the tumor as in example (d). In the two successful scenarios, the CAR T-cells persist at high numbers until the tumor is completely eliminated. In scenario (c), the CAR T-cells begin contracting while a substantial shell of cells remains at the tumor surface. These tumor cells evade CAR T attack and the tumor regrows.

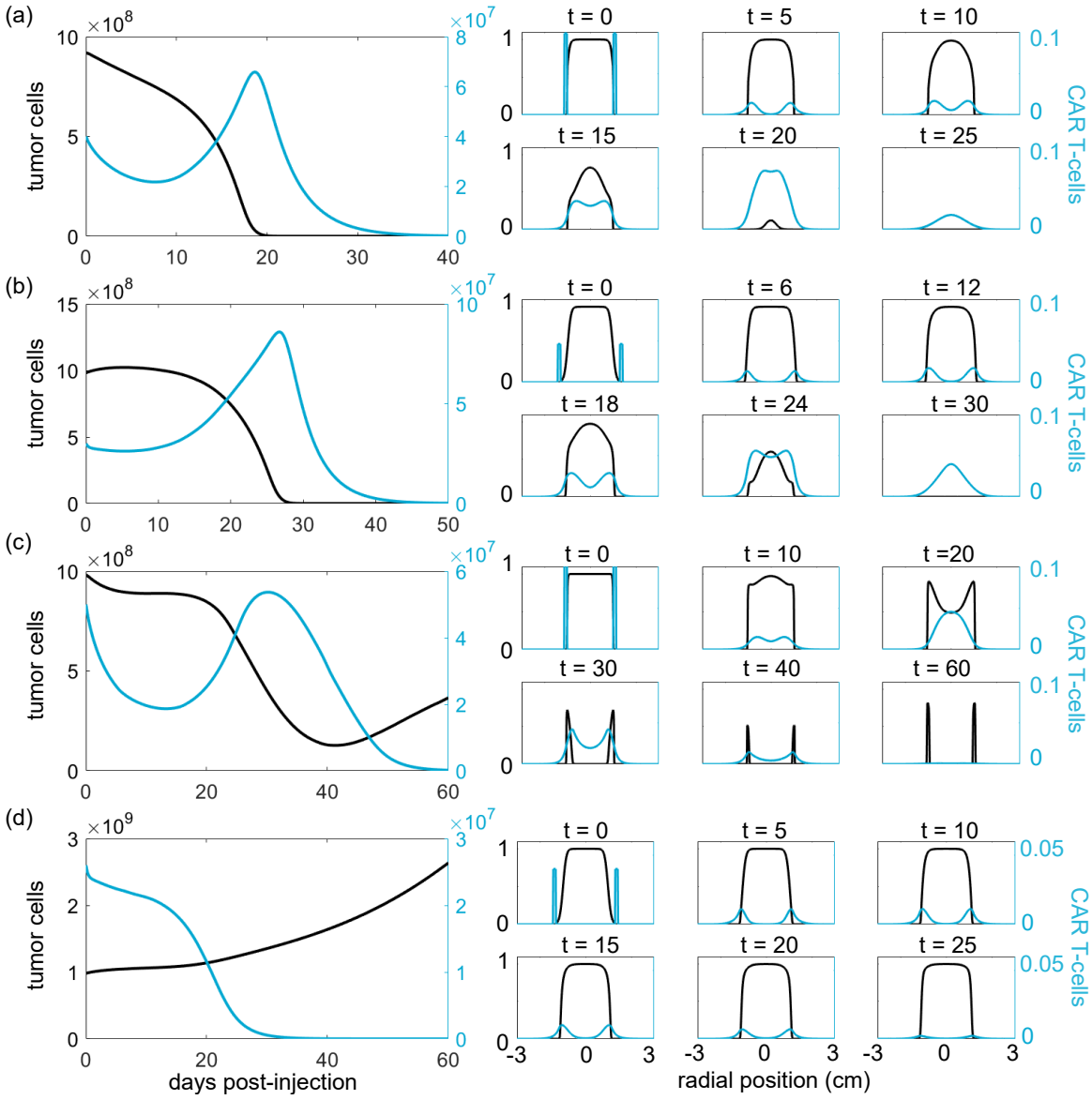
(a)
(b)
(c)
(d)
tumor cells
CAR T-cells
days post-injection
radial position (cm)
t = 0
t = 5
t = 10
t = 15
t = 20
t = 25
t = 6
t = 12
t = 18
t = 24
t = 30
t =20
t = 40
t = 60

Intracavitary Injection

To simulate intracavitary injection of CAR T-cells with this model, we again initiate the system with one of the tumor profiles in Fig. 3.3.2. Now, the initial condition for CAR T-cells is a thin layer concentrated on the surface of the tumor. In particular, the layer has a width of 1 mm and a uniform density at the value necessary to reach the dose level being tested. Over the course of simulation, the CAR T-cells migrate inwards across the tumor from the outer edge towards the center.

As with intratumoral injection, there are two types of successful treatment–one without tumor expansion and one with tumor expansion. If the initial dose is high enough to contain the leading edge of the tumor, CAR T-cells first distribute from areas of high concentration to low, diluting their local density of cells. Then as CAR T-cells advance deeper into the tumor and proliferate, they eradicate the tumor from the outside in, reaching a higher peak density than initially applied before contracting back down as the tumor dies off (Fig. 3.13a). Against tumor type II, when the tumor has a high tumor diffusivity and proliferation rate, the leading edge of the tumor is able to expand slightly as CAR T-cells build up a higher concentration at the tumor front(Fig. 3.13b). This phenomenon is less pronounced with intracavitary injection compared to intratumoral injection for the four tumor types considered here.

With intracavitary injection, we also observe treatment failure with and without CAR T-cell proliferation. For lower doses of CAR T-cells against tumor type I, we see the same phenomenon of initial tumor regression followed by relapse as observed with intratumoral injection (Fig. 3.13c). However across all tumor types, the most common mode of failure is that low doses of CAR T-cells only briefly or never proliferate, instead declining and allowing the tumor to grow uninhibited (Fig. 3.13d).

Comparing Modes of Local Administration

We tested CAR T-cell doses in the range of 1×10^6 to 5×10^8 cells against the four tumor types, administered either at the center of the tumor or at the surface. Given an appropriate parameter regime and initial condition, both modes of local CAR T-cell administration

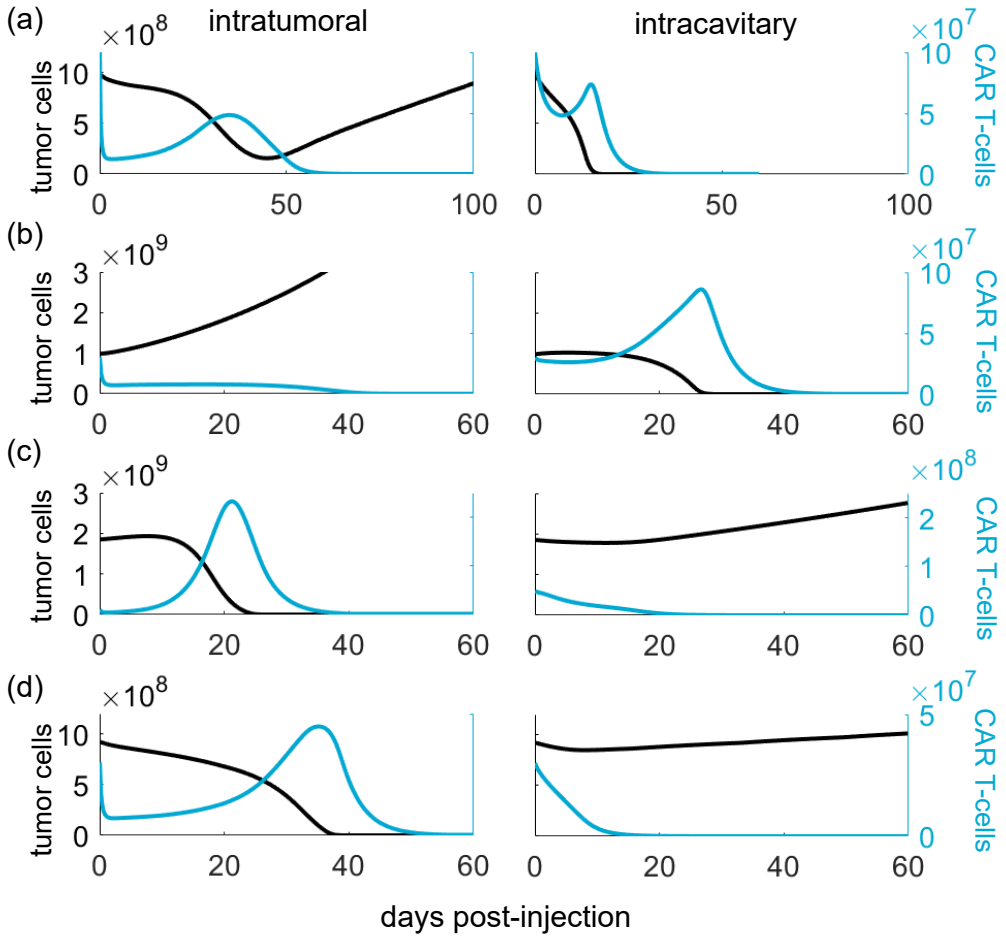

Figure 3.14: For each of the four tumor types, there are doses of CAR T-cells that succeed with one mode of local administration, but fail with the other. For tumor types I and II, doses can be successful when applied at the periphery of the tumor, but fail when applied intratumorally (a-b). For tumor types III and IV, doses can be successful when applied at the center of the tumor, but fail if introduced at the surface.

can induce the 4 general behaviors illustrated in Fig. 3.3.3 -3.13: rapid tumor eradication, eradication after tumor expansion, initial CAR T-cell persistence followed by tumor escape, or rapid tumor escape. Notably, when compared with intracavitary administration, intratumoral injection is more likely to give rise to a period of transient CAR T-cell proliferation even if the tumor eventually escapes, and tumor expansion prior to eventual eradication may be much more significant with intratumoral injection. Though these two modes of local administration produce qualitative behaviors that can be categorized together, across tumor types and between the two modes we observe differences in the key quantities associated with successful treatment: the minimum successful dose, the maximum number of CAR T-cells over the course of treatment, C_{max}, and the time to tumor eradication.

Recall that tumor type I is characterized by high proliferation and low diffusion. This results in a very dense solid tumor with strong proliferation at the boundary. Even at the highest dose levels, CAR T-cells administered intratumorally fail against tumor type I. Though higher doses are able to carve out a substantial initial core from the tumor, the CAR T-cell population peaks and starts to decline before fully clearing the cancerous cells. Consequently the tumor appears to be in remission for about 40 days, before eventually relapsing. According to our model simulations, CART-cells administered intracavitarily successfully eradicate tumor type I above a minimum dose of 10^8 cells. In this case, after initial distribution, CAR T-cells peak at a value of 7.5×10^7 cells around day 16. Unlike with intratumoral administration, a population of cells remain outside of the tumor throughout treatment. These cells are able to avoid exhaustion, allowing for full eradication of the tumor on day 28. With administration at such a high dose, CAR T-cells are immediately able to begin killing tumor cells at the surface and prevent further expansion as they diffuse inwards across the tumor. CAR T-cell density peaks when the wave of CAR T-cells coalesces in the middle and the tumor is eliminated in the center prior to the edges. For even higher CAR T-cell doses, the tumor is eliminated more quickly. This success is precarious though–with even a slightly higher proliferation rate for tumor cells, intracavitary injection also fails at reasonable CAR T-cell dose levels.

Tumors of type II are the most aggressive considered here, characterized by both high proliferation and high diffusion. Against these tumors, intracavitary administration out-

performs intratumoral injection of CAR T-cells, though both are successful at comparable minimum doses. Upon intratumoral injection of 4×10^7 CAR T-cells, the tumor is able to continue expanding at the surface as CAR T-cells proliferate and kill of tumor cells in the center. When the proliferating CAR T-cells reach the surface of the tumor around day 60, they halt further tumor growth and eliminate the remaining tumor fairly rapidly, fully eradicating it on day 80. The peak number of CAR T-cells is 3.5×10^8, reached on day 70. That is an 8.75 fold increase over the injected dose and a 10 fold increase over the minimum level. Further simulations showed that higher doses of CAR T-cells result in earlier tumor eradication, as well as earlier and lower peak numbers of CAR T-cells. The minimum successful dose level when administered intracavitarily is slightly lower: 3×10^7 cells. In this scenario, the peak number of CAR T-cells is just under a 3-fold increase over the initial dose, reaching 8.5×10^7 on day 28. The tumor expands very slightly during the initial CAR T-cell distribution phase. However it is subsequently eradicated on day 36. Tumor elimination occurs fairly rapidly starting from the outer edges and progressing inwards following the wave of CAR T-cell expansion into the tumor. Higher doses of CAR T-cells result in a lower, earlier peak and faster tumor eradication.

Tumor type III has a low proliferation rate, but a high diffusion rate. This balance results in growth dynamics that rapidly colonize new territory, but are slow to populate it to high levels. Consequently, these are the tumors with the lowest average density, though they have the highest total tumor burden at the time of treatment. In this case, the minimum successful dose with intratumoral injection is almost an order of magnitude lower than the dose required for successful intracavitary injection. Intracavitary injection is successful above doses of 5×10^6 cells, expanding by 50 fold to a peak of 2.5×10^8 cells on day 28 and eradicating the tumor on day 38. Immediately following injection, the tumor is able to expand for a period of around 15 days before the CAR T-cells are established in earnest. However, the lower proliferation rate of the tumor allows CAR T-cells to persist. As with treatment of tumor type II, higher doses of CAR T-cells prevent the tumor from expanding significantly, inducing in a lower, earlier CAR T-cell peak and earlier eradication. For intracavitary administration, the lowest successful dose is more comparable to other scenarios, around 4×10^7 cells. This dose expands over 3 fold to a peak level of 1.3×10^8

cells on day 21 before fully eliminating the tumor on day 28. In this scenario, the CAR T-cell population does not expand significantly until reaching the denser core of the tumor. However, even at lower densities, the advancing wave of CAR T-cells smoothly eliminates the tumor from the outside edge inwards as it progresses. In this case, higher doses of CAR T-cells still result in an earlier peak in population and earlier tumor eradication. However, unlike other scenarios, the peak number of CAR T-cells is slightly higher for higher doses. This follows from the lower concentration of tumor cells at the surface of the tumor where CAR T-cells are first introduced.

The final tumor considered is the least aggressive, type IV, which is characterized by both low proliferation and low diffusivity. The tumor density profile at the time of detection is somewhat similar to tumor type II because they have the same proliferation to diffusivity ratio, however the dynamics of the system after treatment differ substantially. The minimum successful intratumoral dose is 3×10^7 CAR T-cells. As with the treatment of other dense tumors, there is a sharp initial decline in CAR T-cells after administration, followed by an expansion of 4.5 fold to a peak of 4.5×10^7 cells prior to eliminating the tumor on day 45. The CAR T-cells expand out from the center of the tumor, maintaining a steady population level in the core as they eliminate the tumor from the inside out. Intracavitary injection against tumor type IV requires a higher dose of 4×10^7 cells. In this case the CAR T-cells gradually diffuse inwards, reducing the tumor burden as they advance. They reach a peak population of 6.5×10^7 cells on day 19, eradicating the tumor on day 27. For both modes of administration, higher doses of CAR T-cells result in lower, earlier peak numbers of CAR T-cells and faster tumor eradication.

All together, our simulations suggest that across both modes of administration, CAR T-cell therapy is most effective against tumors with lower average density. Because of this, CAR T-cell treatment is successful against tumors with low-proliferation (type III and IV) and tumors that have high-proliferation rates, but sufficient diffusivity to reduce the tumor density (type II). In contrast, CAR T-cell treatment can fail completely against dense, highly-proliferative tumors (type I).

If we define effectiveness by the minimum successful dose and the minimum time to eradication, then the preferred mode of administration correlates with the tumor proliferation

rate. For low proliferation tumors (type III and IV), administration via intratumoral injection is successful at lower doses for which intracavitary injection fails (Fig. 3.14). However, for tumors with high proliferation rates (type I and II), administration via intracavitary injection is successful at lower doses than intratumoral injection. When comparing a fixed successful dose level administered either intratumorally or intracavitarily, the mode of administration with the lower minimum successful dose for that tumor type will also have the minimum eradication time (Fig. 3.14). In all scenarios for which eradication is possible, higher doses of CAR T-cells lead to faster eradication times, though not necessarily higher values of C_{max}.

If we instead judge the effectiveness of CAR T-cells by the minimum C_{max} value necessary for successful treatment, we find that the preferred mode of administration correlates with the diffusivity of the tumor. Tumors with high diffusivity (type II and III) can be eliminated with a lower peak number of CAR T-cells if the dose is administered peripherally rather than in the center. Because the growth front is initially unaffected by CAR T-cells introduced at the center of the tumor, the high diffusivity tumors are always able to grow in radius (at least slightly) prior to eradication by intratumoral injection. As the CAR T-cells proliferate outwards to catch this leading edge, they reach a higher peak number. Conversely, tumors with low diffusivity (type I and IV) induce a lower peak in CAR T-cells if injected intratumorally compared with intracavitarily. Introducing a high density of CAR T-cells at the center of the tumor results in an initial drop in CAR T-cell numbers due to the anti-immune effects of the tumor. As the CAR T-cells proliferate and kill the tumor cells around them, they expand in number just enough to advance outward. The danger of skirting the line of minimizing C_{max} is that if C_{max} is too low, then CAR T-cell treatment will fail, as we observe after intratumoral injection against tumor type I.

Validation against Experimental Data

Having established the general behavior of our model, we next compared simulation results with data from clinical and preclinical trials testing the efficacy of CAR T-cells against solid tumors. In order to assess the spatial distribution of cells predicted by our model,

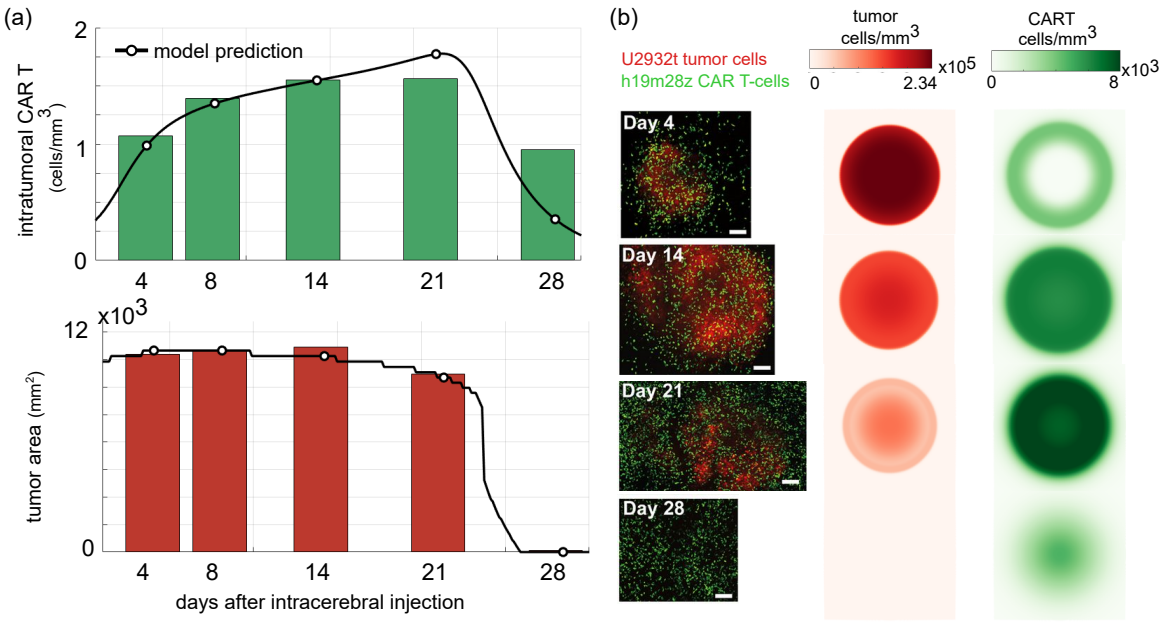

Figure 3.15: Model results qualitatively reflect data from a mouse imaging study tracking CAR T-cell counts following intracavitary injection to treat PSCNL. (a) In particular, the model captures the trend in intratumoral CAR T-cells during the initial proliferation stage very well. The tumor area remains consistently high for the first 21 days before rapidly disappearing between the measurement on day 21 and day 28. (b) Fluorescence microscopy images taken by Mullazanni et al. [121] show CAR T-cells, tagged in green, distributed across the surface of the tumor, tagged in red. The white scale bar indicates 100 μm. Next to each image, we show the tumor and CAR T-cell density predicted by our model on that day, using the same simulation as panel (a). This representation of our model prediction is not perfectly analagous to the images of the cells at the surface of the tumor. However, we can still observe some qualitative consistencies between the experimental images and our model simulation. Namely, CAR T-cells are already evenly spread across the tumor on Day 4, and continue to maintain a notable surface density throughout the first 28 days, even after the tumor is no longer visible. They attain their highest density around day 21. The tumor dynamics are not captured as well by our model which shows a fairly constant area from day 4 to 21, rather than significant growth between day 4 and day 14. However, the timing of tumor decline and eradication aligns with the images shown here.

we compare the density profiles with results from a mouse imaging study of CAR T-cell movement after local administration. We also compare the temporal dynamics of the total CAR T-cell population predicted by our model against data from two clinical trials: one testing CAR T-cell infusion to treat glioblastoma multiform (GBM) and a second testing CAR T-cell infusion to treat non-small cell lung cancer (NSCLC).

Several groups have conducted imaging studies to document the migration of CAR T-cells both *in vitro* and *in vivo* [121, 45, 151], including Keu et al.'s study of FHGB imaging in a human patient with recurrent glioma [88]. These studies confirm the tendency of CAR T-cells to distribute evenly across the tumor fairly rapidly, which supports our choice of initial condition when modeling intracavitary injection. Studies also suggest that if there is poor tumor infiltration by CAR T-cells, then they will be unable to control tumor growth [121]. Failure to fully distribute through the tumor is one potential mode of failure in our model as well.

Mullazanni et al. developed a murine model of primacy central nervous system lymphona and then monitored CAR T-cell dynamics following intracerebral injection by combining a chronic cranial window with 2-photon laser scanning microscopy (TPLSM). They report values for five time points and included some example microscopy images. In Fig. 3.15a we compare our model predictions against their measurements of intratumoral CAR T-cell density and tumor area. We estimated the predicted tumor area from our model simulations by calculating the area of a circle with radius equal to the maximum radial position of the tumor that exceeds a small detection threshold of 10^4 cells/cm^2. Note that the model predictions for radius are not smooth because the minimum change in radius is equal to the spatial grid step size used in numerical simulation. We estimated the average intratumoral CAR T-cell density from the region of the tumor that would be visible using the TPLSM set up described in [121] by integrating over the density from the surface of the tumor inwards to a depth of .4 millimeters from the surface and dividing by the volume of that same region. During the initial stages, our model agrees quite well with the measured CAR T-cell densities. In the later stages, our model appears to overshoot the peak density of CAR T-cells slightly, and we are predicting too fast of a decay in CAR T-cell density. Because our model does not account for memory T-cells, we are not modeling the later stages of CAR T-

cell dynamics carefully, so this disagreement on the tail end is to be expected. We considered slices of the density profiles predicted by our model side-by-side with representative TPLSM images reproduced from [121] in Fig. 3.15b. In the experimental images, tumor cells are tagged with red fluorescent dye while individual CAR T-cells are tagged with green. On day 4, CAR T-cells are already evenly spread across the surface of the tumor in both the images and our model simulation. Between days 4 and 14 it appears that the tumor was able to expand in size even as the CAR T-cells are also proliferating. Our model shows the tumor maintaining a fairly constant area over this same period, as CAR T-cells proliferate. By day 21, in both the images and our model simulation the CAR T-cells have reached an even higher concentration and made a visible impact on the tumor mass, shrinking it below the maximum level. Finally, on Day 28, CAR T-cells still persist, but the tumor is no longer in both the images and our simulation. The parameter values used for this simulation are reported in section 3.3.7.

We can also assess our models predictions by comparing temporal dynamics of the total predicted CAR T-cell population with data from studies that monitored CAR T-cell concentration over time in human patients. Our model qualitatively reflects the four phases in CAR-T cellular kinetics summarized by Liu et al. in their 2021 review of the clinical trial landscape. The authors oberved that regardless of tumor types, dosing regimens, and sampling intensities, CAR T-cells demonstrated distribution, expansion, contraction, and persistence [105]. In our model, across tumor types and administration modes, the CAR T-cell dynamics for the minimum effective dose display these 4 phases. Almost all successful treatments initiated with a reasonable number of CAR T-cells display expansion and contraction phases in our simulations. Only doses of more than 2×10^8 cells are able to eliminate tumors without expanding. The persistence phase is the least well captured by our model. In clinical data, CAR T-cells tend to persist at about $\sim 10\%$ of their peak level [149, 105], but in our model they drop to non-detectable levels. This is to be expected though because our model does not account for memory CAR T-cells, which make up the majority of the immune reservoir. However, our model does reflect the fact that CAR T-cell persistence is important to successful treatment. Increasing the CAR T-cell death or inactivation rate causes treatment to lose effectiveness, and conversely lowering these parameters causes

treatment to be more effective. We also note that successful treatments are marked by a higher peak in CAR T-cells and a relatively slower contraction rate compared to unsuccessful treatments in our model simulations. This pattern was also observed by Liu et al. when comparing responders vs. nonresponders across clinical trials.

We further validated the temporal dynamics of CAR T-cells quantitatively by comparing model simulation results with time series data consolidated by Liu et al. from a clinical trial for GBM (NCT02209376) and for NSCLC(NCT01869166). In both clinical trials, CAR T-cells were administered systemically to treat a solid tumor and the concentration of CAR T-cells in the blood was monitored over time. These concentrations were reported in units of CAR T-cell transgene copies per microgram of DNA. In order to compare our model output with this concentration data, we first integrated the cell density distribution across the spatial domain to get a total cell count. Next we divided this by the area of the domain to get an average cell density in the units of cells/cm^3. This average cell density was then scaled by an appropriate constant to convert to copies per microgram of DNA. This constant was identified using Yamamoto et al.'s data for validating their volume-based unit for CAR T-cell concentration [189].

For each cancer type, we split the patients into two groups to match the reported statistics for the number of responders vs. non-responders. The split was determined based on the depending on the peak height of CAR T-cells over the course of treatment, with responders assumed to have higher peaks. These data points are plotted in light shades in Fig. 3.16a for GBM and Fig. 3.16b for NSCLC. Responders are shown in blue and non-responders shown in orange. We tuned a representative model resulting in a successful patient outcome to reflect the trends in the responder groups, shown by the dashed blue line. For the non-responders, we tuned a representative model that ultimately proves unsuccessful, shown by the dashed orange line. In GBM, we used a high proliferation rate and a high diffusivity for the tumor parameters. The CAR T-cell parameters were varied to match each group. Compared to the model simulation for successful treatment, the unsuccessful model had a higher sensitivity to tumor cell lysis, k, but a maximum tumor lysis rate, d, so CAR T-cells were less effective. Furthermore, the diffusion constant of CAR T-cells was lowered, so CAR T-cells did not spread as easily. With this balance, CAR T-cells may persist at

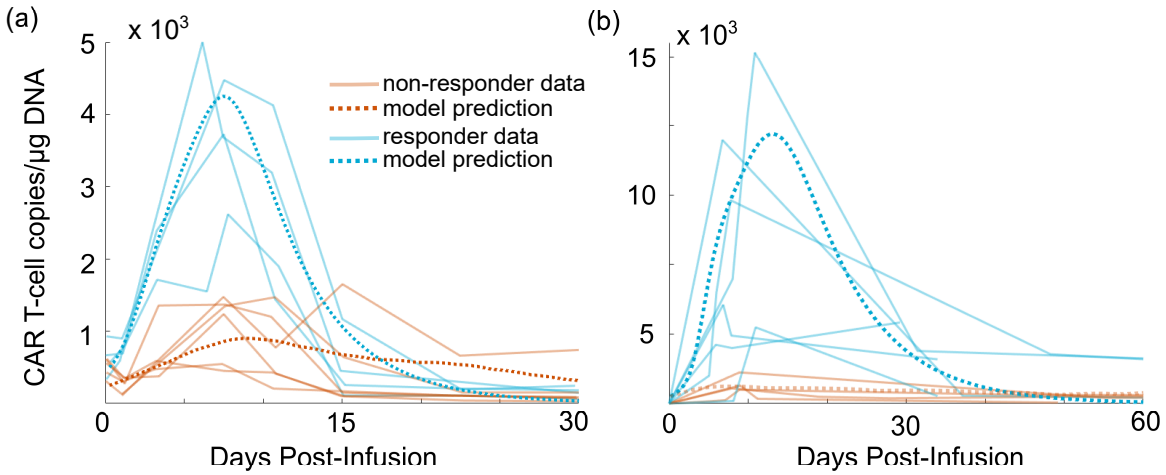

Figure 3.16: (a) Time series measuring CAR T-cell concentration over the course of treatment for 10 patients with GBM are shown in lighter shades. Patients were split into 2 groups, responders and non-responders, and model dynamics were tuned to fit each group, shown by dotted lines. (b) Time series measuring CAR T-cell concentration over the course of treatment for 11 patients with NSCLC shown in lighter shades. Again, patients were split into 2 groups and model dynamics were fit to each group, shown in dashed lines. In both cases the concentration of CAR T-cells was quantified by copies/μg of DNA. Model results were converted to concentration and then further scaled by a constant to match the units of the experimental data.

detectable levels for a time, but they only transiently impact the tumor. We see that the model is flexible enough to reflect the wide range of dynamics observed in the patient data. For NSCLC, the trial categorized two patients as having partial regression, five with stable disease, and 4 with progression. We used the type I tumor parameters and again tuned a subset of the CAR T-cell parameters to match the dynamics of the two patient groups. As with GBM, to fit the NSCLC non-responders parameters determining CAR T-cell efficacy were lowered.

3.3.4 Discussion

In this section we developed a novel reaction-diffusion model for CAR T-cell treatment of solid tumors and characterized it's behavior in a biologically relevant parameter regime. The underlying mechanism that we propose for tumor growth is flexible enough to model a wide range of tumor types. This is particularly valuable when modeling CAR T-cell treatment, because there is significant interest in using CAR T technology to treat diverse cancers. We further demonstrated that this model captures behaviors observed in clinical and preclinical trial data both qualitatively and quantitatively by comparing model predictions with data from mouse-imaging studies tracking intratumoral CAR T-cell movement, and measurements of CAR T-cell concentration in human GBM and NSCLC patients. There is still room for improvement in adapting the forcing functions to be able to capture partial responses to therapy, phenomena like CAR T-cell induced stable disease, and to better reflect the long-term persistence of CAR T-cells.

Using a spatial model for CAR T-cell therapy, rather than ODE models which have been studied previously, allows us to study treatment of solid tumors. Assumptions of well-mixed cell populations do not hold for solid tumors. Furthermore, the movement of CAR T-cells within solid tumors has been identified as an important factor in successful treatment. In particular, our spatio-temporal model exhibits a failure mode in which there is an initial tumor response to treatment followed by relapse. This clinically observed mode of CAR T-cell failure was not captured by the ODE model from Owens and Bozic [139]. Furthermore, our results suggest a relationship between tumor density and minimum successful CAR T-cell dose that cannot be captured by an ODE model tracking the total cell populations over time.

We used the reaction-diffusion framework developed here to compare the response of different tumor types to localized CAR T-cell treatment. In particular we considered dense solid tumors with high proliferation but low diffusivity, aggressive tumors with both high proliferation and high diffusivity, diffuse tumors marked by low proliferation but high diffusivity, and low-grade tumors with both low proliferation and low diffusivity. When testing a wide-range of CAR T-cell doses, we found that CAR T-cell injection was least effective

against tumors with high proliferation and low diffusivity, i.e. very dense, compact tumors. In our model, this is the setting wherein CAR T-cells are most impacted by exhaustion. CAR T-cell treatment was quite effective against the other three tumor types. Surprisingly, the lowest minimum dose was necessary for the low-proliferation, high diffusivity tumors, not tumors with both low proliferation and low diffusivity. That is, CAR T-cell therapy was the most effective in treating the tumor with the smallest average density, not the smallest total tumor burden or the lowest VDT. These findings affirm that CAR T-cells will not perform equally across different types of solid tumors. It may be particularly promising to pursue CAR T-cell therapy for diffusive tumors. Perhaps tumor density should be measured when considering the feasibility of CAR T-cell therapy for a particular patient and/or planning dosages.

With our model for local administration, we compared two different modes of delivery: intratumoral injection vs. intracavitary injection. For many patients, these options may not be accessible due to patient health or tumor location within the body. However, in situations where both are possible, it would be useful to know which should be preferred. In our simulations, we found that intracavitary administration is successful at lower doses when treating highly proliferative tumors (regardless of the diffusivity). For tumors with low proliferation rates, we found the opposite to be true. Low proliferation tumors can be eradicated with lower doses if the CAR T-cells are administered via intratumoral injection. An alternative measure of the effectiveness of CAR T-cell treatment is to compare the peak number of CAR T-cells that occurs over the course of successful treatment. The initial dose is determining whether CAR T-cells become established in the system, but in many cases the CAR T-cell population subsequently expands to a higher peak, and this high number of cells may be associated with patient side effects. Interestingly, where the minimum dose needed tracked with the tumor proliferation rates, the peak number of CAR T-cells is correlated with the tumor diffusivity. When treating highly diffusive tumors, intracavitary administration can result in successful treatment with a lower peak CAR T-cell level. However, when treating tumor type IV, the low proliferation/low diffusivity tumor, intratumoral injection was successful with a lower peak CAR T-cell level. For tumor type I we cannot make a direct comparison because intratumoral injection failed, which in

part could be because the same initial doses lead to lower peak numbers of CAR T-cells. This scenario illustrates that minimizing patient side-effects resulting from on-target effects, like seeing a large expansion phase, is a challenge, since we run the risk of losing treatment efficacy.

Though our model exhibits a wide range of behaviors, it is still only a preliminary spatial model. For the sake of avoiding unnecessary complication as we explore a new system, we used a highly simplified tumor geometry. The assumption of symmetric spherical growth for a large tumor, while convenient mathematically, is unrealistic within the body. Angiogenesis (the development of new blood vessels) is needed to support the growth of a tumor beyond the size of about a million cells, at which point the tumor will no longer develop symmetrically. As more data becomes available tracking the movement of CAR T-cells around and within the tumor, there is also room to refine the initial distributions of CAR T-cells for the two modes of local administration. Because of the lack of conclusive data, we also assumed the simplest possible motion for CAR T-cells: pure diffusion. It is clear, however, that CAR T-cells do preferentially migrate towards the tumor, so incorporating chemotaxis or haptotaxis could also improve the model. Overall this reaction-diffusion model on a simple 3D domain provides an excellent starting point for understanding CAR T-cell therapy in solid tumors.

3.3.5 Nondimensionalization

We nondimensionalize equation (5) with $\tau = at$, $\hat{r} = r/R_0$, $\hat{u} = ub$, and $\hat{v} = vb$, where a is the timescale for tumor proliferation from [139], R_0 is the initial spread of the tumor, and $1/b$ is the local carry capacity for tumor cell density. This gives us the equation

$$\frac{\partial u}{\partial t} = \frac{1}{r^2}\frac{\partial}{\partial r}\left(D_T(u) r^2 \frac{\partial u}{\partial r}\right) + F_1(r,t); \qquad D(u) = \begin{cases} 0 & u(r,t) \leq \hat{u}, \\ D_T^* & u(r,t) > \hat{u}; \end{cases} \tag{6a}$$

$$\frac{\partial v}{\partial t} = \frac{1}{r^2}\frac{\partial}{\partial r}\left(D_C r^2 \frac{\partial v}{\partial r}\right) + F_2(r,t). \tag{6b}$$

with

$$F_1 = \left[1 - u - \gamma \frac{v^l}{su^l + v^l}\right] u(r,t) \tag{7a}$$

$$F_2 = \alpha \left[\ln\left(\frac{\kappa}{v}\right) \frac{v^l u}{su^l + v^l + \zeta v^l u} - \beta u - \chi\right] v(r,t) \tag{7b}$$

where $\hat{u} = u^* b$, $\gamma = d/a$, $\alpha = \frac{dj}{abk}$, $\kappa = Kb$, $\zeta = \frac{d}{bk}$, $\beta = \frac{kq}{dj}$, $\chi = \frac{bkm}{dj}$, and the dimensionless parameters s and l remain unchanged.

3.3.6 Numerical Methods

Finite difference schemes are employed to solve the radially symmetric spherical diffusion equations in the model (6b). Namely, Crank-Nicolson (CN) [30] is used for the results presented in the body of the paper. For the concentration of CAR T-cells, $v_m^n = v(m\Delta r, n\Delta t)$, the CN scheme is fairly standard yielding

$$\begin{aligned} & v_m^{n+1} - v_m^n - \frac{D_C}{r_m}\left[v_{m+1}^{n+1} - v_{m-1}^{n+1} + v_{m+1}^n - v_{m-1}^n\right] \frac{\Delta t}{2\Delta r} \\ & - D_C\left[v_{m+1}^{n+1} - 2v_m^{n+1} + v_{m-1}^{n+1} + v_{m+1}^n - 2v_m^n + v_{m-1}^n\right] \frac{\Delta t}{2(\Delta r)^2} \\ & - \left[F_2\left(u_m^{n+1}, v_m^{n+1}\right) + F_2\left(u_m^n, v_m^n\right)\right] \frac{\Delta t}{2} = 0, \end{aligned} \tag{8}$$

with $v_{m+1} = v_{m-1}$ at $r = 0$ and for $r \in \partial\Omega(u)$

For the tumor concentration, $u_m^n = u(m\Delta r, n\Delta t)$, the diffusivity, D_T, depends on u, which means its dependence on r is changing in time. If u_{m+1}^n and u_{m-1}^n have the same parity with respect to u^* in equation (6a), the central difference for D_T is trivial, and hence D_T is treated as a constant. However, if the parity is different, there is no flux from the side with a concentration less than u^*, and therefore this side can be treated as a Neumann boundary. If u_{m+1}^n and u_{m-1}^n have the same parity we write

$$\begin{aligned} & u_m^{n+1} - u_m^n - \frac{D_T}{r_m}\left[u_{m+1}^{n+1} - u_{m-1}^{n+1} + u_{m+1}^n - u_{m-1}^n\right] \frac{\Delta t}{2\Delta r} \\ & - D_T\left[u_{m+1}^{n+1} - 2u_m^{n+1} + u_{m-1}^{n+1} + u_{m+1}^n - 2u_m^n + u_{m-1}^n\right] \frac{\Delta t}{2(\Delta r)^2} \\ & - \left[F_1\left(u_m^{n+1}, v_m^{n+1}\right) + F_1\left(u_m^n, v_m^n\right)\right] \frac{\Delta t}{2} = 0, \end{aligned} \tag{9}$$

otherwise we write

$$\begin{aligned} u_m^{n+1} - u_m^n - D_T \left[u_\pm^{n+1} - u_m^{n+1} + u_\pm^n - u_m^n\right] \frac{\Delta t}{(\Delta r)^2} \\ - \left[F_1\left(u_m^{n+1}, v_m^{n+1}\right) + F_1\left(u_m^n, v_m^n\right)\right] \frac{\Delta t}{2} = 0, \end{aligned} \tag{10}$$

where $u_\pm = u_{m+1}^n$ if $u_{m+1}^n > 1$ or $r_m = 0$, and $u_\pm = u_{m-1}^n$ if $u_{m-1}^n < 1$.

3.3.7 Sensitivity Analysis of Tumor Parameters

For two fixed tumor proliferation rates, a, we varied the diffusion parameters D_T^* and u^* and recorded the effect on tumor growth in the absence of CAR T-cell treatment. Specifically we computed two quantities for each parameter set: the volume doubling time (VDT) and the detectable tumor burden (TB) at the VDT. VDT was estimated by initiating a simulation with a spherical tumor of radius $r = 2^{-1/3}$ and running it forward in time until the radius of the detectable tumor hit $r = 1$. TB at detection was also calculated at this moment in time by integrating the tumor cell density over the spatial domain. These simulations were run using proliferation rates that differ by an order of magnitude, with a high proliferation rate of $a = 0.18$ day^{-1} (Fig. 3.17a and b), and the low proliferation rate of $a = 0.018$day^{-1} (Fig. 3.17c and d). For both growth rates, increasing D_T^* makes a tumor more aggressive, reflected as faster VDTs. For the high proliferation rate, lower values of u^* also result in lower VDTs. From the TB plot in panel (b), we see that across this parameter range the tumor burdens are always on the same order of magnitude, though they are the lowest when $u^*b \sim 0.3$ and D_T^* is large. In this case, the detectable radius is quickly reached but a large part of the tumor is down near the detectable density level instead of near the local carrying capacity. For a lower diffusion coefficient or a higher threshold u^*b, a larger portion of the detectable tumor is near the local carrying capacity and hence there is a larger number of cells packed into a similar volume of tumor. In contrast, for the low tumor proliferation rate, changing the diffusion threshold u^* has a non-monotonic influence on the VDT across this parameter range. For low values of u^* and high D_T^*, the tumor profile is highly diffuse and so it takes longer for a detectable density to amass at the center of the tumor. Though this type of tumor has a slower doubling time as we have defined it, it is still quite aggressive. Tumors in this parameter regime have the highest tumor burden at

detection because the low density growth front extends far beyond the detectable radius. For moderate values of u^* and low values of D_T^*, the tumor is quite compact as diffusivity and proliferation are again balanced. We see a similar relationship between VDT and TB at time of detection as with the high proliferation tumor growth, except that the doubling times are much slower. This aligns with the findings of Swanson et.al, who observed that the signature density profile of their tumor growth model could be characterized by the ratio of tumor proliferation to tumor diffusion [168]. For even higher values of u^*, the diffusion threshold is high enough that the slowing effect of logistic growth is relevant at the growth front. This creates staltatory growth patterns in which the tumor colonizes new territory and then takes time to fill it to capacity before expanding in another jump in radius.

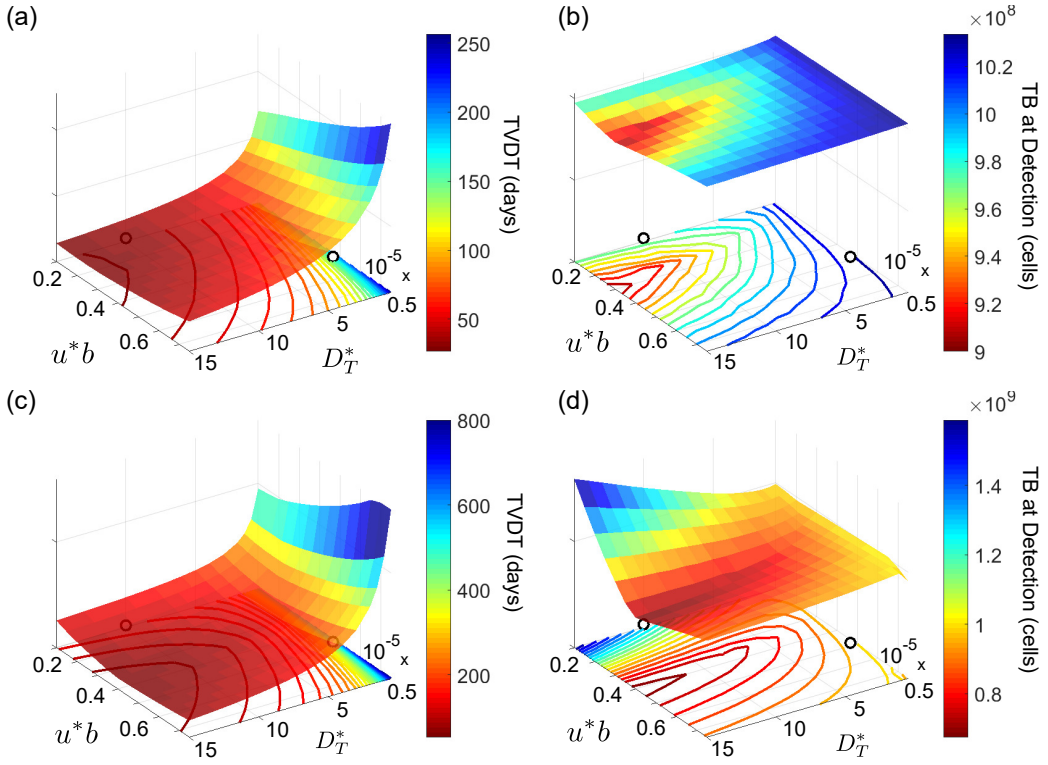

Figure 3.17: Tumor volume doubling time (VDT) and the total tumor burden (TB) when the radius of the detectable tumor reaches 1 cm are mapped out as functions of the tumor diffusion coefficient D_T^* and the tumor diffustion threshold u^* for two values of the tumor growth rate. Panels (a) and (b) reflect the behavior of the system at a high proliferation rate of $a = 0.18$ whereas panels (c) and (d) illustrate system behavior at a low proliferation rate, $a = 0.018$. We model CAR T-cell treatment for 4 types of tumors: Type I has high proliferation and low diffusion, Type II has high proliferation and high diffusion, Type III has low proliferation and high diffusion, and Type IV both low proliferation and low diffusion, indicated by white circles on each map.

Chapter 4

PATTERN FORMATION

Why does a leopard develop spots while a tiger is marked by stripes? Why do most humans have ten fingers and ten toes? Why do we observe rippled patterns in sand? Such questions have fascinated mathematicians, physicists, and biologists for decades. These are all examples of pattern formation, or the development of visibly ordered outcomes through self-organization in a system.

Pattern formation also occurs within microbial communities. For example, many consider *Saccharomyces cerevisiae*, commonly known as baker's yeast, a simple unicellular organism, but yeast colonies can demonstrate complex multicellular patterns. Some strains form complex, wrinkled and ridged colonies under the right environmental conditions. This morphology functions similar to a biofilm, a multicellular aggregate of cells adhering to a surface and embedded in an extracellular matrix [42]. Bacterial biofilms facilitate social cooperation, resource capture, and increased tolerance of environmental stressors, factors which increase drug resistance. In comparison, eukaryotic biofilms have not been studied as fully. Although the biochemical and molecular requirements for patterns resembling biofilms have been examined in yeast, the mechanisms underlying structure formation are not entirely clear [183]. Furthermore it is generally accepted that the ability to develop a complex morphology in yeast strains indicates drug-resistance [74], but conclusive experimental studies have not yet confirmed this hypothesis.

Besides forming interesting patterns, yeast also serves as a powerful model eukaryote for studying the genetic architecture of quantitative traits. Dissecting complex traits poses a challenge in modern genetics. Achieving the statistical power needed to identify variants with small effect sizes and assess the impact of genetic interactions between multiple loci requires large cohorts with accurate genotype and phenotype data. Advances in DNA sequencing technology have made genotyping on this scale feasible and enabled two distinct

approaches: genome wide association studies (GWAS) and linkage-mapping in humans and model organisms. The GWAS approach captures a high proportion of the total genetic variation found in the population being studied, an important advantage towards understanding the underlying genetics of a trait. However, population structure, often complex and unknown, constrains GWAS, by producing false positive signals and reducing the power to identify causative variants and genetic interactions between them. Furthermore, although the GWAS approach attempts to identify genetic variation in the specific genes that causally influence a trait, even when successful, gene mapping studies often delimit large regions of the genome. Linkage-mapping studies in *Saccharomyces cerevisiae* have been performed on scales and with precision not possible in other systems. Recent studies examining large numbers of recombinant progeny from one or more crosses between genetically diverse strains have provided a wealth of insight on the influence of common and rare alleles on complex traits, the extent to which genetic interactions contribute to missing heritability, and the pervasiveness of genetic modifiers. However, most existing resources either capture only a small proportion of the genetic variation in the natural population or produce genetically structured mapping populations. To address these challenges, the Dudley Lab set out to produce a large, highly powered mapping resource that captures a substantial fraction of the genetic variation in a natural population, but which avoids the problems of population structure. In the Yeast Funnel Cross Data Set, they have produced a powerful resource for delineating the genetic architecture of complex and quantitative traits in the budding yeast.

In the rest of this chapter, I will introduce the Yeast Funnel Cross Data Set, highlight some exciting results that have already come from applying Quantitative Trait Locus (QTL) analysis to this mapping population, and discuss the data analysis I performed to extract phenotypic information from images.

4.1 The Yeast Funnel Cross Data Set

In the Yeast Funnel Cross, the Dudley lab generated a mapping population of 11,500 genetically diverse haploid *Saccharomyces cerevisiae* strains, determined their genome sequences, and accurately measured a set of quantitative traits. This library of strains reflects complex genetic backgrounds akin to outbred populations, but without the confounding factors of

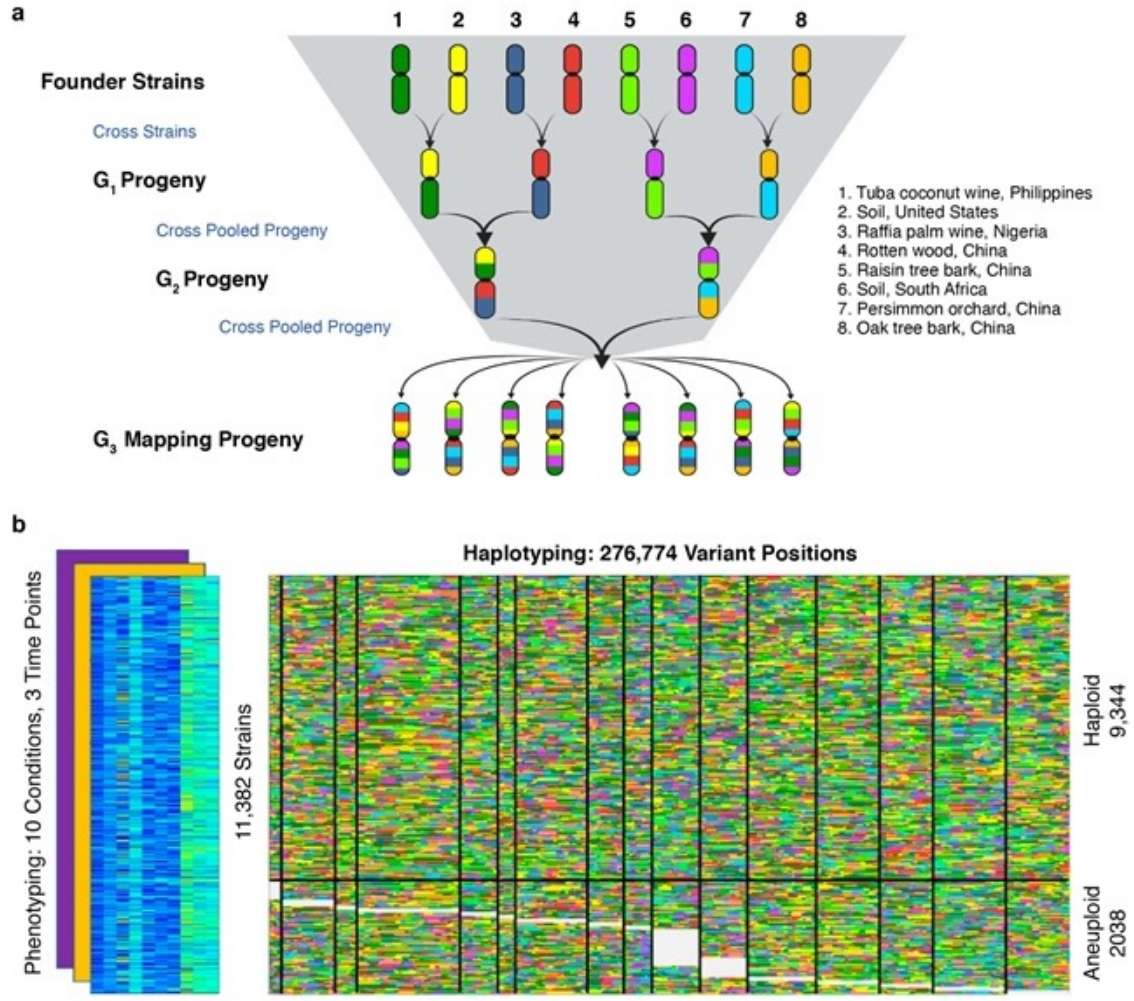

Figure 4.1: Mapping population and dataset. (a) Eight haploid strains that harbor a substantial proportion of the rare and common alleles present in the global S. cerevisiae population were used to generate a mapping population via a funnel cross design. Each founder strain was mated pairwise to produce heterozygous diploids, which were each sporulated to produce pools of 576 MATa and 576 MATα haploid progeny. Two rounds of reciprocal crossing using pooled strains were then carried out to produce the final mapping population of 11484 haploid strains. (b) Each of the strains in the final mapping population was then individually genotyped and karyotyped by low coverage whole genome sequencing. Growth of each strain on agar plates was measured on ten different media, in duplicate, and at 3 time points. After quality control filtering, this resulted in a final population of 9344 euploid and 2038 aneuploid strains each individually genotyped, with phenotypes measured individually on 10 growth conditions.

natural populations that are structured in unknown ways. Using whole genome sequencing, they identified 270k high-quality biallelic single nucleotide polymorphisms (SNPs) among the founder strains, a SNP density of 1 per 44 bases. To construct the mapping population, the group used an eight-parent "funnel cross" approach, an efficient means of generating a set of strains which samples all combinations of alleles in the final mapping population [26, 148, 154, 35, 194]. To maximize genetic the diversity of the progeny strains, they seeded the cross with eight haploid "founder" strains from a variety of geographic and environmental sources (Fig. 4.1A). Several key features of the mapping population make it ideally suited to comprehensively investigate fundamental questions about genetic architecture. First, the founding population captures a large fraction of the currently known genetic diversity in the global population of *S. cerevisiae*, including 32% of biallelic SNPs with a minor allele frequency (MAF) greater than 0.005 and 56% of SNPs with global a MAF greater than 0.05. This diversity produces offspring with complex genetic backgrounds that are more representative of naturally ocurring populations. Second, the large number of offspring provides substantial statistical power to map loci of small effect and identify gene-gene interactions. Third, the funnel design and sample size provide a sufficient amount of recombination to map many loci at single-gene (and in many cases sub-genic) resolution to facilitate the discovery of causal alleles. Fourth, during construction, the use of experimentally introduced genetic changes with large effects on growth (e.g. auxotrophic markers), which can confound analysis of the phenotypic variation resulting from the naturally occurring polymorphisms was avoided [10].

The strains in this mapping population constitute a flexible resource and can be used to dissect the genetic architecture of a trait of interest by combining the existing haplotyping with specific phenotype data. Phenotype data was collected for a set of quantitative traits: growth of yeast on ten different media conditions. These conditions included rich glucose-containing medium (YPD), rich medium with galactose as the carbon source (GAL), and YPD supplemented with cadmium chloride (CAD), caffeine (CAF), calcium chloride (CAL), hydroxyurea (HU), rapamycin (RAP), sorbitol (SOR), caspofungin (CF), or fluconazole (FLZ). The Dudley Lab chose this test set of conditions because they are commonly studied yeast traits involving a diverse set of biological processes, and many had previously been

assayed in other relatively large strain populations, including the yeast deletion collection, a large pairwise cross, and sets of pairwise crosses. To generate high-precision quantitative phenotypes, team members individually quantified the growth of each strain in duplicate, at three timepoints (24, 48 and 72 hours) on different growth media (Fig. 4.1B). Strains were robotically pinned from liquid culture onto solid-media plates, and growth at each timepoint was recorded by taking a top-down photograph of the agar plate. Additionally, after the 72 hour images were taken on the YPD plates, an agar invasion assay was carried out. This entailed rinsing the plates under moderately running water, a "soft wash", and photographing them again. Next plates were rinsed again, this time while gently running a gloved finger over the agar surface. After this "hard wash", the plates were photographed again.

I contributed to this genetic mapping resource by building an automated image analysis pipeline to reliably measure the colony area of each strain in the sets of images taken by team members, described in detail in the following section (4.2). All together, the phenotyping was highly reproducible, with a median r^2 value of 0.93 between the two independent biological replicates. Estimates of broad-sense heritability (H^2), 95-99% at 72h (Fig4.1A), confirmed the high reproducibilty of our measurements, and demonstrated that a very high proportion of the phenotypic variation was genetically heritable.

The team performed linkage mapping for each condition at each timepoint. Because of the high degree of similarity observed across timepoints, the team focused on the 72h results. Our results reveal a variety of genetic architectures underlying the different traits, with some conditions harboring a linkage peak that explains most of the phenotypic variance (e.g. CAD: max LOD =2392; 69% of variance) (Fig. 4.1A) and others that consist of several linkage peaks that each explain smaller, but significant, amounts of variance (e.g. fluconazole, FLZ) (Figs. 4.1A and 4.1C). For each condition, we then assembled an additive genetic model by forward selection and used the full set of 270k high-quality variant sites to resolve the position of each QTL (Methods). For conditions with well-characterized genetics, such as fluconazole-resistance (Fig. 4.1C) and growth on galactose (below), strong condition-specific peaks included known target genes resolved to the one- or two-gene level. Comparison of the additive versus interaction models for all pairs of scaffolding markers in all

conditions confirmed that our dataset is highly powered to detect non-additive interactions. To explore the results in more detail, the team first focused on one trait, growth in the presence of galactose as the sole carbon source. In yeast, galactose utilization (GAL) is a highly conserved metabolic pathway (Fig. 4.3A) for which gene function and regulation is well understood [75]. In our mapping study, growth in galactose was dominated by a single QTL peak (LOD = 1101), which explained 42% of the variance and mapped with single-gene resolution to the master regulator of the galactose pathway, GAL3 (Fig. 4.3a). Haplotypes from founders 1 (Tuba wine, Philippines) and 3 (Raffia wine, Nigeria) associated with a low growth (Gal-) and the remaining six haplotypes associated with a high growth (Gal+). We identified a single shared SNP (T-448C) in the GAL3 promoter of founders 1 and 3 that GWAS studies would suggest caused this low-growth phenotype. To resolve this phenotype to the quantitative trait nucleotide (QTN), we constructed and assayed substitution mutations that changed this SNP in the promoters of founders of 1 and 3 to the reference genome allele. Surprisingly, reverting this shared allele (T-448C) had no effect on the galactose growth of these founder strains (Fig. 4.3c). Instead, our results demonstrated that two different missense alleles in the coding regions of GAL3, one unique to founder 1 (G370A/Gly124Arg) and another unique to founder 3 (G154C/Gly52Arg), were sufficient to confer the loss-of-function phenotype (Fig. 4.3c). These results underscore the fact that because common molecular mechanisms, but not necessarily common genetic variants, drive phenotypic diversity, some of the assumptions made in population based mapping should be applied with caution. The GAL3 loss of function results highlight the need for a gene-centric, functional based approach to GWAS.

To assess the potential to discover fundamental biology using this mapping resource, the team next examined the extent to which they could, in a single experiment using only standing genetic variation, recapitulate decades' worth of genetic and biochemical studies by multiple laboratories. To do so, they further compared our galactose results to previous studies of the well-characterized galactose utilization pathway. They found that with the exception of a single gene, (PGM2), they were able to identify the regulatory and mechanistic components of the complete GAL pathway.

Generating reliable quantifications of yeast patch sizes in the Funnel Cross data set

Figure 4.2: Genetic architecture of ten traits. (a) Proportion phenotypic variance explained by additive, interaction and single-marker models. (b) Additive model QTL number and resolution (genes in 2-LOD interval). (c) Single–marker LODs for fluconazole, chromosomes alternating grey and white. Known resistance genes mapped to 1 (purple), 2 (green) or 3-5 gene (blue) resolution. Asterisks indicate non-FLU-specific peaks. (d) Proportion narrow sense heritability explained by additive models as QTL are added in order of strength. (e) Maximum additional variance explained by inter-chromosomal pairwise interactions with 1% FDR thresholds (red). (f) Effect on total variance explained of allowing non-additive interactions within additive models.

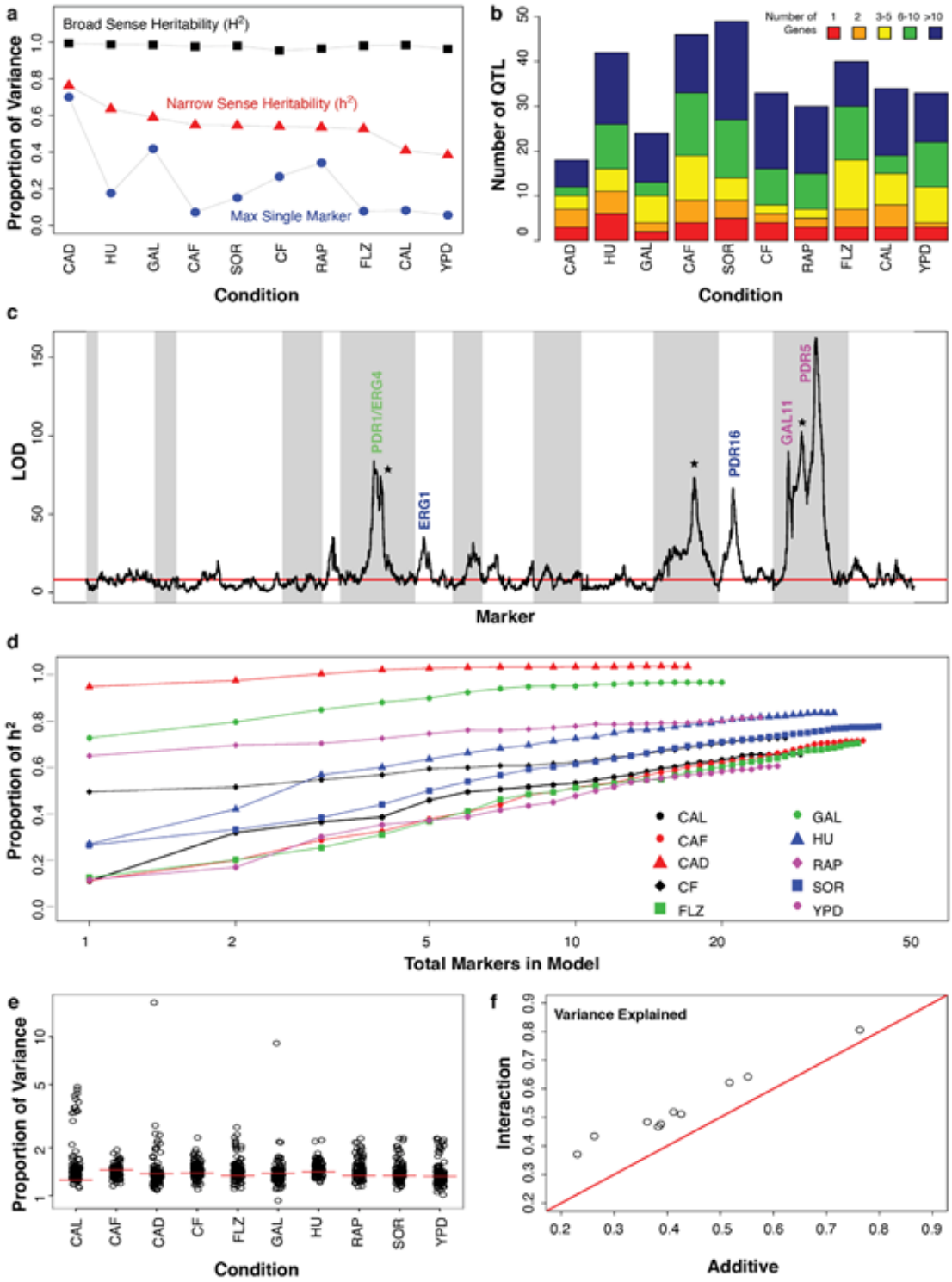
a
Broad Sense Heritability (H²)
Narrow Sense Heritability (h²)
Max Single Marker
Proportion of Variance
Condition
CAD HU GAL CAF SOR CF RAP FLZ CAL YPD
b
Number of QTL
Number of Genes 1 2 3-5 6-10 >10
Condition
c
LOD
Marker
PDR1/ERG4
ERG1
PDR16
GAL11
PDR5
d
Proportion of h²
Total Markers in Model
CAL
CAF
CAD
CF
FLZ
GAL
HU
RAP
SOR
YPD
e
Proportion of Variance
Condition
f
Variance Explained
Interaction
Additive

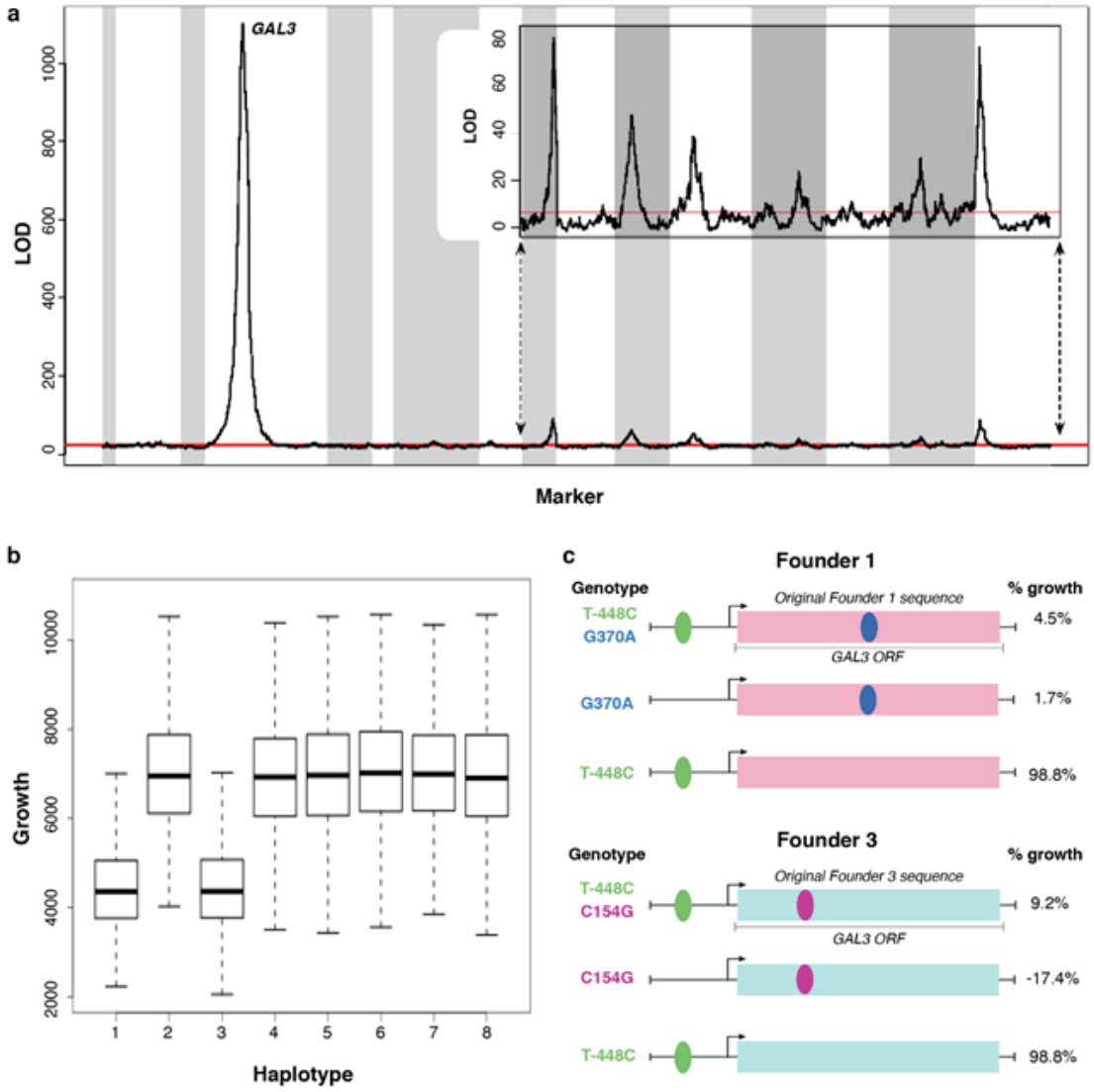

Figure 4.3: (a) LOD scores for linkage mapping on galactose. Insert rescales Y axis to highlight strong QTL other than GAL3. (b) Growth on galactose for strain subpopulations defined by GAL3 haplotype. (c) Effect on founder 1 and founder 3 growth on galactose after transformation with plasmids expressing their own GAL3 allele (top) or derivatives (below). Growth is scaled relative to transformation with the S288c reference allele of GAL3 (100%) and an empty vector (0%).

has already enabled this detailed genetic analysis of growth under different environmental conditions. The phenotyping data makes up half of the puzzle pieces needed to to realize the potential of this remarkable genetic mapping resource. Accessing the phenotypic states of the strains archived by team members through photographs required developing and implementing an automated image processing pipeline.

4.2 Task 1: Robust Automated Segmentation

In order to extract phenotypic measures from the Funnel Cross plate images, I created an open source python package: PyPl8 [137]. This software package allows users to segment and extract quantitative phenotype values from plate images in an automated fashion. Automating phenotype quantification allowed the Dudley lab to scale up their image processing to the high-throughput level necessary to analyze the funnel cross experiment, an increase on previous experiments by multiple orders of magnitude. Previous expert-supervised segmentation methods used by the team would have been prohibitively slow. Though other automated extraction methods exist in the literature, they are not suited to handle the phenotypic variation displayed in the Yeast Funnel Cross Data set. In this section I describe why accomplishing a robust segmentation of the Funnel Cross images is challenging, provide theoretical background for the image processing techniques used, and give an overview of the segmentation method I implemented.

4.2.1 Motivation and Overview

Though numerous automated segmentation tools exist, they were not robust enough to handle the phenotypic variation of yeast growth included in the Funnel Cross or required high resolution images [97, 175]. Yeast patches exhibiting strong growth show up as bright patches against the dark agar background (Fig. 4.4, columns 1-2). Standard intensity-thresholding techniques easily separate these well-growing colonies. However, many strains develop at slower than wild-type growth. Such strains may grow irregularly, containing regions of low-intensity that cannot be captured by global intensity-thresholding. Figure 4.4 illustrates three such patterns. First a patch may exhibit donut or crescent-moon like growth in which regions of high pixel intensity cluster at the edges of the initial pin location,

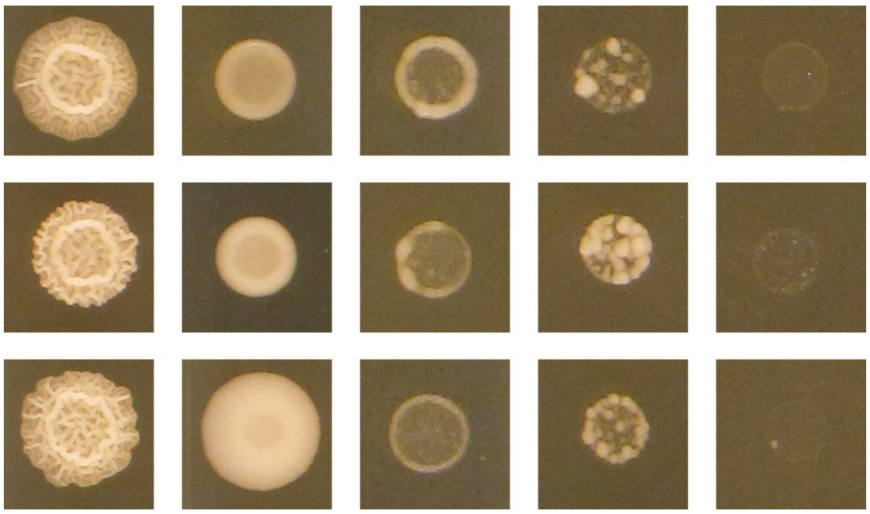

Figure 4.4: Here are representative examples of different types of patch growth included in the Yeast Funnel Cross. The first columns shows that well established yeast patches may grow with a complex colony morphology resulting in varied pixel intensity across the patch surface. The second columns shows the most common growth pattern: a smooth continuous disks. Yeast patches with lower fitness on a given condition may exhibit donut-like growth (column 3) or severe papillation (column 4). Some yeast strains are completely unable to grow on a given condition (column 5).

but near null growth occupies the center. Second, a patch may exhibit papillated growth in which some isolated clumps of cells grow very well, but the background level of growth across the pin remains largely null. Third, a patch may uniformly exhibit faint, nearly null growth. In addition to these types of stunted growth, some patch images display a high level of pixel variability due to bumps and ridges on the colony surface which create shadows. Processing the Funnel Cross data set required developing a segmentation algorithm that could accurately and robustly capture standard, strongly growing colonies, complex textured colonies, and the three types of sub-standard growth.

The steps of the image processing pipeline that I developed break down into three sections (Fig. 4.5). First, preprocessing entails cropping the plate image into 96 square

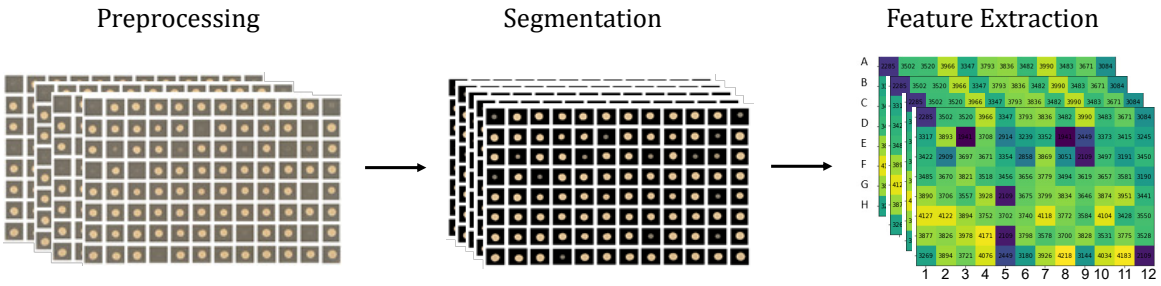

Figure 4.5: The steps of the image processing pipeline break down into three sections. First images are preprocessed to produced square tiles centered on each patch. These 96 regions of interest per plate are then segmented. Finally quatitative features of interest are extracted from the segmented tiles.

regions of interest (ROI), centered on each patch. I will refer to these rectangular ROIs as tiles. After preprocessing, I used a combination of intensity-thresholding and circle-detection to segment each tile. Finally I extracted quantitative features of interest from the segmented tiles, namely area, average pixel intensity and texture scores. As mentioned before, the reproducibility of phenotyping was very high, with a median r^2 value of 0.93 between the two independent measurements on each condition at 72h. Though not dependent on image processing alone, this confirms that our measurements were highly reproducible between the replicates.

4.2.2 Theoretical Background

Before explaining the details of the automated image-segmentation algorithm, I will provide some background on the work-horse methods from image analysis that I used along the way. Digital image processing is a rich field with applications ranging from game development, to law enforcement, to medical diagnosis and beyond. The methods discussed here are a very small foray into this rapidly developing field.

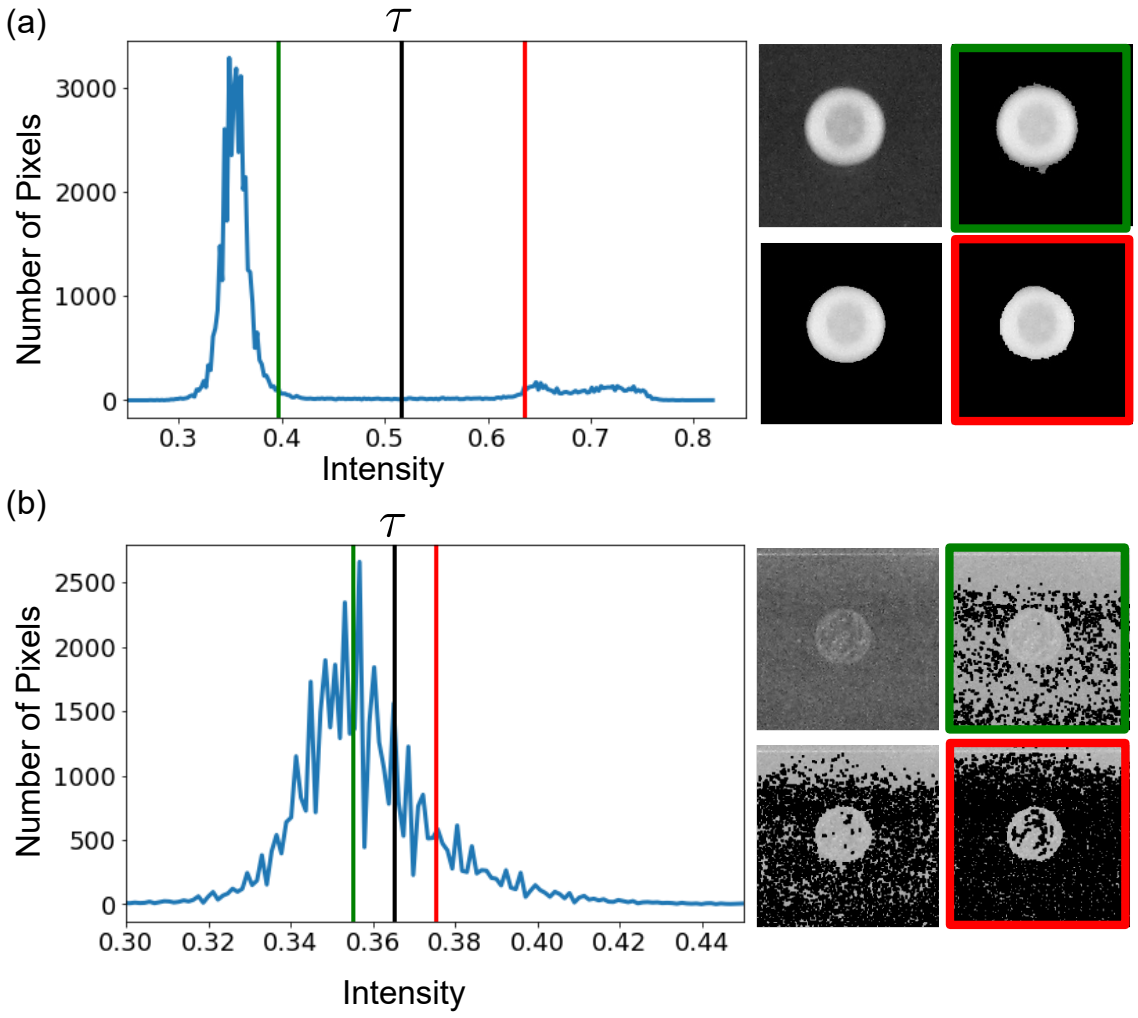

Figure 4.6: An illustration of the optimal threshold for image segmentation as determined by Otsu's method for (a) a patch exhibiting strong growth and (b) a patch exhibiting faint growth. For comparison, image segmentations resulting from a higher threshold and a lower threshold are shown. Using a threshold that is too high cuts off part of the patch, whereas using a threshold that is too low includes parts of the background. In the case of the patch with strong growth, there are two clusters of pixels, one centered at a background intensity of around 0.35 and a lower, wider peak centered at a high intensity just under 0.7. The higher peak results from the pixels containing the yeast patch. Otsu's method produces a threshold roughly half-way between these two peaks. In the case of the poorly growing patch, we no longer observe two distint peaks in the intensity histogram. Under these conditions, intensity thresholding with Otsu's method is not sufficient to reliably isolate the patch.

Otsu Thresholding

Intensity thresholding is a standard technique for segmenting images. In the simplest form, the user applies a single intensity threshold to separate the pixels of a grayscale image into two classes, foreground and background. Many possible methods for automatically choosing the threshold value exist, generally falling into five categories: histogram shape-based methods, clustering-based methods, entropy-based methods, object attribute-based methods, or spatial methods. In PyPl8, I make use of a simple and widely used automatic method for determining the threshold: Otsu's Method. Otsu's method could be considered a histogram shape or clustering-based technique. In his influential 1979 paper, Otsu proposed determining the optimal threshold for separating a given set of pixels by minimizing intra-class intensity variance, or equivalently, by maximizing inter-class variance [135]. This is actually equivalent to a globally optimal k-means clustering with 2 clusters performed on the intensity histogram. The k-means clustering method will be discussed in section 4.3.1, so for now we will consider the method from the histogram shape perspective.

In Otsu's method, we suppose that the pixels in a gray-scale image are split in L intensity bins. Denote the number of pixels in intensity bin i by n_i, so the total number of pixels $N = n_1 + n_2 + \cdots + n_L$. The intensity histogram can be normalized and viewed as a probability distribution. Then we consider splitting the pixels into two classes, C_0 and C_1, at a threshold value of k. In other words C_0 includes the pixels at intensity levels $[1, 2, ..., k]$ and C_1 includes the pixels at intensity levels $[k+1, k+2, ..., L-1, L]$. The probability of a pixel belonging to each class is given by summing over the intensity levels

$$\omega_0(k) = \mathbf{Pr}(C_0) = \sum_{i=1}^{k} p_i \tag{1}$$

and

$$\omega_1(k) = \mathbf{Pr}(C_1) = \sum_{i=k+1}^{N} p_i \tag{2}$$

respectively, where of course $\omega_0(k) + \omega_1(k) = 1$. So the class mean levels will be

$$\mu_0(k) = \sum_{i=1}^{k} i\mathbf{Pr}(i|C_0) = \sum_{i=1}^{k} ip_i/\omega_0(k) \tag{3}$$

and

$$\mu_1(k) = \sum_{i=k+1}^{N} i\mathbf{Pr}(i|C_1) = \sum_{i=k+1}^{N} ip_i/\omega_1(k) \tag{4}$$

And the class variances are given by

$$\sigma_0^2(k) = \sum_{i=1}^{k}(i-\mu_0)^2\mathbf{Pr}(i|C_0) = \sum_{i=1}^{k}(i-\mu_0)^2 p_i/\omega_0(k) \tag{5}$$

and

$$\sigma_1^2(k) = \sum_{i=k+1}^{N}(i-\mu_0)^2\mathbf{Pr}(i|C_1) = \sum_{i=k+1}^{N}(i-\mu_1)^2 p_i/\omega_1(k) \tag{6}$$

respectively. In order to evaluate the "goodness" of a threshold, Otsu introduces a weighted sum of the within-class variances:

$$\sigma_w^2(k) = \omega_0(k)\sigma_0^2(k) + \omega_1(k)\sigma_1^2(k) \tag{7}$$

The idea behind Otsu thresholding is that minimizing this intraclass variance, $\sigma_w^2(k)$, simultaneously maximizes the between class variance for the image segmentation. Because we expect well-thresholded classes to be separated in gray levels, a threshold giving the best separation of classes in gray levels would be the best threshold.

Another important note on intensity thresholding is the choice of global vs local thresholding. In global thresholding, one threshold value is calculated using all image pixels and applied across the full image. In local, or adaptive, thresholding, a different threshold is applied to different parts of the image, based on the local information of the pixels. This can be advantageous when handling images with inconsistent lighting, or if the objects of interest vary in intensity in different parts of the image.

In figure 4.6, we illustrate the output of Otsu thresholding for two grayscale tiles. In the case of a colony with strong growth, there are a wide range of threshold values that would separate the patch from the background adequately. Otsu's threshold returns the value, τ, roughly halfway between the peak on the intensity histogram from the patch and the peak from the background agar (Panel a). In contrast, choosing a lower threshold (green) can result in a noisy patch edge that includes part of the background agar. Choosing a higher threshold (red) can lower the sensitivity too much, causing some of the patch to be lost. In the case of a patch with nearly null growth, within patch pixels and background pixels

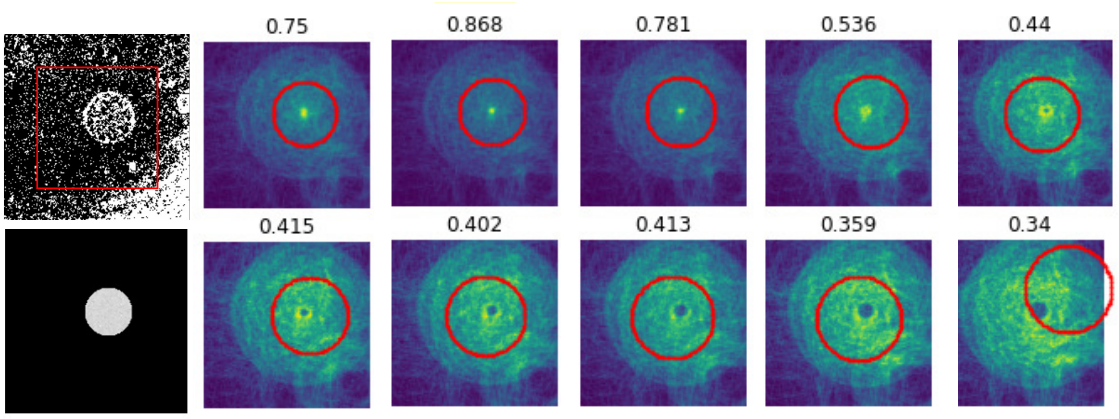

Figure 4.7: An illustration of the Circular Hough Transform applied to a binarized image of a faintly growing patch. The top left panel shows the region of the binarized tile that is used as input into the CHT. The panels in color illustrate the CHT for circles of varying radii. The top candidate center for the circle with each radius is shown in red and the corresponding likelihood is printed above the panel. Note that the more yellow a location is, the higher the probability of a circle at that location. In this example the circle of radius 26 pixels has the highest likelihood, at 0.868. The corresponding mask is applied to the grayscale image to produce the segmentation in the bottom left panel.

do not form distinct peaks in the intensity histogram (Panel b). Again choosing a lower threshold includes more of the background and choosing a higher threshold loses part of the colony even though part of the background is included. In this case, intensity thresholding alone cannot return an acceptable segmentation.

Circular Hough Transform

Intensity thresholding identifies regions of solid yeast growth, which show up as high intensity pixels against the relatively dark agar background. However, intensity thresholding fails when faced with weak separation between the item of interest and the background. Thus Otsu-thresholding will fail to capture regions of null-growth on patches in the Funnel Cross Data set. Instead, to capture faintly growing patches, we can exploit the geometry of the

initial position of the cells. The Funnel Cross plates (and similar yeast growth assays) are set up by stamping a thin layer of yeast cells onto the agar surface using a round pin head. Due to the shape of the pin, patches with faint growth will lightly fill in a circle that closely matches the pin location and area. With this knowledge, we transform our goal of image segmentation into a circle detection task. A commonly used method for circle detection in an image is the Circular Hough Transform (CHT).

The Hough transform in its simplest form is a method to detect straight lines but it can also be used to detect circles or ellipses. Based on an input of detected edges, the algorithm robustly identifies circles despite noise or missing points. No complicated mathematical computation is involved in the implementation, just a majority voting scheme tracked in an "acumulator" array. The intuition behind this method is to make an exhaustive search across the pixels in the image, considering each as a candidate center for a circle of a fixed radius. Given a center, radius pair, $((a, b), r)$, the intensities of pixels along the candidate circle they define, $(x-a)^2+(y-b)^2 = r^2$, are summed and the total is assigned as the CHT value for the pixel at the candidate center location. The pixel with the highest value in the transformed image is the most likely location of a circle with that radius. This process can be repeated for a range of possible raddii and then the maximum across both potential centers and potential radii is taken. See Fig. 4.7 for an illustration of the CHT for a faintly growing patch. The top left panel shows the region of the binarized tile that is used as input into the CHT, while the bottom left panel shows the segmentation of the grayscale obtained by using the most likely candidate circle from the CHT as a mask. The panels in color illustrate the CHT of the binarized tile for circles of radius 25-35 pixels. The top candidate circle for each size is overlaid on top of the CHT in red. I used the algorithm implementation from the sci-kit image library, which is based on the general ellipse detection method proposed by Xie et al. [188].

Image Alignment

The agar invasion assay carried out on the YPD plates from the Funnel Cross produced images of washed plates. By comparing the pixel intensity before and after washing, we

can assess the degree to which yeast cells burrowed into the surface of the agar. However, the washed images do not have clearly defined edges along the the footprint of each patch. Thus the area of interest is generally fairly similar to the agar background intensity or even identical to the background, and far from circular. Instead of segmenting these images, we want to apply the masks derived from segmenting the corresponding 72 hour image to the washed images. In order to apply the masks from a different image, we must first align the images so that the regions of interest overlap. Fortunately the edges of the agar plate produce prominent features in the images, so we can take advantage of feature-based image alignment tools for this task. The mathematical concept underlying feature-based image alignment is that of homography. Two images of a scene are related by a homography under two conditions: (1) the two images are that of a plane (e.g. sheet of paper, credit card, surface of an agar plate.) and (2) the two images were acquired by rotating the camera about its optical axis. Since this is true of pictures taken of the same plate using our experimental camera set up, there exists a homography $H \in \mathbb{R}^3$ relating the pixel (x_1, y_1) in the 72 hour image to the pixel (x_2, y_2) in the washed image via

$$\begin{bmatrix} x_1 \\ y_1 \\ 1 \end{bmatrix} = H \begin{bmatrix} x_2 \\ y_2 \\ 1 \end{bmatrix} \tag{8}$$

If we can learn the appropriate homography to match the reference points between the images, then we can to apply it to all the pixels of the input (washed) image. The desired homography will warp the input image such that it is aligned with the reference image. If 4 or more corresponding points in the two images are known, a linear system of equations to find the homography, can be constructed and solved. In our case, the shared reference points come from applying a global threshold to the pairs of images to detect the outline of the agar plate in each. These steps are illustrated for an example pair of plate images in Fig. 4.8.

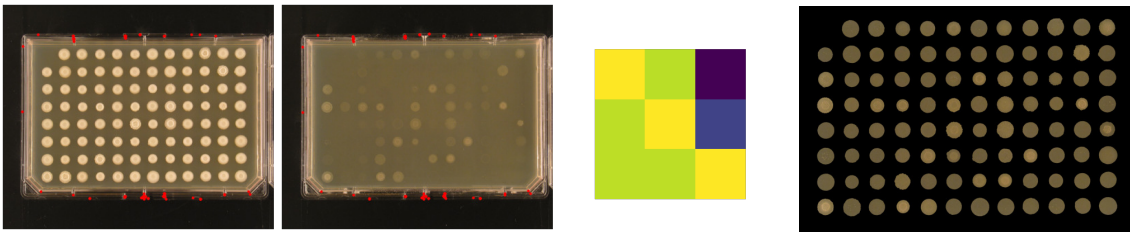

Figure 4.8: Here we illustrate the process of segmenting the hard-wash images from the agar invasion assay. First, reference points (red) are identified that are shared between the reference, 72 hour image (column 1) and the image of the washed plate (column 2). These points cluster along the border of the plate. Next, these pairs of reference images are used to solve for the homography that will align the position of the agar plate in the washed image with the agar plate in the 72 hour image (column 2). Often the shift is very slight. Finally, once the images are aligned, the segmentation from the 72 hour plate is applied to the washed image, isolating the regions of the agar plate that formed the footprint of each patch (column 4).

4.2.3 Algorithm Implementation and Development

Recall that PyPl8 processes images in three steps. First the image is preprocessed to isolate regions of interest containing a single patch. Next each region of interest is segmented using a combination of intensity thresholding and circle detection. Finally, phenotypic features are extracted from the segmented tiles. Here we describe how these steps are accomplished using the techniques surveyed in the previous section.

Preprocessing

With PyPl8, each plate image is first cropped into 96 regions of interest (ROIs) centered at the pin locations, with each region containing a single patch. This pre-processing step is crucial for accurate segmentation of the diverse growth phenotypes present on a single plate because universal segmentation methods do not capture reduced growth phenotypes. In the current version of PyPl8 there are three possible methods available for initiating this

cropping step. Two options solicit user feedback to identify a reference location, the center of the patch in the upper left corner of the plate, either through clicking on the image or entering the location in terms of pixels. Given this reference point and set parameters about the dimensions of the array of patches bounding boxes can be placed around the expected location of each region of interest. The alternative version which forgoes user feedback automatically locates the agar plate in the image through a universal thresholding step. Because consistently sized plates are used in these assays in the Dudley lab, locating the edges of the plate can serve as the reference point for placing the array of regions of interest in the photo.

Subsequent steps of the segmentation process are most accurate when the patch is located in the center of the ROI, or tile, so I also incorporated an option to add an auto-adjustment step. If the auto-adjustment option is "on," then after the initial placement of ROIs, the centroid of the intensities of each binarized tile is found and if necessary the tile boundaries are shifted within the image so that it is centered on this centroid. For patches with non-null growth, this effectively centers the tiles on the patch as long as the initial ROI guess contained only background agar and a portion of that patch. If the initial guess is too far off so that the patch is not the largest bright object in the tile, then this option fails. For patches with non-null growth, no object is detected and the patch is instead recentered based on the average readjustments to other tiles in the same row and column. Once these ROIs have been identified, the upper upper left corner of each ROI within the image and the side length are stored. This provides the necessary information to retrieve each patch tile from the grayscale image for segmentation.

For the Funnel Cross images, team members utilized a consistent camera set up to photograph plates, ensuring that the plates were positioned in roughly the same location in each image. Thus roughly the same cropping locations successfully identify the desired ROIs in the majority of images. The additional automated quality control step of detecting plate edges and applying auto-adjustment allowed for automated processing of images containing slightly crooked or offset plates. The handful of cases in which a plate was highly contaminated or quite crooked within the image triggered a flag during pre-processing and these images were then revisited with one of the user-input methods individually. This flag

was raised if the identified crop locations crossed through pixels with high intensity, as we expect the boundaries of the ROIs to lie on the background agar. All together around 2% of plate images were processed with user input.

Segmentation

After preprocessing, the patch area is segmented from the background agar within each ROI using a combination of intensity thresholding and circle detection. By preprocessing the images as described above, segmenting patches with solid growth has become a trivial task in image processing. In these cases we have a bright, continuous object with high contrast against a dark background. Within the Funnel Cross Data Set there is some variation in lighting and agar color across the different plates and media conditions, so we still want to use a customized threshold based on each individual tile. The Otsu threshold provides an efficient and effective means to accomplish this task [135]. Though the threshold sometimes cuts off patch pixels along the boundary of the patches, this region is very narrow, so it is not a huge detriment to sensitivity of the segmentation, and it does so in a predictable and consistent manner. Recall that the results of Otsu thresholding compared to a higher and lower threshold are shown in Figure 4.6. In the top row, observe that a wide range of thresholds would suffice to identify the strongly growing patch. Hand tuning the threshold value τ to each image could produce a more desirable segmentation than Otsu's method, however it is not feasible to take this time for every image in a large data set, so we opt for the reliability and reproducibility of Otsu's method. This reproducibility is key to being able to use the subsequently measured phenotypes to perform quantitative trait locus analysis.

Thresholding may also leave out shadowed regions from within the patch interior. Because we know that patch growth was initiated as a circle and should cover a contiguous region without holes, we are justified in filling in these gaps by applying the morphological operations of closing and filling. These two steps, Otsu thresholding and filling, constitute the intensity-thresholding step of segmenting the bright patch from the dark background. As shown in the second example in Fig. 4.6, if the threshold returned by Otsu's method is very close to the background agar intensity, this indicates that there is not strong separation

Algorithm 1 Segment Grayscale Tile, t

$\tau \leftarrow$ Otsu threshold of t

if $\tau >$ background $+ \mu$ **then**

mask $= 1 \cdot (t > \tau)$

area $= \sum$ mask

end if

if $\tau <=$ background $+ \mu$ OR area $< \pi r_{pin}^2$ **then**

CandidateCenters = center half of t

circle $\leftarrow$ most likely circle from CHT of CandidateCenters $>$ background $+ \mu$ and $r = r_{pin}, ..., r_{pin} + 10$

if Prob(circle) $<$ MinProb **then**

mask $\leftarrow$ zeros

else if $\tau <=$ background $+ \mu$ **then**

mask $\leftarrow$ circle

else

mask $\leftarrow 1 \cdot$ ((mask + circle) > 0)

end if

end if

Return: mask

between the within-patch pixel intensities and the background intensity. These segmentation results will be unreliable because the resulting mask likely contains large regions of the background agar. However, when the Otsu threshold is sufficiently different from the average background agar intensity, the results of Otsu thresholding are considered meaningful. Futhermore, if the resulting patch area is large enough, the segmentation of this tile is considered complete. Examples of patches that fall into this category are shown in rows 1-2 of Fig. 4.9.

If the threshold returned by Otsu's method is low, close to the average background agar intensity, this indicates potential null growth. Alternatively, if Otsu threshold is high but the detected patch area is small, this indicates that potentially only a portion of the patch

was captured by intensity thresholding. In both of these cases, the segmentation algorithm proceeds by applying a circle detection step. Circle detection was performed by binarizing the image with an adjusted-mean threshold, and applying the Circular Hough transform with a minimum radius equal to the initial pin radius [188]. This exploits the geometry of the pinned cells to capture any regions of patches where growth is too faint to be detected with intensity thresholding. Recall that example results of the CHT for a range of potential radii shown in Fig. 4.7. When the circle radius is too small, votes will be split across multiple candidate centers. When the circle radius is too large, no possible center will fully fill out the perimeter of the circle, so the candidate circles will have lower likelihood. If the results of the intensity threshold were considered significant, these were combined with the detected circle to form the patch mask. Examples of this type of growth are shown in as shown in rows 3 and 4 of Fig. 4.9. However, if the Otsu threshold was similar to the background agar intensity, then the intensity thresholding was discarded and the detected circle alone was used as the patch mask. This final case is illustrated in rows 5 and 6 of Fig. 4.9.

An additional check was performed to rule out unreliable results which may have arisen from a blank or contaminated ROI. If the mean intensity of the masked patch area was too low or the likelihood of the detected circle was too low, then the patch was determined to be empty and assigned a value of N/A. This errs on the side of labeling empty patches with a circle since we had the plate maps available to allow us to ignore false positives.

These segmentation steps were implemented as outlined in Algorithm 1 in python using functions from sci-kit image. The specific parameters used to process the Funnel Cross data set were $\mu = 0.035$, $r_{pin} = 28$, and MinProb= 0.43. These values could be adjusted for different experiments. The background agar value was calculated for each plate image separately by averaging over a small sample of pixels from the corner of all 96 ROIs in that image. Updating the background value for each image was important because the 10 different conditions varied slightly in color.

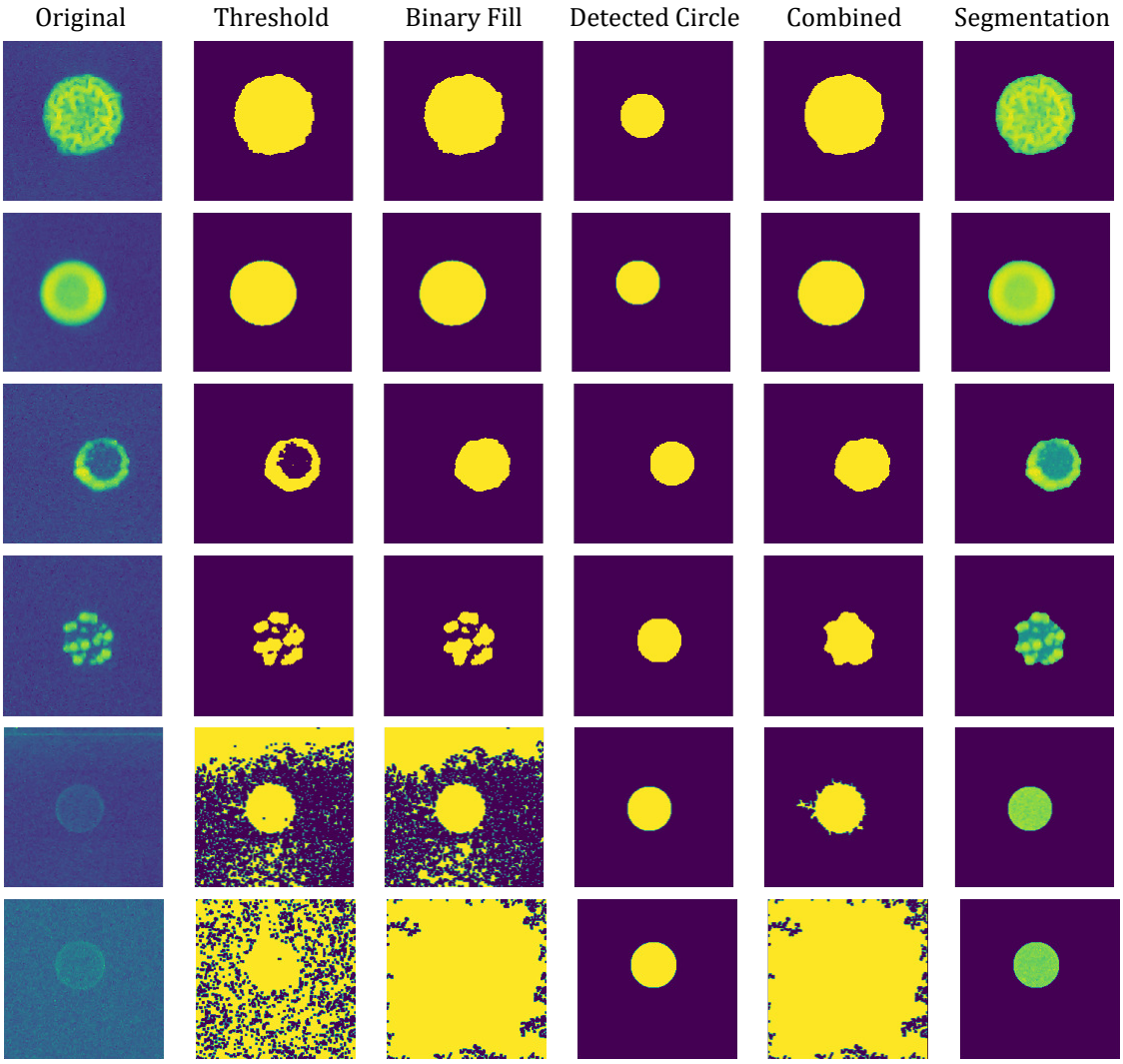

Figure 4.9: The steps of the segmentation algorithm as well as final results are illustrated on an example of each type of growth. In the case of strongly growing colonies, whether smooth or textured, the mask that results from thresholding and performing a binary fill is used. In the cases of uneven growth, including the donut and the papillation patterns, the thresholding and circle detection results are combined. In the case of null growth, the thresholding results are discarded and the detected circle alone is used.

Feature Extraction

Once each tile is segmented, the tiles and their masks encoding the patch area within the tile can be used to extract the desired quantitative phenotypes from each patch. Patch area is simply the sum of the number of pixels in the patch mask. The average gray scale value of the patch is equal to the sum of the intensities of the pixels in the patch divided by its area. These two values provide estimates of the growth or fitness of each yeast strain on a given condition.

As noted, the washed plate images were handled differently. These images were aligned with the corresponding 72 hour image by identifying common features and computing the appropriate homography using functions from the python image processing library, OpenCV. Once the images were aligned, the masks from the 72 hour segmentation were applied to the washed images to isolate the appropriate patch footprints. The sum of the pixel intensities within the patch footprint was computed and saved.

4.3 Task 2: Texture Quantification and Clustering

The Dudley Lab is interested in using QTL analysis to uncover the genetic architecture of non-growth phenotypes in the Yeast Funnel Cross Data set. In the previous section, I already noted how agar invasion scores were calculated by taking the average intensity of the region of the agar that contained the patch prior to washing. These scores constitute one non-growth phenotype. Another interesting axis of natural variation captured in the population is the ability to develop a wrinkled, complex surface structure. In order to use the sophisticated quantitative genetic tools at their disposal to explore the underlying genetic architecture of this trait, the Dudley Lab requires a quantitative and/or categorical score encoding how "fluffy" each patch is. In this section I first explain the raw texture features that were extracted from each segmented patch. Then I explain how these features were further processed using Principal Component Analysis to allow for identification of fluffy patches. I illustrate the effectiveness of this score with the results of clustering in the data set.

4.3.1 Theoretical Background

I utilized several common methods from data science to cluster the Yeast Funnel Cross data based on non-growth phenotypes. Namely, uniform local binary pattern transforms and sobel edge detection serve as raw texture features. Further preprocessing involved normalizing the non-growth features using outlier detection via computing an elliptic envelope and applying Principal Component Analysis for dimension reduction. I ultimately used k-means to cluster the preprocessed texture features. Here I provide a brief introduction to these methods for the interested reader.

Local Binary Patterns

The Local Binary Pattern (LBP) transform is an efficient texture categorization operator first introduced by Ojala et al. [134]. This local representation of texture is constructed by comparing each pixel with its surrounding neighborhood of pixel values. When surrounding pixels are all greater or all less than the reference pixel, that image region is flat (i.e. featureless). When there are continuous stretches of pixels that are all greater or all lesser than the reference pixel, the pattern is considered "uniform." Such patterns can be interpreted as corners or edges. If pixels switch back-and-forth between greater and lesser than the reference pixel, the pattern is considered "non-uniform". One advantage of uniform LBPs as a texture descriptor is that they are rotation invariant. Because the texture of an object does not change with rotation, this is a desirable property for limiting the size of the feature vector encoding textures. To apply the LBP transform, first the image must be converted to gray scale. Next a neighborhood radius of r pixels is selected and the number of regions to partition this neighborhood into, n, is determined. This defines the scale of pattern that you will be looking for. A LBP value is then calculated for each pixel as follows

- For each bin of neighbors that have distance r from the reference pixel, compute the average intensity. Compare the reference pixel to these bin averages, ordered in a circle.

- If the center pixel's value is greater than the neighbor bin's value record a "0" in that

location. Otherwise record a "1."

- Convert this binary sequence to an LBP label based on the number of consecutive "0"s and "1"s

Finally, when an LBP value has been assigned to each pixel in an image, these can be stored in an output array of 2D with the same dimensions as the input grayscale image. Often the numbers of pixels with each LBP label are saved as a vector, which may or may not be normalized. This vector serves as a unique texture descriptor for the full image. Applying uniform LBPs to characterize colony texture has been demonstrated convincingly by Goldschmidt et al.[57].

Edge Detection with the Sobel Operator

Widely used for edge detection in image processing, the sobel operator convolves a center difference template with an image to approximate the gradient of pixel intensity. The method was introduced by Sobel and Feldman at a talk at Stanford Artificial Intelligence Laboratory in 1968*. The Sobel operator is a discrete differentiation operator, computing an approximation of the gradient of the image intensity at each pixel location. For a gray scale image, A, two convolution matrices are defined, one in the horizontal and one in the vertical direction

$$G_x = \begin{bmatrix} -1 & 0 & 1 \\ -2 & 0 & 2 \\ -1 & 0 & 1 \end{bmatrix} * A \qquad \text{and} \qquad G_y = \begin{bmatrix} 1 & 2 & 1 \\ 0 & 0 & 0 \\ -1 & -2 & -1 \end{bmatrix} * A.$$

These can be combined to approximate the gradient of the image

$$G = \sqrt{G_x^2 + G_y^2}. \tag{9}$$

By convolving the image with small, separable, integer-valued filters, the Sobel transform remains relatively inexpensive computationally. The user trades this computational efficiency

*Sobel, I., Feldman, G., "A 3x3 Isotropic Gradient Operator for Image Processing", presented at the Stanford Artificial Intelligence Project (SAIL) in 1968

for a fairly crude approximation to the gradient that does not accurately capture high frequency variations in an image; however, the Sobel Transform is still of sufficient quality to be of practical use in many applications[94]. Applied sequentially after Gaussian blurring, sobel edge detection serves our purpose of estimating the fraction of the patch occupied by edges. We do not require a precise identification of edges for further processing.

When processing the yeast funnel cross data set, I apply the sobel operator to an image twice, actually approximating the second derivative of the intensity, i.e. the rate of change in the intensity gradient. This highlights the sides of ridges within a patch which coincide with regions of rapid change in the gradient.

K-means clustering

Unsupervised learning methods enable exploration and pattern discovery in data. Within the funnel cross phenotype data, we aimed to uncover groups or clusters of strains that display similar texture phenotypes. Assessing the success of a clustering method is an inherently ambiguous task, but one heuristic generally accepted posits that a good clustering minimizes intraclass variance while maximizing interclass variance. K-means clustering, a commonly used unsupervised clustering method, reflects this heuristic by attempting to minimize the total within-cluster distances between each data point and a representative prototype. The earliest mention of k-Means clustering algorithm seems to be a 1967 paper by MacQueeen in which he introduced a partition-based cluster analysis method [109]. Given a number of clusters, k, the k-Means algorithm aims to minimize the within-cluster sum-of-squares criterion, that is the sum of distances between the data points and their assigned cluster centroid. Consider data points $x \in X$ with $|X| = N$ and cluster centroids $c_1, ..., c_k$. These centroids induce partition P on the data, such that $P(x_i) = j$ if x is the closest to centroid c_j. The goal of k-means is to solve the optimization problem

$$\arg\max_{c,P} \sum_{i=1}^{N} ||x_i - c_{P(x_i)}||^2 \tag{10}$$

The algorithm for solving Eq. 10, known as Loyd's algorithm, partitions the feature-space into regions for each group through an iterative scheme. First k centroids are identified,

perhaps randomly to begin with. Next, the remaining data points are assigned to the cluster corresponding to their nearest centroid. A new centroid is then calculated for each group and the process repeats until a stopping criterion is satisfied. Stopping criteria for convergence would be either that points are no longer switching groups, or that the centroids are no longer changing upon iteration. A drawback of k-means is the tendency to fall in local minima. It can be useful to restart the method several times to ensure representative clusters are being identified. In general, k-means works well for data with even cluster sizes, flat geometry, and only a moderate number of clusters. Minimizing the within-cluster sum-of-squares criterion makes the assumption that clusters are convex and isotropic, which is not always the case, hence k-means responds poorly to elongated clusters, or manifolds with irregular shapes. Another potential pitfall is the dependence on distance. In high-dimensional spaces, Euclidean distances tend to become inflated making the minimization problem ill-conditioned. Running a dimensionality reduction algorithm such as Principal component analysis (PCA) prior to k-means clustering can alleviate this problem and speed up the computations [41].

Outlier Detection

Outlier detection poses another unsupervised learning challenge in data analysis. In outlier detection you receive a set of data points and try to flag samples that deviate from the pattern exhibited by the bulk of the data. In this work, we make use of the fast minimum covariance determinant (MCD) method of Rousseeuw et al. [157] to fit an elliptic envelope to the "inlier" data. This approach is a highly robust estimator of multivariate location and scatter, working well on data with an underlying gaussian distribution. The objective is to find h observations (out of n) whose covariance matrix has the lowest determinant. The MCD method identifies these h observations and returns the ellipse defined by their covariances. Data points inside this elliptical envelope are inliers, whereas data points outside this elliptical envelope are labeled outliers. The amount of contamination of the data set, i.e. the proportion of outliers in the data set, comes in as a parameter of the algorithm. Outlier detection from covariance estimation may break or not perform well in

high-dimensional settings, so again dimensionality reduction prior to outlier detection may be necessary. This particular method of fitting an elliptic envelope to the data works best on normally distributed data.

In the funnel cross data set, a large fraction of the patches follow a normal distribution around an average value, but a substantial number of outliers skew towards higher feature values. Using an elliptic envelope we can identify the majority faction of patches and normalize features using these typical trends rather than contaminating our model with the abnormal examples.

Principal Component Analysis

Principal Component Analysis (PCA) is widely used across many applications. This matrix decomposition makes patterns easier to observe and visualize in a data set by applying the optimal rotation and re-weighting of features in a data matrix to maximize variance while minimizing covariance. The process takes a number of possibly correlated variables, and converts them to a set of linearly uncorrelated, or orthogonal, variables called principal components. Hopefully, most of the variance in the system can be captured by a smaller number of principal components than the number of original variables in the system, thereby reducing the order of the feature space. Geometrically, this process can be thought of as fitting an n-dimensional ellipsoid to the n sets of data, where some of the dimensions of the ellipsoid will be much more significant than others. These ideas date back to the work of one of the father's of statistics, Karl Pearson [144] and were further developed by Hotelling several decade later, who introduced the language of principal components [69].

The starting point for PCA in data analysis is an $m \times n$ data matrix $\mathbf{X}$, with m different features collected from n sources of data. PCA can be a helpful pre-processing step for further unsupervised or supervised learning methods, because projecting onto the PCA modes can reduce noise and redundancy in the data. The steps of PCA are as follows. First, the mean of each feature data matrix, X, is calculated, $\bar{X}$. Next, the covariance matrix is computed

$$C_X = \frac{1}{n-1}(\mathbf{X} - \bar{\mathbf{X}})(\mathbf{X} - \bar{\mathbf{X}})^{\mathbf{T}}. \tag{11}$$

Note that the covariance matrix C_X is a square, symmetric $m \times m$ matrix whose diagonal entries constitute the variance of particular features. The off-diagonal terms contain the covariances between features, thus C_X captures the correlations between all possible pairs of measurements. Large off-diagonal terms indicate redundancy amongst features, while large diagonal elements indicate a feature with high variance which is assumed to contain the most interesting descriptors of the system. So by minimizing the off diagonals and maximizing the diagonals, i.e. diagonalizing the covariance matrix, we will identify the most important dimensions of the system and eliminate redundancy simultaneously. Recall that all symmetric positive definite matrices are diagonalizable and have eigendecomposition,

$$C_X = U\Lambda U^* \tag{12}$$

Rather than explicitly forming the covariance matrix and computing the eigendecompostion to obtain the principal components, a powerful linear algebraic tool for diagonalizing the covariance matrix is simply taking the singular value decomposition (SVD) of the de-meaned data matrix.

$$X - \bar{X} = U\Sigma V^* \tag{13}$$

The left singular vectors, or the columns of U in Eq. 13, are the principal components of the data.

4.3.2 Algorithm Implementation and Development

After the plate images were segmented and growth features were estimated as outlined in section 4.2.3, the raw texture features including internal edges, and local binary patterns were quantified.

I computed the internal edge score by first blurring each unsegmented gray scale tile slightly by convolving the image with a gaussian filter of size 7×7, G_7. Then on the softened image I applied the sobel operator twice, choosing the standard 3×3 filter. I then applied the corresponding segmenation mask to the transformed image and summed over the pixels in the patch area, saving this sum as the internal edge score. That is, the raw

edge score was computed as

$$E_{internal} = \sum_{i \in patch} G(G(G_7 * t)) \tag{14}$$

where G is the sobel operator defined in Eq. 9. Blurring and the sobel transform were applied using implementations from sci-kit image. These particular sizes of convolution templates were chosen after trial and error to balance computational efficiency with the desired results. Note that it was important to apply the sobel transform to the original unsegmented image, then apply the mask afterwards. If the mask is applied first, the sharp boundaries created by segmentation produced excessive artifacts along the patch edges.

I computed the uniform local binary pattern transform of the image, as described in the previous section, with a radius of $r = 10$ pixels and neighboring pixels quantized into 8 bins. I used the efficient implementation included in the sci-kit image library. The resulting feature vector is a list of the number of pixels that fall into the 9 possible uniform patterns (corresponding to pixels from flat areas, edges, and corners) and the 10th non-uniform pattern. I then normalized this list by dividing by the area to get the distribution of pixels in each category.

Before further analysis, I normalized the full set of quantitative feature scores against the patch area. Quantities like the sum of the pixel intensities and the sum over interval edges depend on the number of pixels within the patch, so larger patches have the capacity for larger scores. With the local binary patterns, I had already divided by area, but the distributions may be skewed by the fraction of the patch that lies along the perimeter of the patch and the fraction of the patch that remains influenced by the initial pinning of cells. For all of these texture features, growth will be a confounding factor in downstream analysis if we do not correct for these correlations. To normalize each feature, I first fit an elliptic envelope to the densest 50% of the data points when considering that feature and the area. Then I fit a linear model to the inliers and calculated the residual between this line and each data point. I included the outlier detection step rather than simply fitting a linear model to the full data set underlying genetic variation accounts for most of the outliers. We do not want to reduce this variance, but rather zero out only the standard correlation between area and the feature of interest. After the non-growth traits were normalized against area,

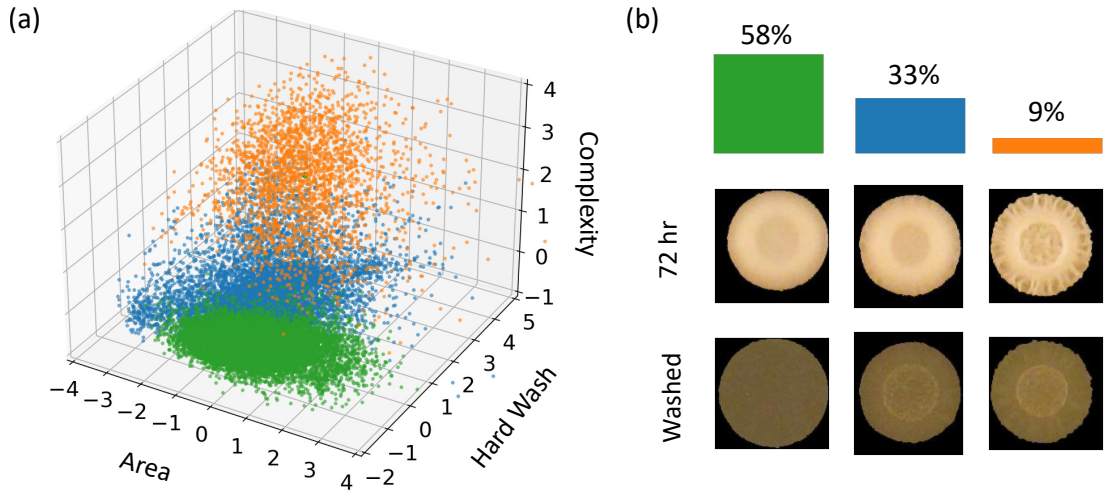

Figure 4.10: Preliminary agglomerative clustering with $n = 3$ identifies a large group that contains mostly smooth, noninvasive patches. The other two groups contain somewhat textured, somewhat invasive patches, and highly textured patches. Here the three groups are plotted on the axis of area, hard wash score and complexity score where the non-area traits have been normalized against their area and all traits have been scaled to have mean zero and standard deviation of one.

every trait was further standardized to have mean zero and a standard deviation of one.

As a first level of clustering, I clustered the texture data from patches grown on YPD into three groups using k-means clustering on the non-local binary pattern features. That is the area, the hard wash score, the internal edge complexity score, and the pixel variance. This preliminary clustering identified a large segment of the population, 58%, the majority of which are neither fluffy nor invading the agar (group 1 (green) in Fig. 4.10). I then applied elliptic envelope outlier detection to this group so that the inliers only include the smooth, non-invasive patches. This pulled out 52% of the patches as smooth and completely non-invasive. Continuing to carry a large number of smooth patches into the next stage of the analysis would limit our ability to learn more nuanced patterns in the interesting textured patches, so I dropped this half of the data points at this stage.

After this preprocessing step, a final texture score was computed. I applied PCA to

the texture features extracted from the 72 hour images for the remaining strains, i.e. the patches in groups 2 and 3 together with the outliers from group 1. The texture features included were the average pixel intensity at 72 hours, the internal edge score at 72 hours, and the 10 local binary patterns. After transforming the data via PCA, I applied k-means clustering with $k = 8$ to the data projected onto the first 5 PCA modes.

4.3.3 Discussion of Results

The analysis pipeline described here produced quantitative scores that reliably and precisely capture two non-growth phenotypes in the Yeast Funnel Cross Data Set: agar invasion and texture complexity, or "fluffiness." These scores will enable team members to perform linkage mapping for non-growth traits within the Yeast Funnel Cross data set, as has already successfully been performed with the growth data. To determine pattern complexity, we can use the coefficient of the patches along the first principal component from PCA on the textured features of the morphologically interesting subset of patches. Second, as a quantitative score for agar invasion, we can use the normalized sum of the pixel intensities in the patch footprint from the hard wash images.

Examining representative examples we observe that the raw texture features capture the relative smoothness vs. fluffiness of each patch. Large, smooth patches do not have pronounced internal edges, and so their area-normalized internal structure score is low (Fig. 4.11a row 1). In contrast,the interior of a highly textured patch is filled with ridges, yielding a high internal structure score (Fig. 4.11a row 4). Though the internal structure score is reproducible and clearly very informative, it does not provide a clean, ordered translation between what an expert views as complexity and a continuous quantitative trait. There is more than one way to be fluffy, and many patches actually display multiple textures as they grow out radially from the initial pin location. Rows 2 and 3 of Fig. 4.11a, illustrate two alternative growth patterns: a bumpy texture and a patch that is relatively smooth in the center, but deeply ridged on the edges. These two patches have intermediate structure scores, but the ordering of them may not reflect the relative levels of complexity in their texture. Hence, the internal structure score serves as a useful benchmark to threshold out

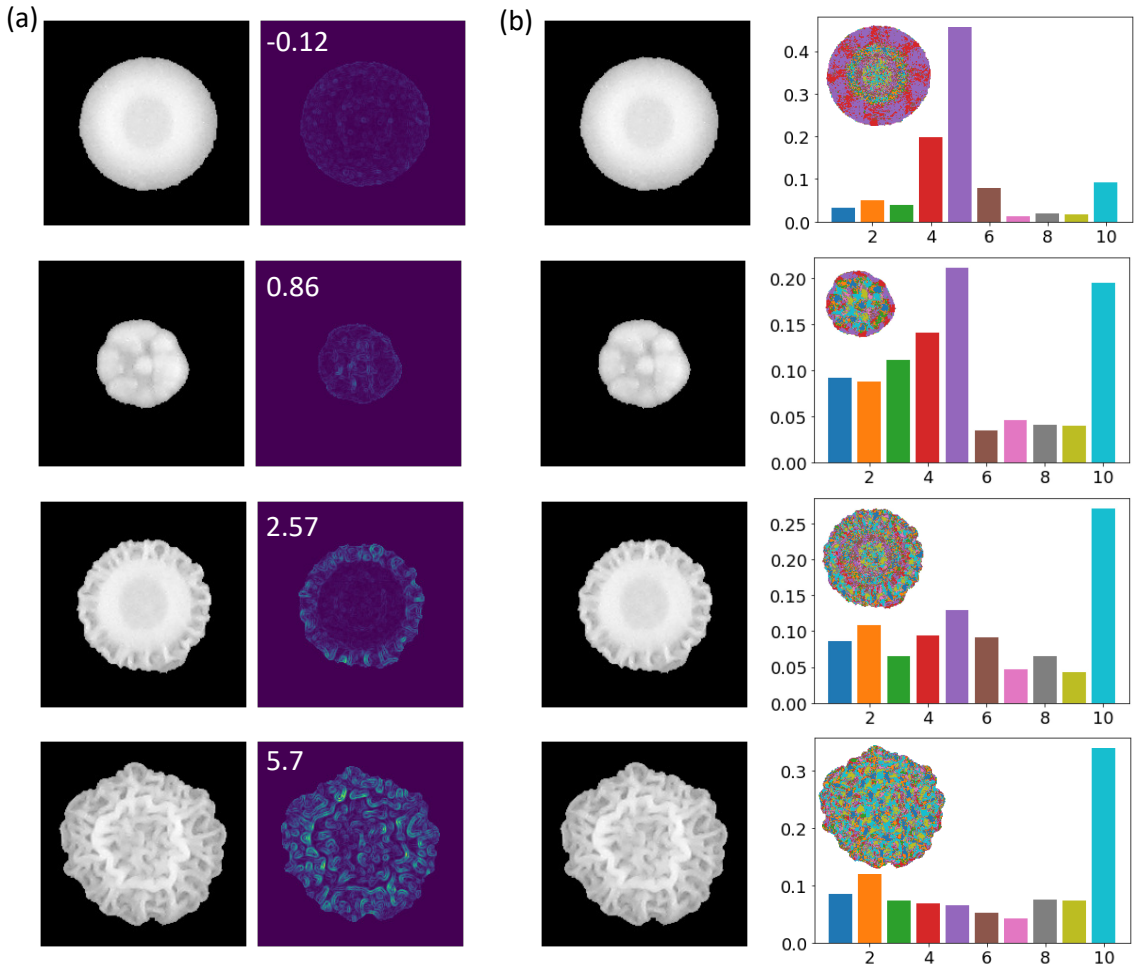

Figure 4.11: Here we illustrate both measures of texture for a variety of growth patterns. (a) The first column shows the grayscale version of the segmented colony and the second column shows the result of applying a sobel filter to the image twice (estimating the second derivative) to pick out edges on the patch. The internal edge complexity score was calculating by summing over the pixels after this transfom and normalizing against the area. (b) The uniform local binary pattern transform was also applied to each segmented image. In the second column we color the pixels in each patch based on it's local binary pattern and chart the distribution of LBPs on the patch with matching colors.

smooth patches, i.e. provides a categorical label. However, it does not provide a quantitative score for fluffiness as a continuous trait. This motivated further feature engineering.

Uniform local binary patterns clearly capture meaningful differences in patch texture. The LBP profiles of smooth patches are generally dominated by the middle categories, i.e. groups 4 and 5 for the example shown in 4.11 b row 1, where as the non-uniform group, 10, is relatively small. The distribution of LBPs for a fully textured patch looks completely different from a smooth patch. For fluffy patches, generally the non-uniform group, 10, constitutes the highest peak by far, while remaining pixels are uniformly distributed between the other groups. Across all the examples in Fig. 4.11b, observe that a central circle on the patch contributes a non-negligible number of non-uniform (cyan) pixels to the profile. This seems to be an artifact from the initial arrangement of yeast cells resulting from the pin head. Consequently, even though the patch in row 3 of 4.11b appears to the eye to have large smooth regions in the center, only a small ring of pixels are classified in groups 4 and 6. The the pin influence obscures a large portion of the patch that appears smooth, the LBP profile still reflects this mixed texture. Follow-up experiments in which strains are grown as colonies initiated from a single cell, rather than patches initiated from a lawn of cells will allow for more precise texture quantification.

These raw texture features are descriptive, but no single trait provides the axis of variation that experts in the Dudley lab were interested in capturing. Applying PCA to the texture features of the morphologically interesting group of strains takes the optimal linear combination of these raw features to reflect the maximal variance in the group. The first principal component has a high positive weight for the internal edge feature as well as high positive weights for the lowest LBP patterns (flat areas) and the highest LBP patterns (nonuniform), and significant negative weights for LBPs 4 and 5 (Fig. 4.12a). These are the same defining features observed differentiating the smooth patch from the other patches in Fig. 4.11. The second principal component has significant negative weights on LBPs 3, 6 and 7. Visualizing the images of patches with the highest vs. the lowest scores for PC2, this feature score appears to reflect the extent to which patch texture is dominated by waves that fan out radially from the center of the patch (low scores) vs. a more randomly distributed pattern. At small but not the lowest values of PC1 and high values of PC2 we have

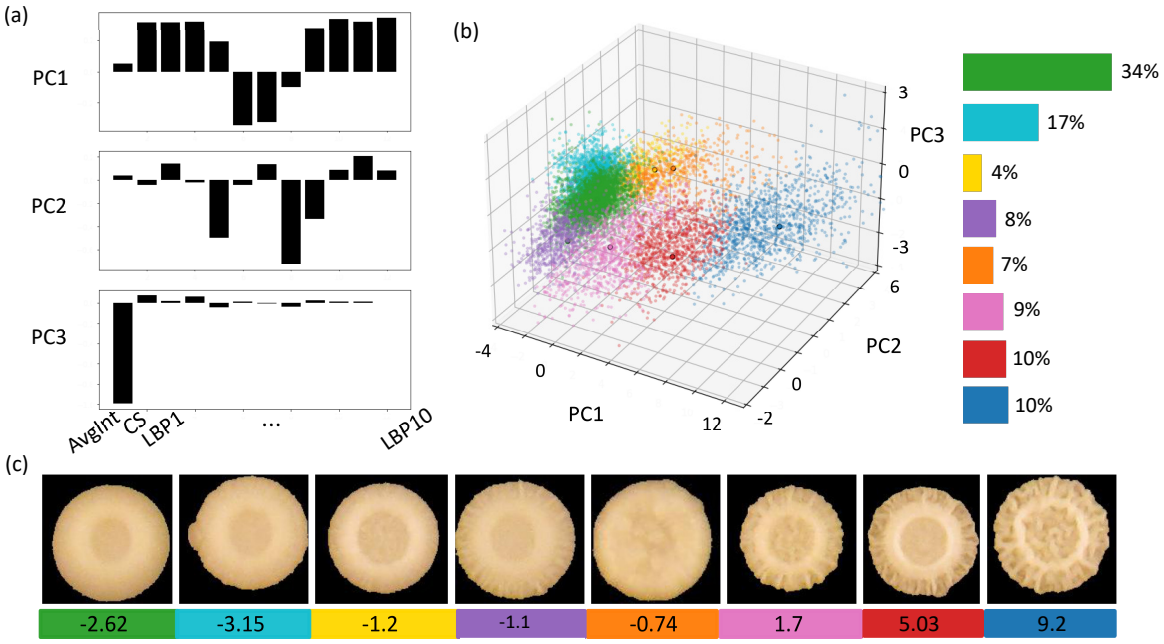

Figure 4.12: The patches from the textured and/or invasive groups from round one of clustering are further analyzed based on their texture features. PCA was used to orthogonalize the average intensity, internal complexity score, and ten local binary pattern scores. The coefficients on each measured feature that constitute the first three PCA modes are shown in panel (a). K-means clustering was applied to the PCA projection of the data with $k = 8$. The distribution of patches across clusters is reported and the patch that is closest to the centroid of each cluster is shown in (c). Note that the representative patches have been reordered from the smallest PC1 value to the largest PC1 value. From examining representative samples from each group, it is clear that PC1 reflects an excellent measure of texture variation.

a subset of patches that appear bumpy across their whole surface (orange group). Whereas at similar values of PC1 but the lowest values of PC2 we see patches that are smooth in the middle with a dimple from the initial pin location and starting to ruffle along the edges (purple group). Similarly, as we move up the branch of the most textured patches (pink, red, and blue groups), the scores for both PC1 and PC2 increase as the ridges become more pronounces and grow in random directions across the patch. The third principal component is heavily dominated by the average intensity score. The fact that this has been singled out from the other texture features, and clusters are largely based on the first two principal components indicates that complex pattern growth on YPD is independent of the average intensity (Fig. 4.12b). Further investigation shows that the highest scores along this dimension distinguish the green group of smooth patches from the cyan group of smooth patches. These two groups both have low pattern complexity.

The rotation and rescaling of features through PCA combines the normalized measured texture features in such a way that the a patch's score along the first principal component reflects it's complexity very well. Upon k-means clustering with $k = 8$, the groups primarily bin the data along the first principal component (Fig. 4.12b). Reordering the groups according to the centroid's PC1 score and visualizing the patch closest to the centroid of each group, we see a progression from smooth patches at negative values of PC1 up to highly textured patches for large positive values of PC1 (Fig. 4.12c). Besides visualising the centroid, we also inspected the inliers from each group to establish the characteristic growth patterns, confirming that these are indeed good representative images. The green and cyan groups of patches appear smooth to the expert eye. Projecting the inliers from the smooth group in the first round of clustering onto these same PCA features lands them in roughly the same region of feature space occupied by the green group.

Normalizing the hard wash scores against the area, produces a clean quantitative score for agar invasion. Patches with a low hard wash score leave little to no trace on the agar surface, whereas patches with the highest scores are bright enough to be detected on their own with intensity thresholding (Fig. 4.13). In the standardized hardwash score, the mean of the full data set is 0 shown in gray in the plots in Fig. 4.13. The distribution has a large tail towards higher scores, though the majority (over 50%) had little to no invasion. When

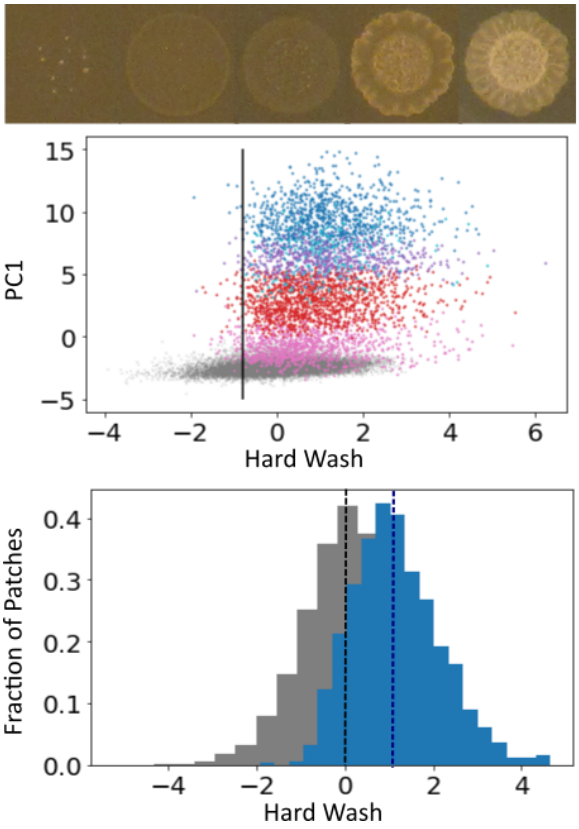

Figure 4.13: The distribution of agar invasion scores following the hard wash for patches that passed the first level of clustering has a large tail skewing towards larger values. From visual inspection, of washed patches with low to high scores from left to right, we can see that the feature is clearly indicative of a continuous phenotype. The blue group from level two of clustering is plotted in blue on the histogram. The highly complex patches have a higher mean agar invasion score than the population in general.

we consider the distribution of hard wash scores both within and across the 8 clusters identified in the second round of texture clustering, we see that highly textured patches have a higher mean hard wash score than the general population (Fig. 4.13, bottom row). Plotting PC1 against the hard wash scores demonstrates a higher floor for the hard wash score of fluffy strains compared to the population at large. It appears that fluffy strains are a subset of invasive strains, i.e., a strain may be highly invasive and not fluffy, but a strain will not be fluffy without having a non-trivial agar invasion score.

Preliminary linkage mapping with these traits produces a strong peak at FLO11, a well-known flocculin that enables yeast cells to form chains. Further analysis will be performed to try to elucidate more nuanced details of the mechanisms of invasion and texture development. In particular, it will be interesting to compare the overlap between strains' ability to invade the agar or develop a biofilm like texture and drug resistance, as captured by the growth scores on caspofungin and fluconazole. In addition to the genetic analysis that may

be performed with this particular data set, the scores quantifying patch texture identify strains of interest for further experimentation. It would not be feasible to collect careful time-course imaging of the growth of all 11,500 strains in the funnel cross library. However, through the two levels of clustering, we have narrowed down the most morphologically interesting patches to 23% of the strains in the full Funnel Cross Data set. These candidates could be studied in detail with more sophisticated imaging technology.

4.4 Code Availability

Interested readers can install the PyPl8 image analyis package from PyPI, using pip [138]. You can also visit the github page to access the source code. Use case examples and detailed documentation are also available on the github page [137].

Chapter 5

CONCLUSION

In this thesis, I have presented three case studies applying mathematical methods to gain insight into the collective behavior of cellular systems. This entailed merging tools from ordinary differential equations and data science to tailor models to each setting.

I started with the idealized theoretical setting of networked oscillators, where an abundance of perfect synthetic "data" allowed me to develop a fully data-driven approach to multi-scale model discovery. The approach presented in Chapter 2 built on related methods that have shown great success on physical systems. However, the need for high fidelity time series measurements in order to accurately estimate derivatives hampers their broad deployment in biology. To overcome this challenge from the methods standpoint, numerous extensions and robustifications are under development that bring SINDy closer to being ready for action in the wild. Simultaneously new technologies are changing the game when it comes to time series data in biology. I am excited to continue working in the field of biological modeling as the progress on these fronts rapidly converges.

In Chapter 3, I posed questions about CAR T-cell therapy in oncology. Because this is a novel immunotherapy, very limited data is available. However, waiting for more data to be published before building models would preclude us from influencing the trends of ongoing trials and current clinical practice. Insight into experimental design would be valuable now during drug development, arguably more so than when the treatment becomes widely available. In order to try to compare refinements to treatment strategies with the currently available data, we took a classical modeling approach, carefully selecting functional forms and deriving parameters from experiments and previous literature. Although these may not be the "best" models for CAR T-cell therapy, they serve a useful purpose, allowing us to compare treatment plans and draw conclusions based on the qualitative results. As we collect more data on the movement of CAR T-cells in the body, we will be able to iterate

on and improve these models. The use of CAR T-cell technology to treat other diseases outside of oncology is also underway. There will be demand for CAR T-cell models in these contexts too.

In the final chapter, I applied methods from data science to quantify the complexity of patterns formed by yeast colonies in the ground-breaking Yeast Funnel Cross Data Set. I introduced the core algorithm behind PyPl8, an open source python package I have made available for automated and robust image analysis. This tool has already served as a crucial link in the chain to producing insights into the genetic architecture of complex traits using the Funnel Cross mapping population. A natural next step is moving forward with mapping the genetic origins of the textured colony traits, as well as exploring how these phenotypes overlap with drug resistance. Though a far cry from building a dynamical model, this body of work sits at the origin of an exciting path towards a mechanistic understanding pattern formation in yeast biofilms. Working with real biological data is challenging and takes time. By laying the groundwork of image processing and feature quantification from the 3 time points in the current data, I set the first route marker for future work. With the classification information from these static measurements, the Dudley Lab is poised to collect highly resolved time series imaging of the development of textured strains. This is the level of quality in data that will make model discovery feasible in biological systems.

The macroscopic behaviors of complex cellular communities constitute life as we know it. From sub-cellular processes up through entire ecosystems, biological systems are inherently multi-scale. Studying systems spanning the level of individual cells to populations of cells is a particularly exciting level to focus on at this moment, as the frontiers of single-cell time series data collection and data-driven model selection converge. The awe-inspiring intricacies and nuances of biological systems can make life seem precarious, and in the midst of a global pandemic, we are painfully aware of the fragility of life. However, simultaneously, we can also be amazed by it's stability and resilience. After all, in a chaotic and changing environment, facing constant perturbation, living organisms continue to exist and flourish. We have to be pretty stable! So as scientists and mathematicians, what do we do with this world of complexity? We build a model and learn something new.

BIBLIOGRAPHY

[1] Prasad S Adusumilli, Leonid Cherkassky, Jonathan Villena-Vargas, Christos Colovos, Elliot Servais, Jason Plotkin, David R Jones, and Michel Sadelain. Regional delivery of mesothelin-targeted car t cell therapy generates potent and long-lasting cd4-dependent tumor immunity. *Science translational medicine*, 6(261):261ra151–261ra151, 2014.

[2] Hirotugu Akaike. Factor analysis and aic. In *Selected papers of hirotugu akaike*, pages 371–386. Springer, 1987.

[3] Francesco Alderisio, Benoît G Bardy, and Mario Di Bernardo. Entrainment and synchronization in networks of rayleigh–van der pol oscillators with diffusive and haken–kelso–bunz couplings. *Biological cybernetics*, 110(2):151–169, 2016.

[4] Hilde Almåsbak, Tanja Aarvak, and Mohan C Vemuri. Car t cell therapy: a game changer in cancer treatment. *Journal of Immunology Research*, 2016, 2016.

[5] Carl M Bender and Steven A Orszag. *Advanced mathematical methods for scientists and engineers I: Asymptotic methods and perturbation theory*. Springer Science & Business Media, 2013.

[6] Peter Benner, Serkan Gugercin, and Karen Willcox. A survey of projection-based model reduction methods for parametric dynamical systems. *SIAM review*, 57(4):483–531, 2015.

[7] Christopher M Bishop. *Pattern recognition and machine learning*. springer, 2006.

[8] Josh C Bongard and Hod Lipson. Nonlinear system identification using coevolution of models and tests. *IEEE Transactions on Evolutionary Computation*, 9(4):361–384, 2005.

[9] Ivana Bozic, Tibor Antal, Hisashi Ohtsuki, Hannah Carter, Dewey Kim, Sining Chen, Rachel Karchin, Kenneth W Kinzler, Bert Vogelstein, and Martin A Nowak. Accumulation of driver and passenger mutations during tumor progression. *Proceedings of the National Academy of Sciences*, 107(43):18545–18550, 2010.

[10] Rachel B Brem, Gaël Yvert, Rebecca Clinton, and Leonid Kruglyak. Genetic dissection of transcriptional regulation in budding yeast. *Science*, 296(5568):752–755, 2002.

[11] Ido Bright, Guang Lin, and J Nathan Kutz. Compressive sensing based machine learning strategy for characterizing the flow around a cylinder with limited pressure measurements. *Physics of Fluids*, 25(12):127102, 2013.

[12] Dirk Brockmann and Dirk Helbing. The hidden geometry of complex, network-driven contagion phenomena. *science*, 342(6164):1337–1342, 2013.

[13] Christine E Brown, Darya Alizadeh, Renate Starr, Lihong Weng, Jamie R Wagner, Araceli Naranjo, Julie R Ostberg, M Suzette Blanchard, Julie Kilpatrick, Jennifer Simpson, et al. Regression of glioblastoma after chimeric antigen receptor t-cell therapy. *New England Journal of Medicine*, 375(26):2561–2569, 2016.

[14] Christine E Brown and Crystal L Mackall. Car t cell therapy: inroads to response and resistance. *Nature Reviews Immunology*, 19(2):73, 2019.

[15] Steven L Brunton and J Nathan Kutz. *Data-driven science and engineering: Machine learning, dynamical systems, and control*. Cambridge University Press, 2022.

[16] Steven L Brunton, Joshua L Proctor, and J Nathan Kutz. Discovering governing equations from data by sparse identification of nonlinear dynamical systems. *Proceedings of the national academy of sciences*, 113(15):3932–3937, 2016.

[17] Steven L Brunton, Joshua L Proctor, and J Nathan Kutz. Sparse identification of nonlinear dynamics with control (sindyc). *IFAC-PapersOnLine*, 49(18):710–715, 2016.

[18] Patricia K Burgess, Paul M Kulesa, James D Murray, and Ellsworth C Alvord Jr. The interaction of growth rates and diffusion coefficients in a three-dimensional mathematical model of gliomas. *Journal of Neuropathology & Experimental Neurology*, 56(6):704–713, 1997.

[19] Kenneth P Burnham and David R Anderson. Multimodel inference: understanding aic and bic in model selection. *Sociological methods & research*, 33(2):261–304, 2004.

[20] Jared L Callaham, James V Koch, Bingni W Brunton, J Nathan Kutz, and Steven L Brunton. Learning dominant physical processes with data-driven balance models. *Nature communications*, 12(1):1–10, 2021.

[21] Madeleine Cartwright and Georg A Gottwald. A collective coordinate framework to study the dynamics of travelling waves in stochastic partial differential equations. *Physica D: Nonlinear Phenomena*, 397:54–64, 2019.

[22] Kathleen Champion, Bethany Lusch, J Nathan Kutz, and Steven L Brunton. Data-driven discovery of coordinates and governing equations. *Proceedings of the National Academy of Sciences*, 116(45):22445–22451, 2019.

[23] Kathleen Champion, Peng Zheng, Aleksandr Y Aravkin, Steven L Brunton, and J Nathan Kutz. A unified sparse optimization framework to learn parsimonious physics-informed models from data. *IEEE Access*, 8:169259–169271, 2020.

[24] Kathleen P Champion, Steven L Brunton, and J Nathan Kutz. Discovery of nonlinear multiscale systems: Sampling strategies and embeddings. *SIAM Journal on Applied Dynamical Systems*, 18(1):312–333, 2019.

[25] Joseph H Choe, Payal B Watchmaker, Milos S Simic, Ryan D Gilbert, Aileen W Li, Nira A Krasnow, Kira M Downey, Wei Yu, Diego A Carrera, Anna Celli, et al. Synnotch-car t cells overcome challenges of specificity, heterogeneity, and persistence in treating glioblastoma. *Science translational medicine*, 13(591), 2021.

[26] Gary A Churchill, David C Airey, Hooman Allayee, Joe M Angel, Alan D Attie, Jackson Beatty, William D Beavis, John K Belknap, Beth Bennett, Wade Berrettini, et al. The collaborative cross, a community resource for the genetic analysis of complex traits. *Nature genetics*, 36(11):1133–1137, 2004.

[27] Ronald R Coifman, Ioannis G Kevrekidis, Stéphane Lafon, Mauro Maggioni, and Boaz Nadler. Diffusion maps, reduction coordinates, and low dimensional representation of stochastic systems. *Multiscale Modeling & Simulation*, 7(2):842–864, 2008.

[28] Ronald R Coifman and Stéphane Lafon. Diffusion maps. *Applied and computational harmonic analysis*, 21(1):5–30, 2006.

[29] Ronald R Coifman, Stephane Lafon, Ann B Lee, Mauro Maggioni, Boaz Nadler, Frederick Warner, and Steven W Zucker. Geometric diffusions as a tool for harmonic analysis and structure definition of data: Diffusion maps. *Proceedings of the National Academy of Sciences of the United States of America*, 102(21):7426–7431, 2005.

[30] J. Crank and P. Nicolson. A practical method for numerical evaluation of solutions of partial differential equations of the heat conduction type. *Proc. Camb. Phil. Soc.*, 43(1):50–67, 1947.

[31] Emiliano Cristiani, Marta Menci, Marco Papi, and Léonard Brafman. An all-leader agent-based model for turning and flocking birds. *Journal of Mathematical Biology*, 83(4):1–22, 2021.

[32] Mark C Cross and Pierre C Hohenberg. Pattern formation outside of equilibrium. *Reviews of modern physics*, 65(3):851, 1993.

[33] Felipe Cucker and Steve Smale. Emergent behavior in flocks. *IEEE Transactions on automatic control*, 52(5):852–862, 2007.

[34] Jing Cui, Qi Zhang, Qi Song, Herui Wang, Pauline Dmitriev, Mitchell Y Sun, Xiaoyu Cao, Yang Wang, Liemei Guo, Iris H Indig, et al. Targeting hypoxia downstream signaling protein, caix, for car t-cell therapy against glioblastoma. *Neuro-oncology*, 21(11):1436–1446, 2019.

[35] A Darvasi and M Soller. Advanced intercross lines, an experimental population for fine genetic mapping. *Genetics*, 141(3):1199–1207, 1995.

[36] Lisette G de Pillis, Weiqing Gu, and Ami E Radunskaya. Mixed immunotherapy and chemotherapy of tumors: modeling, applications and biological interpretations. *Journal of Theoretical Biology*, 238(4):841–862, 2006.

[37] Lisette G de Pillis, Ami E Radunskaya, and Charles L Wiseman. A validated mathematical model of cell-mediated immune response to tumor growth. *Cancer research*, 65(17):7950–7958, 2005.

[38] Ugo Del Monte. Does the cell number 109 still really fit one gram of tumor tissue? *Cell Cycle*, 8(3):505–506, 2009.

[39] Charles B Delahunt and J Nathan Kutz. A toolkit for data-driven discovery of governing equations in high-noise regimes. *arXiv preprint arXiv:2111.04870*, 2021.

[40] Markus Dihlmann, Martin Drohmann, and Bernard Haasdonk. Model reduction of parametrized evolution problems using the reduced basis method with adaptive time-partitioning. *Proc. of ADMOS*, 2011:64, 2011.

[41] Chris Ding and Xiaofeng He. K-means clustering via principal component analysis. In *Proceedings of the twenty-first international conference on Machine learning*, page 29, 2004.

[42] Rodney M Donlan. Biofilms: microbial life on surfaces. *Emerging infectious diseases*, 8(9):881, 2002.

[43] Emmanuel Donnadieu, Loïc Dupré, Lia Gonçalves Pinho, and Vinicius Cotta-de Almeida. Surmounting the obstacles that impede effective car t cell trafficking to solid tumors. *Journal of Leukocyte Biology*, 108(4):1067–1079, 2020.

[44] Maria Michela D'Aloia, Ilaria Grazia Zizzari, Benedetto Sacchetti, Luca Pierelli, and Maurizio Alimandi. Car-t cells: the long and winding road to solid tumors. *Cell death & disease*, 9(3):1–12, 2018.

[45] Karsten Eichholz, Alvason Zhenhua Li, Kurt Diem, Michael Claus Jensen, Jia Zhu, and Lawrence Corey. A car rna fish assay to study functional and spatial heterogeneity of chimeric antigen receptor t cells in tissue. *Scientific Reports*, 11(1):1–13, 2021.

[46] Toshinari Ema, Kazuhito Funai, Akikazu Kawase, Hiroaki Oiwa, Syuhei Iizuka, and Norihiko Shiiya. A solitary fibrous tumor of the pleura for which the tumor doubling time could be calculated by computed tomography: a case report. *Journal of thoracic disease*, 10(7):E592, 2018.

[47] N Benjamin Erichson, Steven L Brunton, and J Nathan Kutz. Compressed dynamic mode decomposition for background modeling. *Journal of Real-Time Image Processing*, 16(5):1479–1492, 2019.

[48] N Benjamin Erichson, Sergey Voronin, Steven L Brunton, and J Nathan Kutz. Randomized matrix decompositions using r. *arXiv preprint arXiv:1608.02148*, 2016.

[49] Urban Fasel, J Nathan Kutz, Bingni W Brunton, and Steven L Brunton. Ensemble-sindy: Robust sparse model discovery in the low-data, high-noise limit, with active learning and control. *arXiv preprint arXiv:2111.10992*, 2021.

[50] Ronald Aylmer Fisher. *The genetical theory of natural selection*. Oxford Press, 1930.

[51] Peter Friedl and Stephanie Alexander. Cancer invasion and the microenvironment: plasticity and reciprocity. *Cell*, 147(5):992–1009, 2011.

[52] Gary Froyland, Georg A Gottwald, and Andy Hammerlindl. A computational method to extract macroscopic variables and their dynamics in multiscale systems. *SIAM Journal on Applied Dynamical Systems*, 13(4):1816–1846, 2014.

[53] Gary Froyland, Georg A Gottwald, and Andy Hammerlindl. A trajectory-free framework for analysing multiscale systems. *Physica D: Nonlinear Phenomena*, 328:34–43, 2016.

[54] Giovanni Fucà, Loic Reppel, Elisa Landoni, Barbara Savoldo, and Gianpietro Dotti. Enhancing chimeric antigen receptor t-cell efficacy in solid tumors. *Clinical Cancer Research*, 26(11):2444–2451, 2020.

[55] Lorenzo Galluzzi, Aitziber Buque, Oliver Kepp, Laurence Zitvogel, and Guido Kroemer. Immunological effects of conventional chemotherapy and targeted anticancer agents. *Cancer cell*, 28(6):690–714, 2015.

[56] Shea N Gardner. A mechanistic, predictive model of dose-response curves for cell cycle phase-specific and-nonspecific drugs. *Cancer research*, 60(5):1417–1425, 2000.

[57] Andy Goldschmidt, James Kunert-Graf, Adrian C Scott, Zhihao Tan, Aimée M Dudley, and J Nathan Kutz. Quantifying yeast colony morphologies with feature engineering from time-lapse photography. *arXiv preprint arXiv:2201.05259*, 2022.

[58] Georg A Gottwald. Model reduction for networks of coupled oscillators. *Chaos: An Interdisciplinary Journal of Nonlinear Science*, 25(5):053111, 2015.

[59] H. P. Granspan. Models for the growth of a solid tumor by diffusion. *Stud Appl Math*, 51(4):317–340, 1972.

[60] John Burdon Sanderson Haldane. A mathematical theory of natural and artificial selection, part v: selection and mutation. In *Mathematical Proceedings of the Cambridge Philosophical Society*, volume 23, pages 838–844. Cambridge University Press, 1927.

[61] Constance Hammond, Hagai Bergman, and Peter Brown. Pathological synchronization in parkinson's disease: networks, models and treatments. *Trends in neurosciences*, 30(7):357–364, 2007.

[62] Helena Harlin, Yuru Meng, Amy C Peterson, Yuanyuan Zha, Maria Tretiakova, Craig Slingluff, Mark McKee, and Thomas F Gajewski. Chemokine expression in melanoma metastases associated with cd8+ t-cell recruitment. *Cancer Research*, 69(7):3077–3085, 2009.

[63] Tilmann Heil, Ingo Fischer, Wolfgang Elsässer, Josep Mulet, and Claudio R Mirasso. Chaos synchronization and spontaneous symmetry-breaking in symmetrically delay-coupled semiconductor lasers. *Physical Review Letters*, 86(5):795, 2001.

[64] Alexandre V Hirayama, Jordan Gauthier, Kevin A Hay, Jenna M Voutsinas, Qian Wu, Ted Gooley, Daniel Li, Sindhu Cherian, Xueyan Chen, Barbara S Pender, et al. The response to lymphodepletion impacts pfs in patients with aggressive non-hodgkin lymphoma treated with cd19 car t cells. *Blood*, 133(17):1876–1887, 2019.

[65] Seth M Hirsh, David A Barajas-Solano, and J Nathan Kutz. Sparsifying priors for bayesian uncertainty quantification in model discovery. *arXiv preprint arXiv:2107.02107*, 2021.

[66] Alan L Hodgkin and Andrew F Huxley. A quantitative description of membrane current and its application to conduction and excitation in nerve. *The Journal of physiology*, 117(4):500, 1952.

[67] John H Holland. *Emergence: From chaos to order*. OUP Oxford, 2000.

[68] Philip Holmes, John L Lumley, Gahl Berkooz, and Clarence W Rowley. *Turbulence, coherent structures, dynamical systems and symmetry*. Cambridge university press, 2012.

[69] Harold Hotelling. Analysis of a complex of statistical variables into principal components. *Journal of educational psychology*, 24(6):417, 1933.

[70] Jiemiao Hu, Chuang Sun, Chantale Bernatchez, Xueqing Xia, Patrick Hwu, Gianpietro Dotti, and Shulin Li. T-cell homing therapy for reducing regulatory t cells and preserving effector t-cell function in large solid tumors. *Clinical Cancer Research*, 24(12):2920–2934, 2018.

[71] AY Huang, Paul Golumbek, Mojgan Ahmadzadeh, Elizabeth Jaffee, Drew Pardoll, and Hyam Levitsky. Role of bone marrow-derived cells in presenting mhc class i-restricted tumor antigens. *Science*, 264(5161):961–965, 1994.

[72] Elizabeth Hunter, Brian Mac Namee, and John D Kelleher. A taxonomy for agent-based models in human infectious disease epidemiology. *Journal of Artificial Societies and Social Simulation*, 20(3), 2017.

[73] Orit Itzhaki, Elad Jacoby, Abraham Nissani, Michal Levi, Arnon Nagler, Adva Kubi, Karin Brezinger, Hadar Brayer, Li-at Zeltzer, Meir Rozenbaum, et al. Head-to-head comparison of in-house produced cd19 car-t cell in all and nhl patients. *Journal for immunotherapy of cancer*, 8(1), 2020.

[74] Mary Ann Jabra-Rizk, William A Falkler, and Timothy F Meiller. Fungal biofilms and drug resistance. *Emerging infectious diseases*, 10(1):14, 2004.

[75] Mark Johnston. A model fungal gene regulatory mechanism: the gal genes of saccharomyces cerevisiae. *Microbiological reviews*, 51(4):458–476, 1987.

[76] Natasha AN Jorge, Jéssica GV Cruz, Marco Antônio M Pretti, Martín H Bonamino, Patricia A Possik, and Mariana Boroni. Poor clinical outcome in metastatic melanoma is associated with a microrna-modulated immunosuppressive tumor microenvironment. *Journal of translational medicine*, 18(1):1–17, 2020.

[77] Hee Young Ju, Ji Won Lee, Che Ry Hong, Hyery Kim, Kyung Duk Park, Hee Young Shin, Seokuee Kim, Kyungho Jang, Kyung-Sang Yu, In-Jin Jang, et al. Pharmacokinetics of fludarabine in pediatric hematopoietic stem cell transplantation, 2014.

[78] Olivia P Judson. The rise of the individual-based model in ecology. *Trends in ecology & evolution*, 9(1):9–14, 1994.

[79] Carl H June and Michel Sadelain. Chimeric antigen receptor therapy. *New England Journal of Medicine*, 379(1):64–73, 2018.

[80] Kadierdan Kaheman, Steven L Brunton, and J Nathan Kutz. Automatic differentiation to simultaneously identify nonlinear dynamics and extract noise probability distributions from data. *arXiv preprint arXiv:2009.08810*, 2020.

[81] Kadierdan Kaheman, J Nathan Kutz, and Steven L Brunton. Sindy-pi: a robust algorithm for parallel implicit sparse identification of nonlinear dynamics. *Proceedings of the Royal Society A*, 476(2242):20200279, 2020.

[82] Eurika Kaiser, J Nathan Kutz, and Steven L Brunton. Sparse identification of nonlinear dynamics for model predictive control in the low-data limit. *Proceedings of the Royal Society A*, 474(2219):20180335, 2018.

[83] Michael Kalos, Bruce L Levine, David L Porter, Sharyn Katz, Stephan A Grupp, Adam Bagg, and Carl H June. T cells with chimeric antigen receptors have potent antitumor effects and can establish memory in patients with advanced leukemia. *Science translational medicine*, 3(95):95ra73–95ra73, 2011.

[84] Alan A Kaptanoglu, Brian M de Silva, Urban Fasel, Kadierdan Kaheman, Jared L Callaham, Charles B Delahunt, Kathleen Champion, Jean-Christophe Loiseau, J Nathan Kutz, and Steven L Brunton. Pysindy: A comprehensive python package for robust sparse system identification. *arXiv preprint arXiv:2111.08481*, 2021.

[85] Kenji Kawashima, Kohei Yokoi, Haruhisa Matsuguma, Noriki Kamiya, and Naoto Miyazawa. Huge localized mesothelioma of the diaphragm in a 17-year-old female—a case report with calculated tumor volume doubling time—. *The Japanese Journal of Thoracic and Cardiovascular Surgery*, 46(2):225–230, 1998.

[86] Felix P Kemeth, Tom Bertalan, Thomas Thiem, Felix Dietrich, Sung Joon Moon, Carlo R Laing, and Ioannis G Kevrekidis. Learning emergent pdes in a learned emergent space. *arXiv preprint arXiv:2012.12738*, 2020.

[87] William Ogilvy Kermack and Anderson G McKendrick. Contributions to the mathematical theory of epidemics. ii.—the problem of endemicity. *Proceedings of the Royal Society of London. Series A, containing papers of a mathematical and physical character*, 138(834):55–83, 1932.

[88] Khun Visith Keu, Timothy H Witney, Shahriar Yaghoubi, Jarrett Rosenberg, Anita Kurien, Rachel Magnusson, John Williams, Frezghi Habte, Jamie R Wagner, Stephen Forman, et al. Reporter gene imaging of targeted t cell immunotherapy in recurrent glioma. *Science translational medicine*, 9(373):eaag2196, 2017.

[89] Jirayr Kevorkian and Julian D Cole. *Perturbation methods in applied mathematics*, volume 34. Springer Science & Business Media, 2013.

[90] Ioannis G Kevrekidis, C William Gear, James M Hyman, Panagiotis G Kevrekidid, Olof Runborg, Constantinos Theodoropoulos, and others. Equation-free, coarse-grained multiscale computation: Enabling mocroscopic simulators to perform system-level analysis. *Communications in Mathematical Sciences*, 1(4):715–762, 2003.

[91] Danny N Khalil, Eric L Smith, Renier J Brentjens, and Jedd D Wolchok. The future of cancer treatment: immunomodulation, cars and combination immunotherapy. *Nature Reviews Clinical Oncology*, 13(5):273, 2016.

[92] Gregory J Kimmel, Frederick L Locke, and Philipp M Altrock. Evolutionary dynamics of car t cell therapy. *BioRxiv*, page 717074, 2019.

[93] Kite. Yescarta (axicabtagene ciloleucel) highlights of prescribing information, 2017.

[94] Josef Kittler. On the accuracy of the sobel edge detector. *Image and Vision Computing*, 1(1):37–42, 1983.

[95] James N Kochenderfer, Robert PT Somerville, Tangying Lu, Victoria Shi, Adrian Bot, John Rossi, Allen Xue, Stephanie L Goff, James C Yang, Richard M Sherry, et al. Lymphoma remissions caused by anti-cd19 chimeric antigen receptor t cells are associated with high serum interleukin-15 levels. *Journal of clinical oncology*, 35(16):1803, 2017.

[96] James N Kochenderfer, Wyndham H Wilson, John E Janik, Mark E Dudley, Maryalice Stetler-Stevenson, Steven A Feldman, Irina Maric, Mark Raffeld, Debbie-Ann N Nathan, Brock J Lanier, et al. Eradication of b-lineage cells and regression of lymphoma in a patient treated with autologous t cells genetically engineered to recognize cd19. *Blood, The Journal of the American Society of Hematology*, 116(20):4099–4102, 2010.

[97] George Kritikos, Manuel Banzhaf, Lucia Herrera-Dominguez, Alexandra Koumoutsi, Morgane Wartel, Matylda Zietek, and Athanasios Typas. A tool named iris for versatile high-throughput phenotyping in microorganisms. *Nature microbiology*, 2(5):1–10, 2017.

[98] Stephan Kruger, Matthias Ilmer, Sebastian Kobold, Bruno L Cadilha, Stefan Endres, Steffen Ormanns, Gesa Schuebbe, Bernhard W Renz, Jan G D'Haese, Hans Schloesser, et al. Advances in cancer immunotherapy 2019–latest trends. *Journal of Experimental & Clinical Cancer Research*, 38(1):268, 2019.

[99] Yoshiki Kuramoto. Self-entrainment of a population of coupled non-linear oscillators. In *International symposium on mathematical problems in theoretical physics*, pages 420–422. Springer, 1975.

[100] J Nathan Kutz. *Data-driven modeling & scientific computation: methods for complex systems & big data*. Oxford University Press, 2013.

[101] J Nathan Kutz. Advanced differential equations: Asymptotics & perturbations. *arXiv preprint arXiv:2012.14591*, 2020.

[102] J Nathan Kutz, Steven L Brunton, Bingni W Brunton, and Joshua L Proctor. *Dynamic mode decomposition: data-driven modeling of complex systems*. SIAM, 2016.

[103] J Nathan Kutz, Xing Fu, and Steven L Brunton. Multiresolution dynamic mode decomposition. *SIAM Journal on Applied Dynamical Systems*, 15(2):713–735, 2016.

[104] Vladimir A Kuznetsov, Iliya A Makalkin, Mark A Taylor, and Alan S Perelson. Nonlinear dynamics of immunogenic tumors: parameter estimation and global bifurcation analysis. *Bulletin of Mathematical Biology*, 56(2):295–321, 1994.

[105] Can Liu, Vivaswath S Ayyar, Xirong Zheng, Wenbo Chen, Songmao Zheng, Hardik Mody, Weirong Wang, Donald Heald, Aman P Singh, and Yanguang Cao. Model-based cellular kinetic analysis of chimeric antigen receptor-t cells in humans. *Clinical Pharmacology & Therapeutics*, 109(3):716–727, 2021.

[106] Alfred James Lotka. *Elements of physical biology*. Williams & Wilkins, 1925.

[107] Bethany Lusch, J Nathan Kutz, and Steven L Brunton. Deep learning for universal linear embeddings of nonlinear dynamics. *Nature communications*, 9(1):1–10, 2018.

[108] Ailene MacPherson, Stilianos Louca, Angela McLaughlin, Jeffrey B Joy, and Matthew W Pennell. Unifying phylogenetic birth–death models in epidemiology and macroevolution. *Systematic Biology*, 71(1):172–189, 2022.

[109] James MacQueen et al. Some methods for classification and analysis of multivariate observations. In *Proceedings of the fifth Berkeley symposium on mathematical statistics and probability*, volume 1, pages 281–297. Oakland, CA, USA, 1967.

[110] Luke Maggs, Giulia Cattaneo, Ali Emre Dal, Ali Sanjari Moghaddam, and Soldano Ferrone. Car t cell-based immunotherapy for the treatment of glioblastoma. *Frontiers in Neuroscience*, 15:535, 2021.

[111] Kris M Mahadeo, Sajad J Khazal, Hisham Abdel-Azim, Julie C Fitzgerald, Agne Taraseviciute, Catherine M Bollard, Priti Tewari, Christine Duncan, Chani Traube, David McCall, et al. Management guidelines for paediatric patients receiving chimeric antigen receptor t cell therapy. *Nature Reviews Clinical Oncology*, 16(1):45–63, 2019.

[112] Niall M Mangan, Travis Askham, Steven L Brunton, J Nathan Kutz, and Joshua L Proctor. Model selection for hybrid dynamical systems via sparse regression. *Proceedings of the Royal Society A*, 475(2223):20180534, 2019.

[113] Niall M Mangan, Steven L Brunton, Joshua L Proctor, and J Nathan Kutz. Inferring biological networks by sparse identification of nonlinear dynamics. *IEEE Transactions on Molecular, Biological and Multi-Scale Communications*, 2(1):52–63, 2016.

[114] Niall M Mangan, J Nathan Kutz, Steven L Brunton, and Joshua L Proctor. Model selection for dynamical systems via sparse regression and information criteria. *Proceedings of the Royal Society A: Mathematical, Physical and Engineering Sciences*, 473(2204):20170009, 2017.

[115] Hans Meinhardt and Alfred Gierer. Generation and regeneration of sequence of structures during morphogenesis. *Journal of theoretical Biology*, 85(3):429–450, 1980.

[116] Leonor Michaelis, Maud L Menten, et al. Die kinetik der invertinwirkung. *Biochem. z*, 49(333-369):352, 1913.

[117] Kimberly D Miller, Leticia Nogueira, Angela B Mariotto, Julia H Rowland, K Robin Yabroff, Catherine M Alfano, Ahmedin Jemal, Joan L Kramer, and Rebecca L Siegel. Cancer treatment and survivorship statistics, 2019. *CA: A Cancer Journal for Clinicians*, 69(5):363–385, 2019.

[118] Reza Bayat Mokhtari, Tina S Homayouni, Narges Baluch, Evgeniya Morgatskaya, Sushil Kumar, Bikul Das, and Herman Yeger. Combination therapy in combating cancer. *Oncotarget*, 8(23):38022, 2017.

[119] Megan Morrison and J Nathan Kutz. Nonlinear control of networked dynamical systems. *IEEE Transactions on Network Science and Engineering*, 8(1):174–189, 2020.

[120] Adilson E Motter, Changsong Zhou, and Jürgen Kurths. Network synchronization, diffusion, and the paradox of heterogeneity. *Physical Review E*, 71(1):016116, 2005.

[121] Matthias Mulazzani, Simon P Fräßle, Iven von Mücke-Heim, Sigrid Langer, Xiaolan Zhou, Hellen Ishikawa-Ankerhold, Justin Leube, Wenlong Zhang, Sarah Dötsch, Mortimer Svec, et al. Long-term in vivo microscopy of car t cell dynamics during eradication of cns lymphoma in mice. *Proceedings of the National Academy of Sciences*, 116(48):24275–24284, 2019.

[122] Kevin P Murphy. *Machine learning: a probabilistic perspective*. MIT press, 2012.

[123] James D Murray, Philip K Maini, and Robert T Tranquillo. Mechanochemical models for generating biological pattern and form in development. *Physics Reports*, 171(2):59–84, 1988.

[124] JD Murray. Parameter space for turing instability in reaction diffusion mechanisms: a comparison of models. *Journal of theoretical biology*, 98(1):143–163, 1982.

[125] Boaz Nadler, Stéphane Lafon, Ronald R Coifman, and Ioannis G Kevrekidis. Diffusion maps, spectral clustering and reaction coordinates of dynamical systems. *Applied and Computational Harmonic Analysis*, 21(1):113–127, 2006.

[126] Ryota Nakamura, Yoshihisa Inage, Rika Tobita, Kazuko Mori, Takeshi Numata, Hidetoshi Yanai, Takeo Endo, Haruo Ohtani, Hiroaki Satoh, Kenji Yuzawa, et al. Epidermal growth factor receptor mutations: effect on volume doubling time of non–small-cell lung cancer patients. *Journal of Thoracic Oncology*, 9(9):1340–1344, 2014.

[127] Seema Nanda, Lisette G de Pillis, and Ami E Radunskaya. B cell chronic lymphocytic leukemia-a model with immune response. 2013.

[128] Piyush Nathani, Purva Gopal, Nicole Rich, Adam Yopp, Takeshi Yokoo, Binu John, Jorge Marrero, Neehar Parikh, and Amit G Singal. Hepatocellular carcinoma tumour volume doubling time: a systematic review and meta-analysis. *Gut*, 70(2):401–407, 2021.

[129] Sattva S Neelapu. Car-t efficacy: is conditioning the key? *Blood, The Journal of the American Society of Hematology*, 133(17):1799–1800, 2019.

[130] Anandani Nellan, Christopher Rota, Robbie Majzner, Cynthia M Lester-McCully, Andrea M Griesinger, Jean M Mulcahy Levy, Nicholas K Foreman, Katherine E Warren, and Daniel W Lee. Durable regression of medulloblastoma after regional and intravenous delivery of anti-her2 chimeric antigen receptor t cells. *Journal for immunotherapy of cancer*, 6(1):1–14, 2018.

[131] Takashi Nishikawa, Adilson E Motter, Ying-Cheng Lai, and Frank C Hoppensteadt. Heterogeneity in oscillator networks: Are smaller worlds easier to synchronize? *Physical review letters*, 91(1):014101, 2003.

[132] Novartis. Kymriah (tisagenlecleucel) highlights of prescribing information, 2017.

[133] Artem S Novozhilov, Georgy P Karev, and Eugene V Koonin. Biological applications of the theory of birth-and-death processes. *Briefings in bioinformatics*, 7(1):70–85, 2006.

[134] Timo Ojala, Matti Pietikainen, and Topi Maenpaa. Multiresolution gray-scale and rotation invariant texture classification with local binary patterns. *IEEE Transactions on pattern analysis and machine intelligence*, 24(7):971–987, 2002.

[135] Nobuyuki Otsu. A threshold selection method from gray-level histograms. *IEEE transactions on systems, man, and cybernetics*, 9(1):62–66, 1979.

[136] Edward Ott and Thomas M Antonsen. Long time evolution of phase oscillator systems. *Chaos: An interdisciplinary journal of nonlinear science*, 19(2):023117, 2009.

[137] Katherine Owens. PyPl8. `https://github.com/lacyk3/PyPl8`.

[138] Katherine Owens. PyPl8–1.0.5. `https://pypi.org/project/PyPl8/1.0.5`.

[139] Katherine Owens and Ivana Bozic. Modeling car t-cell therapy with patient preconditioning. *Bulletin of Mathematical Biology*, 83(5):1–36, 2021.

[140] Adam C Palmer and Peter K Sorger. Combination cancer therapy can confer benefit via patient-to-patient variability without drug additivity or synergy. *Cell*, 171(7):1678–1691, 2017.

[141] Shaowu Pan, Nicholas Arnold-Medabalimi, and Karthik Duraisamy. Sparsity-promoting algorithms for the discovery of informative Koopman invariant subspaces. (Pope 2001), 2020.

[142] Mark J Panaggio and Daniel M Abrams. Chimera states: coexistence of coherence and incoherence in networks of coupled oscillators. *Nonlinearity*, 28(3):R67, 2015.

[143] Pankita H Pandya, Mary E Murray, Karen E Pollok, and Jamie L Renbarger. The immune system in cancer pathogenesis: potential therapeutic approaches. *Journal of Immunology Research*, 2016, 2016.

[144] Karl Pearson. On lines and planes of closest fit to systems of points in space. *The London, Edinburgh, and Dublin philosophical magazine and journal of science*, 2(11):559–572, 1901.

[145] Benjamin Peherstorfer and Karen Willcox. Online adaptive model reduction for nonlinear systems via low-rank updates. *SIAM Journal on Scientific Computing*, 37(4):A2123–A2150, 2015.

[146] David Pettitt, Zeeshaan Arshad, James Smith, Tijana Stanic, Georg Holländer, and David Brindley. Car-t cells: a systematic review and mixed methods analysis of the clinical trial landscape. *Molecular Therapy*, 26(2):342–353, 2018.

[147] Suani Tavares Rubim de Pinho, HI Freedman, and F Nani. A chemotherapy model for the treatment of cancer with metastasis. *Mathematical and Computer Modelling*, 36(7-8):773–803, 2002.

[148] Daniel A Pollard. Design and construction of recombinant inbred lines. In *Quantitative Trait Loci (QTL)*, pages 31–39. Springer, 2012.

[149] David L Porter, Wei-Ting Hwang, Noelle V Frey, Simon F Lacey, Pamela A Shaw, Alison W Loren, Adam Bagg, Katherine T Marcucci, Angela Shen, Vanessa Gonzalez, et al. Chimeric antigen receptor t cells persist and induce sustained remissions in relapsed refractory chronic lymphocytic leukemia. *Science translational medicine*, 7(303):303ra139–303ra139, 2015.

[150] Mason A Porter and James P Gleeson. Dynamical systems on networks: A tutorial. *arXiv preprint arXiv:1403.7663*, 2014.

[151] Saul J Priceman, Dileshni Tilakawardane, Brook Jeang, Brenda Aguilar, John P Murad, Anthony K Park, Wen-Chung Chang, Julie R Ostberg, Josh Neman, Rahul Jandial, et al. Regional delivery of chimeric antigen receptor–engineered t cells effectively targets her2+ breast cancer metastasis to the brain. *Clinical Cancer Research*, 24(1):95–105, 2018.

[152] Markus Quade, Markus Abel, J Nathan Kutz, and Steven L Brunton. Sparse identification of nonlinear dynamics for rapid model recovery. *Chaos: An Interdisciplinary Journal of Nonlinear Science*, 28(6):063116, 2018.

[153] Benjamin Ribba, Gentian Kaloshi, Mathieu Peyre, Damien Ricard, Vincent Calvez, Michel Tod, Branka Čajavec-Bernard, Ahmed Idbaih, Dimitri Psimaras, Linda Dainese, et al. A tumor growth inhibition model for low-grade glioma treated with chemotherapy or radiotherapy. *Clinical Cancer Research*, 18(18):5071–5080, 2012.

[154] Matthew V Rockman and Leonid Kruglyak. Breeding designs for recombinant inbred advanced intercross lines. *Genetics*, 179(2):1069–1078, 2008.

[155] Katja Rösch, Markus Scholz, and Dirk Hasenclever. Modeling combined chemo- and immunotherapy of high-grade non-hodgkin lymphoma. *Leukemia & Lymphoma*, 57(7):1697–1708, 2016.

[156] Steven A Rosenberg, Nicholas P Restifo, James C Yang, Richard A Morgan, and Mark E Dudley. Adoptive cell transfer: a clinical path to effective cancer immunotherapy. *Nature Reviews Cancer*, 8(4):299–308, 2008.

[157] Peter J Rousseeuw and Katrien Van Driessen. A fast algorithm for the minimum covariance determinant estimator. *Technometrics*, 41(3):212–223, 1999.

[158] Samuel Rudy, Alessandro Alla, Steven L Brunton, and J Nathan Kutz. Data-driven identification of parametric partial differential equations. *SIAM Journal on Applied Dynamical Systems*, 18(2):643–660, 2019.

[159] Samuel H Rudy, Steven L Brunton, and J Nathan Kutz. Smoothing and parameter estimation by soft-adherence to governing equations. *Journal of Computational Physics*, 398:108860, 2019.

[160] Samuel H Rudy, Steven L Brunton, Joshua L Proctor, and J Nathan Kutz. Data-driven discovery of partial differential equations. *Science Advances*, 3(4):e1602614, 2017.

[161] Eun Bi Ryu, Jung Min Chang, Mirinae Seo, Sun Ah Kim, Ji He Lim, and Woo Kyung Moon. Tumour volume doubling time of molecular breast cancer subtypes assessed by serial breast ultrasound. *European radiology*, 24(9):2227–2235, 2014.

[162] Prativa Sahoo, Xin Yang, Daniel Abler, Davide Maestrini, Vikram Adhikarla, David Frankhouser, Heyrim Cho, Vanessa Machuca, Dongrui Wang, Michael Barish, et al. Mathematical deconvolution of car t-cell proliferation and exhaustion from real-time killing assay data. *Journal of the Royal Society Interface*, 17(162):20190734, 2020.

[163] Hayden Schaeffer. Learning partial differential equations via data discovery and sparse optimization. *Proceedings of the Royal Society A: Mathematical, Physical and Engineering Sciences*, 473(2197):20160446, 2017.

[164] Eli Shlizerman, Konrad Schroder, and J Nathan Kutz. Neural activity measures and their dynamics. *SIAM Journal on Applied Mathematics*, 72(4):1260–1291, 2012.

[165] Daniel L Silbergeld and Michael R Chicoine. Isolation and characterization of human malignant glioma cells from histologically normal brain. *Journal of neurosurgery*, 86(3):525–531, 1997.

[166] Jennifer E Smith-Garvin, Gary A Koretzky, and Martha S Jordan. T cell activation. *Annual Review of Immunology*, 27:591–619, 2009.

[167] Steven H Strogatz. From kuramoto to crawford: exploring the onset of synchronization in populations of coupled oscillators. *Physica D: Nonlinear Phenomena*, 143(1-4):1–20, 2000.

[168] Kristin R Swanson, Carly Bridge, JD Murray, and Ellsworth C Alvord Jr. Virtual and real brain tumors: using mathematical modeling to quantify glioma growth and invasion. *Journal of the neurological sciences*, 216(1):1–10, 2003.

[169] Taddei, T., Perotto, S., and Quarteroni, A. Reduced basis techniques for nonlinear conservation laws. *ESAIM: M2AN*, 49(3):787–814, 2015.

[170] Kunihiko Taira, Steven L Brunton, Scott Dawson, Clarence W Rowley, Tim Colonius, Beverley J McKeon, Oliver T Schmidt, Stanislav Gordeyev, Vassilios Theofilis, and Lawrence S Ukeiley. Modal analysis of fluid flows: An overview. *AIAA Journal*, 55(12):4013–4041, 2017.

[171] Julia Tchou, Yangbing Zhao, Bruce L Levine, Paul J Zhang, Megan M Davis, Jan Joseph Melenhorst, Irina Kulikovskaya, Andrea L Brennan, Xiaojun Liu, Simon F Lacey, et al. Safety and efficacy of intratumoral injections of chimeric antigen receptor (car) t cells in metastatic breast cancer. *Cancer immunology research*, 5(12):1152–1161, 2017.

[172] Daniela S Thommen and Ton N Schumacher. T cell dysfunction in cancer. *Cancer Cell*, 33(4):547–562, 2018.

[173] D'Arcy W Thompson and JT Bonner. 1942. on growth and form. *Camb. Univ. Press: Cambridge*, 1917.

[174] P Tracqui, GC Cruywagen, DE Woodward, GT Bartoo, JD Murray, and EC Alvord Jr. A mathematical model of glioma growth: the effect of chemotherapy on spatio-temporal growth. *Cell proliferation*, 28(1):17–31, 1995.

[175] Hayden Tronnolone, Jennifer M Gardner, Joanna F Sundstrom, Vladimir Jiranek, Stephen G Oliver, and Benjamin J Binder. Tammicol: Tool for analysis of the morphology of microbial colonies. *PLoS computational biology*, 14(12):e1006629, 2018.

[176] Alan Mathison Turing. The chemical basis of morphogenesis. *Bulletin of mathematical biology*, 52(1):153–197, 1990.

[177] Cameron J Turtle, Laïla-Aïcha Hanafi, Carolina Berger, Theodore A Gooley, Sindhu Cherian, Michael Hudecek, Daniel Sommermeyer, Katherine Melville, Barbara Pender, Tanya M Budiarto, et al. Cd19 car–t cells of defined cd4+: Cd8+ composition in adult b cell all patients. *The Journal of clinical investigation*, 126(6):2123–2138, 2016.

[178] Peter Uhlhaas, Gordon Pipa, Bruss Lima, Lucia Melloni, Sergio Neuenschwander, Danko Nikolić, and Wolf Singer. Neural synchrony in cortical networks: history, concept and current status. *Frontiers in integrative neuroscience*, 3:17, 2009.

[179] Floris Van Van Breugel, J Nathan Kutz, and Bingni W Brunton. Numerical differentiation of noisy data: A unifying multi-objective optimization framework. *IEEE Access*, 8:196865–196877, 2020.

[180] Laetitia Vercellino, Roberta Di Blasi, Salim Kanoun, Benoit Tessoulin, Cedric Rossi, Maud D'Aveni-Piney, Lucie Obéric, Caroline Bodet-Milin, Pierre Bories, Pierre Olivier, et al. Predictive factors of early progression after car t-cell therapy in relapsed/refractory diffuse large b-cell lymphoma. *Blood advances*, 4(22):5607–5615, 2020.

[181] Jessie Villanueva and Meenhard Herlyn. Melanoma and the tumor microenvironment. *Current oncology reports*, 10(5):439–446, 2008.

[182] Vito Volterra. Fluctuations in the abundance of a species considered mathematically. *Nature*, 118(2972):558–560, 1926.

[183] Karin Voordeckers, Dries De Maeyer, Elisa van der Zande, Marcelo D Vinces, Wim Meert, Lore Cloots, Owen Ryan, Kathleen Marchal, and Kevin J Verstrepen. Identification of a complex genetic network underlying s accharomyces cerevisiae colony morphology. *Molecular microbiology*, 86(1):225–239, 2012.

[184] Xiao Wang, Irene Scarfò, Andrea Schmidts, Mehmet Toner, Marcela V Maus, and Daniel Irimia. Dynamic profiling of antitumor activity of car t cells using micropatterned tumor arrays. *Advanced Science*, 6(23):1901829, 2019.

[185] Evan W Weber, Kevin R Parker, Elena Sotillo, Rachel C Lynn, Hima Anbunathan, John Lattin, Zinaida Good, Julia A Belk, Bence Daniel, Dorota Klysz, et al. Transient rest restores functionality in exhausted car-t cells through epigenetic remodeling. *Science*, 372(6537), 2021.

[186] E Weinan, Bjorn Engquist, and others. The heterogeneous multiscale methods. *Communications in Mathematical Sciences*, 1(1):87–132, 2003.

[187] Stephen Wiggins. *Introduction to applied nonlinear dynamical systems and chaos*, volume 2. Springer Science & Business Media, 2003.

[188] Yonghong Xie and Qiang Ji. A new efficient ellipse detection method. In *Object recognition supported by user interaction for service robots*, volume 2, pages 957–960. IEEE, 2002.

[189] Syunsuke Yamamoto, Shin-ichi Matsumoto, Akihiko Goto, Miyuki Ugajin, Miyu Nakayama, Yuu Moriya, and Hideki Hirabayashi. Quantitative pcr methodology with a volume-based unit for the sophisticated cellular kinetic evaluation of chimeric antigen receptor t cells. *Scientific Reports*, 10(1):1–10, 2020.

[190] Yoichiro Yamamoto, Chetan P Offord, Go Kimura, Shigehiko Kuribayashi, Hayato Takeda, Shinichi Tsuchiya, Hisashi Shimojo, Hiroyuki Kanno, Ivana Bozic, Martin A Nowak, et al. Tumour and immune cell dynamics explain the psa bounce after prostate cancer brachytherapy. *British Journal of Cancer*, 115(2):195–202, 2016.

[191] Toshinori Yamashita and Takeo Kuwabara. Estimation of rate of growth of malignant brain tumors by computed tomography scanning. *Surgical neurology*, 20(6):464–470, 1983.

[192] Zhi-Zhang Yang, Anne J Novak, Steven C Ziesmer, Thomas E Witzig, and Stephen M Ansell. Attenuation of cd8+ t-cell function by cd4+ cd25+ regulatory t cells in b-cell non-hodgkin's lymphoma. *Cancer research*, 66(20):10145–10152, 2006.

[193] Ge Zhang, Lei Wang, Honglian Cui, Xiaomin Wang, Ganlin Zhang, Juan Ma, Huamin Han, Wen He, Wei Wang, Yunfeng Zhao, et al. Anti-melanoma activity of t cells redirected with a tcr-like chimeric antigen receptor. *Scientific Reports*, 4:3571, 2014.

[194] Chaozhi Zheng, Martin P. Boer, and Fred A Van Eeuwijk. A general modeling framework for genome ancestral origins in multiparental populations. *Genetics*, 198(1):87–101, 2014.

[195] Peng Zheng, Travis Askham, Steven L Brunton, J Nathan Kutz, and Aleksandr Y Aravkin. A unified framework for sparse relaxed regularized regression: Sr3. *IEEE Access*, 7:1404–1423, 2018.